Alpha-synuclein spreading pathology in Parkinson's disease: the influence of iron and the Rho-kinase inhibitor fasudil

Dissertation

for the award of the degree

"Doctor rerum naturalium"

of the Georg-August-Universität Göttingen

within the doctoral program

"Cellular and Molecular Physiology of the Brain"

of the Georg-August University School of Science (GAUSS)

submitted by

Karina Joppe

from Einbeck

Göttingen, January 2020

Thesis Committee

Prof. Dr. Paul Lingor (Department of Neurology, University Medical Center Göttingen; Department of Neurology, Klinikum rechts der Isar, TU München)

Prof. Dr. Tiago Fleming Outeiro (Department of Experimental Neurodegeneration, University Medical Center Göttingen)

Prof. Dr. Markus Zweckstetter (Translational Structural Biology in Dementia, German Center for Neurodegenerative Diseases Göttingen; Protein structure determination using NMR, Max Planck Institute for Biophysical Chemistry Göttingen)

Members of the Examination Board

1st Referee: Prof. Dr. Paul Lingor (Department of Neurology, University Medical Center Göttingen; Department of Neurology, Klinikum rechts der Isar, TU München)

2nd Referee: Prof. Dr. Tiago Fleming Outeiro (Department of Experimental Neurodegeneration, University Medical Center Göttingen)

Further members of the Examination Board

Prof. Dr. Markus Zweckstetter (Translational Structural Biology in Dementia, German Center for Neurodegenerative Diseases Göttingen; Protein structure determination using NMR, Max Planck Institute for Biophysical Chemistry Göttingen)

Prof. Dr. Tim Salditt (Institute for X-Ray Physics, Georg-August-University Göttingen)

Prof. Dr. Christine Stadelmann-Nessler (Institute of Neuropathology, University Medical Center Göttingen)

Prof. Dr. Thomas Dresbach (Department of Anatomy and Embryology, University Medical Center Göttingen)

Date of oral examination: 10.03.2020

Declaration

I, Karina Joppe, hereby declare that the doctoral thesis entitled

"Alpha-synuclein spreading pathology in Parkinson's disease: the influence of iron and the Rho-kinase inhibitor fasudil"

has been written independently and with no other sources and aids than quoted.

Göttingen, January 2020   Karina Joppe

Preface

Parts of the Chapter 1 "Introduction" were already published in an altered and abbreviated version as a review article in the journal *Frontiers in Neuroscience*. For this doctoral thesis, the text was rephrased and mainly integrated in the sections 1.3.1, 1.3.2, 1.4.1 and 1.5. The Figure 1 was adapted from the same aforementioned article. Detailed information of the review article: Joppe K, Roser A-E, Maass F and Lingor P (2019). The Contribution of Iron to Protein Aggregation Disorders in the Central Nervous System. Front. Neurosci. 13, 15.

Two manuscripts were prepared which resemble parts of this doctoral thesis in form and content of the description and discussion of results as well as in methods. Related figures were modified for this document.

The first manuscript is related to the results described in chapter 3.1.1 and 3.1.2 as well as to the corresponding method chapters (2.2.1.1 – 2.2.1.3, 2.2.6) and discussion chapters (4.1.1, 4.1.2). Detailed information of the manuscript: Joppe K, Nicolas J-D, Grünewald T A, Eckermann M, Salditt T and Lingor P (2020). Elemental quantification and analysis of structural abnormalities in neurons from Parkinson's-diseased brains by X-ray fluorescence microscopy and diffraction. Biomed. Opt. Express 11(7), 3423-3443, https://doi.org/10.1364/BOE.389408.

The second manuscript is related to the results described in chapter 3.2 and 3.3 as well as to the corresponding method and discussion chapters. Preliminary information on title and authors of the manuscript: Joppe K, Tatenhorst L, Carboni E, Caldi Gomes L, Roser A-E, El DeBakey H, Bähr M, Vogel-Mikuš K, Ip C W, Becker S, Zweckstetter M and Lingor P. Iron-induced reduction of α-synuclein spreading and microglia accumulation (in preparation).

Meiner Familie

Hindernisse und Schwierigkeiten sind Stufen,

auf denen wir in die Höhe steigen.

– Friedrich Nietzsche

Table of contents

List of abbreviations

5-CSRTT: 5-choice serial reaction time task

6-OHDA: 6-hydroxydopamine

α-syn: alpha-synuclein

Aβ: amyloid-beta

AAS: atomic absorption spectroscopy

AD: Alzheimer's disease

ALP: autophagy-lysosomal pathway

ALS: amyotrophic lateral sclerosis

AraC: cytosine arabinoside

BBB: blood-brain-barrier

BSA: bovine serum albumin

bw: body weight

CD3+: CD3-positive

CD11b: Integrin α-M

CD11b+: CD11b-positive

CMF: Calcium-magnesium-free medium

CNS: central nervous system

CO: control (patient group)

CSF: cerebrospinal fluid

Ctrl: control mice (treated with vehicle instead of iron)

DAB: diaminobenzidine-HCl

DAPI: 4′,6-Diamidin-2-phenylindole

DLB: dementia with Lewy bodies

doi: day of injection

dpi: days post injection

div: day in vitro/ days in vitro

DMTP: delayed matching to position

DNMTP: delayed nonmatching to position

E18.5: embryonic day 18.5

EDX: energy-dispersive X-ray spectroscopy

ESRF: European Synchrotron Radiation Facility

Exp.: experiment

F: female

FCS: fetal calf serum

GC-MS: Gas chromatography-mass spectrometry

GPe: external globus pallidus

GPi: internal globus pallidus

H_2O_2: Hydrogen peroxide

HBSS: Hank's Balanced Salt Solution

HCl: Hydrochloric acid

HPLC: high performance liquid chromatography

hum α-syn: human α-syn

ICP-MS: inductively coupled plasma mass spectrometry

IHC: immunohistochemistry

IRE: iron responsive element

IREs: iron responsive elements

IRP: iron regulatory protein

LAG3: lymphocyte-activation gene 3

LA-ICP-MS: Laser ablation inductively coupled plasma mass spectrometry

LBs: Lewy bodies

LBDBS: Lewy body disease (α-synucleinopathy) brain-stem predominant

LBDN: Lewy body disease (α-synucleinopathy) neocortical predominant

LDL: low density lipoprotein

L-DOPA: L-3,4-dihydroxyphenylalanine / levodopa

LPS: lipopolysaccharide

LTM: long-term memory

M: male

MAO-B: monoamine oxidase-B

MPTP: 1-methyl-4-phenyl-1,2,3,6-tetrahydropyridine

MRI: magnetic resonance imaging

MS: multiple sclerosis

ms α-syn: mouse α-syn

MSA: multiple system atrophy

MTBE: methyl-tert-butyl ether

N/A: not available

nANOVA: nested ANOVA

NaOH: sodium hydroxide

NaN$_3$: sodium azide

NCEH-1: neutral cholesterol ester hydrolase 1

NDDs: Neurodegenerative diseases

NGS: normal goat serum

NHS: normal horse serum

Nissl+: Nissl-positive

NOR: Novel object recognition (test)

NOX2: NADPH oxidase 2

Nramp1: natural resistance-associated macrophage protein-1

n.s.: not significant

p10-17: postnatal day 10-17

PBS: Phosphate buffer solution

PD: Parkinson's disease

PFA: para-formaldehyde

PFFs: α-syn preformed-fibrils

PIXE: particle-induced X-ray emission

PLL: poly-L Lysine Hydrate

PP: polypropylene

pS129-α-syn: α-syn phosphorylated at S129

QSM: quantitative susceptibility mapping

ROCK: Rho-associated protein kinase

ROI: region of interest

ROIs: regions of interest

ROS: reactive oxygen species

RT: room temperature

SDC: members of the syndecan

SDS: sodium dodecyl sulphate

SN: substantia nigra

SNpc: substantia nigra pars compacta

SNpr: substantia nigra pars reticulata

SOD1: superoxide dismutase 1

SSS: sufficient summary statistics

STM: short-term memory

STXM: scanning transmission X-ray microscopy

SW: Shapiro-Wilk test

TBS: tris-buffered saline

TBS-T: TBS-Tween 20

TDP-43: TAR DNA-binding protein 43

TFEB: nuclear transcription factor EB

TH: tyrosine hydroxylase

TH+: tyrosine hydroxylase-positive

UPDRS: Unified Parkinson's Disease Rating Scale

UPS: ubiquitin proteasome system

XRD: X-ray diffraction

XRF: X-ray fluorescence

List of figures

List of tables

1   Introduction

1.1   Neurodegenerative diseases

Neurodegenerative diseases (NDDs) can be characterized by the progressive degeneration of neurons in the central nervous system (CNS) as well as in the peripheral nervous system. The neurodegeneration is the fundamental pathology of NDDs but the symptomatology of NDDs differs depending on the affected cell types and brain structures. For instance, a decline of motoric, sensory or cognitive functions is triggered depending on the affected brain areas. Alzheimer's disease (AD), Parkinson's disease (PD), Huntington's disease, amyotrophic lateral sclerosis (ALS) and prion diseases belong to the most prominent and frequently occurring NDDs worldwide (Stroo et al., 2017).

Although earlier research put focus on the differences of NDD pathomechanisms, it is known that NDDs share certain characteristics, such as protein aggregation. Misfolding, aggregation and accumulation of proteins seems to be one major reason for neurodegeneration in the brain. Depending on the individual NDD, different proteins are involved in the pathophysiology such as amyloid-beta (Aβ) and Tau in AD, alpha-synuclein (α-syn) in PD, superoxide dismutase 1 (SOD1) and TAR DNA-binding protein 43 (TDP-43) in ALS. However, amyloidogenic proteins were found to interact and reinforce aggregation thereof mutually. For instance, recent insights indicated a supportive effect of Aβ on Tau aggregation (Bennett et al., 2017; He et al., 2017; Vasconcellos et al., 2016), of Tau on α-syn (Arai et al., 2001; Badiola et al., 2011; Ishizawa et al., 2003) and SOD1 (Pace et al., 2018), of α-syn on Tau (Oikawa et al., 2016) and SOD1 (Helferich et al., 2015; Koch et al., 2016) as well as an effect of SOD1 on TDP-43 accumulation (Jeon et al., 2019; Zeineddine et al., 2017). Not only protein aggregation causes neuronal loss, also mitochondrial dysfunction or pathways of programmed cell death are involved. Iron dyshomeostasis is also suggested as a causative agent for such devastating mechanisms in NDDs such as AD or PD (Ashraf et al., 2018).

It is still under investigation if protein misfolding and iron accumulation are causative mechanisms for the pathology or if they are caused by other mechanisms. Since aging appears to be a risk factor for NDDs, the constantly rising age is additionally challenging the whole society (Fu et al., 2018; Gan et al., 2018). No cure can be provided so far and in the best cases therapeutic actions only alleviate the symptomatology. Therefore, it is

important to investigate the underlying pathomechanisms of NDDs to identify biomarkers and curative medicine preventing and stopping disease progression.

1.2 Parkinson's disease

In 1817, James Parkinson firstly described the disorder by publishing his observations about the symptomatology (Parkinson, 1817). Affecting approximately 1 % of the population above 60 years of age, PD is the second most common neurodegenerative disorder after AD (De Lau and Breteler, 2006). In 2016, globally 6.1 million people were affected from PD. The prevalence was greatly increasing since 1990 when just 2.5 million cases were reported. This observation is not only explicable by increased numbers of aging people. Other reasons for increased prevalence numbers could be for example an increase in awareness for NDDs and the improvement of study methodology. Due to the industrialization also in rural areas of the world, the population is also affected by occupational environmental factors, such as pesticides or solvents. Moreover, the disease duration of PD patients increases resulting in a higher prevalence even with unchanged incidence (Dorsey et al., 2018). Based on the Global Burden of Disease Study it is assumed that with the currently existing growth rate of PD cases the number will increase up to 12.9 million cases in 2040 (Dorsey and Bloem, 2018). Focusing at the United States solely, it is estimated that by 2030 1 million people in the US will be affected by PD (Marras et al., 2018). A recent literature search (Abbas et al., 2018) separating the whole world's population into Western (Russia, Europe, Australia, New Zealand and whole America) and Eastern countries (Asia and Middle East) revealed interesting differences regarding incidence, prevalence and gender dominance. Accordingly, PD is an age-dependent disease which is predominant for males and the rates for prevalence and incidence are slightly higher in the Western countries compared to the Eastern countries (Abbas et al., 2018).

1.2.1 Symptomatology

PD patients show a progressive and chronic loss of the motor function which affects for example balance, control of fine motor and gross motor skills. PD patients show symptoms such as bradykinesia (slowing of movements) accompanied with resting tremor, rigidity, postural instability, freezing of movements or circular hand movements called pill-rolling type of tremor (Sveinbjornsdottir, 2016). The main cause of the symptoms is the neurodegeneration, which starts 5 to 15 years before first motor symptoms become

apparent. At the timepoint of diagnosis already 40-60 % of neurons in the substantia nigra (SN) are degenerated (Berg et al., 2012).

Besides motor function abnormalities non-motor symptoms have been reported several years before the initial motor symptomatology. Fatigue, pain, anxiety, hypophonia, dysphagia, hallucinations, cognitive dysfunction and dementia are exemplary non-motor symptoms. It has been suggested that these non-motor anomalies can be classified into different stages based on the disease progression (Schapira et al., 2017). The earliest symptoms occurring years before the diagnosis are reduced olfaction (hyposmia), REM sleep behavior disorder, development of depression and constipation. However, due to their limited specificity, these alterations are usually not recognized as prodromal PD symptoms (Schapira et al., 2017; Schrag et al., 2015).

The onset time of symptoms, such as freezing of gait, is related to disease progression and to an occurrence of specific non-motor symptoms (Virmani et al., 2015). Accordingly, forming PD subtypes based on age at diagnosis or specific symptoms can help estimating disease progression, survival or related non-motor symptomatology (De Pablo-Fernández et al., 2019; Virmani et al., 2015). Another study found that specific non-motor symptoms and their severity levels can also be assigned to subtypes formed on the occurrence of specific motor symptoms (Huang et al., 2019). This leads to the assumptions that patients possibly express different symptomatic patterns and PD is a collective term incorporating several subtypes.

1.2.2 Pathophysiology

One of the major hallmarks of PD is the degeneration of neuromelanin-containing dopaminergic neurons within the SN pars compacta (SNpc) as part of the midbrain (Lees et al., 2008). The SN belongs to the extrapyramidal system which contributes to the control processes of the motor function. The loss of cell bodies within the SN is likely a downstream finding in PD. In accordance to the 'dying back' hypothesis firstly described by (Hornykiewicz, 1998), it is assumed that axonal terminals within the striatum degenerate prior to the death of neuronal cell bodies within the SN. Studies could show that motor symptoms are observed when approximately 30 % of dopaminergic neurons are lost. However, at this time point approximately 50-60 % of striatal projections are degenerated (Cheng et al., 2010). Due to this degeneration of striatal projections and cell loss within the

SN, a depletion of dopamine arises which triggers the prominent motor impairments in PD patients broadly described in chapter 1.2.1.

Neuromelanin-positive dopaminergic neurons in the SN belong to the basal ganglia and, therefore, they contribute to voluntary movement control. The nuclei of the basal ganglia are interconnected. Since long axons of nigral dopaminergic neurons project into the striatum, dopamine modulates the activation of spiny neurons in the striatum through dopamine receptors. Striatal neurons are in turn directly and indirectly connected with the globus pallidus and the SN. According to the direct pathway, an excitatory input leads to an activation of the dopamine receptor D1 on GABAergic spiny cells in the striatum which project to the internal globus pallidus (GPi). This induces an inhibition of the GPi which in turn triggers an excitation of the thalamus and motor cortex. In an indirect pathway, the transmission of inhibitory inputs to the external globus pallidus (GPe) is dependent on other spiny neurons expressing D2 dopamine receptors. This leads to a decrease of the excitatory output of the subthalamic nucleus which in turn activates the GPi and thus inhibits the thalamus and motor cortex. Being the brain region of motor behavior controlling, the motor cortex is targeted by efferences from the ventral nucleus of the thalamus and it provides further input to the spinal cord, striatum and SN pars reticulata (SNpr) (DeLong and Wichmann, 2007; Obeso et al., 2000).

Dopamine transmitted from neurons in the SN plays an important role in these basal ganglia circuits. The release of dopamine within the striatum either supports the direct pathway or suppresses the indirect pathway. Thereby dopamine ensures that both pathways are balanced. Since voluntary movement can just be controlled when these circuits operate efficiently, motor disturbances in PD can be explained by a transmitter dyshomeostasis. Accordingly, in PD patients, a dopamine depletion in axon terminals within the striatum increases the activation of the GPi which thereafter triggers an activity decrease of the thalamus and motor cortex (DeLong and Wichmann, 2007; Obeso et al., 2000).

1.3 Etiology of PD

PD patients are assigned to either idiopathic/sporadic or familial disease etiology. It is presumed that the majority of patients suffer from idiopathic PD. Estimations on the proportion of cases with a genetic linkage vary, but in recent reviews it is assumed that 5-30 % of cases can be explained by heritability (Alves et al., 2008; Balestrino and Schapira,

2019; Billingsley et al., 2018; Zhang et al., 2018). The development of an inherited form of PD can be triggered by autosomal mutations in different genes such as SNCA, LRRK2, PARKIN, PINK1, ATP13A2 and DJ-1 (Fu et al., 2018).

Although the genetic predisposition determines the development of PD in the inherited cases, idiopathic and inherited PD cases show several common underlying mechanisms which possibly trigger neurodegeneration such as α-syn misfolding and aggregation, reactive oxygen species (ROS) production as well as mitochondrial dysfunction or neuroinflammation (Johnson et al., 2019). These possible pathomechanisms can affect each other mutually. For instance, α-syn is able to trigger reactive microgliosis as a part of neuroinflammation which leads to neurodegeneration (Duffy et al., 2018). Another study highlighted that neuroinflammation and α-syn show synergistic effects (Gao et al., 2011). Furthermore, α-syn can trigger oxidative stress and mitochondrial dysfunction (Hsu et al., 2000), whereas oxidative stress enhances α-syn aggregation (Scudamore and Ciossek, 2018). Metal dyshomeostasis, especially of iron, also plays an important role in neurodegeneration and can mediate the above-mentioned mutual effects of α-syn and oxidative stress (Deas et al., 2016; Levin et al., 2011; Li et al., 2011).

This multitude of mechanisms possibly causing, facilitating or aggravating PD pathology leads to the assumption that PD describes a cluster of pathological subtypes which differ regarding their exact pathomechanism (Johnson et al., 2019). Aggregation of α-syn and its spreading as well as metal dyshomeostasis play an essential role in the pathogenesis of PD and are regarded as important disease causes or triggers. Therefore, both pathological events are discussed in detail in the following chapters.

1.3.1 The role of α-syn and its aggregation

Consisting of 140 amino acids, α-syn is a small protein with a molecular weight of around 14 kDa. It is part of the synuclein protein family which is completed by β- and γ-syn. All together they are neuronal nuclear proteins, but α- and β-syn are also present in axons and presynaptic nerve terminals (George, 2002). Even if not all functions of α-syn are known, membrane remodeling, vesicle packaging as well as their release and trafficking have been studied in detail (Bendor et al., 2013; Rocha et al., 2018). Furthermore, α-syn is an important player in the synaptic machinery due to its high numbers of interaction partners at the synapse (reviewed in (Longhena et al., 2019). In the last decades, α-syn was found to play an important role in the pathogenesis of different NDDs such as PD, multiple

system atrophy (MSA) or dementia with Lewy bodies (DLB) so that all of these α-syn-affiliated disorders were summarized under the synonymous 'synucleinopathies' (Goedert et al., 2010).

In PD pathophysiology, special attention is paid to the protein α-syn due to the involvement of the SNCA gene, encoding for α-syn, in the familial type of disease. Either point mutations or an α-syn overproduction triggered by multiplications of the SNCA gene was shown to cause PD. Six identified point mutations for SNCA named A30P, E46K, H50Q, G51D, A53T, and A53E were found to trigger a biophysical change in terms of amino acid substitutions (Appel-Cresswell et al., 2013; Ki et al., 2007; Krüger et al., 1998; Lesage et al., 2013; Pasanen et al., 2014; Zarranz et al., 2004).

Furthermore, α-syn has been related to another pathological hallmark in brains of PD patients: Lewy bodies (LBs). LBs are intracytoplasmatic protein aggregate inclusions containing for example ubiquitin and neurofilaments, but the most abundant protein in LBs is α-syn (Spillantini et al., 1997, 1998). Whereas LBs are globular structures found in the perikarya of cells, spindle-shaped, aggregated structures in neurites are called Lewy neurites (Spillantini et al., 1998). Such aggregates were not only found in dopaminergic neurons within the SN, as the mainly affected brain region in PD, they rather spread throughout the whole brain (Braak et al., 2003).

It is still a contentious issue if LBs are neurotoxic and trigger neurodegeneration (Braak et al., 2003; Lu et al., 2005) or if they act neuroprotectively by trapping pathological species of α-syn (Kramer and Schulz-Schaeffer, 2007; Recasens et al., 2014). Studies suggest that the toxicity originates from presynaptically available α-syn species (Kramer and Schulz-Schaeffer, 2007) and that oligomeric species are neurotoxic that are formed preceding to aggregates contained in LBs. Accordingly, a study verified that cell damage was caused before aggregate structures were detected (Pinotsi et al., 2016). Therefore, the misfolding and different conformational states of α-syn play an important role in the disease progression.

The sequence of α-syn is fundamental to explain its structural plasticity and is comprised of three different parts: the amino terminus (residues 1-60), the non-amyloid-component (NAC) domain (residues 61-95) and the negatively charged carboxyl terminus. The NAC region constitutes the central hydrophobic region and it enables β-sheet formation of α-syn, which is crucial to perform self-aggregation (Breydo et al., 2012; Li et

al., 2002). Based on the environmental circumstances, α-syn adopts different conformations (Uversky, 2003). It is supposed that α-syn undergoes structural shifts from monomer to β-sheet enriched fibrils by passing conformational changes to oligomers, ribbons and protofibrils. These intermediate, pathogenic stages are also called α-syn 'strains'. Various α-syn strains show different levels of neurotoxicity and provoke thereby different PD-characteristic effects such as cell loss or motor deficits in animal models. These observations possibly explain pathological heterogeneity of synucleinopathies (Peelaerts and Baekelandt, 2016; Peelaerts et al., 2015). However, a recent study might refute that one specific strain belongs to one specific disease, since fibrils amplified from tissue of PD and MSA patients showed a strong structural variability. Patient-derived fibrils differed from recombinant α-syn fibrils and extracts from PD brains showed more structural heterogeneity compared to MSA brain extracts. This might suggest that different α-syn aggregate structures can be associated with specific PD subtypes identified by distinct phenotypes or characteristics in disease progression (Strohäker et al., 2019).

Investigating aggregation processes in the genetic context, different α-syn mutations were found to trigger its oligomerization similarly. However, the effect on the aggregation process and inclusion formation depend on the specific mutation (Lázaro et al., 2014). Even if in some patients the genetic component explains α-syn pathology, tissue of idiopathic PD patients also exhibit LB pathology with α-syn aggregate formation (Baba et al., 1998; Braak et al., 2003), assuming that the machinery of protein handling and degradation is defected in both disease types. For instance, it is supposed that oxidative stress affects control systems for conformational changes of proteins. As key mechanisms to handle intracellular protein aggregates under physiological conditions the ubiquitin proteasome system (UPS) and the autophagy-lysosomal pathway (ALP) have been reviewed. Regarding the ALP, mainly chaperon activity and macroautophagy via autophagosomes are involved in α-syn degradation (Stroo et al., 2017; Xilouri et al., 2013). It has been shown that UPS and the ALP are linked and exhibit a complex crosstalk, so that in case of malfunction one mechanism is able to compensate the other (Ebrahimi-Fakhari et al., 2011; Yang et al., 2013). However, LB-like α-syn aggregates can affect these mechanisms. For instance, in one study the aggregates induced an impairment of the macroautophagy and were resistant against degradation (Tanik et al., 2013).

In case of extracellular aggregate deposits, different cell types are supposed to help in the degradation process such as glia cells (Stefanis et al., 2019). Microglia were shown

to be the major scavenger cells of α-syn aggregates. However, the phagocytic ability of microglia is dependent on the conformational state of α-syn (Choi et al., 2015; Lee et al., 2008; Park et al., 2008). Also astrocytes were shown to affect α-syn degradation by trapping α-syn and clearing the deposits (Loria et al., 2017). Taken together, α-syn misfolding and aggregation plays an important role in PD development. Available clearing processes of α-syn species are multifaceted but are not able to prevent aggregation.

1.3.1.1 Propagation of α-syn

Even if the neurodegeneration process within the SN is the main characteristic of PD responsible for the motor dysfunctions in patients, it is now common sense that PD pathology is not initiated within this region. Braak and colleagues described that LB pathology as conceivable trigger of neurodegeneration possibly starts within the medulla oblongata/pontine tegmentum and the olfactory bulb/anterior olfactory nucleus (Braak et al., 2003). The authors suggest a LB pathology progression through the brain in accordance to six different stages. The findings support the hypothesis that α-syn pathology affects interconnected brain regions and therefore follows hierarchical, predictable patterns (Braak et al., 2003, 2004).

Furthermore, the hypothesis of a prion-like behavior of α-syn arose due to several observations. It is proposed that α-syn may self-propagate and its cell-to-cell transmission finally triggers misfolding and aggregation of endogenous α-syn. This assumption was firstly supported by the identification of host-to-graft transmission of aggregates in brains of PD patients (Kordower et al., 2008a, 2008b; Li et al., 2008). Accordingly, it was assumed that extracellularly available α-syn due to neuronal release or dying cells is uptaken by the grafted neurons. In grafted tissue, α-syn triggers misfolding of endogenous α-syn and thereby transfers its pathogenic conformation to native proteins. The conversion of an α-helical structured protein to the β-sheet structured fibrils of α-syn seems to be a crucial step for the self-propagation and resembles the process shown by prion proteins (Fonseca et al., 2015; Recasens and Dehay, 2014). However, more research is needed to confirm these suggested mechanisms underlying pathology progression in PD. In this context it is also still investigated how α-syn spreads from cell to cell. Spreading to interconnected regions suggests anterograde and retrograde transport of α-syn variants which has been verified *in vitro* (Emmanouilidou & Vekrellis, 2016; Tran et al., 2014; Volpicelli-Daley et al., 2011) and *in vivo* (Recasens et al., 2014). Other approaches indicate that non-classical exocytosis

(Jang et al., 2010; Lee et al., 2005), exosomal transport (Alvarez-Erviti et al., 2011; Emmanouilidou et al., 2010; Xia et al., 2019) and tunneling nanotubes (Abounit et al., 2016; Dieriks et al., 2017) play also a role in the transmission of pathological α-syn variants.

1.3.2 Metal dyshomeostasis

Being the most abundant trace element in the brain, iron contributes to many important processes in neurons and glia cells such as the mitochondrial respiration, oxygen transport or the metabolism of neurotransmitters (Ashraf et al., 2018; Ward et al., 2014). Under physiological conditions, iron import, export and storage proteins, which are important for iron metabolism, are regulated by the iron responsive elements (IREs). The mRNA translation of the mentioned proteins is controlled by an iron regulatory protein (IRP) which binds to IREs in the presence of iron (Joppe et al., 2019). In the aging process, it is known that the metabolism of iron is impaired and iron accumulates in specific brain regions (Ward et al., 2014). During aging, the L- and H-subunits of the iron storage protein ferritin were shown to be more abundant and within the first two decades of life concentrations of both subunits were increasing within the SN. Afterwards, the levels of H- and L-ferritin does not change significantly (Zecca et al., 2001). In contrast, in brains of PD patients reduced ferritin levels but increased iron accumulation were documented in the SN (Dexter et al., 1991). This increased nigral iron content could be verified in other studies analyzing postmortem tissue (Genoud et al., 2017; Popescu et al., 2009; Szczerbowska-Boruchowska et al., 2012) or the living patients (An et al., 2018; Chen et al., 2019). The disturbance of the iron homeostasis induces an excessive formation of ROS and accompanied oxidative stress. Iron provides the basis for catalyzed redox processes, which are described by the *Fenton* and *Haber-Weiss* reactions. Specifically, iron reacts with intracellularly abundant hydrogen peroxide (H_2O_2) and leads to the formation of free hydroxyl radicals (HO•). The thereby formed ROS result in oxidative stress which in turn induces a dysfunction of mitochondria and cell death (Singh et al., 2014; Zecca et al., 2004). Therefore, iron is supposed to play a crucial role in the neurodegeneration of PD patients.

Besides the dyshomeostasis of iron, also other trace elements were shown to be dysregulated in PD. SN samples of PD patients exhibited decreased copper and increased zinc levels (Dexter et al., 1991). Alterations in copper could be verified in SN tissue from patients using inductively coupled plasma mass spectrometry (ICP-MS) or X-ray-based

techniques, whereas zinc level alterations were inconsistent (Davies et al., 2014; Genoud et al., 2017). These results indicate that it is still not fully understood which other elements are in dyshomeostasis in the context of PD and whether and how they might contribute to disease progression. Since other trace elements also potentially undergo redox reactions, it is likely that they lead to the formation of ROS.

1.4 Need for therapeutic approaches

The diagnosis of PD is made based on the occurring motor symptoms in patients. However, at this time point, the underlying pathology is already progressed so that markers are needed which spot earlier disease stages. The case that available drugs for PD only lead to a relief of symptoms but do not prevent or cure PD pathology point to the need of new therapeutic strategies. To name a widespread treatment of PD patients, L-3,4-dihydroxyphenylalanine also known as levodopa (L-DOPA) is a common orally applied prodrug to increase the dopamine precursor level attenuating the symptomatology. An attenuation of the dopamine breakdown is aimed by administering inhibitors of monoamine oxidase-B (MAO-B) to patients. Furthermore, dopamine agonists, anticholinergics or catechol-O-methyltransferase inhibitors are also used for treatment in the early disease state (Connolly and Lang, 2014; Hayes et al., 2019). Since iron dyshomeostasis as well as α-syn aggregation and spreading describe particular hallmarks of PD, new approaches try to intervene in the underlying mechanisms of these two pathological events. The effectiveness of iron chelation in PD is stated in chapter 1.4.1. Regarding the α-syn pathology, in chapter 1.4.2 Rho-kinase inhibition by fasudil is described in more detail as a potential treatment strategy in PD, which is so far only tested in cell culture and animal models.

1.4.1 Iron chelation

Since iron accumulation is a widespread finding in brains of NDD patients, iron overload is a popular experimental therapeutic target. Aim of these experimental approaches is to cope with the overload of iron by therapeutically removing excess iron. Chelators show a high affinity for metals and lead to their sequestration. Iron chelators were extensively tested in preclinical cell culture and animal models of PD to reveal their effects on the underlying pathomechanisms. Various beneficial effects such as the prevention of iron accumulation in SN, less formation of nigral α-syn aggregates, loss of dopaminergic neurons in the SN and rescued motor as well as cognitive functions of the animals were

observed (Billings et al., 2016; Carboni et al., 2017a; Finkelstein et al., 2016, 2017; Mandel et al., 2004). Therefore, iron chelators were also used in clinical trials analyzing the effect of chelators in patients.

The most common iron chelators are deferoxamine, deferiprone and deferasirox, clinically approved by the US FDA. Deferoxamine has a short plasma half-life period so that subjects require continuous injections to ensure an optimal treatment. Further disadvantages of deferoxamine are dose-dependent neurotoxicity and the time-consuming and expensive treatment application (Mobarra et al., 2016). For therapeutic usage a chelator should be non-toxic and brain-permeable (Zecca et al., 2004), which is valid for deferasirox and deferiprone so that they can be applied orally. Deferiprone is the most promising iron chelator to treat patients with regional iron overload, since this substance can cross the blood-brain-barrier (BBB) and mobilizes iron. Furthermore, it has a well-known safety profile. Various clinical studies exist which tested the efficiency of different chelators in patients suffering from NDDs such as ALS (Moreau et al., 2018) or Friedreich ataxia (Boddaert et al., 2007; Pandolfo et al., 2014; Velasco-Sánchez et al., 2011).

In PD, deferiprone was already used for clinical trials. With deferiprone treatment, patients reached better scores in the Unified Parkinson's Disease Rating Scale (UPDRS) and showed a reduced iron content within the SN measured by R2* magnetic resonance imaging (MRI; FAIR-PARK-I, NCT00943748) (Devos et al., 2014). Another clinical trial (DeferipronPD, NCT01539837) showed reduced iron content inside the dentate and caudate nucleus for deferiprone-treated patients (Martin-Bastida et al., 2017). Due to these promising results a new randomized, parallel-grouped and placebo-controlled phase III trial was initiated, including multiple European centers (FAIRPARKII, NCT02655315) (recently reviewed in (Joppe et al., 2019)).

1.4.2 Fasudil-induced Rho-kinase inhibition

In NDDs, the signaling pathway of the Rho-associated protein kinase (ROCK) has been described as an interesting target. As recently reviewed, ROCK is involved in several cellular processes of particular importance in NDDs such as autophagy, synaptic dysfunction or degeneration of axons (Koch et al., 2018). Already a decade ago, first studies revealed neuroprotective and pro-regenerative properties of pharmacological inhibitors of ROCK (Lingor et al., 2007, 2008; Planchamp et al., 2008).

The isoquinoline-derivative fasudil is one inhibitor of ROCK. Fasudil was approved in 1995 for clinical human use in Japan and is used to treat subarachnoid hemorrhage-induced vasospasms (Suzuki et al., 2007, 2008). In the last years, fasudil gained attention in the field of neurodegeneration for its beneficial effects on animal- and cell-based ALS models (Günther et al., 2017; Tönges et al., 2014). A multicenter clinical phase IIa trial is currently investigating disease-modifying effects of fasudil treatment in ALS patients (Lingor et al., 2019).

Furthermore, the interest arose to test the effects of fasudil in the context of PD. In PD models using a treatment with the toxin 1-methyl-4-phenyl-1,2,3,6-tetrahydropyridine (MPTP), fasudil effected a reduced loss of dopaminergic neurons in an *in vivo* and an *in vitro* setup. Motor behavior of MPTP-treated mice was also rescued with fasudil treatment (Tönges et al., 2012). Other studies using the MPTP mouse model verified improvements in motor behavior and neuroprotective effects on dopaminergic neurons with fasudil treatment. Additionally, the inflammatory response was suppressed by fasudil treatment (Li et al., 2017; Zhao et al., 2015). The therapeutic combination of fasudil and bone marrow-derived neural stem cells further enhanced the mentioned positive effects of fasudil in an MPTP mouse model (Li et al., 2017). In mice with an intranasal administration of lipopolysaccharide (LPS) fasudil treatment improved motor behavior and attenuated the inflammatory response, the loss of dopaminergic neurons and the accumulation of α-syn (He et al., 2016). Another study emphasized the connection of fasudil with α-syn in PD. The authors described that fasudil can bind to α-syn at two tyrosine residues of its C-terminal region (Y133 and Y136) and showed that α-syn aggregation was attenuated by fasudil supplementation *in vitro*. In A53T mice, fasudil treatment via drinking water prevented cognitive and motor decline of the mice and effected less α-syn pathology in the midbrain (Tatenhorst et al., 2016). Therefore, fasudil seems to be a promising candidate for new treatment strategies in PD.

1.5 The interplay of iron and α-syn

Iron and α-syn are important therapeutic targets in PD. As described in chapter 1.4, several drugs used to affect the iron dyshomeostasis have been tested in animal models and some of them were even verified in PD patients. However, it is important to investigate how different pathological hallmarks are connected to each other to identify appropriate treatment opportunities. One of the major findings connecting iron and α-syn pathology

was the accumulation of iron in LBs (Castellani et al., 2000). Since α-syn has been previously described as a major component in LBs (Spillantini et al., 1998), an interaction with iron is likely.

Supporting this hypothesis, it has been found that both oxidation states of iron can bind to α-syn. Whereas for Fe^{2+} a binding constant of 5.8×10^3 M^{-1} was revealed, the binding constant of Fe^{3+} was 1.2×10^{13} M^{-1} (Peng et al., 2010b). Fe^{2+} specifically binds at Asp-121, Asn-122, and Glu-123, located at the C-terminus of α-syn (Binolfi et al., 2006). The affinity of Fe^{2+} to bind α-syn is even increased when α-syn is phosphorylated at pY125 or pS129 (Lu et al., 2011). Fe^{3+} is also supposed to have two bindings sites at the C-terminus of α-syn (Davies et al., 2011). Besides direct binding, there is further evidence that iron has an influence on the transcriptional and translational level of α-syn. One study suggests that α-syn levels are regulated by iron due to its 5′-UTR which shows a close homology to the IRE of the ferritin mRNA (Friedlich et al., 2007). In HEK293 cells, the polysome-associated endogenous α-syn mRNA was decreased by the iron chelator deferoxamine. Thereby, an Fe^{3+}-related control of the α-syn mRNA translation was assumed (Febbraro et al., 2012). Since an IRP knockdown in the SK-N-SH cell line induced an upregulation of the α-syn transcription and thereby enhanced its aggregation, the authors suggested that the aggregation process is partially controlled by iron through the IRE/IRP system (Li et al., 2011).

Almost two decades ago, it has been shown that iron directly induces α-syn aggregation and fibrillation (Uversky et al., 2001). Several studies could verify this observation (Golts et al., 2002; Kostka et al., 2008; Levin et al., 2011). Even low Fe^{3+} concentrations in a micromolar range triggered the formation of large sodium dodecyl sulphate (SDS)-resistant α-syn oligomers (Kostka et al., 2008). In contrast, α-syn did not form this kind of oligomers in the presence of Fe^{2+} (Levin et al., 2011). Since oxidative stress induced by H_2O_2 treatment did not trigger α-syn oxidation and oligomerization, it was suggested that trivalent ions plan an important role in the oligomerization (Kostka et al., 2008). Oxidizing agents such as H_2O_2 rather affect α-syn aggregation indirectly by oxidizing ferrous iron to ferric iron through the Fenton reaction. Accordingly, the authors reported that Fe^{2+} treatment triggered the oligomerization of α-syn in the presence of H_2O_2 (Levin et al., 2011). Therefore, oxidative stress could play an important indirect role for iron-mediated α-syn aggregation. Another study also emphasized the effect of oxidative stress, since treatment of SK-N-SH cells with antioxidative vitamin E led to an attenuation

of the α-syn aggregation (Li et al., 2011). Furthermore, external circumstances such as aerobic or anaerobic conditions could also have an influence on the α-syn aggregate conformation triggered by iron. *In vitro*, it was observed that under aerobic conditions treatment with Fe^{2+} triggered a polymerization into antiparallel soluble α-syn oligomers. Under anaerobic conditions, parallel β-sheet α-syn aggregates were formed by Fe^{2+} but also by Fe^{3+} treatment (Abeyawardhane et al., 2018).

Iron was also shown to provoke α-syn aggregation indirectly by affecting the autophagosome-lysosome pathway. Accordingly, in SN4741 cells, iron promoted α-syn aggregation by decreasing the expression of the nuclear transcription factor EB (TFEB). TFEB functions as transcriptional regulator of the autophagosome-lysosome pathway. The nuclear translocation of TFEB was inhibited through an activated Akt/mTORC1 pathway. The inhibition of the TFEB-mediated autophagosome-lysosome fusion resulted in an enhanced α-syn aggregation. In addition, the authors showed that cell-to-cell transmission of α-syn was also enhanced by iron enrichment, whereas TFEB overexpression attenuated this effect (Xiao et al., 2018).

Therefore, the current state of research offers different mechanisms on how iron interacts with α-syn or fosters the aggregation and spreading. On the one hand, direct binding of iron and α-syn could form the basis. On the other hand, studies suggest indirect influences which affect the interaction of iron on α-syn.

Vice versa, some studies showed that α-syn has an influence on iron. Accordingly, in PC12 cells α-syn overexpression fostered an increase of iron and its accumulation which was predominantly observed in the perinuclear region of PC12 cells (Ortega et al., 2016). Furthermore, it was shown that α-syn acts as a ferrireductase which implicates the ability of α-syn to reduce Fe^{3+} to Fe^{2+} (Davies et al., 2011). In contrast, another study indicated the formation of an α-syn-Fe^{3+} complex which inhibited the reduction of Fe^{3+} to Fe^{2+} (Levin et al., 2011). It is supposed that ferrireductase activity is exerted by a membrane-associated helical-rich α-syn tetramer (Angelova and Brown, 2018; McDowall et al., 2017).

In addition to iron also other trace elements are discussed to interact with α-syn in PD. It has been shown that α-syn has different metal binding sites (McLeary et al., 2019). Furthermore, some trace elements such as aluminum, copper or manganese were able to foster the aggregation of α-syn (Uversky et al., 2001). A recent study could demonstrate that the exposure to Mn^{2+} could enhance the cell-to-cell transmission of oligomeric α-syn

through exosomes in both *in vitro* and *in vivo* models (Harischandra et al., 2019). Therefore, the interaction of trace elements and α-syn can offer new approaches to investigate pathomechanisms in PD.

Taken together, the current state of research shows on the one hand that iron can interact with α-syn directly and indirectly and this interaction affects the aggregation of α-syn. On the other hand, α-syn can act as a ferrireductase and can influence the homeostasis of iron. The mentioned interactions of iron and α-syn are schematically summarized in Figure 1 (adapted from Joppe et al., 2019).
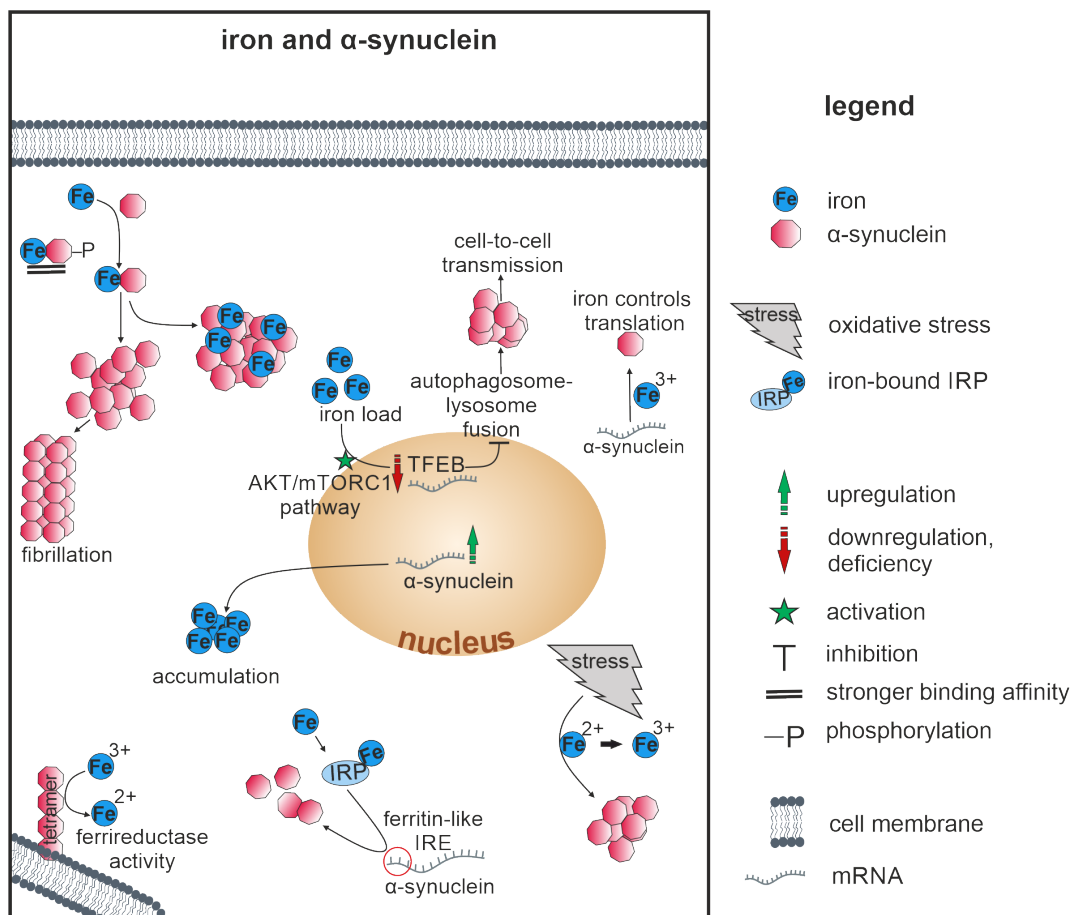
Figure 1. The interaction of iron and α-syn. Iron-induced aggregation of α-syn could be accomplished by direct binding or via oxidation. Iron also impacts α-syn indirectly affecting the transcriptional and translational level of α-syn. In contrast, iron accumulation is fostered by the overexpression of α-syn, which could also function as a ferrireductase. Adapted from (Joppe et al., 2019).

1.6   Animal models of PD

Animal models of PD enable to investigate underlying pathomechanisms even if the complex pathophysiology of PD in humans cannot be entirely mimicked. The advantage of several disease-related animal models is that specific parts of the disease pathology and symptomatology can be investigated untangling the complexity of the disease into underlying single mechanisms. Since neurodegeneration is one of the main hallmarks of PD, toxin-based models were firstly tested in animals to mimic the degeneration of the nigrostriatal pathways. On the one hand, intracerebral injections of the toxin 6-hydroxydopamine (6-OHDA) were used, since 6-OHDA is not able to cross the BBB (Schober, 2004). On the other hand, the toxin MPTP is able to cross the BBB so that it can be applied intraperitoneally or subcutaneously to induce a Parkinsonism-like disease in mice mimicking different pathological aspects of PD. The conversion of MPTP into the toxic compound MPP+ occurs in glial cells (Konnova and Swanberg, 2018). Thereby, neurotoxicity is triggered which effects for instance neurodegeneration, behavioral deficits or increased α-syn levels and inclusion formation depending on an acute or chronic treatment of MPTP (Fornai et al., 2005; Jackson-Lewis and Przedborski, 2007; Meredith et al., 2002; Zhang et al., 2017a). Similar to MPTP and 6-OHDA toxin-based pathology models, a treatment with the pesticides rotenone and paraquat has also been used to study the underlying mechanisms of PD-like symptoms (Konnova and Swanberg, 2018).

Based on known gene mutations causing familial PD (e.g. SNCA, LRRK2, PRKN, DJ-1, PINK-1 or UCH-L1) also genetic animal models are frequently used to analyze PD pathology. Since α-syn pathology is a crucial step in the disease progression, transgenic disease models with mutations in the SNCA gene encoding for α-syn have been widely investigated (Konnova and Swanberg, 2018). Frequently, the transgenic α-syn mouse model B6;C3-Tg(Prnp-SNCA*A53T)83Vle/J (A53T mice) (Giasson et al., 2002) is used to analyze disease progression in PD.

Since α-syn spreading and iron enrichment are common pathological events in PD, in the following subchapters models of iron intoxication and α-syn preformed-fibrils (PFFs) injections will be described in more detail, forming the basis for the related studies of this doctoral thesis.

1.6.1 Iron intoxication models

Iron dyshomeostasis and accumulation is a well-known hallmark in PD as extensively described in chapter 1.3.2, therefore the relevance of iron in context of PD has been analyzed in different animal models. MPTP treatment of transgenic A53T mice was shown to induce an increase of nigral iron levels, which could be caused by the MPTP-dependent decrease in levels of the iron export protein ferroportin. This observation highlights the generation of an iron dyshomeostasis in PD pathology (Finkelstein et al., 2017). The result that iron chelator treatment of A53T mice showed positive effects e.g. on behavior or α-syn aggregate formation additionally emphasizes the role of iron in PD (Finkelstein et al., 2016). Therefore, further studies used an iron application model to investigate the consequences of iron overload in the brain.

Most commonly iron was administered to rodents per gavage, either in form of Fe^{2+} ions (Fredriksson et al., 1999, 2000; de Lima et al., 2005a, 2007) or as elemental carbonyl iron (Billings et al., 2016, 2019; Carboni et al., 2017a; Chen et al., 2015; Kaur et al., 2007; Peng et al., 2009, 2010a). In most cases carbonyl iron was applied at a daily rate between postnatal day 10 and 17 (p10-17) (Billings et al., 2016, 2019; Carboni et al., 2017a; Chen et al., 2015; Kaur et al., 2007; Peng et al., 2009, 2010a) in a dosage of 120 mg/kg body weight (Chen et al., 2015; Kaur et al., 2007; Peng et al., 2009, 2010a). The model of iron enrichment itself is not PD-specific and is rather used to investigate general effects of iron, for instance iron-induced behavioral abnormalities of rodents (Fredriksson et al., 2000; de Lima et al., 2005b). To further relate effects of iron enrichment to PD pathology, some studies used A53T mice overexpressing human α-syn. In both species, A53T and wild-type mice, neonatal oral iron application induced iron enrichment in the midbrain, specifically in the SN. In addition, iron overload triggered a significant increase of protein carbonyls and a loss of dopaminergic neurons (Billings et al., 2016, 2019; Kaur et al., 2007). In one study the authors suggested that iron treatment of A53T mice led to a resistance against iron chelation with clioquinol (Billings et al., 2016). These results indicate detrimental effects if iron overload is paired with a PD-specific model. Furthermore, the effect of iron overload in PD-specific toxin-based models was investigated by treating mice with MPTP or paraquat. Iron and paraquat treatment led to a strong microglia increase in the SN and a loss of dopaminergic neurons, which differed significantly to the effect of paraquat treatment without iron enrichment (Peng et al., 2009, 2010a). In an MPTP-based model,

iron treatment augmented the effect on nigral neuron loss compared to mere MPTP treatment (Kaur et al., 2007).

Taken together, several studies proved the deleterious effects of iron overload in context of PD and showed that Parkinsonian models could consequently trigger a dyshomeostasis of iron. Therefore, different iron chelators such as deferiprone, desferrioxamine and clioquinol or other components such as green tea, therapeutical nanoparticles and the quinazoline compound PBT434 were tested in animal models. Trying to affect the iron dyshomeostasis and related pathological events, the mentioned components showed a wide range of beneficial effects on pathology and symptomatology (Carboni et al., 2017a; Dexter et al., 2011; Finkelstein et al., 2017; Kaur et al., 2003; Wang et al., 2017; Xu et al., 2017).

1.6.2 The α-syn PFFs spreading model

The spreading pathology of α-syn has been recently studied administering α-syn PFFs to different animal species and using different application methods such as an intraglossal application or an intramuscular, intraperitoneal, intracerebral, gut or sciatic nerve injection. Most commonly, intracerebral injections were conducted into brain regions such as the hippocampus, olfactory bulb, cortex, SN or striatum (Chung et al., 2019). Interestingly, a recent study showed that intravenous or oral application of PFFs led to an infiltration of phosphorylated α-syn fibrils into the CNS and to a similar extent of α-syn pathology in the brain compared to an intracerebral injection (Lohmann et al., 2019).

Due to the frequent usage of intracerebral PFFs injections, precise protocols of the preparation of α-syn monomers, generation of PFFs, surgery process, perfusion, tissue processing and cleaning after α-syn usage are available (Patterson et al., 2019a; Polinski et al., 2018; Zhang et al., 2019a). Besides different injection areas, studies differ also in the genotype of the used animals (e.g. wild-type, A53T or A30P mice), in the injection side (unilateral or bilateral injections), species of the injected recombinant PFFs (e.g. mouse or human), the amount of injected PFFs (e.g. 5 or 10 µg) or the post-injection observation period which ranges mostly between 30 days and 9 months post injection (Chung et al., 2019). In general, it was shown that the injection site determines the distribution of α-syn aggregates through the brain. Accordingly, the α-syn spreading pattern at one month following an intrastriatal injection differed from its distribution after an injection into other brain regions such as SN or entorhinal cortex (Masuda-Suzukake et al., 2014).

From now on, studies are reported which performed unilateral, intrastriatal PFFs injections in mice to analyze the spreading of α-syn. Investigations showed that the longer the evaluation period the stronger is the α-syn spreading pathology respectively the presence of α-syn inclusions in different brain regions (Luk et al., 2012b, 2012a; Okuzumi et al., 2018; Paumier et al., 2015). In a recent study, separating both hemispheres through callosotomy before or one day after the intrastriatal PFFs injection could reveal that α-syn only need one day to spread to the contralateral hemisphere in a rate that is comparable to mice without callosotomy. When hemispheres were separated before PFFs injection, α-syn deposits spread almost exclusively to the ipsilateral hemisphere. In this case, the spreading to cortex, entorhinal cortex or amygdala was more than double compared to mice without callosotomy (Okuzumi et al., 2018). In general, α-syn spreads stronger to brain regions such as SN, amygdala or striatum in the ipsilateral hemisphere than to the contralateral hemisphere (Luk et al., 2012b; Okuzumi et al., 2018; Paumier et al., 2015).

Different studies investigating PFFs-induced α-syn spreading at 90 days post injection (dpi) showed α-syn pathology in similar brain regions. In some of these studies no spreading maps were available and only few brain regions were analyzed. However, it has been commonly reported that for instance the striatum, SN, amygdala and different cortex areas were strongly affected. Most of the affected regions were innervating the striatum so that the results support the hypothesis of a connectivity-dependent spreading pattern (Blumenstock et al., 2017; Kim et al., 2016; Luk et al., 2012b, 2012a; Terada et al., 2018). At 90 dpi, a marmoset monkey injected with PFFs into the putamen and caudate nucleus showed α-syn signal especially within the neocortex, SN, globus pallidus, thalamus and amygdala, resembling spreading pattern in rodent studies (Shimozawa et al., 2017).

Besides PFFs-induced α-syn spreading through the brain, studies investigated other effects of the intrastriatal injection such as impairment in motor behavior. Whereas an injection of 5 µg mouse α-syn PFFs only resulted in significant motor abnormalities at 180 dpi (Luk et al., 2012a), an injection of 10 µg mouse PFFs made an impact at 90 dpi in the rotarod test (Masuda-Suzukake et al., 2014). Both beforementioned studies used the wire hang test as another motor behavior test. Interestingly, mice injected with 5 µg PFFs showed a motor decline in this test at 90 dpi (Luk et al., 2012a), but mice injected with 10 µg showed no significant results (Masuda-Suzukake et al., 2014). Despite the direct connection of the striatum as injection site and the SN, a significant loss of dopaminergic neurons in SN and a decrease of the striatal dopamine concentrations occurred only at 180

dpi (Luk et al., 2012a). Therefore, pathological abnormalities other than α-syn spreading pathology occur rather late in this model.

1.7   The usage of X-ray-based techniques for analyses of human samples

One common X-ray-based analytical technique is the detection of X-ray fluorescence (XRF). XRF allows to identify several elements simultaneously so that an exact composition of an analyzed matter can be defined. The photoelectric absorption is the underlying principle of XRF which enables to identify the available elements (Figure 2). Accordingly, an incoming X-ray photon interacts with an electron of an inner orbital shell of an atom. The absorption of the photon energy of this electron leads to the ejection of the photoelectron from the inner shell of the atom causing a state of instability. To regain its stability, an electron from an outer orbital shell fills the vacancy of the ejected photoelectron. Since this electron drops from a higher energy level to a lower energy level, it releases another X-ray photon with lower energy compared to the incoming X-ray photon, which can be detected and assigned to a specific element (Seibert and Boone, 2005).
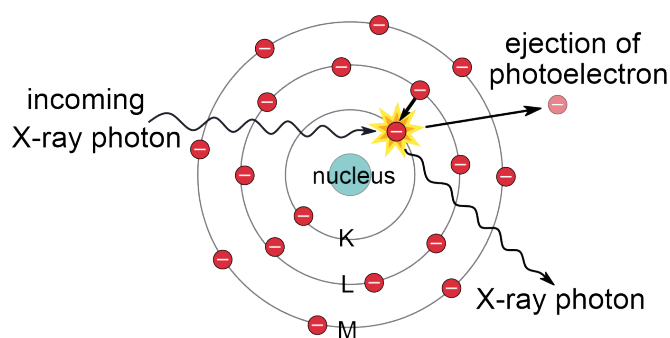
Figure 2. Scheme of the photoelectric absorption as elementary principle of XRF. An incoming X-ray photon induces the ejection of a photoelectron of the inner shell of the atom. A photoelectron from an outer shell releases an X-ray photon by replacing the vacancy. The released X-ray photon is specific for the present element. Illustration designed based on (Seibert and Boone, 2005).

For the sake of completeness, except the photoelectric absorption the incoming X-ray photon can also interact in two other ways with an electron of the atom which are called Rayleigh scattering and Compton scattering. Therefore, an X-ray detector can additionally measure the energy released by Rayleigh scattering and by Compton scattering. The Rayleigh scattering describes the case that the incident X-ray is just scattered caused by an interaction with an electron. No energy is transferred to the electron and the electron is not

ejected so that energy of both scattered and incoming X-ray photons are equal. According to the Compton scattering, the incoming beam loses some energy since it leads to an ejection of an electron from an outer shell and this event effects the scattering of the beam (Seibert and Boone, 2005).

XRF enables both a spatial resolution and quantification of trace elements. Already some years ago, both XRF and scanning transmission X-ray microscopy (STXM) have been described as well-established and useful techniques to perform a microanalysis on neuronal tissue or more specific structures such as cells (Fahrni, 2007; Salditt and Dučić, 2014). Many studies exist which used XRF-based techniques to analyze the trace element content either in human brain tissue (Popescu et al., 2009; Surowka et al., 2015; Szczerbowska-Boruchowska et al., 2004, 2012), or brains of rodents (James et al., 2011; Tian et al., 2015) or in cell culture (Ortega et al., 2016; Vogt et al., 2003). One study indicated that different fixation procedures potentially alter the elemental content of samples (James et al., 2011). This implicates the favored usage of native tissue for trace element measurements. Next to the mapping and quantification of trace elements, XRF was also used to further analyze cell signaling. In this context of cell signaling, one study combined XRF microscopy with a fluorescent copper sensor and revealed that neuronal cells show a calcium-dependent copper redistribution (Dodani et al., 2011). With a limit of approximately 0.1 µg g^{-1} to 1 µg g^{-1} the sensitivity of XRF to map absolute concentrations of trace elements is similar to electron-based microanalysis (Bourassa and Miller, 2012).

XRF is only one of many methods which enable to analyze the elemental composition of brain samples. In previous studies, methods such as ICP-MS, atomic absorption spectroscopy (AAS), analytical electron microscopy or Nano-secondary Ion mass spectrometry were also used for a quantification approach of trace element within SN neurons or in the extracellular space (Biesemeier et al., 2016; Fernández et al., 2017; Genoud et al., 2017). As a promising approach, high spatial resolution in XRF cannot only be used for an elemental quantification in cells but also in subcellular structures. Furthermore, XRF approaches are advantageous since they are non-destructive compared to other mentioned techniques which lead to a destruction of the analyzed tissue (Grochowski et al., 2019).

In addition to XRF, X-ray diffraction (XRD) measurements can be performed. XRD is used for a structural characterization detecting crystals and highly ordered structures of

the analyzed matter (Bunaciu et al., 2015). The XRD measurements can be performed in combination with XRF using different detectors. The scattering signal is generated when the focused X-ray beam raster-scans the tissue. Two-dimensional maps can be generated including structural parameters such as tissue density, presence of crystalline components or short range order. In a previous study investigating human SN tissue, the XRD analysis could determine an increased amount of crystallized cholesterol in one PD sample compared to a control sample, whereas the XRF measurement showed PD-specific alterations in concentrations of trace elements (Carboni et al., 2017b).

1.8 Aims of this doctoral thesis

The spreading of α-syn aggregates in the brain is an essential part of the multifaceted PD pathology, but its causes and triggers still remain elusive. Unraveling pathomechanisms which cause or influence α-syn propagation is aimed to identify novel treatment strategies for PD to stop the disease progress. Since iron and other trace elements are known to interact with α-syn in particular in its aggregation process, trace element dyshomeostasis is a possible pathogenic event reinforcing the disease progression. X-ray techniques are powerful tools to detect trace elements and to perform a structural characterization of tissue. In this thesis, X-ray techniques were used in order to complement the conventional biochemical methods to analyze α-syn pathology.

The aim of this doctoral thesis was to identify PD-related changes of trace elements in dopaminergic neurons and subcellularly in LBs to link the role of trace elements to α-syn pathology. *In vivo* and *in vitro*, specifically the influence of iron on PFFs-induced α-syn spreading was investigated. Beyond that, this thesis contained a second approach to modulate α-syn fibrils propagation investigating the effect of ROCK inhibition by fasudil as a therapeutic approach.

In the following, I will point out the central questions of this thesis:

1. **Is it possible to depict PD-related trace elemental changes in neuromelanin-positive neurons of patients by XRF? Can X-ray-based techniques be applied to visualize LBs due to the presence of partially crystalline structures and to reveal their elemental profile?**

XRF was used to analyze midbrain tissue sections of PD and control patients with the goal to identify a PD-related dyshomeostasis of trace elements in dopaminergic

neurons. We aimed to compare these microscopic data from neurons with the elemental profile in LBs to verify, which dysregulated trace elements accumulate in LBs. XRD was used to attempt a structural characterization of LBs, whereas the distribution of different trace elements within LBs was measured by XRF.

2. Does postnatal iron treatment modulate PFFs-induced α-syn spreading in a mouse model? Do intrastriatal PFFs injections and iron supplementation affect motor or cognitive behavior of mice?

To address these questions, postnatal iron treatment of mice was combined with intrastriatal PFFs injections. The cognitive and motor performance of the mice was monitored to find treatment-related changes and the α-syn spreading pathology was analyzed to gain a better understanding, which role iron plays within mechanisms underlying α-syn spreading.

3. Can iron treatment change α-syn PFFs spreading *in vitro* and do the results mimic changes in the *in vivo* model?

To investigate α-syn PFFs transmission *in vitro*, a microfluidic chamber model was used and the effect of iron on α-syn spreading in cortical neurons was analyzed.

4. Does ROCK inhibition by fasudil treatment prevent or reduce α-syn PFFs-induced pathology in a PD mouse model?

The α-syn PFFs injection mouse model was used to investigate the effect of ROCK inhibition by fasudil on α-syn spreading to get a better understanding of the underlying pathomechanism and to assess the therapeutic potential of fasudil in the context of PD.

2 Materials and Methods

2.1 Material

2.1.1 Equipment

6-, 12- and 24-well cell culture plates	Sarstedt (Nümbrecht, Germany)
96 well micro test plate	Sarstedt (Nümbrecht, Germany)
Blades Teflon-coated DB80 LX, #14035843496	Leica Biosystem (Nussloch, Germany)
Cage incubator	Okolab (Pozzuoli, Italy)
Camera Legria HFM36	Canon (Krefeld, Germany)
Capillary puller P-97	Sutter Instruments (Novato, CA, USA)
Cover slide Ø 18 mm	Menzel (Braunschweig, Germany)
Cover slides 24 × 60 mm	Menzel (Braunschweig, Germany)
Cover slides Ø 12 mm	Menzel (Braunschweig, Germany)
Cover slips 24 × 55 mm #1	Menzel (Braunschweig, Germany)
Cryomatrix	Thermo Scientific (Waltham, CA, USA)
Cryomatrix 3801480S	Leica Microsystems (Mannheim, Germany)
Cryomold (Tissue-Tek, Intermediate, 15 × 15 × 5 mm)	Sakura Finetek (Torrance, USA)
Cryostat CM 3050S	Leica Microsystems (Mannheim, Germany)
FluoroDishTM, dish Ø 35 mm, glass Ø 3 mm	World precision instruments (Berlin, Germany)
Gilson pipettes	Gilson (Villiers de belle, France)
Glass capillaries	World Precision Instruments (Berlin, Germany)
IVC animal cages	Tecniplast (Hohenpeißenberg, Germany)
Micro Injector Nanoliter 2000 Pump Head	World Precision Instruments (Berlin, Germany)
Micro-centrifuge 5415R	Eppendorf (Hamburg, Germany)
Microfluidic chambers, round device 450 µm	Xona (Temecula, CA)
Microtome blades	Feather Safety Razor Co. (Seki, Japan)
Mini drill with 0.8 mm drill head	Dremel (Leinfelden-Echterdingen, Germany)
Mouse jaw holder with ear bars	World Precision Instruments (Berlin, Germany)
Parafilm sealing film	Starlab International GmbH (Hamburg, Germany)
Peristaltic perfusion pump	Idex (Wertheim, Germany)
Plastic feeding tubes, 22 ga × 25 mm	Instech Laboratories (Plymouth Meeting, PA, USA)

Rotarod 47600	Ugo Basile (Gemonio, Italy)
Spark 10M multimode microplate reader	Tecan (Männedorf, Switzerland)
Stereotactic frame	David Kopf Instruments (Tujunga, CA, USA)
SuperFrost Plus Microscope Slides	Menzel (Braunschweig, Germany)
SYS Micro4 controller	World Precision Instruments (Hamburg, Germany)

2.1.2 Reagents

2-Methylbutane	Honeywell (Offenbach, Germany)
4′,6-Diamidin-2-phenylindole (DAPI)	Sigma Aldrich (Taufkirchen, Germany)
B-27 Supplement	Gibco (Karlsruhe, Germany)
Bepanthene	Braun (Melsungen, Germany)
Sodium Bicarbonate solution	Gibco (Karlsruhe, Germany)
Bovine serum albumin (BSA)	Applichem (Darmstadt, Germany)
Carbonyl iron	Sigma Aldrich (Taufkirchen, Germany)
Citric acid	Roth (Karlsruhe, Germany)
cytosine arabinoside (AraC)	Sigma Aldrich (Taufkirchen, Germany)
DEPC water	Sigma Aldrich (Taufkirchen, German
Dermabond	Ethicon (Norderstedt, Germany)
DNAse	Sigma Aldrich (Taufkirchen, Germany)
D-Sorbitol	Sigma Aldrich (Taufkirchen, Germany)
Enthellan	Merck Millipore (Darmstadt, Germany)
Ethanol absolute	Applichem (Darmstadt, Germany)
Fasudil	LC Laboratories (Woburn, USA)
Fetal calf serum (FCS)	Biochrom; PAA (Berlin; Pasching, Germany)
Glucose 45 %	Merck (Darmstadt, Germany)
Glutamax	Gibco (Karlsruhe, Germany)
Glycerol	Roth (Karlsruhe, Germany)
Glycine	Applichem (Darmstadt, Germany)
Hank's Balanced Salt Solution (HBSS)	Gibco (Karlsruhe, Germany)
Hemalum solution	Roth (Karsruhe, Germany)
Hydrochloric acid 37 %	Applichem (Darmstadt, Germany)
Iron(II) chloride tetrahydrate	Sigma Aldrich (Taufkirchen, Germany)
Isopropanol	Applichem (Darmstadt, Germany)
Ketamine	Medistar (Ascheberg, Germany)
Levamisol hydrochloride	Sigma Aldrich (Taufkrichen, Germany)
Metamizole	Zentiva (Frauenfeld, Switzerland)
Methanol	Applichem (Darmstadt, Germany)
Mineral oil	Sigma Aldrich (Taufkirchen, Germany)
Mowiol - 488	Sigma Aldrich (Taufkirchen, Germany)
Naphtol As-BI phosphate	Sigma Aldrich (Taufkirchen, Germany)
Neurobasal medium	Gibco (Karlsruhe, Germany)

New fuchsin	Sigma Aldrich (Taufkirchen, Germany)
Normal goat serum (NGS)	Cedarlane (Burlington, NC, USA)
Normal horse serum (NHS)	PAA (Berlin; Pasching, Germany)
Hydrogen peroxide 30 % (H_2O_2)	Applichem (Darmstadt, Germany)
Para-formaldehyde (PFA)	Roth, Applichem (Darmstadt, Germany)
Pen-Strep-Neomycin	Gibco (Karlsruhe, Germany)
Phosphate buffer solution (PBS)	Applichem (Darmstadt, Germany)
Poly-L Lysine Hydrate 100 mg (PLL)	Sigma Aldrich (Taufkirchen, Germany)
Potassium ferricyanide (II)	Honeywell (Offenbach, Germany)
Roti-Histokitt	Roth (Karlsruhe, Germany)
Sodium azide (NaN_3)	Sigma Aldrich (Taufkirchen, Germany)
Sodium dodecyl sulphate (SDS)	Applichem (Darmstadt, Germany)
Sodium hydroxide (NaOH)	Applichem (Darmstadt, Germany)
Sodium nitrite, 67398-1G	Sigma Aldrich (Taufkirchen, Germany)
Sterofundin	Braun (Melsungen, Germany)
Sucrose	Applichem (Darmstadt, Germany)
Sudan black	Applichem (Darmstadt, Germany)
Thionine acetate	Sigma Aldrich (Taufkirchen, Germany)
Tris base	Applichem (Darmstadt, Germany)
TritonX 100	Applichem (Darmstadt, Germany)
Trypsin	Sigma Aldrich (Taufkirchen, Germany)
Tween20	Applichem (Darmstadt, Germany)
Xylazine	Ecuphar (Greifswald, Germany)
Xylene	Sigma Aldrich (Taufkirchen, Germany)

2.1.3   Buffer and solutions

Blocking solution for immunohistochemistry (IHC): 10 % NHS, 5 % BSA (IgG free), 0.3 % TritonX, 25 mM glycine in PBS

Borate buffer: 0.927 g boracic acid (150 mM) diluted in < 100 ml H_2O with NaOH adjusted to pH 8.4, filled up to 100 ml with H_2O, sterile filtered

Citrate buffer (100 ml): 10mM citric acid (monohydrate 0.21 g) in H_2O, pH-value of 6.0 adjusted with 1N NaOH, 0.05 % Tween 20

Calcium-magnesium-free medium (CMF): 450 ml H_2O, 50 ml of 10x HBSS, 600 µl sodium bicarbonate solution 7.5 %

Cortex cell culture medium: 660 µl 45 % glucose, 500 µl 100x glutamax, 500 µl 100x Pen/Strep, 1 ml 50x B27 diluted in 47,34 ml Neurobasal medium

DAPI solution: 1 µg/ml DAPI in PBS

DNAse: 25 mg/ml in CMF

Mowiol: 6 g glycerin, 2.4 g Mowiol, 6 ml H_2O, 12 ml 0.2 M Tris pH 7.2

PBS: 9.55 g/L PBS salt solution in distilled H_2O

PFA (4 %) solution: 40 mg/ml PFA, 9.5 mg/ml PBS, 1-3 pellets NaOH in distilled water

PLL: Hydrate 100 mg PLL in 50 ml 0.1 M borate buffer, sterile filtered (stock of 2 mg/ml). Stock diluted 1:4 in distilled H_2O

Sudan black: 0.1 g per 100 ml 70 % ethanol

TBS: 10 mM Tris HCl, 150 mM NaCl in distilled water

TBS-T: 0.1 % Tween20 in TBS, pH 7.6

Tris: 10 mM Tris-buffered saline pH 8.0

Trypsin solution: 50 mg trypsin diluted in 26.7 HBSS pH 7.4, sterile filtered

2.1.4 Primary antibodies

Anti-α-syn (LB509)	from mouse	Covance (Princeton, NJ, USA)
Anti-α-syn (phospho S129; EP1536Y)	from rabbit	Abcam (Cambridge, United Kingdom)
Anti-MAP2	from mouse	Merck Millipore (Darmstadt, Germany)
Anti-mouse CD3 conjugated with Alexa Fluor 488	from rat	Biolegend (San Diego, CA, USA)
Anti-mouse CD11b	from rat	Bio-Rad Laboratories (Hercules, CA, USA)
Anti-tyrosine hydroxylase	from rabbit	Zytomed (Berlin, Germany)

2.1.5 Secondary antibodies

Anti-mouse	alkaline phosphatase	from goat	Dako (Hamburg, Germany)
Anti-rabbit	Cy3	from goat	Dianova (Hamburg, Germany)
Anti-rabbit	biotinylated	from goat	Dianova (Hamburg, Germany)
Anti-mouse	Cy5	from goat	Jackson ImmunoResearch (Cambridge, United Kingdom)

2.1.6 Kits

Vectastain ABC PK-4000 Peroxidase Kit	Vector Laboratories (Burlingame, USA)
DAB Peroxidase SK-4100 substrate kit	Vector Laboratories (Burlingame, USA)
ToxiLight bioassay kit	Lonza (Cologne, Germany)

2.1.7 Software

AxioVision SE64 Rel. 4.9	Carl Zeiss
CorelDraw Graphics Suite 2019	Corel Corporation
EthoVision XT 8.5	Noldus
Graphpad Prism 5.04 and 8.2.1	GraphPad software Inc.

Inkscape 0.92	The Inkscape Team
PyMCA 5.3.1	Sourceforge.net
SparkControl V1.2	Tecan
SPSS Statistics 25.0	IMB Statistics
Stereo Investigator 9.0	Micro Bright Field Inc.
ImageJ 1.50b	N.I.H.
Mendeley	Elsevier

2.2 Methods

2.2.1 Analysis of human midbrain tissue from PD and control patients

Human midbrain samples were used to analyze the elemental composition of neuromelanin-positive cells and the elemental distribution in LBs of PD patients. The X-ray-based analyses of the human tissue were performed in collaboration with Prof. Dr. Tim Salditt and Dr. Jan-David Nicolas (Institute for X-ray Physics, Göttingen, Germany). Also Kilian Frank, Marina Eckermann and Tilman A. Grünewald were involved in the measurements of the samples at the European Synchrotron Radiation Facility (ESRF) in Grenoble, France (Joppe et al., 2020). For an overview on these X-ray experiments, Figure 3 illustrates the processing of the human midbrain tissue and the procedure of the consecutive analyses. MATLAB and Python analyses for XRD and XRF data were also performed in collaboration with the Institute for X-ray Physics in Göttingen.

In a parallel study, human midbrain samples were analyzed regarding their cholesterol amounts. The lipid extraction and cholesterol analysis were performed in collaboration with Dr. Cornelia Herrfurth and Sabine Freitag from the Lab of Prof. Dr. Ivo Feußner (Department for Plant Biochemistry, Göttingen, Germany).

2.2.1.1 Tissue preparation for X-ray analyses

Human tissue was obtained from the UK Brain Bank (Parkinson's UK, London, England). The Multicenter Research Ethics Committee granted the ethical approval (07/MRE09/72). In order to analyze the elemental profile of PD patients with XRF, brain sections of four PD patients and four controls (three cancer patients and one multiple sclerosis (MS) patient) were prepared (Table 1).

frozen
tissue blocks

transfer to
cryostat

Kapton and
PP rings

Kapton   PP

sectioning and
mounting on rings

immunostaining
for α-synuclein

microscopy

X-ray
fluorescence

X-ray
diffraction

PyMCA
analysis

statistical analyses
MATLAB and Python

MATLAB
analyses
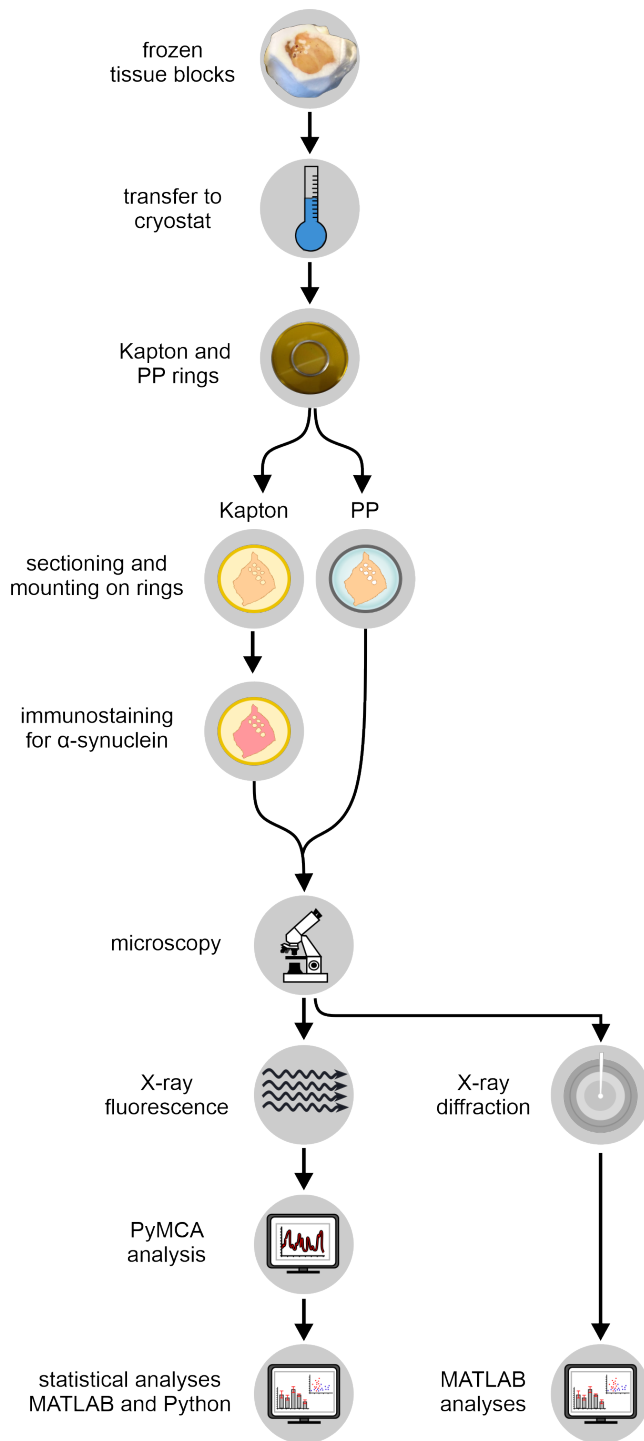
Figure 3. Processing of human midbrain tissue and the analysis procedure. Frozen human tissue blocks received from the UK PD brain bank were transferred to the cryostat and sectioned into 30 μm thick slices. The sections were mounted on rings covered with polypropylene (PP) or Kapton foil. Sections on PP rings were not further processed, whereas tissue sections on Kapton rings were immunolabelled for α-syn. Microscopy was used to identify neuromelanin-positive neurons on native tissue and LBs on immunostained tissue. Trace elements were measured in both preparations using XRF. XRF data were processed with the software PyMCA and statistically analyzed with MATLAB and Python. Structural analysis of the tissue was performed by using XRD measurements.

Snap frozen midbrain tissue blocks of PD and control (CO) patients were used as starting material (Figure 4A). The samples were transferred from −80 °C to the cryostat (−21 °C) at least one hour before sectioning. Tissue blocks were cut into 30 μm thick tissue sections using iron-free teflon-coated blades to avoid friction-dependent particle contamination. Two adjacent sections were prepared for each patient. The first section was

mounted on a ring covered with Kapton foil (ring diameter 50 mm; Kapton thickness 30 µm); the second section was mounted on a PP-covered ring (diameter 25 mm, PP thickness 1 µm). Sections mounted on PP foil were dried at 60 °C for 15 min and afterwards another PP ring was put on top of each section. Both rings covering one section were sealed with nail polish. The sections on Kapton rings were dried for 3 min at 60 °C and fixed with methanol for 10 min at −20 °C. These sections were kept at room temperature (RT) for immunohistochemical staining.

The sections on Kapton rings used for the α-syn staining were rehydrated in tris-buffered saline (TBS) for 20 min. Afterwards, the tissue underwent antigen retrieval in a citrate buffer made of sodium citrate at pH 3 for 1 h at 60 °C. After 30 min of cooling down, the citrate buffer was removed and the sections were washed 3 × 5 min in TBS. Blocking was done in 5 % NGS in TBS with 0.1 % Tween 20 (TBS-T) for 1 h. Afterwards, the sections were incubated over night at 4 °C with the first antibody (mouse anti α-syn, LB509), 1:250 diluted in 5 % NGS dissolved in TBS. On the next day, the sections were washed (3 × 10 min in TBS) and were then incubated with a secondary antibody conjugated with alkaline phosphatase (goat anti-mouse IgG/alkaline phosphatase), 1:150 diluted in TBS for 45 min. Sections were washed again (3 × 10 min in TBS). Adding Naphthol As-BI phosphate to the alkaline phosphatase, the fission product reacts with the added triphenylmethane dye new fuchsin (0.1 mg/ml) effecting a red staining of α-syn. After an incubation with the new fuchsin for around 20 min, a washing step followed (5 min in distilled H_2O) to rinse any unbound new fuchsin from the tissue. The sections were dried at RT. On the next day, distilled H_2O was used to rehydrate the tissue (5 min). Afterwards, the sections were incubated for 8 s in hemalum solution to stain cell nuclei. After blueing of the samples (10 min in H_2O), the tissue dried at RT. Due to the yellow color of the Kapton foil, the nuclei staining (hemalum) of the sections mounted on Kapton was not visible in recorded optical micrographs. After covering the section with another Kapton ring, both rings were sealed with nail polish. The Axio Imager.Z2 microscope (Zeiss, Göttingen, Germany) was used to identify and document LB-like structures within sections from PD patients (Figure 4B) (Joppe et al., 2020).

Table 1. Characterization of the used human samples for X-ray analyses. Samples and detailed information were provided by the UK brain bank. The column 'analysis target' describes if a section of the sample was used for the analysis of neuromelanin-positive cells (cells) or for the Lewy body (LB) analysis. For PD2, one native section was used for the cell analysis and a stained section was used for the LB analysis. CO: control patient, PD: Parkinson's disease, MS: multiple sclerosis, F: female, M: male, postmortem interval: time between death and tissue freezing, N/A: not available. Adapted with permission from (Joppe et al., 2020) © The Optical Society.

Simplified ID	Case ID	Patient group	Main diagnosis	Analysis target	Analyzed cells	Age (y)	Gender	α-syn pathology (Braak stage)	Disease duration (y)	Post mortem interval (h)
PD1	PD50	PD	PD	cells	5	82	F	6	14	18
PD2	PD334	PD	PD	cells/LB	8/1	87	M	N/A	9	21
PD3	PD458	PD	PD	cells	8	73	M	6	19	10
PD4	PD153	PD	PD	cells	6	76	F	6	7	12
LB	PD29	PD	PD	LB	1	76	M	6	7	15
CO1	CO46	CO	cancer	cells	5	75	M	N/A	N/A	24
CO2	CO28	CO	cancer	cells	7	60	F	N/A	N/A	13
CO3	PDC35	CO	cancer	cells	6	89	F	N/A	N/A	13
MS1	MS520	CO	MS	cells	8	74	M	N/A	N/A	21

A

B
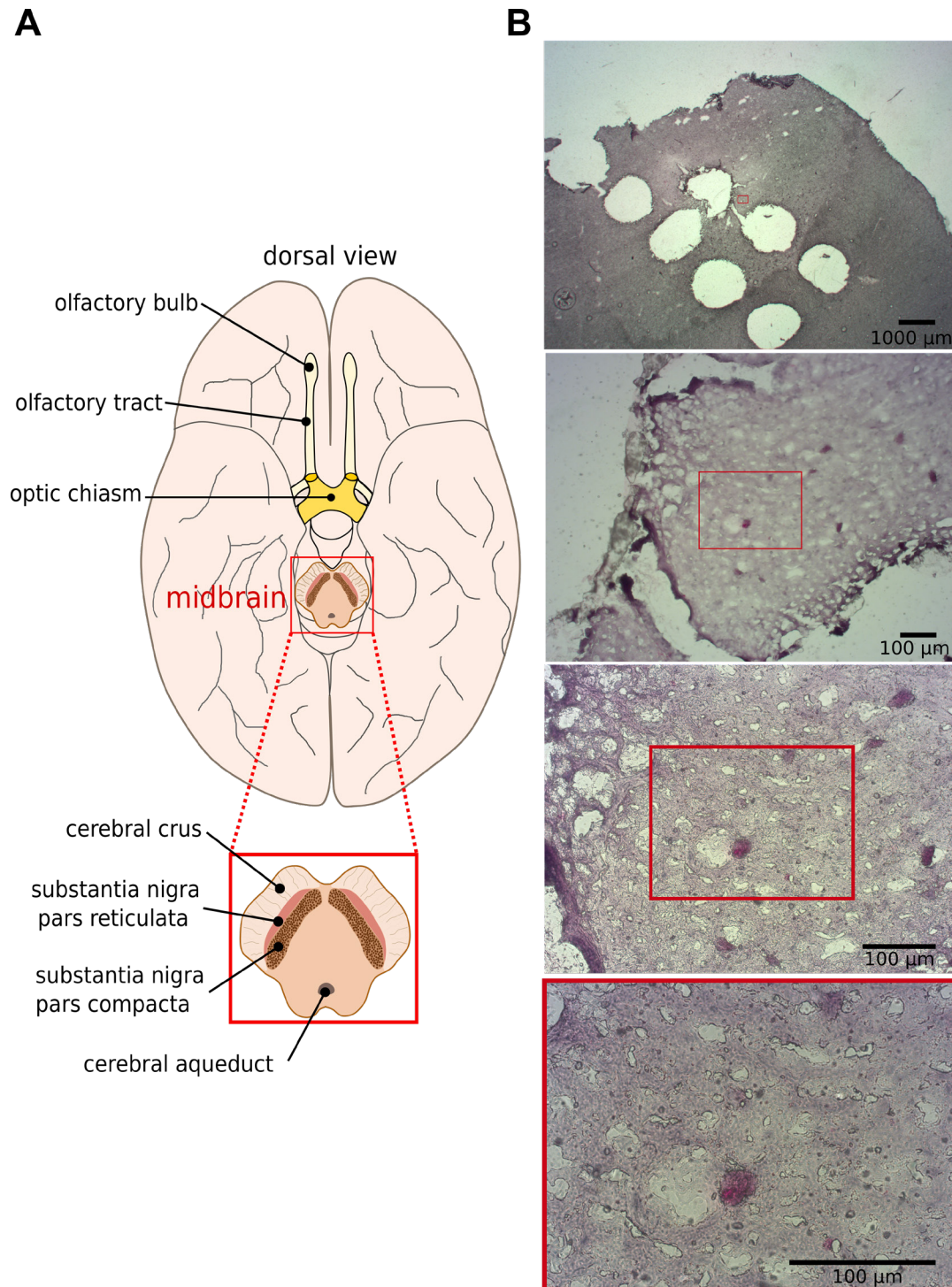
Figure 4. Human tissue description and microscopic images of a LB as guidance for X-ray-based analyses.
(A) Schematic anatomical representation of the SN within the midbrain as region of interest (ROI). **(B)** Microscopy images of different magnifications focused on an immunostained LB inside a neuromelanin-positive neuron of the SN. Tissue was immunostained against α-syn with an alkaline-phosphatase-based new fuchsin staining. Holes inside the tissue originated from biopsy punches used for another project. Red squares are used to highlight the position of the LB in lower magnifications. Adapted with permission from (Joppe et al., 2020) © The Optical Society.

2.2.1.2   X-ray-based measurements of human midbrain sections

Data were recorded at the ESRF (Grenoble, France) using the nanofocus experiment endstation (EH3) of the beamline ID13. We aimed at analyzing neuromelanin-positive neurons and LBs in these cells and used an in-line microscope for identification. The experimental configuration is depicted in Figure 5.
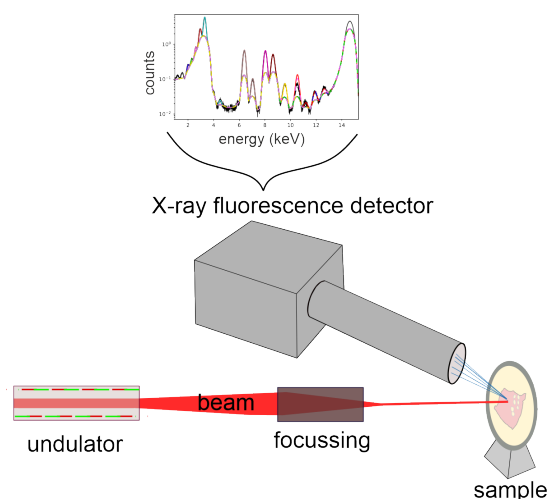
Figure 5. Principle of XRF measurements. Experimental setup for XRF measurements. The detector records an electrical signal proportional to the energy of an absorbed photon. With proper calibration, the number of photons per energy interval can be calculated, which can be visualized in a spectrum.

For the experiment, a photon energy of 14.8 keV with an energy spread of $\Delta E/E = 0.1\ \%$ defined by a Si(111) channel-cut monochromator was used. A two-dimensional single-photon counting X-ray detector (Eiger 4M, Dectris) was used to capture XRD. An energy-sensitive silicon-drift X-ray detector recorded XRF photons (Vortex EM, SII NanoTechnology Inc.).

A standard reference material and the pyFAI-calib software (Ashiotis et al., 2015) were utilized to calibrate the detector distance of the Eiger detector. At distances $z_{Eiger} = \{303.194,\ 503.067,\ 901.188,\ 1298.137\}$ mm, the Eiger detector distance and position of the primary beam (and detector tilt) was calibrated. Two different distances for the XRF detector were chosen, $z_{Vortex} = 25.5$ mm and 35.5 mm, depending on the size of the sample holder. All other relevant parameters for the configuration of the XRF detector are summarized in Table 2.

Table 2. Parameters used for the configuration of the Vortex EM silicon drift detector. An aluminum cap with a circular aperture was used as a collimator by placing it on the detector. Adapted with permission from (Joppe et al., 2020) © The Optical Society.

Parameter	Value
Sample − collimator aperture (mm)	15.5 ± 1 (PP foils)
	20.5 ± 1 (Kapton foils)
Distance aperture − entrance window (mm)	10
Aperture opening diameter (mm)	3.6
Entrance window − Si chip (mm)	3
Thickness Si chip (µm)	500
Thickness Be window (µm)	8
Active area (mm^2)	40
Tilt angle (degrees)	15.62

A stack of compound refractive lenses was used achieving X-ray focusing. Due to the usage of two sets of nanofocusing Si compound refractive lenses, a focal spot of 240×250 nm^2 was generated. We assumed a constant photon flux at $I_0 = 8.4 \times 10^9$ photons s^{-1}. Fluorescence spectra were calibrated to the amplitude of the Argon K$_\alpha$ fluorescence line (Joppe et al., 2020).

2.2.1.3 Analysis of XRF data

In order to analyze the elemental composition of cells and LBs in PD and CO samples, each sample was placed directly into the focus of the X-ray beam. Regions of interest (ROIs) on each section were raster scanned. The detector generated a spectrum of the recorded XRF photons at each scan point. Afterwards, spectra could be averaged over specific areas within the raster scanned ROIs (Figure 6A). In order to quantify intra- and extracellular levels of recorded trace elements separately and to generate area-specific mean spectra for analysis, measured cells within the ROIs had to be contoured in a next step. The intensity image of XRF data and fluorescence maps from specific elements were therefore compared with an optical micrograph. Selenium was relatively homogeneous distributed within the measured cells, therefore, the selenium Kα fluorescence intensity map was used to delimit the neuron from surrounding tissue (Figure 6B).

A

B
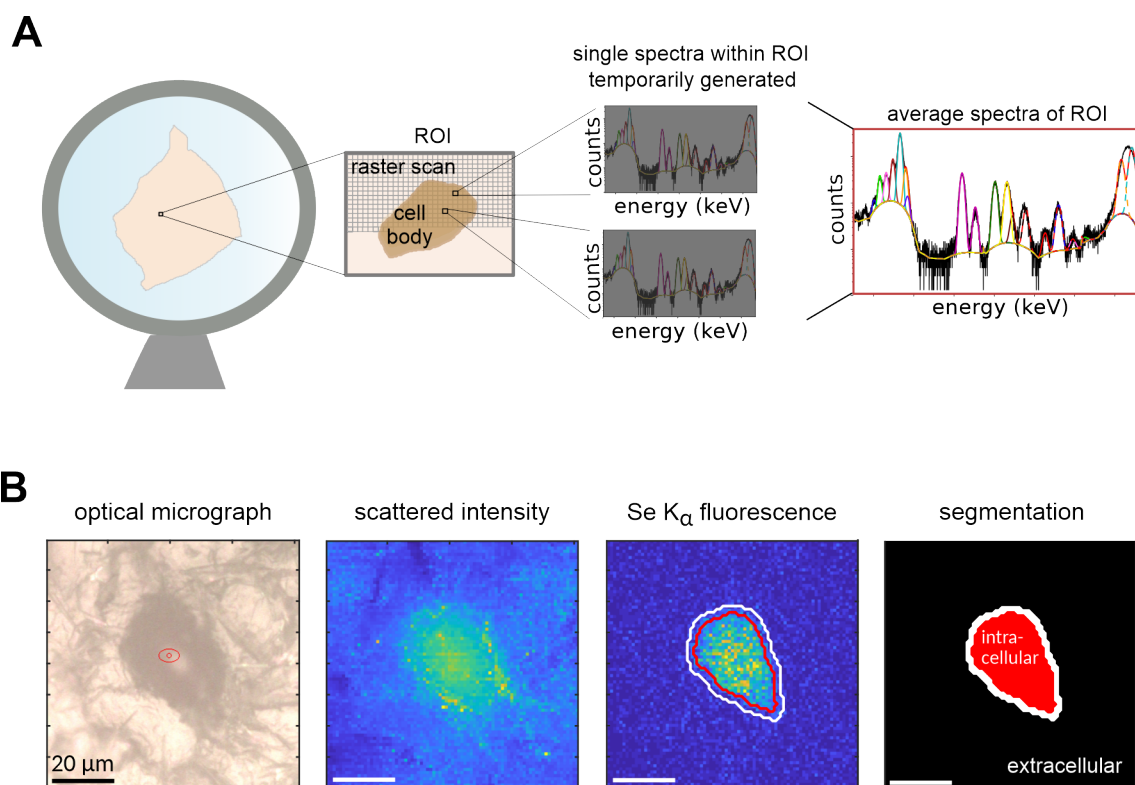
Figure 6. Processing of XRF data and intracellular area delimitation. (A) A ROI which contained at least one neuromelanin-positive neuron was defined at the brain section and was raster scanned with a focused X-ray beam. At each scan point a single fluorescence spectrum was recorded, which were averaged for subsequent analyses. **(B)** For quantification, the intracellular area was delimited from the extracellular region at the ROI. The map of the selenium K_α fluorescence intensity was used to delimit the cell. Using MATLAB, the selenium fluorescence map was filtered with a Gaussian and a manual threshold was applied to divide each image into an intra- and extracellular area. By slightly enlarging and inverting the intracellular area, the extracellular compartment could be identified. Adapted with permission from (Joppe et al., 2020) © The Optical Society.

In a next step, PyMCA (Solé et al., 2007) was used to identify which trace elements were detected in our sample based on the spectral line intensities. For energy calibration and fitting the peaks of the spectral lines to the corresponding elements, the averaged spectrum of a cell in each scan or the extracellular area of a scan was analyzed by using PyMCA. In addition, the NIST Standard Reference Material 1577b (bovine liver) was fitted in PyMCA. The bovine liver served as a calibration standard to determine absolute element concentrations (area density in g cm^{-2}) in human tissue sections (Table 3).

Table 3. Elemental composition of the NIST Standard Reference Material 1577b bovine liver. The area density of each element within the bovine liver was used to calculate the element concentration in human tissue. X-ray emission energies were obtained from (Thompson et al., 2009). Adapted with permission from (Joppe et al., 2020) © The Optical Society.

Elements	$K_{\alpha 1}$ (keV)	Mass fraction (g [100 g]$^{-1}$)	Area density (g cm^{-2})
K	3.31	0.994	1.12×10^{-8}
Ca	3.69	160	1.31×10^{-12}
Mn	5.90	10.5	1.19×10^{-13}
Fe	6.40	184	2.08×10^{-12}
Cu	8.05	160	1.81×10^{-12}
Zn	8.64	127	1.44×10^{-12}
As	10.54	0.05	5.65×10^{-16}
Se	11.22	0.73	8.25×10^{-15}
Br	11.92	9.7	1.10×10^{-13}

To calculate the absolute concentration c_i of a specific element i, the following formula was used:

$$c_i = c_i^{bov} \cdot \left(\frac{A_{Ar}^{bov}}{A_{Ar}}\right) \cdot \left(\frac{A_i}{A_i^{bov}}\right) \cdot \left(\frac{d}{d_{ref}} \frac{t_{ref}}{t}\right)$$

The term $\left(\frac{A_{Ar}^{bov}}{A_{Ar}}\right)$ means the fit area ratio of the Argon K_α line of both the bovine liver and the sample and c_i^{bov} abbreviates the certified reference concentration of the element in the bovine liver. While A_i^{bov} expresses the fit area of the element in the bovine liver spectrum, A_i contains the fit area of the element in the midbrain sample spectrum. The actual thickness of the bovine liver of 150 μm is termed d and the exposure time t. t_{ref} is the rescaled exposure time of the bovine liver to 1 s and d_{ref} an effective thickness of 30 μm to match the midbrain sample thickness. Figure 7 shows the fitted spectrum of the averaged bovine liver (A) and an averaged spectrum of a cell of a control sample (B) containing all detectable elements. The continuum background was determined with PyMCA using manually chosen parameters for the 'strip' filtering algorithm (Joppe et al., 2020).

2.2.1.4 Tissue preparation for cholesterol analysis

Midbrain tissue from nine PD and ten CO patients (three cancer and seven MS patients) was used to compare the amount of cholesterol between these two groups (Table

4). Therefore, on dry ice small pieces were cut out of the tissue block. For each patient three tubes were prepared with approximately 30 mg of tissue inside to have both technical and biological replicates for the lipid extraction. The tissue was stored at −80 °C until further preparation for the lipid extraction, accomplished by our collaboration partners Dr. Cornelia Herrfurth and Sabine Freitag (Department for Plant Biochemistry in Göttingen).
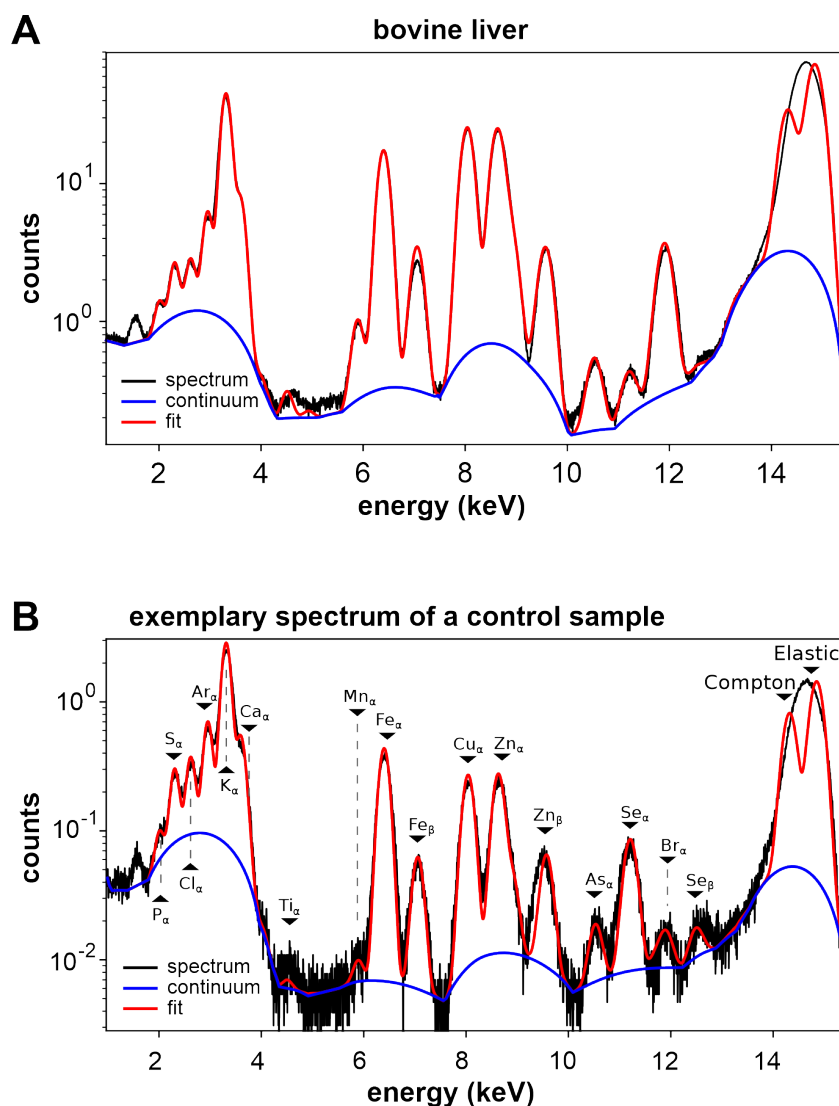
Figure 7. XRF spectrum of a bovine liver and a control sample. For both XRF spectra, PyMCA was used to fit the data. A red line indicates the averaged fit, whereas the spectrum of the measured material is shown in black and the continuum background is indicated by a blue line. **(A)** Average spectrum of over 10000 individual spectra obtained from the measurement of a 150 μm thick section of a bovine liver. The continuum background was determined with PyMCA using manually chosen parameters for the 'strip' filtering algorithm. **(B)** An exemplary average spectrum of a control patient (intracellular region). The instrumental settings did not allow to resolve the Compton and elastic scattering peak. Minimum amounts of titanium found in both spectra are probably caused by contamination within the collimation system of the fluorescence detector. Adapted with permission from (Joppe et al., 2020) © The Optical Society.

Table 4. Characterization of the used human samples for cholesterol analysis. Samples and detailed information were provided by the UK brain bank. CO: control patient group, PD: Parkinson's disease, MS: multiple sclerosis, F: female, LBDBS: Lewy Body disease (α-synucleinopathy) brain-stem predominant, LBDN: Lewy Body disease (α-synucleinopathy) neocortical predominant, M: male, post mortem interval: the time in hours (h) between death and tissue freezing, N/A: not available, y: years.

Case ID	Disease type	Classification	Age	Gender	Braak stage	Neuropathological diagnosis	Disease duration [y]	Post mortem interval [h]
PD29	PD	PD	76	M	6	LBDBS	7	15
PD39	PD	PD	82	F	5	LBDBS	15	12
PD50	PD	PD	82	F	6	LBDBS	14	18
PD74	PD	PD	85	M	6	LBDBS	9	17
PD153	PD	PD	76	F	6	LBDN	7	12
PD268	PD	PD	72	M	6	LBDN	20	8
PD458	PD	PD	73	M	6	LBDN	19	10
PD334	PD	PD	87	M	N/A	LBDN	9	21
PD666	PD	PD	93	F	6	LBDN	15	24
MS506	MS	CO	61	F	N/A	N/A	50	21
MS517	MS	CO	48	F	N/A	N/A	25	12
MS520	MS	CO	74	M	N/A	N/A	42	21
MS523	MS	CO	63	F	N/A	N/A	32	20
MS528	MS	CO	45	F	N/A	N/A	25	17
MS530	MS	CO	42	M	N/A	N/A	21	15
MS536	MS	CO	47	F	N/A	N/A	21	30
CO28	cancer	CO	60	F	N/A	diffuse hypoxic damage	N/A	13
CO46	cancer	CO	75	M	N/A	N/A	N/A	24
PDC035	cancer	CO	89	F	N/A	diffuse hypoxic damage	N/A	13

2.2.1.5 Lipid extraction and cholesterol analysis

The following procedure of lipid extraction was performed using an adapted protocol for extraction of cholesterol from the brain samples. The protocol was provided and performed by the Department for Plant Biochemistry in Göttingen. First, the samples were grinded using the Mixer Ball Mill MM200 with stainless steel grinding jars (Retsch GmbH, Haan, Germany). From approx. 30 mg gross weight of the tissue, 10 mg were extracted as previously described applying some modifications (Matyash et al., 2008). Sample extraction was performed using 0.75 ml of methanol, which contained 3.1 µmol ergosterol as internal standard. Samples were vortexed, 2.5 ml of methyl-*tert*-butyl ether (MTBE) were added and the extract was shaken for 1 h at RT. Phase separation was initiated by adding 0.6 ml of distilled water. Afterwards, an incubation of the mixture for 10 min at RT and centrifugation at 450 x g for 15 min followed. While the upper phase was collected, the lower phase was re-extracted with 0.7 ml methanol/water (3:2.5, v/v) and 1.3 ml MTBE as described above. Streaming nitrogen was used to dry the combined upper phase. Then, it was resuspended in 0.5 ml of hexane.

Prior the analysis, a 20-fold dilution of the sample in hexane was performed and 5 µl of pure N,O-bis(trimethylsilyl)trifluoroacetamide (Sigma, Germany) were added to 10 µl of each sample. For analysis, an Agilent 5977B mass selective detector connected to an Agilent 7890B gas chromatograph equipped with a capillary HP-5MS UI column (30 m × 0.25 mm; 0.25 µm coating thickness; Agilent) was used. Helium served as carrier gas (1 ml/min) and the injection port temperature was 280 °C. The temperature gradient reached 180 °C for 1 min, 180 – 320 °C at 5 K/min and 320 °C for 5 min. For the transfer line, the following set up was used: electron energy of 70 eV, an ion source temperature of 230 °C, and a temperature of 280 °C. Under the mentioned conditions, the retention times of the trimethylsilyl ether derivatives of cholesterol and ergosterol were detected at 23.9 and 25.0 min, respectively. Using a mass range of m/z 50-650, the mass spectrometer was operated in the scan mode. Gas chromatography-mass spectrometry (GC-MS) data analysis was performed using the Agilent ChemStation data analysis software.

2.2.2 Animal handling and tissue processing

2.2.2.1 Animals

Wild-type C57BL/6J mice were used for the experiments of this thesis, which were obtained from Charles River (Sulzfeld, Germany). During ongoing experiments, the animals were kept in the mouse room of the Neurology department with standard ad libitum feeding and 12 hours dark/light cycle. Five animals were maximally housed in one individual ventilated cage. For experiments using animals of an age of 10 weeks and older, the mice were resettled to our animal facility two weeks before starting the experiment to allow habituation to the new environment. For experiments with mouse pups, mice (wild-type C57BL/6J) were paired in the central animal facility, University Medical Center Göttingen. The pregnant mother animals were transferred to the mouse room of the Neurology department some days before the delivery of the pups. All animal experiments were governed by the national German animal protection law listed under the grant no. 33.9-42502-04-15/1982 (LAVES Niedersachsen) and the approval was given by the local authorities. For preparation of primary cortex neuron cultures, pregnant C57BL/6J mice (central animal facility, University Medical Center Göttingen) were used as donor animals for embryos of embryonic day (E) 18.5.

2.2.2.1.1 Overview on the used animal models

Animal models were used to analyze the impact of iron as well as fasudil on the α-syn spreading pathology in the brain. Both study models are used to understand and clarify the effect mechanism of the α-syn propagation as one of the major characteristics in PD. In a first study, mouse pups were treated with carbonyl iron between p10 and p17 per gavage. At an age of approximately 12 weeks, mice were injected with α-syn PFFs or monomers to analyze the mutual effect of iron and α-syn on motor and cognitive behavior as well as the effect on α-syn propagation at 90 dpi (Figure 8A). In a parallel experiment, uninjected animals were used to analyze the iron enrichment in mouse brains.

In a therapeutic approach, mice were injected with α-syn PFFs or monomers and additionally treated with fasudil via drinking water between the injection and their sacrifice (Figure 8B). An overview on the used animal models is given in Table 5. The model-based treatment and injection method will be described in the following chapters.
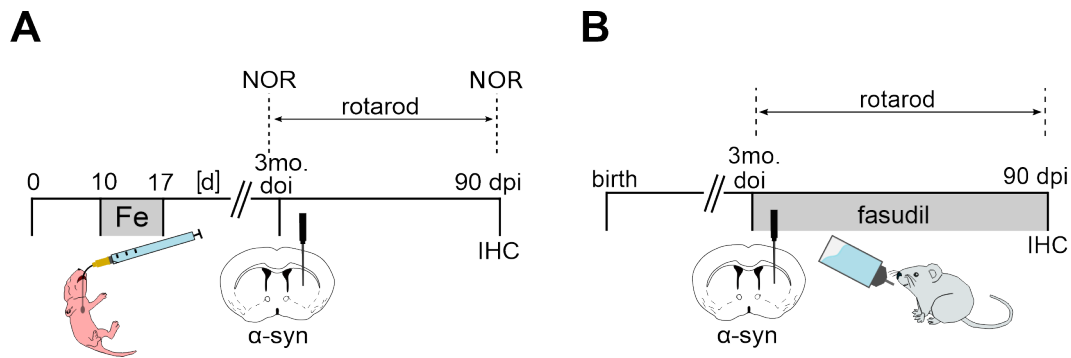
Figure 8. Experimental layouts of the main *in vivo* studies. (A) Experimental procedure of a study investigating the influence of iron on PFFs-induced α-syn spreading. Iron was treated per gavage, α-syn was injected intrastriatally. Novel object recognition test (NOR) and rotarod test were performed to assess the behavior. **(B)** Experimental procedure of a study investigating the influence of fasudil on PFFs-induced α-syn spreading. Mice were injected with α-syn PFFs intrastriatally and received fasudil via drinking water. In both studies animals were sacrificed at 90 days post injection (dpi). Doi: day of injection, d: days, IHC: immunohistochemistry, mo.: months.

2.2.2.2 Treatment of mice

2.2.2.2.1 Iron intoxication

Mouse pups (C57BL/6J) were fed with iron or sorbitol (control condition) between p10 and p17 by oral gavage. Within this time frame, the blood brain barrier is still open, so that iron treatment should lead to an increased iron load inside the brain. Based on the weight of the pups they were fed with between 50 and 80 µl of iron or control solution. Before applying, carbonyl iron was dissolved in 5 % aqueous sorbitol solution, which served as vehicle. Iron was fed in three different concentrations: 60 mg iron per kg body weight, 120 mg iron per kg body weight and 240 mg iron per kg body weight. For convenience only, from now on the iron treatment groups are mentioned as 60 mg/kg Fe, 120 mg/kg Fe and 240 mg/kg Fe. The control group was treated with 5 % aqueous sorbitol solution. Between p10 and p14 plastic feeding tubes were used for the gavage while metal tubes had to be used between p14 and p17. During the whole iron treatment time frame, pups were still in the cage with the mother animal. Since pups ingest their own excrements, which could thus contain different iron amounts (due to gavage with different iron dosages), pups from the same litter were treated with the same iron dosage. All animals respectively both sexes were included in the experiment.

Table 5. Overview on the used mouse models. In an iron intoxication model, the treatment with sorbitol is a vehicle/control condition for iron treatment. Iron was prepared in three different dosages diluted in 5 % sorbitol. Iron and fasudil concentrations were stated as mg/kg body weight (bw). As injection solution either human (hum) or mouse (ms) α-syn was used. Mice were injected with either α-syn monomers or preformed fibrils (PFFs) diluted in PBS. F: female, Fe: iron, ICP: inductively coupled plasma, IHC: immunohistochemistry, M: male, XRF: X-ray fluorescence.

Study model	Mouse line	Treatment	Injection	Sample size (n)	n per gender	Analysis method
iron pathology	C57BL/6J	sorbitol	hum α-syn monomer	9	4×F 5×M	IHC
iron pathology	C57BL/6J	sorbitol	hum α-syn PFFs	13	7×F 6×M	IHC
iron pathology	C57BL/6J	60 mg/kg bw Fe	hum α-syn monomer	10	6×F 4×M	IHC
iron pathology	C57BL/6J	60 mg/kg bw Fe	hum α-syn PFFs	12	6×F 6×M	IHC
iron pathology	C57BL/6J	120 mg/kg Fe	hum α-syn monomer	9	3×F 6×M	IHC
iron pathology	C57BL/6J	120 mg/kg Fe	hum α-syn PFFs	14	6×F 8×M	IHC
iron pathology	C57BL/6J	240 mg/kg bw Fe	hum α-syn monomer	8	4×F 4×M	IHC
iron pathology	C57BL/6J	240 mg/kg bw Fe	hum α-syn PFFs	13	4×F 9×M	IHC
iron pathology	C57BL/6J	sorbitol	/	5	1×F 4×M	ICP spectrometry
iron pathology	C57BL/6J	60 mg/kg bw Fe	/	6	3×F 3×M	ICP spectrometry
iron pathology	C57BL/6J	120 mg/kg bw Fe	/	5	2×F 3×M	ICP spectrometry
iron pathology	C57BL/6J	240 mg/kg bw Fe	/	5	2×F 3×M	ICP spectrometry
iron pathology	C57BL/6J	/	/	2	1×F 1×M	XRF
iron pathology	C57BL/6J	60 mg/kg bw Fe	/	4	2×F 2×M	XRF
iron pathology	C57BL/6J	120 mg/kg bw Fe	/	2	2×F	XRF
fasudil treatment	C57BL/6J	/	ms α-syn monomer	10	10×M	IHC
fasudil treatment	C57BL/6J	/	ms α-syn PFFs	8	8×M	IHC
fasudil treatment	C57BL/6J	30 mg/kg bw fasudil	ms α-syn PFFs	10	10×M	IHC

2.2.2.2.2 Fasudil application

In a therapeutic approach, the ROCK inhibitor fasudil was tested in regard to its effects on α-syn spreading. Fasudil treatment started directly after the injection of mouse α-syn PFFs and the treatment was continued until mice were sacrificed. Mice were treated with fasudil daily via drinking water with a dosage of 30 mg/kg bw per day, adjusting the application of fasudil to previously published studies of our lab (Tatenhorst et al., 2014, 2016).

2.2.2.3 Intrastriatal injection of α-syn

2.2.2.3.1 α-syn PFFs production

Monomeric and fibrillized α-syn solutions were provided by Dr. Stefan Becker (Max Planck Institute for Biophysical Chemistry, Göttingen, Germany). Both human and mouse α-syn were expressed recombinantly in E. coli and purified as described before (Hoyer et al., 2002). For the preparation of pure monomeric α-syn (aggregate-free), the protein was dialyzed against PBS buffer (pH 7.4), centrifuged at 106.000 x g for 1 h at 4 °C and filtrated through 0.22 µm ULTRAFREE-MC centrifugal filter units (Millipore). The protein concentration of α-syn monomers diluted in PBS was finally adjusted to 5 mg/ml.

For fibrillization, both monomeric human and mouse α-syn were incubated in PBS buffer at RT and 37 °C, respectively, with constant stirring at 200 rpm. The fibrillization progress was monitored with a thioflavin T fluorescence assay (Hoyer et al., 2004). The steady state of fibrillization of human α-syn was reached after 7-9 days, while fibrillization of mouse α-syn took up to 11 days until it reached steady state. After preparation, monomeric α-syn and PFFs were shock frozen in liquid nitrogen and were stored at −80 °C.

2.2.2.3.2 Preparation of α-syn PFFs for injection

α-syn PFFs were defrosted at RT immediately before use whereas α-syn monomers were kept on ice. Directly before the injection, the PFFs solutions (PFFs amounts in stock solution: 3.4704 mg/ml) were diluted with PBS to achieve the desired dosage (5 µg in 2 µl) and were sonicated (30 sec, 1 cycle, 10 % power; Volpicelli-Daley et al., 2014). The sonication ensures that long-chain molecule fibrils are shortened, which is a crucial step to generate small seeds.

2.2.2.3.3 Anesthesia and surgical procedure

C57BL/6J mice received an analgesic treatment with Metamizole (1.5 mg/ml) in drinking water, starting two days before surgery and ending two days after the injection of α-syn. Mice were anesthetized with an intraperitoneal injection of ketamine (150 mg/kg bw) and xylazine (10 mg/kg bw) solution. In order to verify the depth of the anesthesia, the toe pinch reflex and eyelid reflex were checked before the surgery.

Under anesthesia, the skull of the mouse was fixed within a stereotactic frame (Figure 9A). The skin was opened with a longitudinal cut to determine the Bregma and Lambda coordinates at the cranial roof. Measuring coordinates of both anatomical points, the coordinate in the dorsoventral axis should not vary more than 0.3 mm, otherwise the skull position was corrected. The stereotactic injection was performed into the striatum at the right hemisphere for every mouse and the injection coordinates were calculated based on the Bregma point of each mouse by means of the following information taken from the Paxinos Mouse Brain Atlas (Paxinos & Franklin, 2003): Anteroposterior axis + 0.4 mm; mediolateral axis −1.8 mm; dorsoventral axis −3.5 mm.

The injectional plane and injection site are visualized in Figure 9B. A drilled hole into the skull enabled a slow insertion of a thin glass capillary into the brain tissue until the target coordinate of depth (dorsoventral axis) was reached. After the injection (injection volume 2 μl, injection rate 500 nl/min) the needle was left in place for 4 minutes to prevent reflux of the injected substance via the injection pathway. The capillary was slowly removed, the skin above the skull was closed with DermaBond (tissue glue) and the mouse received an injection of 1 ml of the sterofundin electrolyte solution (warmed up at 37 °C) into the nuchal fold to prevent from dehydration. Under observation, the mice were sleeping at a warming pad under a thermal lamp until they woke up from anesthesia.

2.2.2.4 Behavioral tests

After the stereotactic injection, the weight of the mice was weekly controlled as an indicator for recovery and physical health of the mice until the sacrifice. In order to detect treatment-related behavioral changes or pathological abnormalities, behavioral tests were conducted during both the iron α-syn study and the fasudil α-syn study. Animals performed the rotarod test weekly (once a week). Mice included in the study analyzing the contribution

of iron on α-syn spreading were additionally tested with the novel object recognition test (NOR) starting two days before the α-syn injection and two days before sacrifice at 90 dpi.
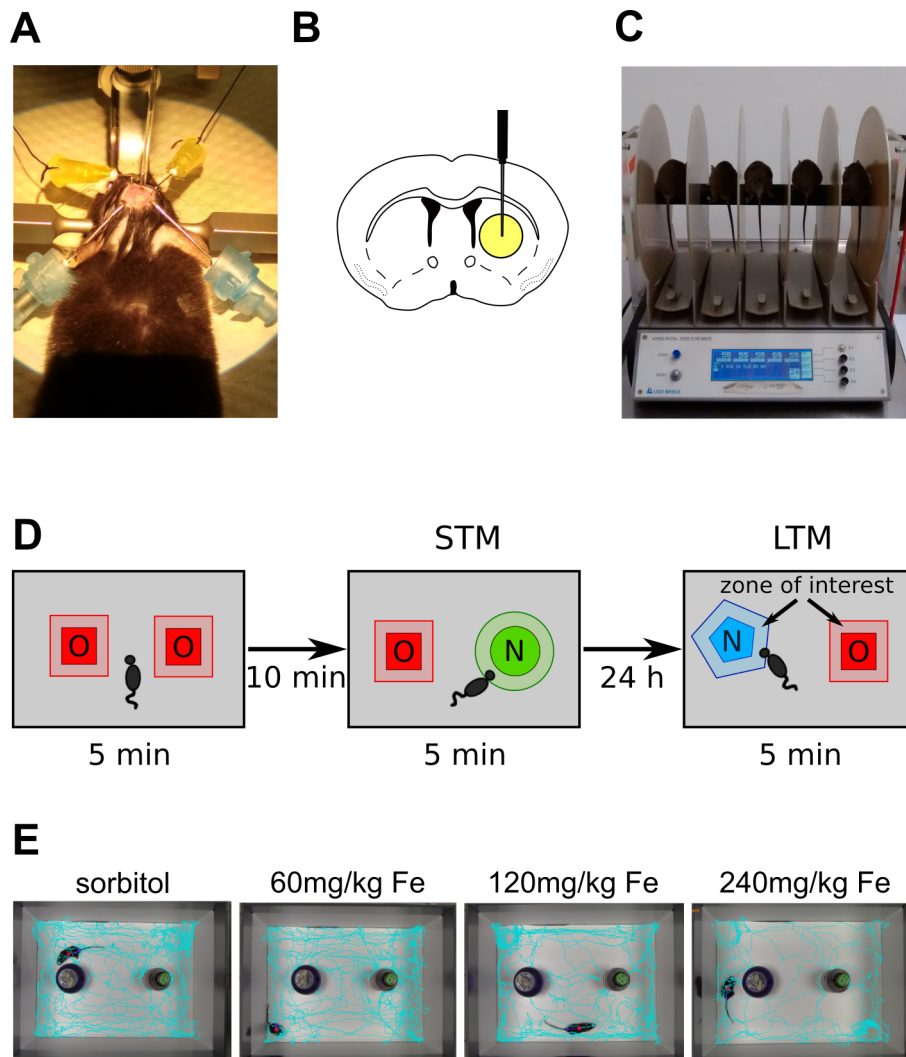
Figure 9. Illustrations on the stereotactic injection procedure and used behavioral tests. (A) Stereotactic injection. The skull of the mouse is fixed with ear bars and a teeth holder. A glass capillary is inserted inside the brain to inject α-syn. **(B)** The scheme illustrates the coronal view on the injection site in the striatum (adapted from Paxinos and Franklin, 2003). **(C)** Rotarod device. In parallel, up to five mice are running on the rotarod with accelerating speed from 5 to 40 rpm for maximum 300 seconds. **(D)** The procedure of the NOR. After a habituation phase inside the empty arena, the mouse is placed inside the arena with two identical objects for 5 min to get used to these objects. After a recovery phase, the short-term memory (STM) is tested by recording the mouse while exploring a familiar and one novel object. The long-term memory (LTM) is tested after 24 h. The Ethovision XT 8.5 software determines the head direction to the object within 2 cm of the object's diameter, which is hereby called the zone of interest. **(E)** Exemplary images on the movement of the mice within the experimental cage with two different objects – one familiar and one novel object. The exemplary images represent mice belonging to the four different treatment groups (sorbitol = vehicle, 60 mg/kg Fe, 120 mg/kg Fe, 240 mg/kg Fe) before α-syn injection.

2.2.2.4.1 Rotarod

The rotarod test was used to analyze motor behavior. Motor coordination, balance ability and endurance are required to complete the rotarod test properly. Up to five mice can be tested simultaneously on the rotating rod, which has a diameter of 3 cm (Figure 9C). Large disks separate the mice from each other. Placing the mice on the rod, a constant speed of 5 rpm is kept. In order to familiarize the mice to the test and to reach stability in the test performance, the mice were pretrained on the rotarod at a constant speed of 15 rpm (three trials for 5 min) on two consecutive days before the first official assessment.

During the experiment, the spin speed of the rotating rod was automatically accelerating from 5 rpm to 40 rpm within 5 min of testing and the time was recorded after how many seconds the mouse fell from the rod (between 0 and 300 sec). At each testing day, mice performed three times on the rotarod with an intertrial interval of 30 min to reduce stress and fatigue. The test was performed at a similar time of day.

2.2.2.4.2 Novel object recognition test

One mouse was placed into an arena of 48 cm × 35 cm. After a 3-minute habituation phase within the empty arena, two identical objects were put inside the arena for 5 min. This phase aimed to familiarize the mouse with the objects. Afterwards, the mouse was transferred back into its cage for 10 min. Subsequently, the mouse was placed again into the arena with one of the familiar objects and one novel object for 5 min, meanwhile the mouse behavior was recorded with a camera placed above of the arena. With this 10-minute interval between habituation and recording phase, short-term memory (STM) of the mouse was assessed. In order to assess the long-term memory (LTM) of the mice, 24 h after the habituation phase, the mouse was again exposed to one familiar object and one novel object for 5 min. Figure 9D illustrates the NOR procedure measuring STM and LTM. The short-term and long-term experimental setup were analyzed with the Ethovision XT 8.5 software from Noldus. The software measured the duration (s) of the head direction to the object within 2 cm of the object's diameter, which is hereby called the zone of interest (indicated in Figure 9D). For the analysis, a discrimination ratio was generated relativizing the time spent with the novel object to the time spent with both objects, as previously described (Bevins and Besheer, 2006; Tatenhorst et al., 2016). The software could also give an output on the explorative behavior within the arena. Mice of all iron treatment groups showed explorative behavior, which is demonstrated by exemplary images in Figure 9E. To gather

information on the mobility of the mice, the distance moved was recorded for each mouse during 5 min of testing.

2.2.2.5 Transcardial perfusion and brain processing

In order to histologically analyze brain tissue of mice injected with α-syn, a transcardial perfusion was performed. Deeply anesthetized mice were transcardially perfused with ice-cold PBS for 5 min and afterwards with 4 % ice-cold PFA in PBS for 5 min. The brains were removed and post-fixed with 4 % PFA in PBS for 24 h at 4 °C. On the next day, the brains were transferred to 30 % sucrose in PBS and stored at 4 °C for two days for tissue dehydration as cryo-protection. Finally, the dehydrated brains were stored at −80 °C until cryo sectioning.

For the quantification of iron within whole mouse brains via inductively-coupled plasma (ICP) spectrometry, 6 month-old iron-treated mice were sacrificed, PBS perfused, and their extracted brains were frozen at −80 °C. Each brain was put in a tube with 500 µl Milli-Q water and homogenized (3 × 45 sec). Hyphenated ICP spectrometry analysis was accomplished by Prof. Dr. Bernhard Michalke (Helmholtz Institute, Munich, Germany).

For XRF analysis, 6 month-old iron (60 or 120 mg/kg Fe) treated mice and control mice were sacrificed and PBS perfused. Mice of the control group were not treated with iron. Brains were extracted, the hemispheres were divided and cut into 5 mm thick slices. These single blocks were mounted in cryo matrix and were cryofixed for 2 min in −160 °C cold 2-methyl butane to avoid ice crystal formation. Samples were stored in liquid nitrogen until usage. 30 µm cryosections were cut, freeze-dried and mounted between two layers of 4 µm ultralene foil (SpexSamplePrep) (Vogel-Mikuš et al., 2014).

2.2.2.6 Cryosectioning

For the analysis of fixed mouse tissue, brains were covered with a cryo matrix at −20 °C directly before cutting. 30 µm thick sections of the brain were cut. Half of all cut sections of the SN were directly mounted on Superfrost object slides whereas the other half was stored in 24-well plates filled with PBS. Sodium azide solution was added to each well of the plate (0.1 % sodium azide in PBS) to conserve the free-floating sections, and the plates were stored at 4 °C. Slices on object slides were stored at −20 °C until usage.

2.2.3 Cell culture

Cell culture experiments were performed to investigate the contribution of iron to α-syn spreading *in vitro* mimicking the *in vivo* model. Cortical cultures were used to establish iron treatment. To analyze spreading of α-syn, neurons were seeded into microfluidic chambers. Cells were treated with iron and α-syn on consecutive days.

2.2.3.1 Coating of culture plates and imaging dishes

Cell culture 24-well plates were coated with PLL and stored at 37 °C overnight. The plates were washed two times with PBS and once with Neurobasal and were stored at 4 °C until usage. For microfluidic chamber experiments, petri imaging dishes were coated with PLL over night at 37 °C. Afterwards, the dishes were washed twice with distilled water and the chambers were assembled with the dishes as described in chapter 2.2.3.2.

2.2.3.2 Preparation of microfluidic chambers

The microfluidic chambers were constantly reused for the experiments. Therefore, a precise cleaning procedure was applied prior to new cultures. Directly after use, the chambers were carefully cleaned with soap water. Afterwards, chambers were rinsed with distilled water (milliQ) and were kept overnight in a jar filled with distilled water at 37 °C. For the whole cleaning procedure, the microgroove side of the chamber has to face up. On the next day, chambers were transferred into a plastic dish and dried in the 60 °C warm incubator. Debris was removed from the chambers using scotch tape. In order to sterilize the chambers, they were incubated for at least 15 min in sterile 70 % ethanol under the cell culture hood. Afterwards, the chambers were dried for 1 h. In parallel, distilled H_2O was removed from PLL-coated imaging dishes and they were dried for 1 h, and then the chambers and imaging dishes were assembled. 200 µl warm cortex medium was filled inside one compartment of the chambers. After approximately 3 h, the other compartment was also filled with 200 µl medium. These ready-to-use chambers were left in the 37°C incubator until cell culture preparation.

2.2.3.3 Primary cortex neuron culture

C57BL/6J embryos (E 18.5) were used for primary cortex neuron cultures. All embryos were transferred to ice-cold CMF. Under aseptic conditions, meninges were removed, and the cortices were isolated. Cortex tissue was collected in ice-cold CMF and

centrifuged at 1 rcf for 2 min at RT. CMF was removed, and the pellet was incubated with 1 ml trypsin ($\geq$ 9,000 U/mg; 1.87 mg/ml) in 37 °C for 12 min under occasionally shaking movements. 100-150 µl DNAse (~400 U/mg) was added and the cell suspension was centrifuged for 1 min at 1 rcf. The supernatant liquid was exchanged with 1 ml FCS to inactivate the remaining trypsin. Under trituration with fire polished Pasteur pipettes, cells were dissociated and afterwards centrifuged for 4 min at 1 rcf at RT. The remaining pellet was resuspended in cell culture medium. A Neubauer counting chamber was used to quantify the number of cells within the solution. 250,000 cells/well were plated on PLL-coated coverslips inside a 24-well plate in 500 µl medium. 120,000 cells were seeded into the primary cell compartment of the microfluidic chambers and 250,000 cells at the opposing secondary cell compartment exactly one week later. All cells were stored in an incubator at 37°C with 5 % CO_2 and 95 % humidity. One day after preparation, half of the medium was replaced with 4 µM cytosine arabinoside containing medium (AraC; stock 1 mM) to reach a final concentration of 2 µM AraC within each well. AraC is an inhibitor of the DNA synthesis and is therefore used to control the proliferation and to decrease the amount of glia cells within the cultures. Every 2-3 days half of the medium in each well was replaced with fresh medium containing 2 µM AraC.

2.2.3.4   Iron treatment of cortex cells

A stock solution of 5 mM iron(II) chloride ($FeCl_2$) was prepared by dissolving $FeCl_2$ in 5 % glucose in distilled H_2O (sterile solution). For neuron cultures in 24-well plates, iron stock solution was diluted in cell culture medium to gain final treatment concentrations of 10, 50, 100 and 200 µM $FeCl_2$. As a control/vehicle condition, 5 % aqueous glucose was added to the medium in the same amount as in the iron conditions. Cells were incubated with iron or vehicle for 24 h. After treatment, cells were washed three times with medium. For the microfluidic chamber model, stock solution was diluted in warm cortex medium containing 2 µM AraC to obtain a treatment solution of 100 µM $FeCl_2$. At day *in vitro* (div) 2, the existing medium was removed from the cell side of the microfluidic chambers and 200 µl of the iron solution was added. As a control condition, the same amount of 5 % aqueous glucose was mixed with cortex medium as in the iron condition. After 24 h, the whole chambers were washed two times with fresh medium and were treated with α-syn.

2.2.3.5 PFFs treatment of cortex cells

Mouse α-syn monomers and PFFs stored at −20 °C were thawed – monomer at 4 °C and PFFs at RT – and both protein solutions were diluted 1:10 in sterile PBS. Then, α- syn PFFs were sonicated for 30 sec at RT at cycle 1 and with 10 % power. In microfluidic chambers, cells were treated with 1 µg PFFs or monomers diluted in 200 µl fresh cell culture medium. After 24 h of treatment starting at div3, the cells were washed three times with fresh medium. As a separate control condition, cells were treated with PBS instead of α-syn.

2.2.3.6 Fixation of cells

Cells in 24-well plates were rinsed with PBS and then fixed with 4 % PFA in PBS for 10 min at RT. Afterwards, PFA was replaced by PBS and the cell-containing coverslips were stored in PBS at 4 °C until staining. For longer storage of the unstained cells, PBS was replaced by 0.1 % sodium azide diluted in PBS.

The fixation procedure of cells within microfluidic chambers differs marginally from the above-mentioned procedure. First, the whole imaging dish, where the chamber was placed in, was filled with PBS to facilitate detaching of the chamber to the coverslip. After removing the chamber, PBS was replaced by 4 % PFA in PBS for 10 min. The following step was the same as above mentioned for 24-well plates.

2.2.4 Molecular biology and biochemical techniques

For the analyses of mouse tissue, immunohistochemical methods were applied. Depending on the evaluation method, the following antibody-based staining protocols were used: either fluorescence-based or peroxidase-based staining. An immunocytochemical approach, a modified Prussian blue staining and a ToxiLight Assay were used to analyze cortex neurons.

2.2.4.1 Immunohistochemistry

2.2.4.1.1 Fluorescence-marked antibody staining

In order to analyze α-syn spreading pathology through coronal mouse brain sections, a fluorescence-based antibody staining of α-syn was applied. For this staining, 30 µm thick sections, already mounted on object slides and stored at −20 °C, were used. The tissue was

rehydrated in PBS for one hour and afterwards incubated in citrate buffer (pH = 6.0) at 80 °C for 30 min. The sections were cooled down to RT within 30-60 min and then washed in PBS 2 × 5 min. The tissue was incubated for 20 min in 25 mM glycine in PBS and washed in PBS twice for 5 min. After incubation with 0.1 % Sudan black for 15 min, the sections were rinsed with water and washed with PBS 2 × 5 min. In order to block unspecific antibody binding, sections were incubated for 1.5 h at RT in a blocking solution inside a moist chamber. Afterwards, the tissue was incubated with the first antibody over night at 4 °C. Rabbit anti-phospho S129 α-syn antibody (EP1536Y, #ab51253, Abcam) was utilized to recognize α-syn aggregates in a dilution of 1:1000 in blocking solution.

On the following day, slides were washed 3 × 15 min in PBS and incubated with the second antibody in a moist chamber for 1.5 h at RT (Cy3 goat anti-rabbit, 1:500, #111-165-006, Dianova). Another washing step 3 × 10 min followed, and the sections were incubated in DAPI solution for 2 min to achieve staining of the nucleus since DAPI is known to bind to adenine-thymine rich regions in the DNA. The slides were washed with PBS 2 × 10 min and dried at 37 °C for 10 min. The sections were embedded with Mowiol and then dried at 60 °C for 10 min for a better expansion of the Mowiol. The slides were kept at RT overnight and were stored afterwards at 4 °C.

CD3-positive (CD3+) T cell stainings were performed by our collaboration partner PD Dr. Chi Wang Ip (University Hospital Würzburg, Germany). 30 μm thick brain sections of SN (pars compacta and pars reticulata) and the pre-commissural, commissural and post-commissural parts of the striatum of iron-treated mice were stained. Free floating sections were preincubated for 3 h at RT on a shaker with 5 % BSA / 5 % NGS in 0.01 M PBS. Afterwards sections were incubated for 2 h at RT with primary rat anti mouse CD3 antibody conjugated with Alexa Fluor® 488 (Biolegend, #100210) diluted in 1 % BSA / 1 % PBS in 0.01 M PBS. DAPI was used to label cell nuclei.

2.2.4.1.2 Peroxidase-based antibody staining

In order to stereologically quantify the dopaminergic neuron population in SNpc, 30 μm thick brain sections were stained free floating against tyrosine hydroxylase (TH) followed by an on-slide Nissl staining. Every fourth section of SNpc was washed 3 × 5 min with TBS in net tubes. The following quenching of endogenous peroxidase was performed by a 15 min incubation in 40 % methanol and 1 % H_2O_2 dissolved in TBS. After another washing step with TBS, sections were incubated in 5 % NGS in TBS for 60 min at RT to

block unspecific antibody binding. The incubation with the primary rabbit anti-TH antibody, diluted 1:1000 in 2 % NGS in TBS, took place for 48 h on a shaker at 4 °C.

The antibody solution was decanted, and the sections were washed three times in TBS. The secondary anti-rabbit (biotinylated) antibody was diluted 1:200 in TBS and stayed on the sections for 2 h at RT, followed by three times washing in TBS. For enhancing the signal power, the sections were incubated with the VECTASTAIN Elite ABC Peroxidase Standard kit (Vector Laboratories) for 2 h at RT. After washing with TBS (three times), the diaminobenzidine-HCl (DAB) Peroxidase Substrate kit was used to visualize TH staining through the chromogen DAB. Sections were incubated for about 20 min and the DAB reaction was stopped by an incubation in distilled water for 5 min. Subsequently, sections were transferred to Superfrost object slides and were dried for 5 days at RT.

Afterwards, the Nissl staining was performed. The tissue was rehydrated in distilled water for 5 min and stained with thionine acetate solution for 7 min, followed by another washing step in distilled water for 5 min. Dehydration of the tissue was reached by a step-by-step incubation in 70 % (2 min), 90 % (2 min) and 95 % (5 min) ethanol. After repeating all previously performed staining steps, sections were incubated in 100 % isopropanol for 5 min and then 3 times in xylene respectively for 5 min. Finally, slides were mounted with Entellan and stored at RT until stereological counting.

For the analysis of CD11b+ cells in brains of iron-treated animals, the related staining procedures were performed by our collaboration partner PD Dr. Chi Wang Ip (University Hospital Würzburg, Germany). 30 μm coronal cryo-sections of the SN (pars compacta and pars reticulata) and the pre-commissural, commissural and post-commissural parts of the striatum were used. Sections were preincubated free floating for 3 h at RT on a shaker with 5% BSA / 5 % NGS in 0.01 M PBS. Afterwards, they were incubated on a shaker overnight at 4°C with the primary rat anti mouse CD11b antibody (Bio-Rad Laboratories, #MCA74G), diluted in 1 % BSA / 1 % PBS in 0.01 M PBS. Sections were then incubated for 2 h with the biotinylated secondary antibody against rat Igs (Vector Laboratories), which was diluted in 1 % PBS / 1 % NGS in 0.01 M PBS, followed by an incubation with the avidin/biotin reagent (Thermo Fisher Scientific). In a next step, tissue was incubated and stained with DAB and H_2O_2. Cells were additionally stained with Hematoxylin.

2.2.4.2 Immunocytochemistry

In order to analyze the α-syn PFFs pathology in cortex cells, an antibody-based fluorescence staining was applied. Cells were washed twice in PBS and were incubated with 25 mM glycine in PBS for 20 min. After another step of 2 × 5 min washing in PBS, cells were incubated with blocking solution for 1.5 h at RT. The primary antibodies (rabbit anti-α-syn pS129, 1:1000, #EP1536Y; mouse anti-MAP2, # MAB3418) were diluted in blocking solution and cells were incubated with first antibodies over night at 4 °C. At the second day of staining, the cells were washed 3 × 15 min with PBS. Afterwards, cells were incubated with the secondary antibodies for 1.5 h at RT (Cy3 goat anti-rabbit, 1:500, #111-165-006; Cy5 goat anti-mouse, #111-175-146). The cells were washed with PBS for 3 × 10 min and incubated with DAPI for 2 min for nucleus staining. After another washing step for 2 × 10 min with PBS, cells were mounted with Mowiol and stored at 4°C.

2.2.4.3 Modified Prussian blue staining

In order to stain Fe^{3+} ions, a previously reported protocol was adapted (Höpken, 2005). The protocol is based on the classical known Prussian blue staining from Perls (1867) detecting Fe^{3+} combined with a DAB approach to intensify the iron signal (Nguyen-Legros et al., 1980).

Cells were washed 2 × 10 min in PBS with 0.3 % Triton and afterwards incubated with 5 % potassium ferricyanide(II) dissolved in distilled H_2O for 30 min at RT. Following, the cells were incubated with 2 % potassium ferricyanide(II) dissolved in distilled H_2O in a 1:1 dilution with 2 M HCl for 30 min at RT. The addition of potassium ferricyanide(II) to iron in an acidic environment resulted in a blue staining of iron. To intensify the signal of iron, cells were incubated with DAB and nickel, mixed according to the description in the DAB kit (2.5 ml H_2O, 1 drop buffer, 1 drop nickel, 2 drops DAB) for 15 min at RT. Afterwards, an incubation for 15 min at RT in DAB, nickel and H_2O_2 followed (2.5 ml H_2O, 1 drop buffer, 1 drop nickel, 2 drops DAB, 1 drop H_2O_2). Cells were washed twice in PBS with 0.3 % Triton for 10 min. For slight staining of the nuclei, nuclear fast red was used (15 min). After another washing step of 2 × 2 min in PBS, coverslips were dipped in 100 % ethanol for 2 min and mounted with Histokit on an object slide.

2.2.4.4 ToxiLight Assay

To assess if iron treatment provokes toxicity in cortical neuron cultures, cell medium was collected from different time points prior and post iron treatment: directly before iron treatment (div 2), at the end of iron treatment (24 h post treatment start, div 3), 5 days post treatment start (div 7) and 12 days post treatment start (div 14). Medium was stored at -80 °C until usage. The cells were previously treated with 10, 50, 100 or 200 µM $FeCl_2$ or vehicle (only with 5 % Glucose). ToxiLight Assay was performed using the kit from Lonza. Medium was defrosted and 30 µl of each sample was pipetted into a 96-well plate (three replicates per condition). An equal amount of the kit solution was added to the sample and after 5 min of incubation the luminescence was monitored for each well with the Tecan Spark 10M multimode microplate reader (SparkControl software). The release of adenylate kinase from damaged cells was quantitatively measured. A mean value of the three replicates per condition was calculated and a negative control (medium from a blank well, without cells inside) was subtracted from all other conditions.

2.2.5 Microscopy and analyses of *in vivo* and *in vitro* experiments

2.2.5.1 Image processing and analyses of α-syn PFFs of the *in vivo* model

For the analysis of PFFs-induced α-syn pathology in mouse brain tissue, immunostained sections were imaged with a Zeiss Axioplan microscope (Zeiss, Göttingen, Germany). The MosaiX module of the AxioVision SE64 Rel. 4.9 software was used to generate images of whole brain sections (magnification of 10x). The same exposure time was used for all images in one experiment. For the evaluation of the images of one experiment, the same color intensities were used. Afterwards, only α-syn phosphorylated at S129 was quantified. From now on α-syn phosphorylated at S129 will be referred to as pS129-α-syn. The quantification of pS129-α-syn in whole sections was realized using two different methods: manual counting or threshold-based particle quantification. Both methods are separately described in the following chapters. In order to compile pS129-α-syn spreading maps and to assess the spread amounts of α-syn in specific brain regions per section, another manual rating approach was established, described in chapter 2.2.5.1.3.

Using the three above-mentioned approaches to investigate α-syn spreading in the mouse brain, six different coronal brain sections were analyzed. According to the Paxinos mouse brain atlas (Paxinos and Franklin, 2003) the following sections were analyzed

named after their distance to the Bregma point: 1.54 mm, 0.38 mm, 0.02 mm, -1.58 mm, -3.08 mm, -3.28 mm.

2.2.5.1.1 Manual α-syn spreading analysis

For a manual quantification of pS129-α-syn, merged images of both channels DAPI (nuclei staining) and Cy3 (pS129-α-syn) were imported to the vector graphics software Inkscape 0.92. Merged images (scale 0.65 µm / pixel) were overlaid with a grid. Each box of the grid covered an area of 150 µm × 150 µm (230.8 pixel × 230.8 pixel). The whole section was manually raster scanned by the investigator on a subjective perception. Signal within each box was rated as follows:

Low signal amounts: 1-5 α-syn-positive structures

Medium signal amounts: 6-10 α-syn-positive structures

High signal amounts: >10 α-syn-positive structures

To illustrate the rating, boxes in the grid were marked with dots in yellow (low signal), orange (medium signal) or red (high signal). The procedure is exemplarily depicted in Figure 10. For further analysis, both ipsilateral hemisphere (injected hemisphere) and contralateral hemisphere were individually examined. The total count of yellow, orange or red marked boxes was relativized to the total number of boxes covering the respective hemisphere to provide the percentual affected area. Graphs based on this 3-stage method give an idea on how much area of the hemisphere is highly affected by α-syn or how much area of the hemisphere is marginally affected.

In order to illustrate how much area of the whole brain section is generally affected (independent on the quantity evaluated in each counted box) a sum of all rated boxes (low, medium, high signal amounts) on both hemispheres was calculated, relativized to the box numbers of the total section and given as percentage (%).
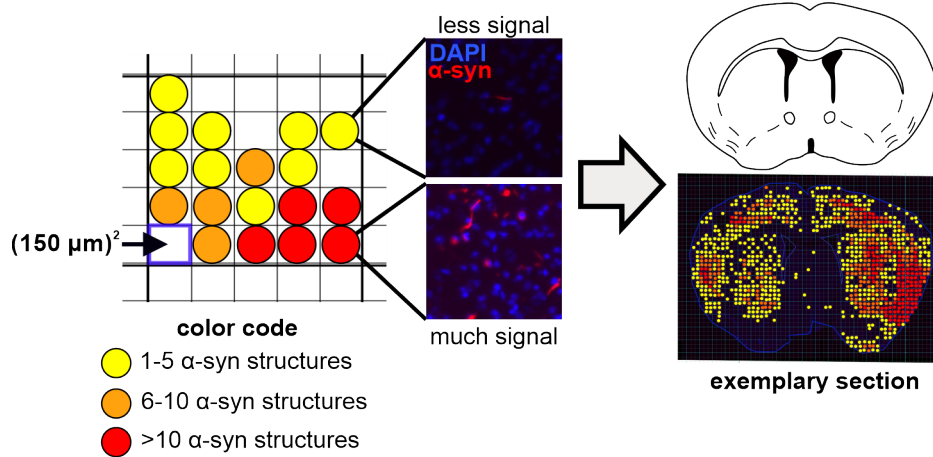
Figure 10. The procedure of the manual quantification analysis of α-syn spreading. Brain sections were covered with a grid. Immunolabeled α-syn structures were counted within each box of the grid using a 3-stage rating.

2.2.5.1.2 Threshold-based α-syn spreading analysis

The aim was to quantify pS129-α-syn signal in different brain sections of mice injected with α-syn PFFs. The threshold procedure is illustrated in the upper part of Figure 11. Therefore, processed microscopy images as described earlier in 2.2.5.1 were used. Images of the Cy3 channel were imported to the ImageJ software and converted to 8-bit images. The threshold function of ImageJ was used (default mode) and the threshold of interest was manually adjusted for each single image due to individual background signal (noise) (threshold of greyscale 231-250). After applying the selected threshold, the corresponding image of the DAPI channel was considered to surround and calculate the area of the injected and contralateral hemisphere separately. In another step, both contours were assigned to the threshold image and a tool named 'analyze particles' calculated the area of the α-syn-positive signal within each contour. Results were given as percentage resulting from the observed signal area divided by the total area of the corresponding hemisphere.

microscopy

threshold analysis of whole sections

set manual
threshold in
imageJ

close up image

definition of ROI

threshold image with ROI

quantification

region-specific rating analysis

image overlay

threshold image + DAPI image   close up image

comparison
with Paxinos

4 = strong
3 = moderate
2 = mild
1 = few
0 = no signal

pathology rating
per region

one marker (color) per sample

translation into
color code scale

++++

+++

++

+

-

Figure 11. Quantitative analysis of α-syn distribution after PFFs injections in mice. α-syn immunostained mouse brain sections were imaged and analyzed with ImageJ threshold-based particle analysis tool. For a quantitative analysis, α-syn signal was quantified within the ROI, which is either the injected or contralateral hemisphere. For a distributional analysis of pS129-α-syn, an overlay image of the threshold image and DAPI channel in grey-scale was generated. Comparing the overlay image with the Paxinos atlas figure (Paxinos and Franklin, 2003), α-syn signal was rated per brain region (rating scale from 0 to 4) using the cell counter function as aid. One marker represented one animal and per region 0 to 4 counts of each marker were set demonstrating the α-syn signal in the specific brain region of each animal. To visualize the group-specific average distribution of α-syn in different brain sections, the rating scale was translated into a color code. For a better overview, average values of the groups within the rating scale from 0 to 4 were translated into: −, +, ++, +++ and ++++.

Since the threshold was manually adjusted for each image in this quantification analysis, it was tested if the underlying thresholds per mouse differ significantly from each other. The analysis showed that the used threshold values did not vary significantly between the investigated groups (240 mg/kg Fe vs. control; one-way ANOVA; Figure 12).
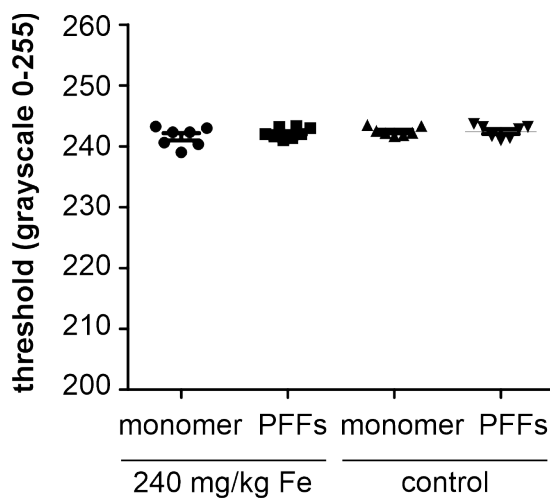
Figure 12. Manual threshold variance. The averages of the manually selected thresholds per group do not differ significantly between the four treatment groups. One-way ANOVA; n = 6-8 (average of 4-6 sections per mouse), data given as mean ± SEM.

2.2.5.1.3 Region-specific rating analysis of α-syn spreading and a connectome-based analysis

A region-specific rating analysis was performed to show an overview on affected brain regions and an estimation on the severity of the pathology within the regions. The analysis procedure is illustrated in the lower half of Figure 11. The same six sections per animal were analyzed as used for the quantitative threshold-based analysis described in the previous chapter. In the aforementioned analysis, the whole hemispheres of the sections were analyzed in a threshold-based quantification manner, which provides the difference

compared to this analysis. In this analysis, we aimed to visualize the distribution of α-syn through the brain and the amount of α-syn per brain region to compare this signal between groups in spreading maps. Therefore, we manually classified the observed α-syn signal per brain regions in a 5-stage rating scale as described below.

ImageJ was used to overlay the generated threshold image from 2.2.5.1.2 with the image of the DAPI channel showing the brain structures on the section due to the stained nuclei. The related Paxinos atlas figure of the identical section was opened with ImageJ and brain regions on the Paxinos figure were marked using the cell counter tool where the overlay-images showed α-syn signal. In addition, the occurrence of pS129-α-syn signal was graded in each different brain region as follows: − no positive signal, + sparse (few positive structures), ++ mild (minor clusters of positive structures), +++ moderate (dense signal covering a big area of the brain region) or ++++ severe (huge clusters of positive signal throughout the whole region). Exemplary micrographs are shown in Figure 13. Per group 6-8 animals were evaluated and a mean signal amount was calculated for each positively graded brain region. A color code was assigned to the scale and the results were illustrated as heat maps.
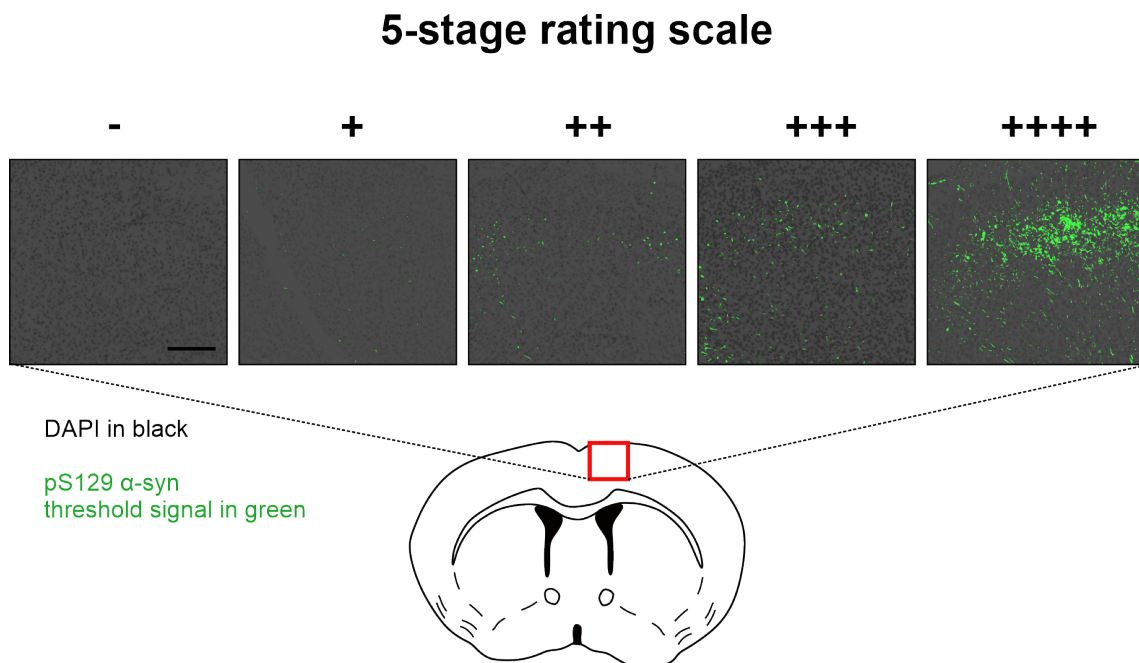
Figure 13. Exemplary images for spreading of α-syn using the 5-stage rating scale. Threshold images indicating pS129 signal (green) were overlaid with DAPI images (black) to visualize the presence of α-syn per region. From left to right the images show increased amounts of α-syn pathology visualized in green. Scale bar 200 μm.

In order to assess whether pS129-α-syn pathology spreads according to the anatomical connectivity starting from the injection site, the Allen Mouse Brain Connectivity Atlas (©2020 Allen Institute for Brain Science. Allen Mouse Brain Connectivity Atlas, available from: https://connectivity.brain-map.org/) was used (Oh et al., 2014). This platform includes mouse EGFP injection experiments and indicates its specific injection sites and volumes.

For the current study, the injection radius was computed based on the volume of 2 µl. Experiments included in the mentioned software were selected which used injection sites within our radius. Two injection sites (Exp. 158916311: https://connectivity.brain-map.org/projection/experiment/158916311; Exp. 100142580: https://connectivity.brain-map.org/projection/experiment/100142580) were selected to reconstruct the anatomical connectivity in our experiment. The software illustrated EGFP signal in different sections throughout the whole mouse brain. For a better visualization of the EGFP signal in brain sections, it was displayed in 'projection segmentation' maps showing the signal in front of a black background. In six defined brain sections, regions were marked which showed EGPF spreading signal and were illustrated in maps. Finally, these connectivity maps were compared to α-syn spreading maps of the current study.

2.2.5.2   Stereological quantification of dopaminergic neurons in mice

Stereological cell counting was used to assess the cell population of TH-positive (TH+) and Nissl-positive (Nissl+) neurons in the SNpc due to intrastriatal α-syn injections in mice. The mouse tissue was stained with a DAB-reaction as well as Nissl staining as described in chapter 2.2.4.1.2. Immunohistochemistry and evaluation were proceeded as previously described (Tatenhorst et al., 2014; Tönges et al., 2012). Using a Zeiss microscope and the compatible Stereo Investigator software (Stereo Investigator 9.0; Micro Bright Field Inc, Colchester, USA), every fourth section of an animal through the SNpc (8 - 10 sections in total) was analyzed. Specifically, cell population of TH+ and Nissl+ neurons were determined for each mouse in both hemispheres. Therefore, contours of the area of SNpc were outlined at 2.5x objective magnification level, while neuron quantification was performed at the 40x objective magnification level. A counting frame size of 50 µm × 50 µm was set for the optical fractionator application, furthermore a grid size of 100 µm × 100 µm, an interval of every fourth section through SNpc and a manual focus on top of the 30 µm thick section were chosen. Considering the manually counted

Nissl+ and TH+ neurons, the software calculated and projected the absolute cell population within the whole SNpc of each animal. The quantification of Nissl+ neurons was performed to exclude a mere downregulation of TH-immunoreactivity and to confirm the predominant loss of neurons.

2.2.5.3   CD11b+ and CD3+ analyses

The analysis of CD11b+ microglia and CD3+ T cells in mouse sections from animals treated with iron and α-syn were performed by our collaboration partner PD Dr. Chi Wang Ip (University Hospital Würzburg, Germany). At a magnification of 40x, CD11b+ microglia were quantified within an ocular grid of a defined area of 0.0625 mm^2 using a light microscope (Olympus BH2, Olympus, Hamburg, Germany). Axio Imager.M2 fluorescence microscope (Zeiss, Göttingen, Germany) was used to quantify T cell amounts inside the mouse sections. Since T cells were rarely present, the entire regions of the SNpc and SNpr, the pre-commissural, commissural and post-commissural parts of the striatum were respectively analyzed on each section. For each animal the α-syn injected and contralateral hemisphere were investigated separately by quantifying 2-3 grids per region and 2 sections per region in average. CD11b+ microglia amounts were calculated per square millimeter.

2.2.5.4   Analyses of iron in mouse brain tissue

In order to assess the iron amount within whole mouse brains of mice treated with different dosages of iron, samples were investigated by Prof. Dr. Bernhard Michalke (Helmholtz Institute, Munich, Germany) via ICP spectrometric analysis as previously described (Fernsebner et al., 2014).

To analyze the iron amounts within single sections of SN of mouse brains, Prof. Dr. Katarina Vogel-Mikuš performed the XRF imaging and analysis at the XRF beamline of Synchrotron Elettra (Karydas et al., 2018). Therefore, frozen hemispheres were cut to 30 μm slices by CM3060 Leica Cryostat, freeze-dried and mounted between two 4 μm ultralene foil layers (SpexSamplePrep) (Vogel-Mikuš et al., 2014). The samples were positioned at 45° and afterwards they were scanned by 75 μm × 75 μm beam at excitation energy of 10 keV. The silicon drift detector for XRF detection (Bruker, Nano GmbH, XFlash 5030) was placed on the incident beam horizontal plane, perpendicular to the

primary beam. The silicon drift detector has a 30 mm^2 nominal crystal area, exhibits a thickness of 450 μm and has a nominal resolution equal to 131 eV (at Mn-K).

XRF spectra fitting was performed in PyMCA (Solé et al., 2007) and quantification was done according to (Kump and Vogel-Mikuš, 2018). Pure metal foils were used to calibrate the XRF system (MicromatterTM Technologies Inc., Canada). For validation a standard reference material (NIST 1537a Tomato Leaves, Sigma Aldrich) was measured. Absorption utilized to determine the sample thickness was detected by a photodiode placed behind the sample and the scattering of X-rays on the sample (Kump and Vogel-Mikuš, 2018).

2.2.5.5   Imaging and analysis of microfluidic chambers

Cortex cells cultured inside microfluidic chambers were imaged using the Axio Imager.Z2 microscope (Zeiss). The tiles option of the software served to image both cell compartments almost completely and the groove area in the middle of the chamber in total. The channels Cy3, Cy5 and DAPI were always imaged with the same exposure time for all cover slips. Per each tiles image, the focus was adjusted manually for 50 single tiles. The threshold function of ImageJ was used to assess the pS129-α-syn signal. One threshold was defined for each culture. The secondary cell compartment was contoured and defined as ROI. A percentage based on signal area and ROI area was calculated for each microfluidic chamber. An average of 1-3 chambers per condition and culture was calculated. The relative signal (%) of the PBS condition was subsequently subtracted from the relative signal (%) of the monomer or PFFs conditions, respectively.

2.2.6   Statistical analysis

Statistical analyses of XRF data from *ex vivo* human tissue were performed by Dr. Jan-David Nicolas (Institute for X-ray Physics, Göttingen, Germany) using MATLAB and Python. Python (version 3.6.6.) was used to analyze and display the data (matplotlib and seaborn modules). The Python package SciPy (version 1.0.0.) was used to perform normality tests. For statistical analysis, the Welch test was accomplished by MATLAB (R2018b). Scripts of Dowding and Haufe (2018) were used for the sufficient summary statistics (SSS) approach. The SSS and the nested ANOVA (nANOVA) approach were implemented in MATLAB (R2018b). The cluster analysis was conducted by Scikit-learn (version 0.20.1).

For statistical analyses of mouse and cell culture experiments, SPSS statistics 25.0 and Graphpad Prism 5.04 and 8.2 were used. Detailed information about the used statistical tests and the sample sizes are indicated in the respective results part. Data were tested for normality with Shapiro-Wilk, Kolmogorov-Smirnov or D'Agostino-Pearson omnibus normality test and tested for homogeneity of variances with the Levene, Bartlett's or Brown-Forsythe test. For the evaluation of *in vivo* and *in vitro* experiments, Fisher's exact test, the ANOVA with repeated measurements, one-way ANOVA, Welch-ANOVA, Student's t-test, Mann-Whitney-U test and Kruskal-Wallis test were calculated. For multiple group comparisons, Tuckey's or Dunn's post-hoc tests followed. After Welch-ANOVA, Games-Howell post hoc test followed. Data are given as mean ± SEM and statistical differences within the data were considered as significant if $p < 0.05$ (* $p < 0.05$, ** $p < 0.01$, *** $p < 0.001$).

3 Results

3.1 Characterization of human postmortem midbrain tissue of PD patients

In order to analyze the role of trace elements in PD assuming metal dyshomeostasis or accumulation as a potential causative factor in PD, neuromelanin-positive neurons of PD and CO patients were raster scanned using XRF at the ID 13 (nanofocus experimental endstation, EH3) of the ESRF (Grenoble, France) (Joppe et al., 2020). Neuromelanin-positive neurons degenerate within the SN as one major characteristic of PD, firstly described by Tretiakoff in 1912 (Lees et al., 2008). Since neuromelanin is a brown pigment, it is easily visible within unstained sections simplifying the identification of these neurons. Further studies revealed significant differences in the accumulation of trace elements as copper, iron or zinc in cell bodies within the SN from PD patients compared to controls (Carboni et al., 2017b; Davies et al., 2014; Szczerbowska-Boruchowska et al., 2012). In this study, we used a higher sample size as well as respective neuron count and employed higher magnification using a nanofocus beamline to precisely determine trace element levels within cell bodies. For the analysis of the metal content in neuromelanin-positive neurons, native tissue sections were analyzed to avoid contamination by processing. Furthermore, little is known about metal dyshomeostasis within LBs of PD patients which could possibly clarify the contribution of trace elements to LB formation or α-syn pathology. Therefore, in this study, midbrain sections were immunostained with an antibody which recognized α-syn aggregates helping to identify LBs inside neuromelanin-positive cells. The same sections were used to detect the distribution of trace elements within the LBs (Joppe et al., 2020).

A previous XRD study from our lab suggested that tissue of a PD sample from the same cohort showed higher cholesterol amounts compared to a CO sample (Carboni et al., 2017b). Therefore, in a side project, the cholesterol amount within our patient cohorts (nine PD, ten CO) was investigated using the biochemical approach of lipid extraction.

3.1.1 XRF analysis – the elemental composition of neuromelanin-positive neurons of PD patients and controls

For the element quantification in neuromelanin-positive neurons, tissue of four PD and four CO patients were measured. Per patient, five ROIs were raster-scanned with one to two neurons located on each ROI. Intracellular trace element amounts (average of five to seven cells per patient) or extracellular amounts (cell-surrounding regions in ROIs) were detected of the following 12 trace elements: iron (Fe), manganese (Mn), copper (Cu), zinc (Zn), arsenic (As), selenium (Se), bromine (Br), calcium (Ca), potassium (K), chlorine (Cl), sulfur (S), phosphorus (P). In Figure 14A, the element concentrations inside and outside of 26 cells from the CO group and 27 cells from the PD group are visualized. Surprisingly, the intra- and extracellular levels of bromine exceeded levels of zinc and selenium. Mostly, the area density of each element did not differ much comparing the concentration within the intracellular and the extracellular space. The relative concentrations were computed from the PD (cPD) and CO (cCO) concentrations calculating (cPD – cCO) / cCO. Relative changes can be observed in Figure 14B showing that chlorine, manganese, iron and zinc concentrations are increased in PD samples compared to CO in both intra- and extracellular space, while potassium, copper, arsenic, selenium and bromine amounts are, both intra- and extracellularly, decreased in the PD sample cohort. Phosphorus and sulfur levels were almost unaltered. For calcium the intracellular level was decreased in PD patients whereas the extracellular amount was slightly increased.
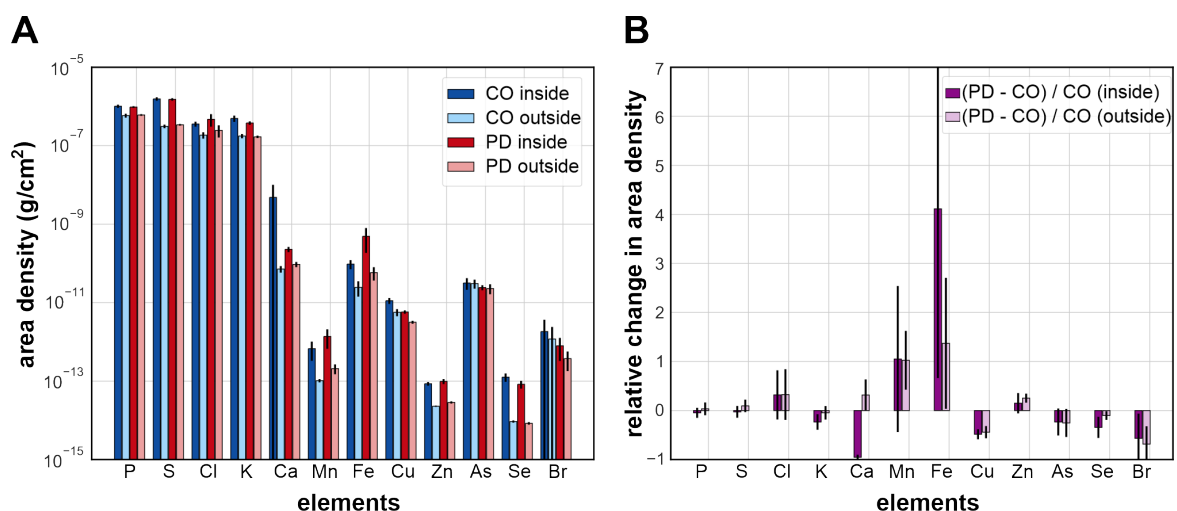
Figure 14. Averages of absolute and relative trace element concentrations in neuromelanin-positive neurons of PD and CO patients. **(A)** Absolute trace element concentrations given as area density are shown separately for both, intracellular and extracellular area. Data of PD patients (n = 27 cells from four patients)

are represented in red, whereas control patient values (CO, n = 26 cells from four patients) are shown in blue. Data are given as mean ± SEM. **(B)** Relative changes in element-specific area density of PD samples relative to CO. A value of 1 implies a concentration increase of 100 %. A value of −0.5 corresponds to a 50 % decrease of a specific element in the PD samples relative to the CO samples. Data are given as mean ± SEM. Adapted with permission from (Joppe et al., 2020) © The Optical Society.

For the following analyses, elements with $Z < 21$ (proton number within the nucleus of the specific atom < 21) were omitted, since the nominal concentrations are affected by self-absorption in the sample. Probably not all parameters for corrections are sufficiently known, in particular the absorption coefficient of the tissue. Therefore, self-absorption could erroneously alter the concentrations of elements with $Z < 21$. Focusing intracellular element concentrations, a polar bar chart was used to visualize the results of single cells (Figure 15). The used illustration allows deeper insights on intra- and interindividual variances and facilitates to identify outliers of single cells which probably distort the group average of an element concentration. For example, the overall signal of bromine within the CO group is dominated by two single cells from patient CO1. For arsenic, great variability was detected for PD3 showing only one cell with high arsenic concentration whereas the arsenic levels in other cells were close to the detection level.
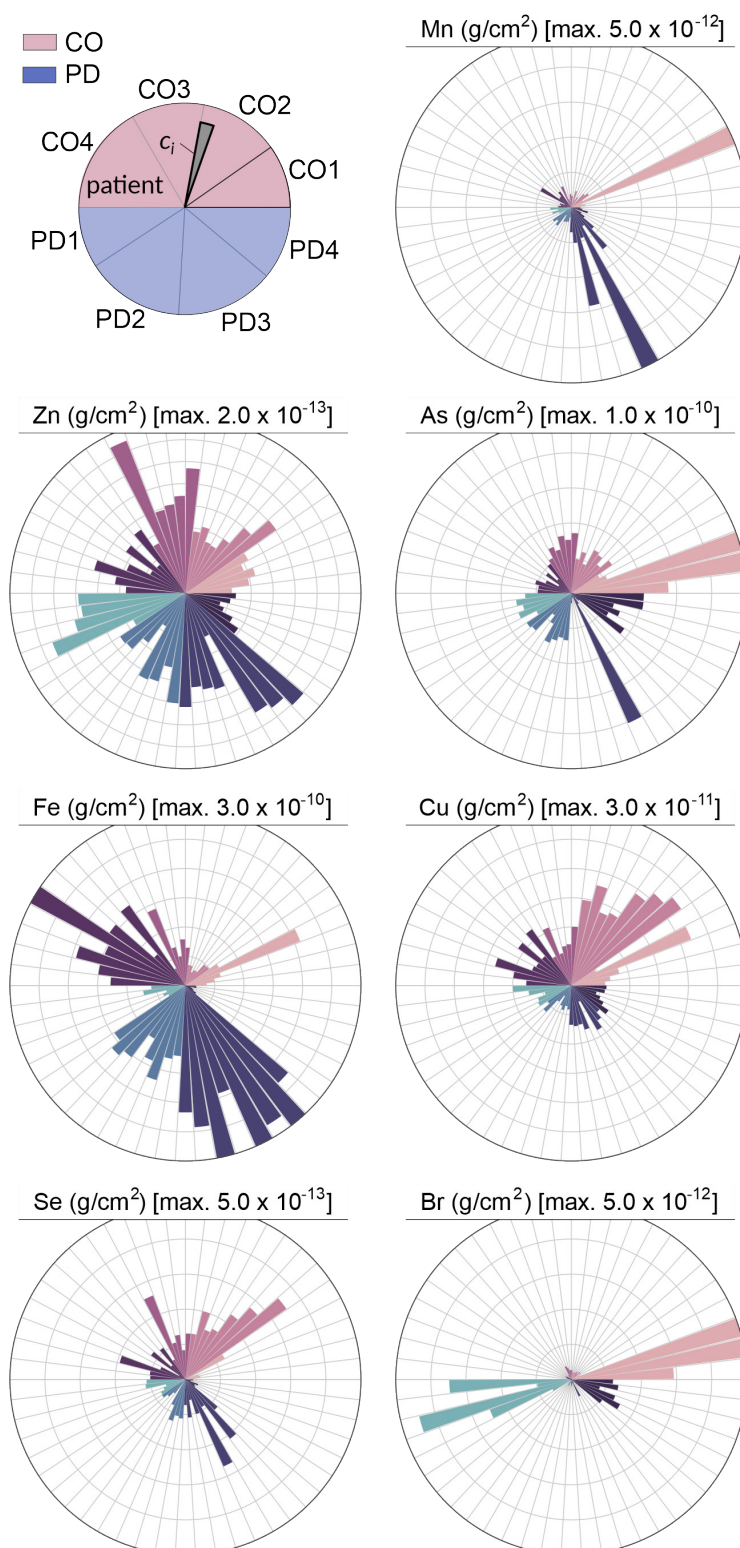
Figure 15. Polar bar charts of element concentrations in single neuromelanin-positive cells. Polar bar charts of Mn, Zn, As, Fe, Se, Cu and Br indicate absolute element concentrations (g/cm^2) within cells. Each bar represents the absolute concentration (c_i) of a specific element in one cell. Bars of the same color belong to the same patient. The upper half of the diagram corresponds to the four CO samples whereas the bottom part corresponds to the PD patients (n = 4, 5-8 cells per each patient). Adapted with permission from (Joppe et al., 2020) © The Optical Society.

Above mentioned data on element concentrations were further grouped by patients and groups in Figure 16 for a better overview on interindividual differences. For example, focusing on iron, PD3 showed a much higher concentration compared to the other PD samples. In parallel, this illustration also visualizes the fluctuation of values within a patient given by a relatively low number of cells per patient. For example, levels of manganese are widely ranging between cells within PD3.

In order to identify statistical significance between both groups, normality and significance tests were calculated based on the pooled data including all neurons of all patients per group. A Shapiro-Wilk normality test revealed that for most of the trace elements the concentrations within groups were not normally distributed (Table 6). For a first impression on statistical group differences, the Welch test for data with unequal variances was performed and revealed significantly decreased amounts of copper in PD patients. It had to be considered that a normal pooled data analysis obtains wrong results, when inter-subject variances are existing but ignored. Since this study showed high interindividual differences for some elements (Figure 16), there is a high risk to underestimate the variance and obtain smaller p-values. To consider any between-subject variance, the following two statistical tests were performed: the SSS approach and nANOVA. All results of the used statistical tests are summarized in Table 6.

Assuming random effects and inverse variance weighting, the SSS was calculated as described in (Dowding and Haufe, 2018) with an effect size measured by the mean of each sample. For nANOVA, random effects were assumed. For both tests, two layers of the data set were modelled. The first layer differentiated between the disease type (PD or CO). The second layer considered the individual patients (four patients per group). For all analyzed trace elements, no significant results were found. The obtained p-values were orders of magnitude larger than results of a Student's t-test on the pooled data not considering inter-subject variances. The most discriminant trace element of our analysis was copper, however, no significant difference between the two groups was found in SSS and nANOVA (p = 0.07 in both analyses; Table 6). Both analyses highlight how important it is to carefully consider interindividual variances, since these variations could strongly affect the statistics.
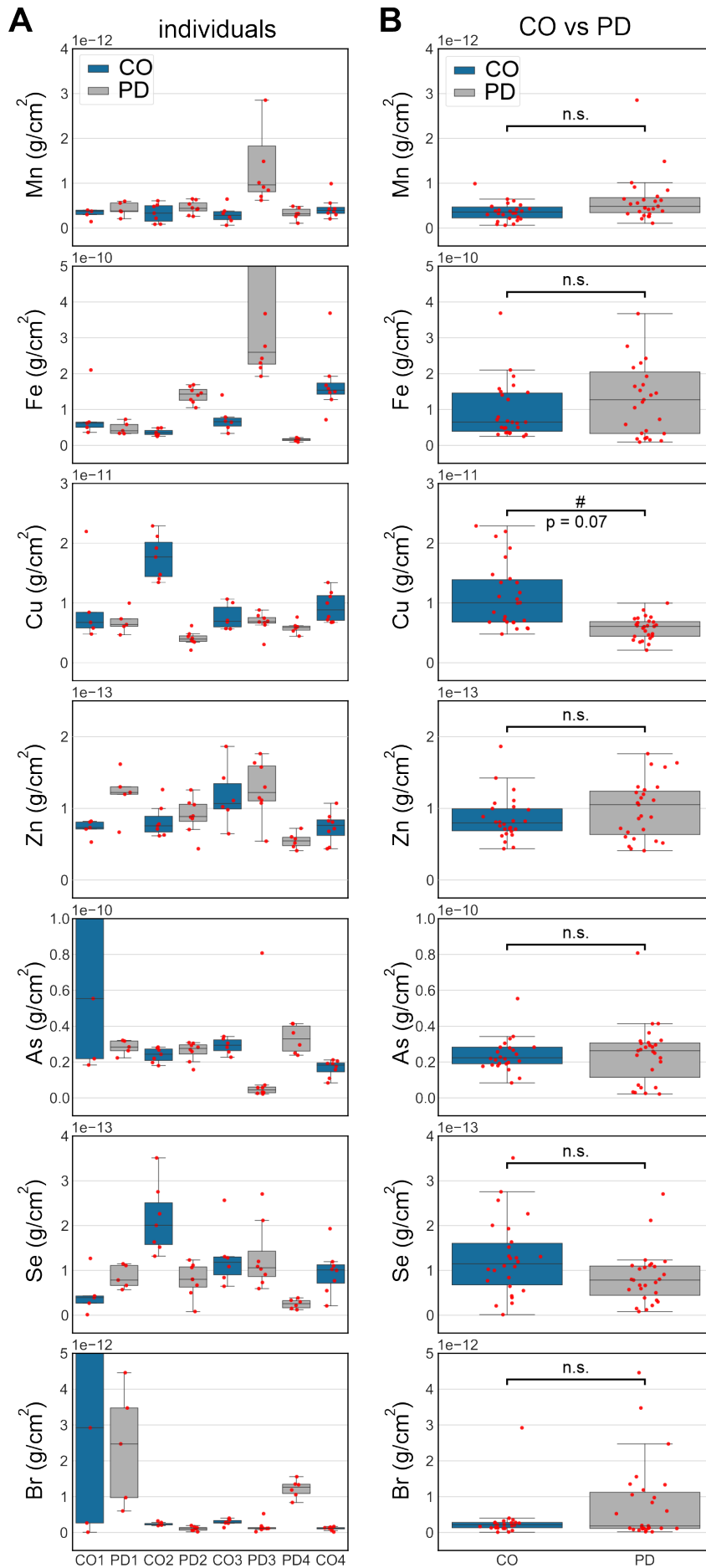
Figure 16. Box-Whisker plot analysis of neuromelanin-positive cells of PD and CO samples. (A) Box-Whisker plots representing intracellular element concentrations for single patients (5-8 cells per patient; n = 4 per group). Element concentrations are shown for Mn, Fe, Cu, Zn, As, Se and Br. **(B)** Box-Whisker plots of intracellular element concentrations grouped by categories PD (grey; n = 27 cells) and control (CO, blue, n = 26 cells). Element concentrations are shown for Mn, Fe, Cu, Zn, As, Se and Br. In both, **(A)** and **(B)** values of single cells are represented as red dots. Results of SSS / nANOVA are shown. # indicates marginal significance of p = 0.07. n.s.: not significant. Adapted with permission from (Joppe et al., 2020) © The Optical Society.

In a *k*-means clustering approach, an unsupervised classification of each data point to their *a priori* known class (PD or CO) was aimed. Outlier showing an element concentration of less or more than the interquartile rage of the distribution were excluded from this analysis. Running a *k*-means algorithm for *k* = 2, only two labels were returned from the algorithm which were afterwards compared to the *a priori* known classes PD and CO. Merely, 65.5 % of the cases were classified with the correct label by the algorithm. Taken together, the prediction rate was negligible, since high intragroup variances disallowed unsupervised automated classification of groups (Figure 17).

Table 6. Statistical tests used for the XRF analysis. Welch test was performed by using total cell counts as n per group (PD n = 27, CO n = 26). Bold numbers for Welch test highlight p-values below an α level of 5 %. Shapiro-Wilk (SW) test was used to test normality of the data. Normal distribution of data is shown in bold within the columns of SW(CO) and SW(PD). Both, the sufficient-summary-statistic approach (SSS) described in (Dowding and Haufe, 2018) as well as a nested ANOVA (nANOVA), compute p-values considering between-subject variance. Bold numbers indicate the element with the lowest p-value. Adapted with permission from (Joppe et al., 2020) © The Optical Society.

Elements	Welch test	SW (CO)	SW (PD)	SSS	nANOVA
Mn	0.40	4.04e-10	1.71e-10	1.00	0.64
Fe	0.25	1.14e-4	1.32e-10	0.82	0.42
Cu	**0.42e-4**	6.20e-3	**9.79e-1**	**0.07**	**0.07**
Zn	0.20	5.79e-3	**2.00e-1**	0.51	0.57
As	0.28	9.94e-8	1.65e-3	0.96	0.45
Se	0.35	**1.67e-1**	3.09e-3	0.26	0.34
Br	0.43	3.53e-10	4.71e-6	0.36	0.52
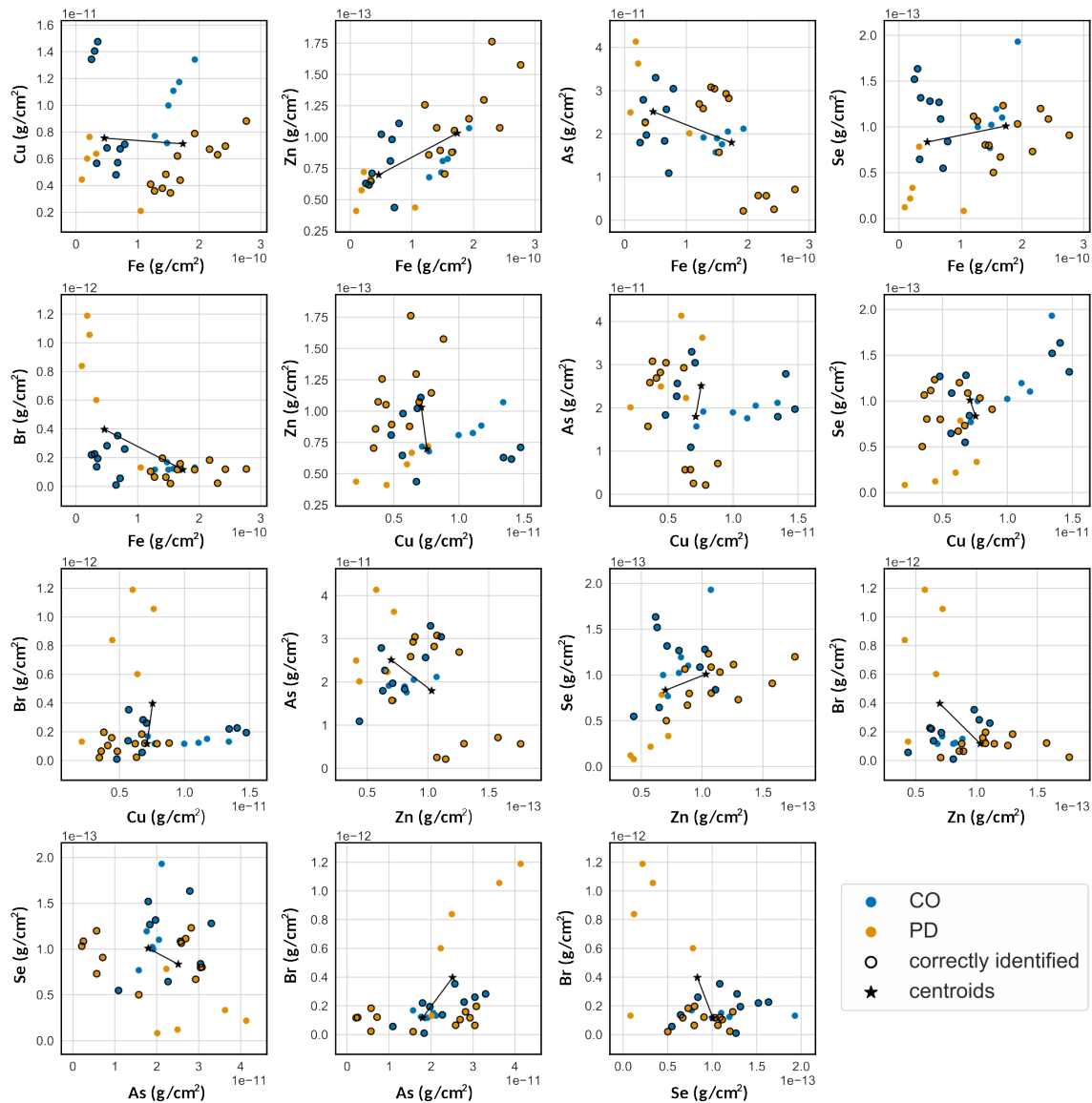
Figure 17. *k*-means clustering approach represented in two-dimensional plots. Seven spectral lines were used for the clustering algorithm. Outliers were excluded from further analyses. The algorithm was determined to output two labels ($k = 2$), which were finally compared to the *a priori* known classes (PD or CO). A solid black line indicates matching classes. Black stars indicate the two centroids which are linked with a solid black line stating the distance between both centroids. Merely 65.5 % of the datapoints were identified correctly by the algorithm (5-8 cells per patient; n = 4 per group). Adapted with permission from (Joppe et al., 2020) © The Optical Society.

3.1.2   X-ray analysis of LBs in PD patients

Since α-syn aggregation was found to be fostered by various trace elements and α-syn is one of the major components within LBs in PD patients, XRF was used to analyze the elemental content of two LBs from two different patients. For this analysis, sections had to be mounted on Kapton foil since this foil allows immunohistochemical staining of the sections but can be also used as an X-ray transmissive sample window. This prevents

from cutting neighboring sections of which one is stained and one can be measured with XRF. Microscopy-identified LBs were analyzed with XRF and XRD.

In a first analysis, XRD scattering signal of one LB was compiled in a map. XRD was able to detect a signal that was likely a feature that is indicative of the LB (Figure 18A,B). The averaged background signal was subtracted from the scattering data of the LB and the gathered signal was azimuthally integrated. In Figure 18C the scattering signal of all scan points is shown plotting the one-dimensional scattering intensity with the scattering vector. The scattering vector is defined as $q = (4\pi/\lambda) \sin(\theta)$, where λ is the wavelength of the radiation and 2θ the scattering angle between the primary and scattered beam (Joppe et al., 2020). The feature of the LB exhibited a prominent intensity peak at 13.6 nm^{-1}. This peak is characteristic for dried α-syn pellets but also for secondary structures of proteins as especially β-sheet structures. Therefore, it is still pending if α-syn crystals caused the scattering signal, in particular, since cells of a CO patient (in green) showed a similar diffraction curve with a similar peak as the LB (in blue).
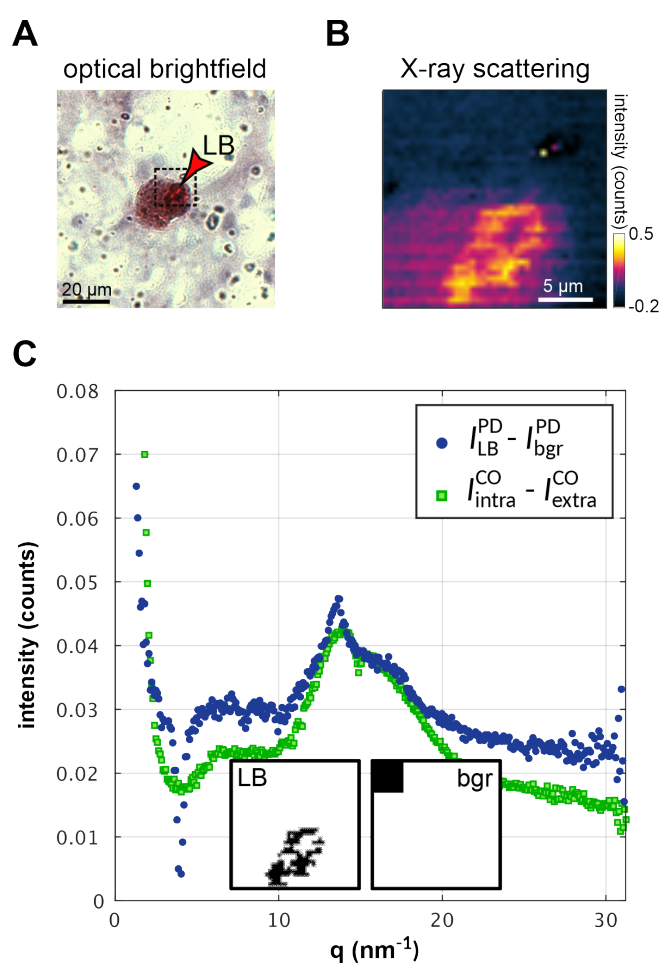
Figure 18. XRD analysis of a LB. (A) Microscopy image of a LB-containing neuromelanin-positive cell of a PD patient. LB is visualized by a new fuchsin staining and indicated by a red arrow. XRD-scanned region is indicated with a dashed square. **(B)** Visualization of XRD scattering intensity representing the LB. The background-subtracted one-dimensional intensity is shown in this graph. **(C)** The q-distribution of scattering from the LB resembles the distribution of a cell from a CO patient (CO1). A prominent peak is observable at 13.6 nm^{-1}, which is the scattering peak of dried α-syn pellets and also characteristic for a secondary structure of proteins, in particular β-sheets. Bgr: background, extra: extracellular, intra: intracellular. Adapted with permission from (Joppe et al., 2020) © The Optical Society.

Signal gathered from the XRF was analyzed to assess the chemical composition of the two measured LBs. For the first LB, which was already described in Figure 18, the main fluorescence signal resulted from bromine (Figure 19A,B). Other trace elements as iron, arsenic and selenium also correlated well with the feature of the LB whereas the distribution of copper anti-correlated with the LB feature. Low-Z elements as potassium and calcium were the primary element composition of small features appearing around the cell. In a second LB from another patient fluorescence signal from bromine was again highly localized with the feature of the LB (Figure 19C,D). The signal of bromine anti-correlated once again with the fluorescence signal of copper and it showed no correlation with other trace elements. Iron was distributed in the whole cell but rather slightly less in the LB. Therefore, both LBs showed quite diverse fluorescence signals of the different trace elements but exhibited similar distribution patterns of bromine and copper.
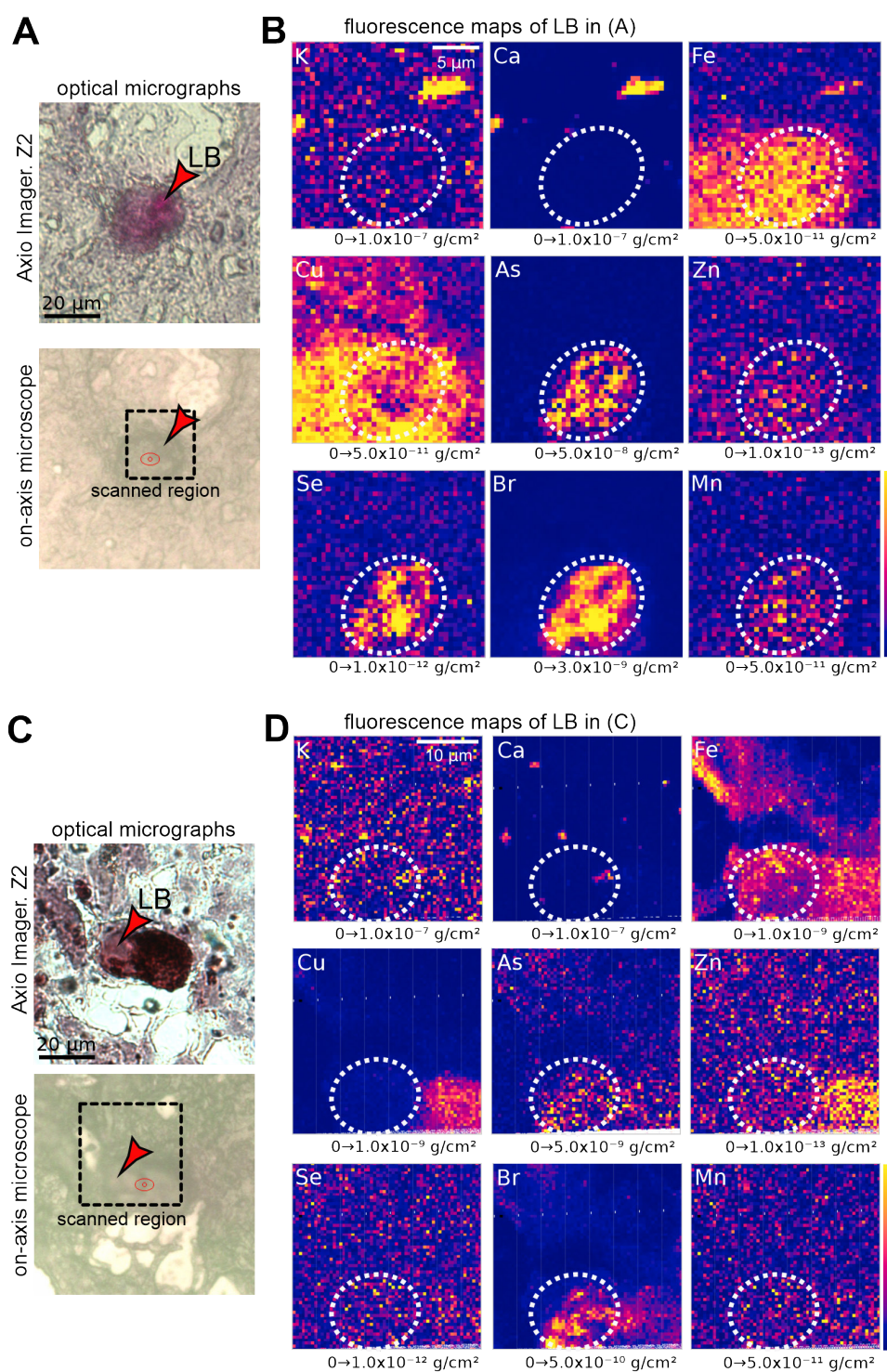
Figure 19. XRF analysis of two LBs. (A) Optical brightfield image of a stained LB (antibody recognizing α-syn) and a micrograph of the section recorded before XRF measurements. The LB is marked by a red arrow. The black dashed square in the image of the on-axis microscope indicates the XRF scanned region. **(B)** XRF maps of a LB shown in **(A)**. LB is marked with a dashed circle. **(C)** A LB from another PD sample indicated in an optical brightfield image and in a micrograph recorded before XRF measurements. The LB is marked by a red arrow. The black dashed square in the image of the on-axis microscope indicates the XRF scanned region. **(D)** XRF maps of a LB shown in **(C)**. LB is marked with a dashed circle. Adapted with permission from (Joppe et al., 2020) © The Optical Society.

3.1.3 Increased cholesterol levels in human midbrain tissue of PD patients

A previous X-ray-based study of our work group found increased amounts of cholesterol crystallites within PD tissue compared to a MS patient measured by XRD (Carboni et al., 2017b). Since this study only compared one PD and one MS patient, a verification of these results was intended using a higher sample size and a different technique for a well-established quantification of cholesterol. A biochemical lipid extraction of human midbrain tissue was performed to assess the cholesterol content (Figure 20A). The analysis was performed in collaboration with the Department for Plant Biochemistry, Göttingen, Germany. In this analysis, MS and cancer patients were included in the CO group. Midbrain tissue of PD patients (0.34 ± 0.07 µmol/mg) showed increased cholesterol amounts compared to CO samples (0.18 ± 0.04 µmol/mg). Group comparison analysis (Student's t-test) revealed a trend to statistical significance (p = 0.057; Figure 20B).
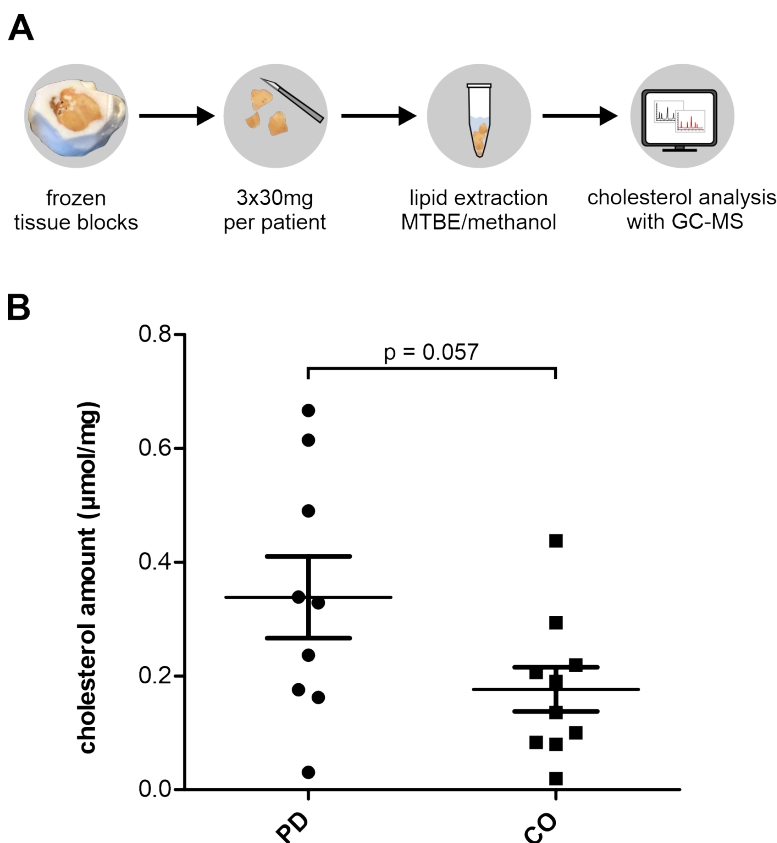
Figure 20. Quantification of cholesterol in human midbrain tissue of PD and CO samples. (A) Experimental procedure. Three tissue pieces of ca. 30 mg each were cut to have biological replicates for the following lipid extraction. Afterwards, cholesterol amounts were quantified using GC-MS. **(B)** The scatter plot shows cholesterol amounts (µmol/mg) of human midbrain samples from PD (n = 9) and controls (n = 10). Data given as mean ± SEM. Student's t-test was performed.

3.2   The interplay of iron and α-syn *in vivo*

The present study aimed to elucidate if neonatal iron treatment could alter the effect of intrastriatal α-syn PFFs injections on behavior and PFFs-induced spreading of the α-syn pathology in C57BL/6J mice. The animals were treated with iron between p10 and p17 and received a stereotactic intrastriatal injection of either monomeric α-syn or PFFs at an age of approximately 12 weeks. Animals which were treated with the vehicle solution instead of iron are stated as control group and in figures abbreviated as ctrl in following chapters. The first part of this chapter focuses on the investigation of iron load in mouse brain sections and on the effects of iron and α-syn PFFs on the living animals in terms of treatment-related behavioral abnormalities. Other subchapters are dealing with analyses on mouse brain sections investigating α-syn spreading and its distribution through the brain as well as accumulation of immune cells.

3.2.1   Quantification of iron in an iron intoxication mouse model

Aiming to verify whether neonatal iron treatment per gavage leads to iron enrichment inside the adult mouse brain, two different analyses were used to assess iron load. In a first attempt, hyphenated ICP spectrometry was used to determine the iron amount in whole mouse brains. Therefore, mice were treated with different dosages of iron (60 mg/kg Fe, 120 mg/kg Fe, 240 mg/kg Fe) or sorbitol as control and were sacrificed at six months of age (Figure 21A). The analysis was performed by Prof. Dr. Bernhard Michalke (Helmholtz Institute, Munich, Germany). The analysis showed that the iron amount in whole brains of vehicle-treated mice (65.70 ± 1.74 mg/kg Fe), 60 mg/kg Fe (66.57 ± 1.04 mg/kg Fe), 120 mg/kg Fe (68.24 ± 3.34 mg/kg Fe) and 240 mg/kg Fe-treated mice (66.66 ± 1.01 mg/kg Fe) did not differ significantly (Figure 21B).

A

B
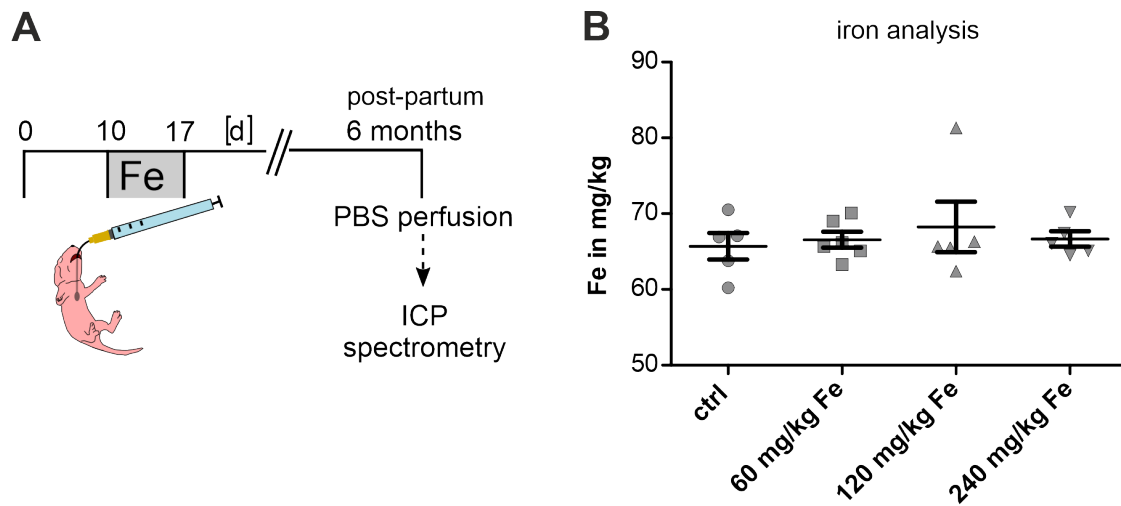
Figure 21. Hyphenated ICP spectrometry analysis of brain tissue from iron-treated mice. (A) Experimental layout. C57BL/6J mice were treated with carbonyl iron (p10-17) and sacrificed at 6 months of age. **(B)** ICP spectrometric analysis of iron (mg/kg) measured in tissue from mice treated with different iron dosages (60 mg/kg, 120 mg/kg, 240 mg/kg) or 5 % sorbitol as control. Data given as mean ± SEM; 60 mg/kg Fe n = 6, other groups n = 5; one-way ANOVA.

Since similar studies of neonatal iron feeding verified iron enrichment specifically within the SN (Billings et al., 2016; Kaur et al., 2007), in another experiment, cryofixed mouse brains sections were freeze-dried and, subsequently, the iron amount (µg/g) in the SN on single sections was analyzed with XRF (Figure 22A). The XRF analysis was performed by Prof. Dr. Katarina Vogel-Mikuš (Faculty of Biology, University of Ljubljana, Slovenia) at the Elettra Synchrotron in Trieste, Italy.

Photographs and XRF-based heat maps of one exemplary brain section of an iron-treated and an untreated control animal are shown in Figure 22B,C. The analyzed SN-containing areas are indicated within the exemplary sections as rectangles (Figure 22B,C). Compared to untreated control animals, mice treated with 60 mg/kg Fe or 120 mg/kg Fe showed increased iron amounts within the SN (Figure 22D). However, due to the inferior sample size of n = 2 per group, no statistical analysis could be applied.
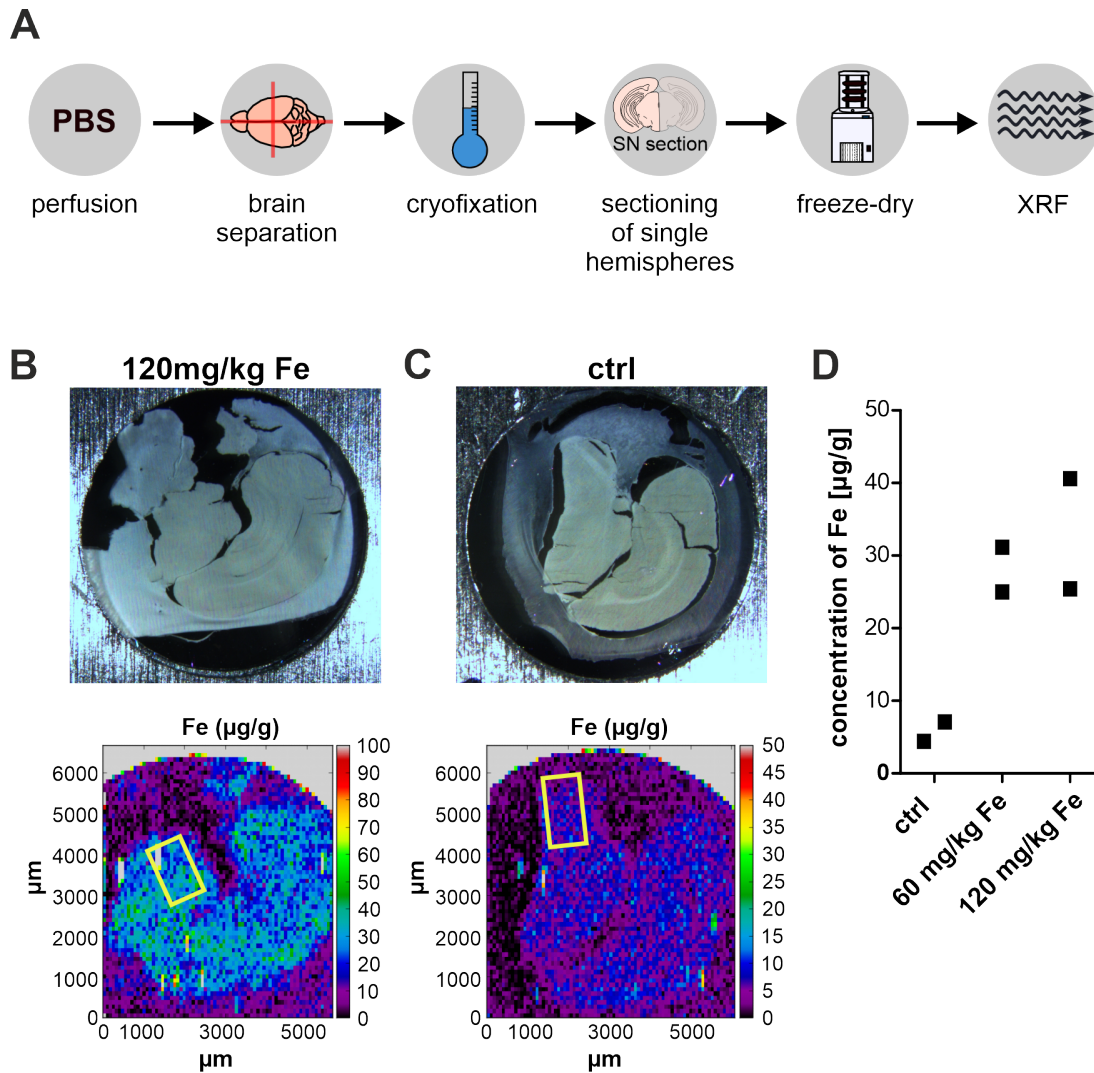
Figure 22. XRF-based iron analysis of iron-treated mice. (A) Experimental procedure. Iron-treated C57BL/6J mice were sacrificed at six months of age. Brains were separated and cryofixed. 30 µm thick brain sections were freeze-dried and then analyzed by XRF. **(B)** A photomicrograph and a X-ray-based iron heatmap of an exemplary nigral brain section of an animal treated with 120 mg/kg Fe. Rectangle indicates SN region in which iron was quantified. **(C)** A photomicrograph and a X-ray-based iron heatmap of an exemplary nigral brain section of a control animal. Rectangle indicates SN region in which iron was quantified. **(D)** XRF results within the SN of control mice as well as iron-treated animals (60mg/kg or 120mg/kg Fe). No statistical analysis was performed due to inferior sample size per group of n = 2.

3.2.2 The influence of iron and α-syn on motor and cognitive behavior

To investigate the effects of iron treatment and α-syn PFFs injections on motor and cognitive behavior, mice performed the rotarod test and NOR test. All animals performed the rotarod weekly between day of α-syn injection (doi) and sacrifice and the NOR test twice – directly before the doi to investigate single iron effects and directly before sacrifice to investigate mutual effects of iron and α-syn PFFs on cognition (Figure 23A).
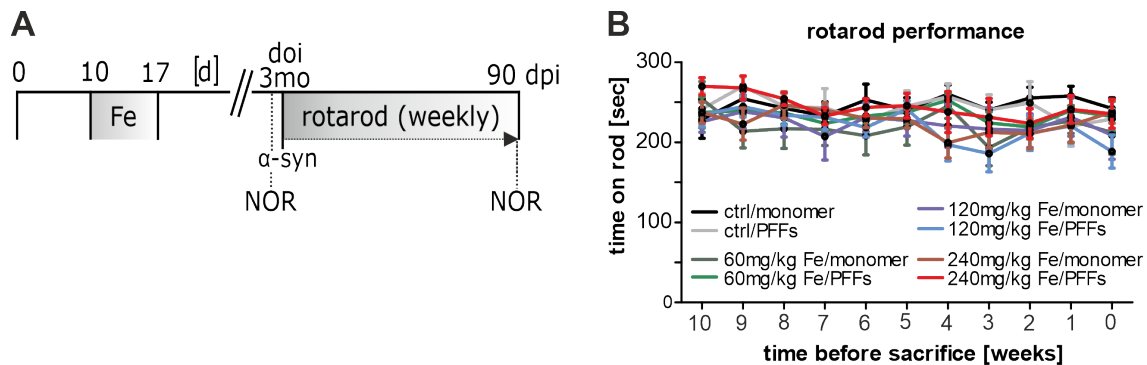
Figure 23. Experimental layout and motor behavior of iron- and α-syn-treated mice. (A) Experimental layout. C57BL/6J mice were treated with carbonyl iron between postnatal day 10 and 17 and were injected with α-syn at ca. 3 months of age. Rotarod was performed weekly and NOR test was performed twice. **(B)** Results of the weekly performed rotarod test starting 10 weeks before sacrifice. The graph shows the averaged mouse performance per treatment group (n = 6-8 per group) over time. The vehicle-treated control group is labeled as ctrl. Data given as mean ± SEM, one-way ANOVA with repeated measures.

To get stability in the mouse performance on the rod, the mice were pre-trained on the rotarod before the first test run. Rotarod results are demonstrated in Figure 23B. All animals showed inconsistent performances on the rotarod over time, evidenced by the significant changes in the means of the repeated measures over time (variable 'time in weeks'; comparing means of the different time points; **$p < 0.01$; ANOVA with repeated measures). Joint and separate effects of the two treatment variables 'iron treatment' and 'α-syn injection' were analyzed considering both variables as separate between-subjects factors within the ANOVA with repeated measures. Neither the combination of iron × time ($p = 0.180$), nor α-syn × time ($p = 0.622$), nor the interaction effect of iron × α-syn × time ($p = 0.786$) showed significant results within the ANOVA with repeated measures. Since the Mauchly-test for sphericity turned out significant for this analysis, the reported p-values are given as Greenhouse-Geisser correction. Furthermore, it is also important to highlight

that homoscedasticity measured by the Levene test is not true for the time points '8 and 7 weeks before sacrifice'. In conclusion, the treatment groups did not show significant differences in their motor behavior measured by the rotarod test.

To investigate the influence of iron and PFFs on cognitive behavior, the NOR test was used. Both STM and LTM were tested by modifying the timeframe between habituation and experimental phase (10 min vs. 24 h). Based on the interaction of the mouse with the novel and the familiar object a discrimination ratio was calculated as described beforehand (Bevins and Besheer, 2006; Tatenhorst et al., 2016) and compared between the treatment groups to assess the memory function. Data gathered at the STM time point meaning 10 min post habituation are shown in Figure 24. In order to assess the general mobility of the mice 10 min post habituation, the distance moved within the arena (in cm) was analyzed for both timepoints – before injection and before sacrifice of the mice. Since data of the 60mg/kg iron group were not normally distributed (Shapiro-Wilk test) at the timepoint before α-syn injection (Figure 24B), Kruskal-Wallis test was performed between all four iron groups, turning significant but without any significant pairwise group comparisons (Kruskal-Wallis test with Dunn's post hoc test). Before sacrifice (Figure 24C), mice from the different treatment groups were also equally agile (two-way ANOVA).

The NOR performed before α-syn injection revealed no significant STM difference between iron treatment groups (Figure 24D; one-way ANOVA). At 90 dpi, neither a significant interaction effect of iron × α-syn on STM nor a main effect of the separate treatment conditions was found (Figure 24E; two-way ANOVA, Levene test significant). Since the Levene test results showed that the requirement of homoscedasticity was not fulfilled for the latter analysis, treatment conditions of iron and α-syn were grouped. Subsequently, one-way Welch-ANOVA with Games-Howell post hoc test was performed, respectively, which also did not show significant difference between the groups.

Data gathered at 24 h post habituation are shown in Figure 25. The mobility of mice at 24 h post habituation was analyzed for both recorded time points. Before α-syn injection (Figure 25B), iron treatment groups significantly differed in their mobility. Mice of the 240 mg/kg iron group were significantly less mobile compared to both the 120 mg/kg iron group (*p < 0.05) and the 60 mg/kg iron group (**p < 0.01; one-way ANOVA with Tuckey's post hoc test). No significant differences in the distance moved were found at the time point before sacrifice (two-way ANOVA; Figure 25C).
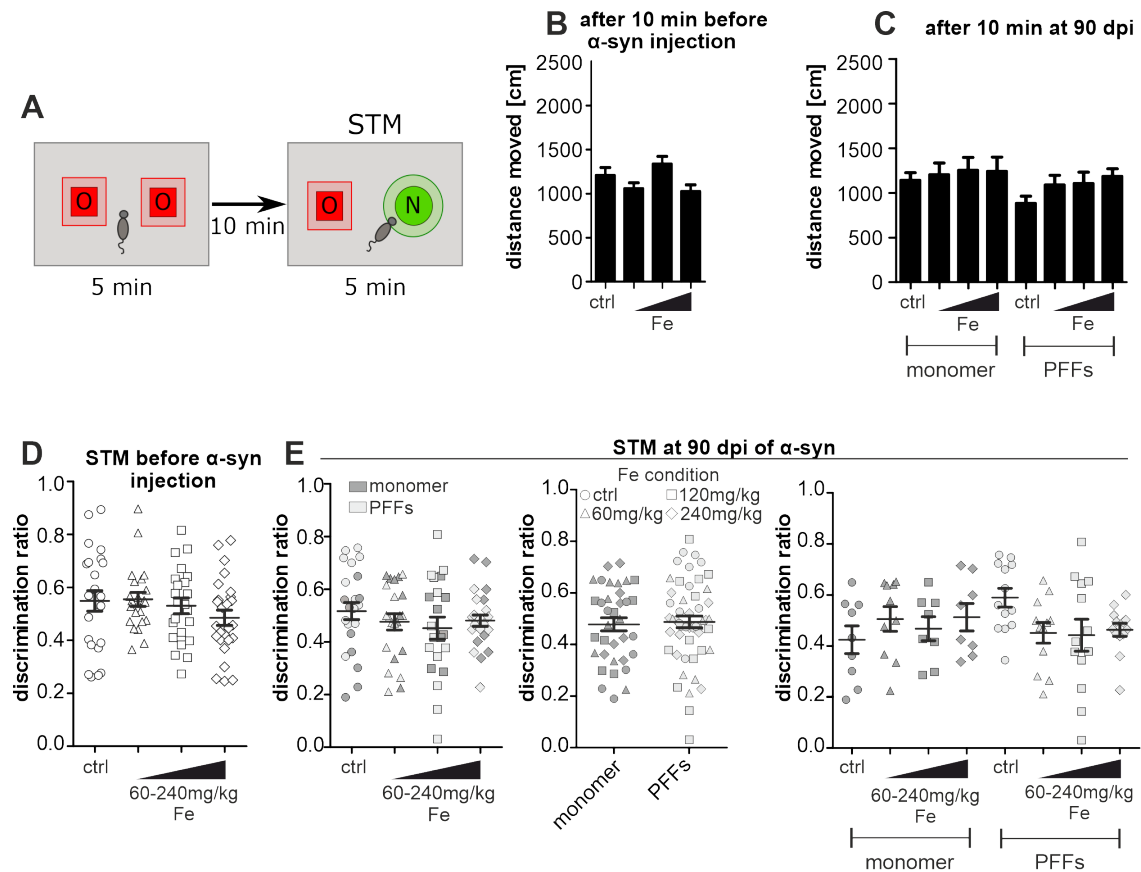
Figure 24. STM analysis of iron- and α-syn-treated mice. (A) Experimental procedure of the NOR. C57BL/6J mice were habituated to two identical objects for 5 min. After a 10 min break within the familiar cage, the STM was recorded while presenting one old/familiar (O) and one novel (N) object**. (B,C)** The distance moved was analyzed as an indicator of mobility at two time points – **(B)** before α-syn injection (n = 22-29) or **(C)** at 90 dpi (n = 8-14 per group). **(D)** STM performance of iron-treated mice before α-syn injection (n = 21-22). **(E)** STM analysis performed at 90 dpi. Two single graphs display the main effects of the two single variables – iron treatment and α-syn injection. Another graph shows the combined effects of iron and α-syn treatments (n = 8-13 per group). Data are shown as mean ± SEM, One-way and two-way ANOVA as well as Kruskal-Wallis test. Low, middle and high iron dosage (60, 120 and 240 mg/kg Fe) are indicated in graphs as iron-triangle.

The analysis of LTM showed that before α-syn injection mice treated with 240 mg/kg iron performed significantly worse in the NOR compared to mice of the 60 mg/kg iron group (Figure 25D; *p < 0.05; due to significant Shapiro-Wilk test the Kruskal-Wallis test with Dunn's post hoc test was used). LTM results showed no interaction effect of both variables iron × α-syn and also no main effect of the iron treatment at 90 dpi. However, a significant main effect of the variable 'α-syn injection' was found indicating that PFFs-

injected animals performed significantly worse in LTM compared to monomer-injected ones (Figure 25E; two-way ANOVA, *p < 0.05).
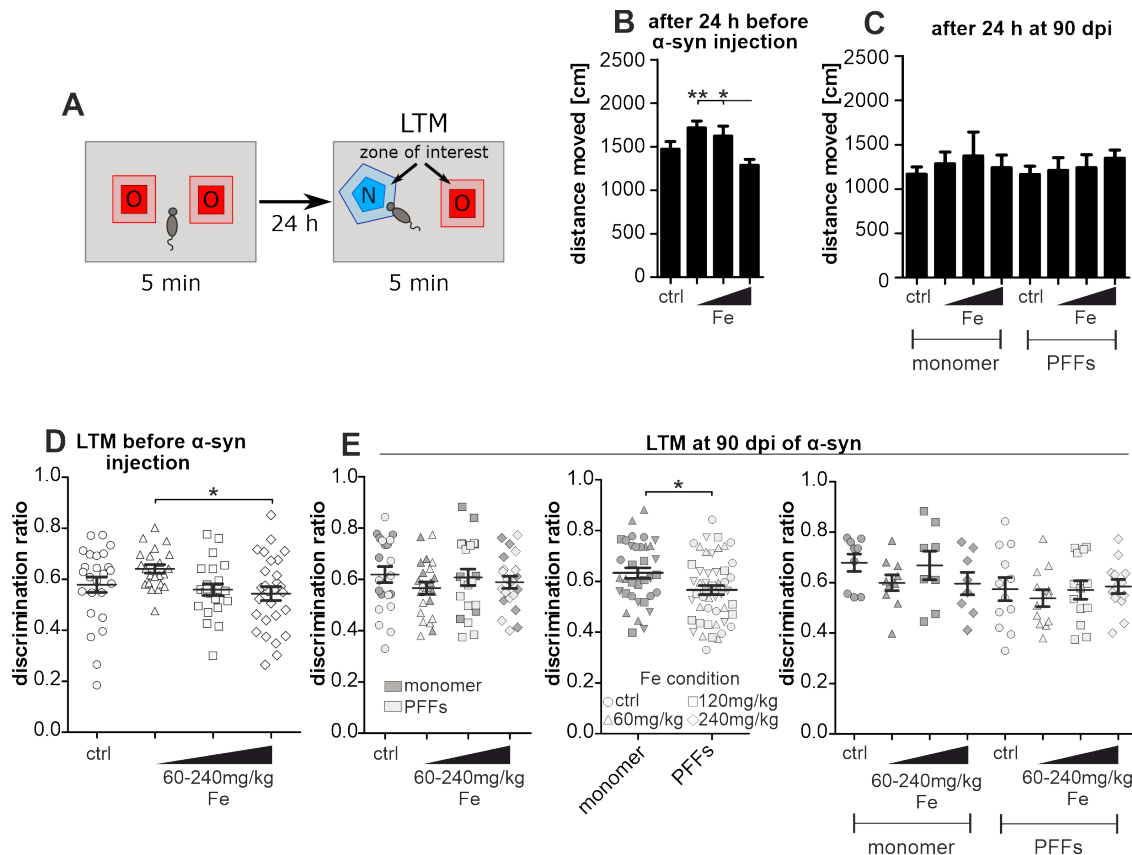
Figure 25. LTM analysis of iron- and α-syn-treated mice. (A) Experimental procedure of the NOR. 24 h after a habituation phase with two identical objects, LTM was analyzed while presenting one old (O) and one novel (N) object. **(B,C)** The distance moved was analyzed at two time points – **(B)** before α-syn injection (n = 22-29) and **(C)** at 90 dpi (n = 8-14). **(D)** LTM performance of iron-treated mice before α-syn injection (n = 21-22). **(E)** LTM analysis at 90 dpi. Two single graphs display the main effects of the two independent treatment variables (iron and α-syn). Another graph shows the combined effects of iron and α-syn treatments (n = 8-13 per group). Data are presented as mean ± SEM. One-way and two-way ANOVA with Tuckey's post hoc test as well as Kruskal-Wallis test. Low, middle and high iron dosage (60, 120 and 240 mg/kg Fe) are indicated in graphs as iron-triangle.

Taken together, iron-treatment had a significant effect on LTM of mice before α-syn injection, whereas α-syn PFFs treatment affected LTM at 90 dpi. No interaction effect of iron and α-syn treatment was found on LTM or STM. Before α-syn injection, recordings at 24 h post habituation revealed significant differences between iron treatment groups in the moved distance inside the arena as an indicator of general activity.

3.2.3 The influence of iron on α-syn spreading

A major aim of this study was to investigate if postnatal iron feeding had an impact on α-syn spreading pathology. Therefore, six coronal brain sections were analyzed, which were stained with an antibody recognizing aggregated α-syn (anti-α-syn phospho S129 antibody, EP1536Y). First, the amount of pS129-α-syn was quantitatively analyzed to determine iron-induced effects on α-syn spreading. The results of a semi-automated pS129-α-syn quantification in whole brain sections are demonstrated in the following subchapter 3.2.3.1. A second analysis method was used to assess the pS129-α-syn amounts in specific brain regions per section. Manually, the affected brain regions were marked, and it was assessed in which brain regions iron caused altered spreading pathology. These distributional effects are shown in subchapter 3.2.3.2.

3.2.3.1 Quantitative analysis of α-syn spreading – iron reduced α-syn spreading

For a quantitative analysis of α-syn spreading in mouse brains after iron and PFFs treatment, pS129-α-syn signal was evaluated in six different coronal brain sections named after their coordinates relative to Bregma. α-syn signal was calculated within the ROI which was either the injected or contralateral hemisphere by relativizing the signal area to the total analyzed area. Within the injected hemisphere of all six brain sections, α-syn monomer-injected mice showed almost no signal (Figure 26A-F), an expected result due to the specificity of the applied antibody to aggregated forms. For that reason, the monomer-injected animals were used as internal controls. Statistical analyses were only performed on basis of the four different iron-treated PFFs groups (ctrl/PFFs, 60 mg/kg Fe/PFFs, 120 mg/kg Fe/PFFs, 240 mg/kg Fe/PFFs), not comparing PFFs and monomer groups. Animals of the ctrl/PFFs group were treated with vehicle instead of iron.

PFFs-injected groups showed signal in all six sections. Four out of six rostral brain sections contained parts of the striatum which was the injected brain region. Even if the iron-free control group always showed a higher average on α-syn signal compared to the iron conditions, these differences did not reach significance in all four striatal sections (Figure 26A-D). The two caudal SN-containing sections exhibited more prominent group differences (Figure 26E-F). However, only the most caudal section (Figure 26F) showed a significant difference between the control and the high-dosed iron group (*$p < 0.05$; Kruskal-Wallis test with Dunn's post hoc test).
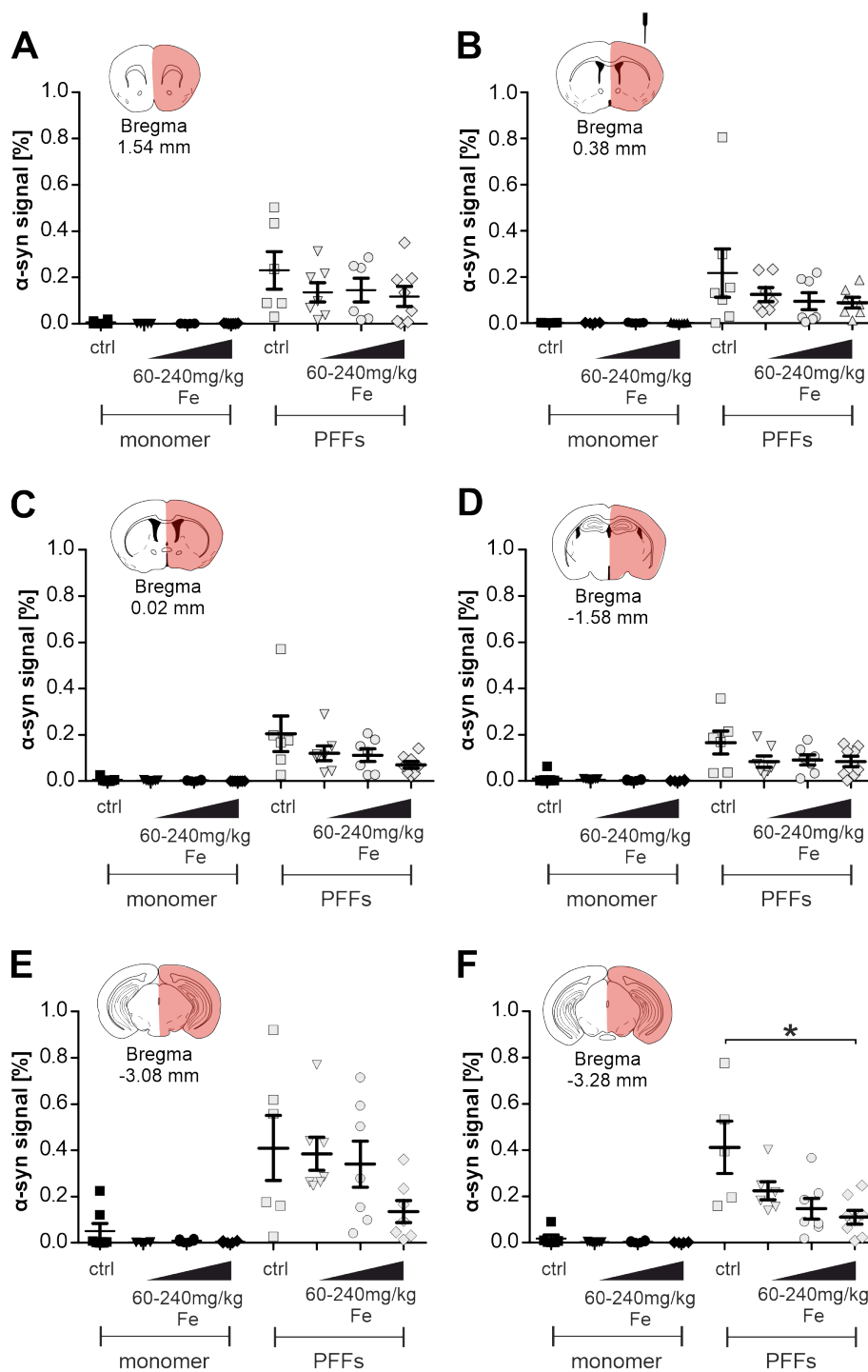
Figure 26. Threshold-based quantification of α-syn at the injected hemisphere of single sections. At 90 dpi, immunostained (pS129-α-syn) brain sections were analyzed with the particle analysis tool of the software ImageJ. All six sections were selected based on the Paxinos mouse brain atlas (Paxinos and Franklin, 2003). **(A-F)** Scatter plots are used representing α-syn signal of each mouse per group (one data point = one mouse). The following sections were evaluated: **(A)** Bregma 1.54 mm (n = 5-8), **(B)** Bregma 0.38 mm as the injectional plane (n = 5-7), **(C)** Bregma 0.02 mm (n = 6-8), **(D)** Bregma -1.58 mm (n = 6-8), **(E)** Bregma -3.08 mm (n = 6-7) and **(F)** Bregma -3.28 mm (n = 5-8). Low, middle and high iron dosage (60, 120 and 240 mg/kg Fe) are indicated in graphs as iron-triangle. The indicated control group (ctrl) was treated with the vehicle solution instead of iron. Data are presented as mean ± SEM; Kruskal-Wallis test with Dunn's post hoc test.

Furthermore, a signal average of all available brain sections per mouse was calculated separately for signal in both, the contralateral (Figure 27A) and ipsilateral hemisphere (Figure 27B). At the contralateral hemisphere no significant group differences were observed. At the injected hemisphere, the crtl/PFFs group showed significantly higher pS129-α-syn signal amounts compared to the 240 mg/kg iron group (*$p < 0.05$). In total, the α-syn amounts at the contralateral hemisphere were markedly lower compared to signal at the injected hemisphere of PFFs-injected mice.
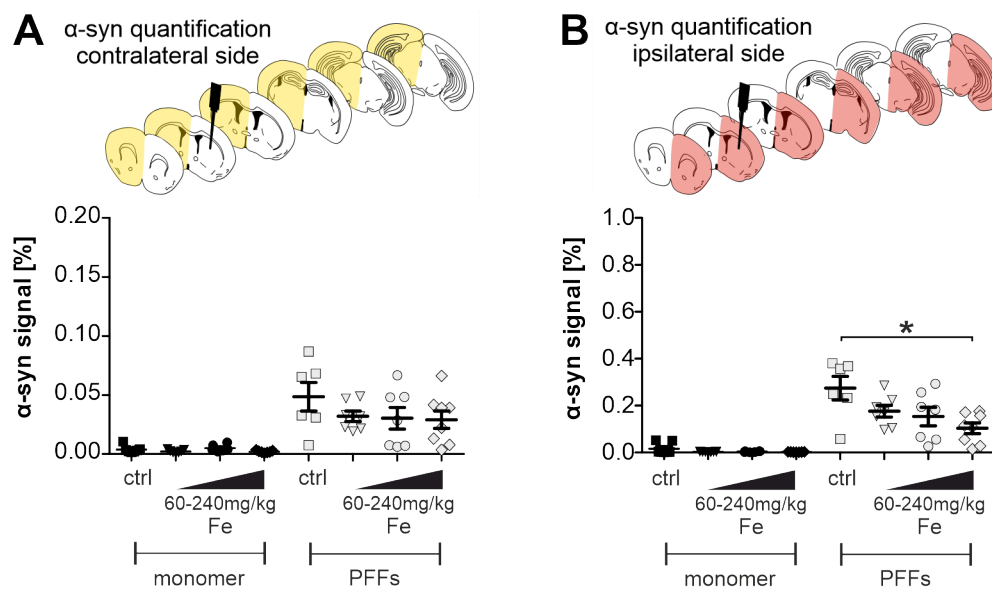
Figure 27. Averaged α-syn signal within both the injected and the contralateral hemisphere of iron- and PFFs-treated mice. Threshold-based α-syn signal analysis of immunostained (pS129-α-syn) brain sections at 90 dpi. An average of α-syn signal in four to six brain sections was calculated per mouse (n = 6-8). The averaged α-syn signal per mouse is shown individually for both **(A)** the contralateral hemisphere and **(B)** ipsilateral hemisphere. Each data point within the scatter plots represents the α-syn signal of one evaluated mouse per group. Low, middle and high iron dosage (60, 120 and 240 mg/kg Fe) are indicated in graphs as iron-triangle. The indicated control group (ctrl) was treated with the vehicle solution instead of iron. Data are presented as mean ± SEM; Kruskal-Wallis test with Dunn's post hoc test.

Figure 28 shows pS129-α-syn signal at the contralateral hemisphere of all six individual sections. No significant differences between the four iron-treated PFFs groups were found. Taken together, α-syn pathology spread stronger to the injected than to the contralateral hemisphere and iron-treatment dose-dependently reduced α-syn amounts compared to mice of the control group.
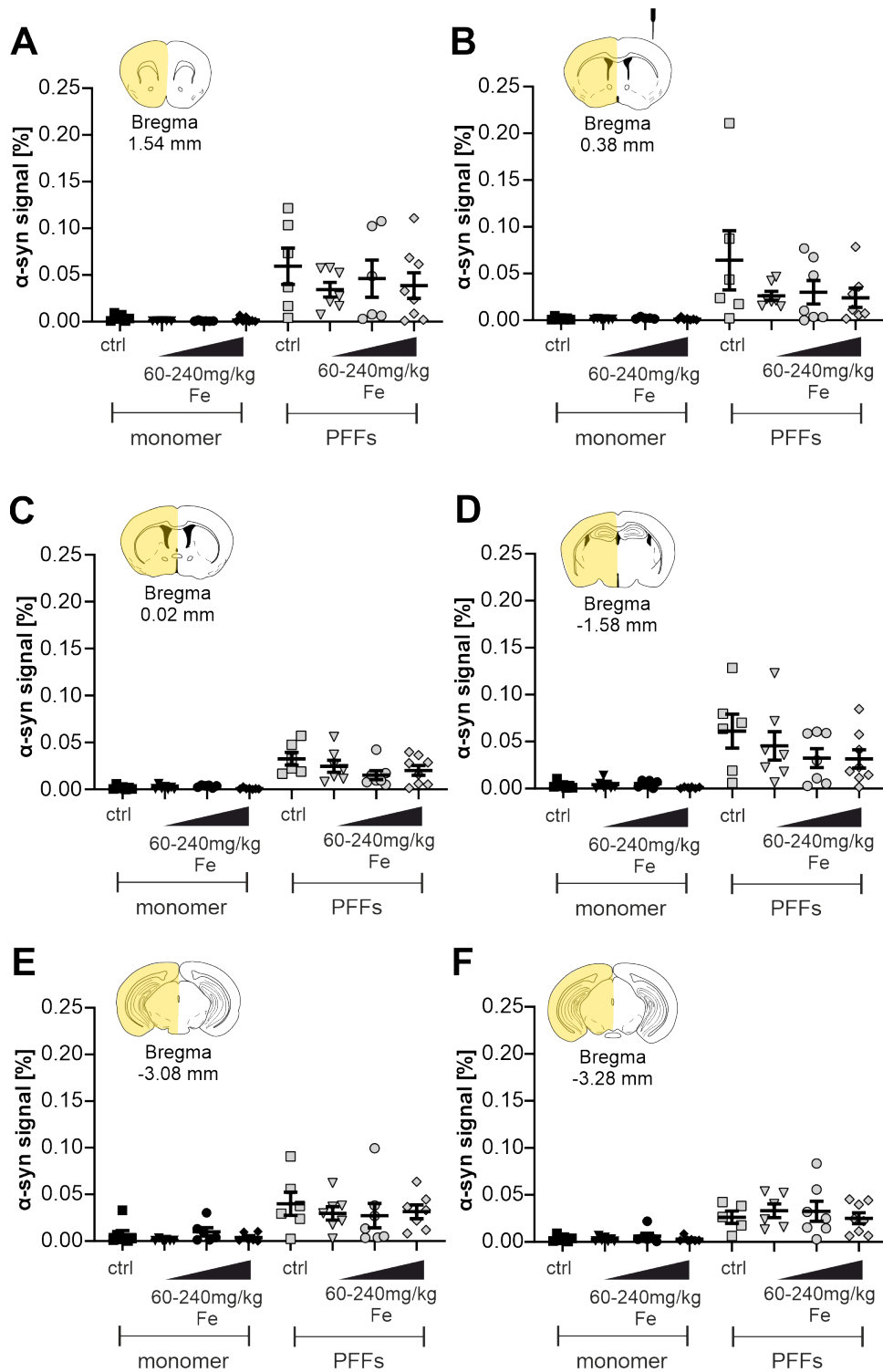
Figure 28. Threshold-based quantification of α-syn at the contralateral hemisphere of single sections. Threshold-based α-syn signal analysis of immunostained (pS129-α-syn) brain sections at 90 dpi. The following sections were evaluated: **(A)** Bregma 1.54 mm (n = 5-8), **(B)** Bregma 0.38 mm as the injectional plane (n = 5-7), **(C)** Bregma 0.02 mm (n = 6-8), **(D)** Bregma -1.58 mm (n = 6-8), **(E)** Bregma -3.08 mm (n = 6-7) and **(F)** Bregma -3.28 mm (n = 5-8). Low, middle and high iron dosage (60, 120 and 240 mg/kg Fe) are indicated in graphs as iron-triangle. The indicated control group (ctrl) was treated with the vehicle solution instead of iron. Data are presented as mean ± SEM; Kruskal-Wallis test.

3.2.3.2 Qualitative analysis of α-syn spreading to specific brain regions

For a distributional analysis of α-syn clustering in brain regions, pS129-α-syn signal was rated per region with a 5-stage scale (−, +, ++, +++, ++++) and visualized in spreading maps (Figure 29). The darker the color in the heat maps the more signal was found within the brain regions. Spreading maps were only generated for PFFs-injected mice of the control group which was treated with vehicle and of the highest iron dosage group (240 mg/kg Fe), since this iron group showed the strongest effects on pS129-α-syn quantification demonstrated in chapter 3.2.3.1. This rating approach served as a rough region-specific quantification to assess the α-syn amount in brain regions and was rather used to focus differences in the distribution. Differences in the pathology stages between the groups, e.g. + vs. ++ pathology, do not imply statistical significance. In this concrete example, the difference in a specific brain region states that on average the α-syn pathology was rated one level higher in mice of one group compared to the other group. Thereby the maps represent trends of pathological differences between groups. A statistical analysis of group means per region is mentioned after the following description of the pathology maps.

The pS129-α-syn spreading maps of both groups show that mostly the same brain regions were affected but with distinct differences in the quantity of aggregated α-syn. The rating approach revealed that PFFs-injected mice with vehicle treatment showed more regions with strong α-syn pathology (+++ or ++++). Group rating differences are visualized in subtraction heat maps (Figure 29).

High α-syn pathology discrepancy between the two analyzed groups in specific regions with at least two level of distance (e.g. + vs. +++) were observed at the injected hemisphere within the cingulate cortex area 1, the primary motor cortex, perirhinal cortex, lateral amygdaloid nucleus, stria terminalis and the amygdalohippocampal area. Within the mentioned brain regions, the control group showed more pronounced pathology. At the contralateral hemisphere, such a distinct difference in pathology was only seen in the agranular insular area of the cortex showing stronger α-syn pathology for iron-treated mice. In other brain regions which showed an α-syn increase in iron-treated mice only one rating level distance between pathology in iron-treated mice and pathology in vehicle-treated mice was observed such as − vs. + or + vs. ++. The case that in some regions α-syn pathology was stronger for iron-treated than for vehicle-treated mice was more frequently found at

the contralateral hemisphere than on the injected hemisphere (Figure 29). As stated above, the mentioned group differences do not represent statistically significant differences.
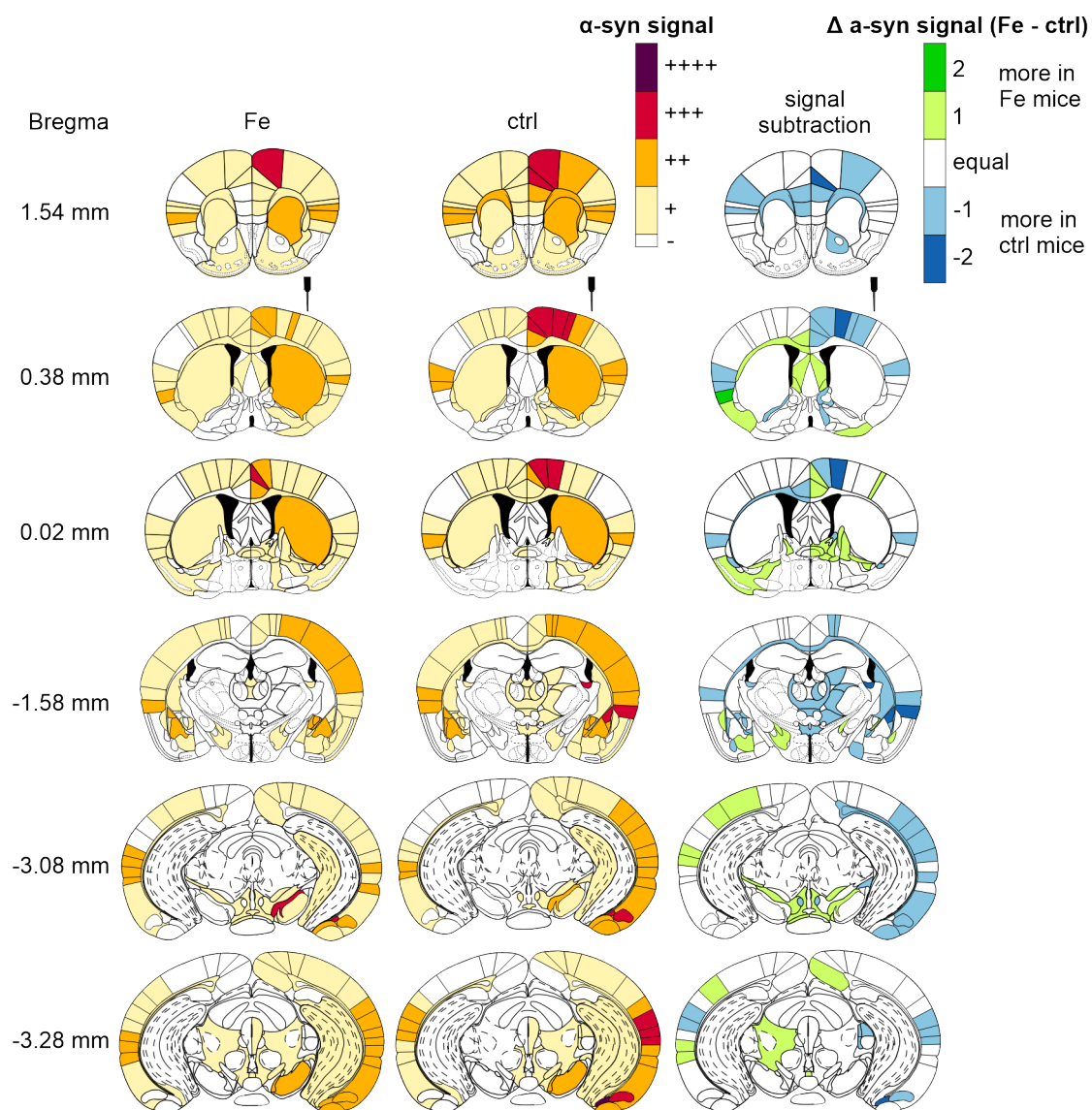
Figure 29. Heat maps representing the distribution of pS129-α-syn in six coronal brain sections. The first two columns of heat maps represent pS129-α-syn signal of iron-treated (240 mg/kg Fe) or vehicle-treated (ctrl) PFF-injected mice, respectively, at 90 dpi. Pathology in brain regions was graded with a 5-stage scale as follows: '−' no positive structures, '+' few (some positive structures), '++' mild (more positive structures), '+++' moderate (many positive structures covering a widespread part of the brain region), '++++' severe (almost the whole brain region is covered with α-syn signal). For each brain region, the average per treatment group was calculated (n = 5-8 per group) and a color code was assigned to the scale. In the third column, signal subtraction heat maps comparing both treatment groups are shown. Therefore, signal stages of the control group were subtracted from the iron group meaning that equal signal stages were rated as 0 and represented in white. More α-syn pathology for iron animals is shown in green, whereas more α-syn pathology for the control group is shown in blue.

For a statistical analysis, the Mann-Whitney-U-test was performed. The p-values as well as the group means and SEM values per evaluated brain region are listed in Suppl. Table 1 to Suppl. Table 6. Due to the low sample size and high variability in the α-syn pathology per group, statistical significance is rarely found in the individual brain regions.

Associated to the subtraction heat map, a fourfold table summarizes the number of brain regions in which more α-syn signal was either found in iron-treated mice or in the vehicle-treated mice (Table 7). At the injected hemisphere, PFFs-injected control-treated mice exhibited more α-syn in a greater number of regions. The Fisher's exact test of this 2×2 contingency table shows a significant result (p = 0.0186) indicating the influence of iron on α-syn pathology.

Table 7. Fourfold table associated to the subtraction heatmap of α-syn pathology in iron-treated PFFs-injected mice. The quantity of brain regions is described which show more α-syn in PFFs-injected mice treated with either iron or vehicle (ctrl group). Fisher's exact test indicates a significant difference (*p < 0.05).

	Regions with more α-syn in the ctrl group	Regions with more α-syn in the iron group
Injected hemisphere	60	25
Contralateral hemisphere	26	26

3.2.3.3 Connectivity analysis of α-syn spreading

This chapter is associated to the results presented in chapter 3.2.3.2. Accordingly, α-syn signal was rated per brain region in six different brain sections using a 5-stage scale ranging from 0 = no pS129-α-syn signal to 4 = severe α-syn pathology. We aimed to further analyze differences of PFFs-injected mice treated with either iron or vehicle in the α-syn spreading to anatomically connected regions (Figure 30). Two intrastriatal injection sites described in the Allen Mouse Brain Connectivity Atlas (Oh et al., 2014) (©2020 Allen Institute for Brain Science. Allen Mouse Brain Connectivity Atlas, available from: https://connectivity.brain-map.org/) were used as described in chapter 2.2.5.1.3 to define the connectome of the injection site of the current experiment. Figure 30C displays all connectome-specific brain areas in the six evaluated brain sections. Afterwards, the connectivity maps were overlaid with the α-syn spreading maps and the subtraction heat map to indicate which group shows stronger spreading to areas anatomically connected to our injection site.

A injection site in current experiment

2 µl PFFs injection radius
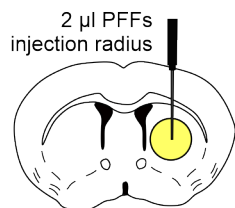
B injection sites in Allen Brain Atlas

Exp.158916311   Exp.100142580
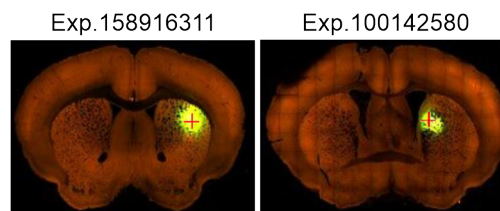
Image credit: Allen Institute.

C connectivity
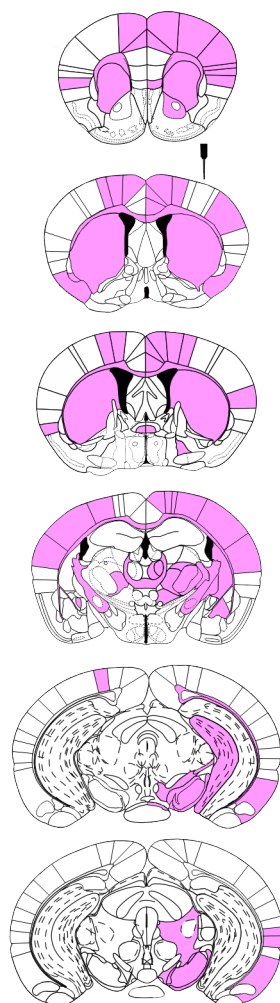
D α-syn signal (color) + connectivity (stars)
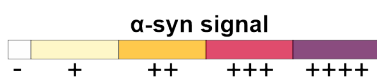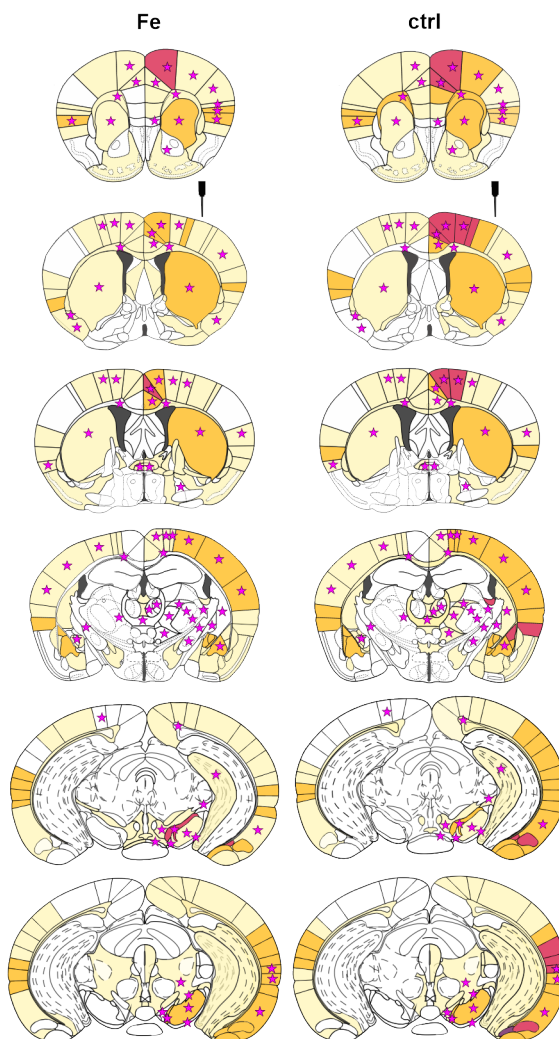
Fe   ctrl

E signal subtraction (color) + connectivity (stars)

α-syn signal

\- + ++ +++ ++++
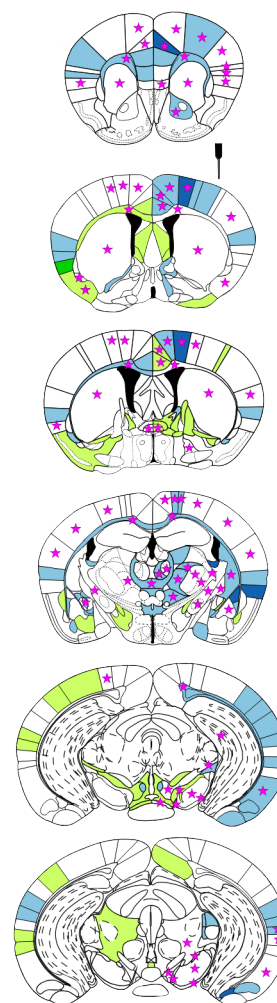
Δ α-syn signal (Fe - ctrl)

-2 -1 equal 1 2

more in ctrl mice

more in Fe mice

Figure 30. PS129-α-syn pathology in anatomically connected brain areas. **(A)** Striatal injection site of the current experiment. The circle indicates the injection radius according to injected volume of PFFs. **(B)** Serial two-photon tomography illustrations of the Allen Brain Atlas connectivity platform (©2020 Allen Institute for Brain Science. Allen Mouse Brain Connectivity Atlas, available from: https://connectivity.brain-map.org/) containing two intrastriatal injection sites which are marked with a red hair cross. The injection sites of two experiments (Exp. 158916311: https://connectivity.brain-map.org/projection/experiment/158916311; Exp. 100142580: https://connectivity.brain-map.org/projection/experiment/100142580) are located within the injection radius of the current experiment. **(C-E)** Illustration of six sectional planes assigned to the Bregma levels which are described in Figure 29. **(C)** Maps of six brain sections showing the connectivity (based on ©2020 Allen Institute for Brain Science. Allen Mouse Brain Connectivity Atlas) of brain regions to the injection site of the current study. EGPF spreading signal of both experiments mentioned in **(B)** were combined to illustrate the connectivity in the current study. **(D)** Pathology maps of pS129-α-syn as shown in Figure 29. Stars highlight regions connected to the injection site according to the Allen Brain Connectivity Atlas as illustrated in **(C)**. **(E)** Signal subtraction heat maps as shown in Figure 29. Stars highlight regions connected to the injection site according to the Allen Brain Connectivity Atlas as illustrated in **(C)**.

Interestingly, in both groups α-syn spread to most regions of the connectivity maps, but also to several other brain regions. The fourfold table (Table 8) gives an overview on how many connectome-specific and other areas were affected by α-syn pathology. Accordingly, the vehicle-treated mice showed more connectome-specific brain areas with α-syn pathology compared to the iron group and less unspecific brain regions affected by α-syn compared to the iron group. However, the Fisher's exact test of this 2×2 contingency table shows no significant association of the groups and the two outputs (connectome-specific vs. other brain areas; $p = 0.3636$).

Table 8. Fourfold table associated to the connectivity heat maps. The quantity of connectome-specific and other brain regions with α-syn pathology are described for PFFs-injected mice treated with either iron or vehicle (ctrl group). Fisher's exact test not significant ($p = 0.3636$).

	Fe group	Ctrl group
Connectome-specific brain areas with α-syn signal	66	75
Other brain areas with α-syn signal	166	155

For a more detailed analysis on the α-syn amounts in the connectome-specific and other brain areas, in Figure 31 the α-syn rating average per brain area is shown which correspond to the means listed in Suppl. Table 1 – Suppl. Table 6. In Figure 31A, all connectome-specific brain regions were included (n) in which at least one of both groups detected pS129-α-syn signal. The data show significantly higher amounts of α-syn signal in connectome-specific brain areas for the control group. In connectome-independent brain areas no significant difference was found between both groups (Figure 31B).
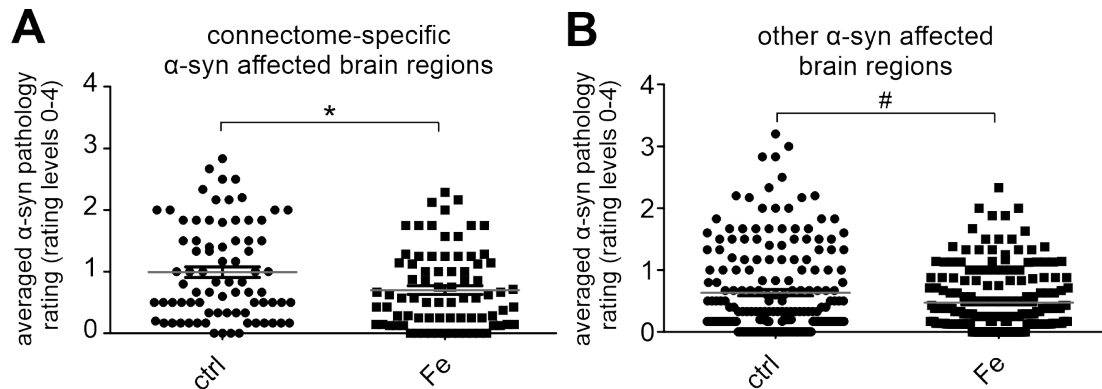
Figure 31. Averaged pS129-α-syn pathology rating in connectome-specific and other brain regions. The data are related to the 5-stage rating scale used in Figure 29 and represent pS129-α-syn affected brain regions in both contralateral and injected hemisphere. All brain regions were included in which at least one group showed α-syn signal. **(A)** A comparison of the averaged α-syn pathology ratings in connectome-specific brain regions (n = 78 brain areas) of PFFs-injected mice treated with either iron or vehicle as control (ctrl). The graph is related to the data in Figure 30. **(B)** A comparison of the averaged α-syn pathology ratings in other brain regions (n = 198 brain areas) outside the connectome of PFFs-injected mice treated with either iron or vehicle as control (ctrl). The graph is related to the data in Figure 30. Mann-Whitney-U test. Mean ± SEM; *p < 0.05; #p < 0.1.

3.2.4 Iron-induced effects on the accumulation of immune cells

After demonstrating that iron-treatment resulted in an altered distribution of pS129-α-syn, the present analyses aimed to elucidate if iron also influenced inflammatory responses inside the brain which could contribute to changes in α-syn spreading pathology. Therefore, brain sections were used to analyze microglia and T cell amounts within the striatum as injection site and the SN as a known iron-enriched brain region of iron-treated animals. For the microglia analysis, immunolabeled CD11b+ cells were quantified (Figure 32A). Three striatal sectional planes were analyzed: anterior (B), middle (C) and posterior striatum (D).
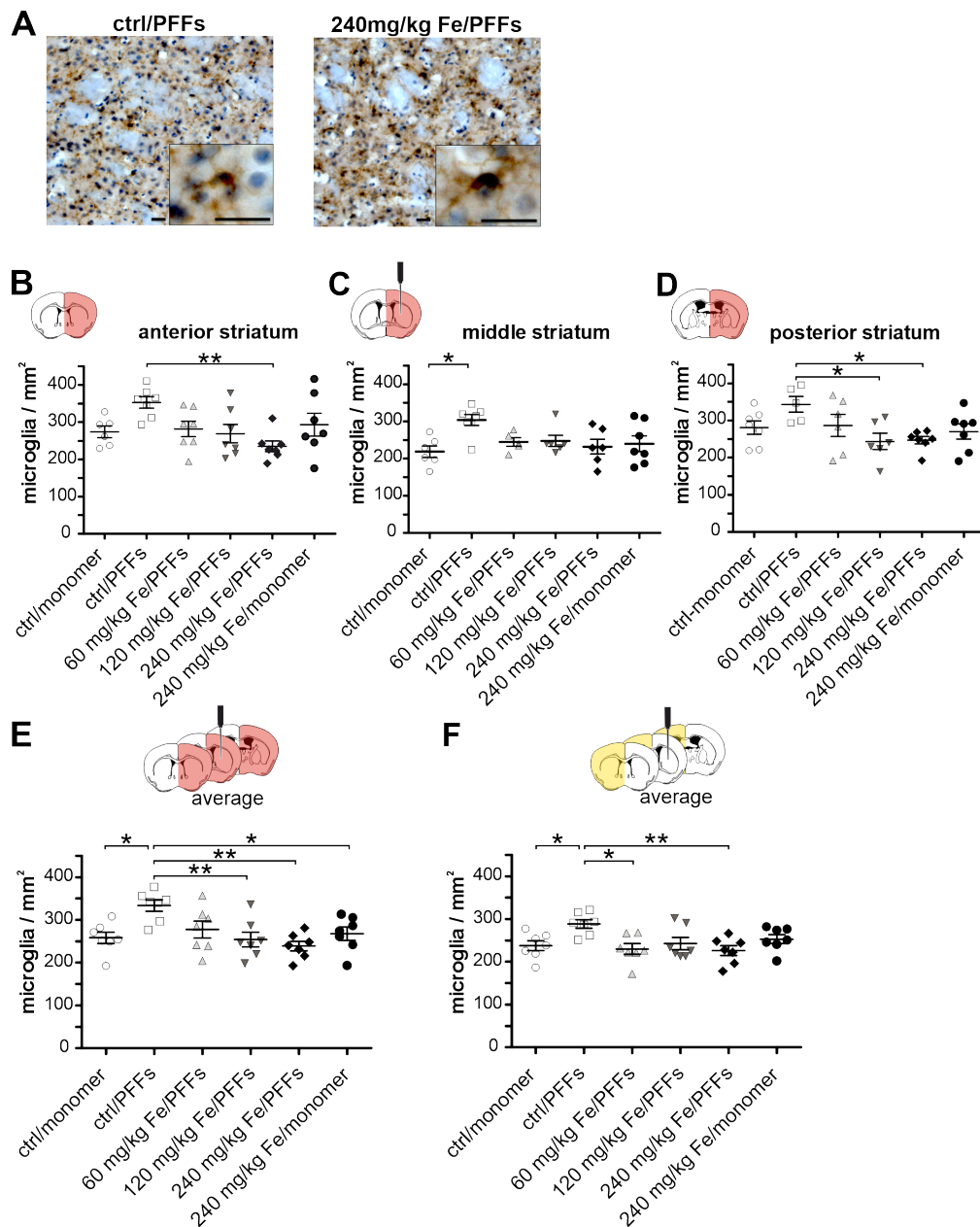
Figure 32. Analysis of CD11b+ microglia in striatal sections of iron- and α-syn-treated mice. Immunostained brain sections of 30 μm thickness were analyzed. CD11b signal is shown in brown due to a DAB reaction and cells are shown in blue (Hematoxylin staining). **(A)** Micrographs of CD11b+ cells from mice treated with vehicle or 240 mg/kg Fe are shown. A close-up image is shown in the right corner of each micrograph. Scale bar 20 μm. **(B-D)** In brain sections containing **(B)** anterior (n = 6-7), **(C)** middle (60mg/kg Fe/PFFs n = 4; other groups n = 6-7) and **(D)** posterior (n = 5-7) striatum CD11b+ microglia of iron- and α-syn-treated C57BL/6J mice were quantified. Data of the injected hemisphere is shown. **(E,F)** Microglia counts were averaged over the three evaluated striatal sections. Data of **(E)** the injected hemisphere (all groups n = 7) and **(F)** the contralateral hemisphere (all groups n = 7) are shown separately. Data given as mean ± SEM, one-way ANOVA with Tuckey's post hoc test; *p < 0.05, ** p < 0.01.

First, the intrastriatal microglia accumulation at the injected hemisphere of the analyzed sections is described. Mice of the ctrl/PFFs or ctrl/monomer group were treated with vehicle instead of iron. At the anterior striatum, microglia numbers of the vehicle/PFFs group did not significantly differ from the monomer-injected groups (vehicle/monomer and 240 mg/kg Fe/monomer). Compared to the 60 mg/kg Fe/PFFs and 120 mg/kg Fe/PFFs group, the vehicle/PFFs group showed no significant changes in the microglia number, but a significant increase was observed compared to the highest iron dosage group (240 mg/kg Fe/PFFs; $p < 0.01$; Figure 32B). At the middle striatum, microglia accumulation was significantly increased in the vehicle/PFFs groups compared to the vehicle/monomer group ($p < 0.05$; Figure 32C). All of the three iron dosages in combination with PFFs injections showed unaltered microglia accumulation compared to the vehicle/PFFs and to the monomer-injected groups. At the posterior striatum, the microglia number of the vehicle/PFFs group did not differ significantly from the vehicle/monomer group. The vehicle/PFFs group showed also no microglia number changes compared to the 60 mg/kg Fe/PFFs group, however, it showed a significant increase of microglia compared to the 120 mg/kg Fe/PFFs and the 240 mg/kg Fe/PFFs group ($p < 0.05$; Figure 32D).

Furthermore, an average of the microglia number within the injected hemisphere of all three sections was calculated. The vehicle/PFFs group showed a significant increase in microglia compared to both monomer-injected groups (vehicle/monomer; 240 mg/kg Fe/monomer; $p < 0.05$). No difference was found between the vehicle/PFFs and 60 mg/kg Fe/PFFs group. However, the microglia number of the vehicle/PFFs group was significantly increased compared to the 120 mg/kg Fe/PFFs and 240 mg/kg Fe/PFFs group ($p < 0.01$; Figure 32E). In addition to striatal sections, one SN section (part of the middle SN) was analyzed. All analyzed groups did not differ in the nigral microglia number at the injected hemisphere of this section (Figure 33A).

Second, the contralateral hemisphere of all sections was analyzed regarding the microglia accumulation in striatum and SN. An average of the microglia number of all three sections was calculated. The vehicle/PFFs group showed a significant microglia increase compared to the vehicle/monomer group ($p < 0.05$) as well as to the 60 mg/kg Fe/PFFs ($p < 0.05$) and 240 mg/kg Fe/PFFs group ($p < 0.01$). No significant difference was observed compared to the 120 mg/kg Fe/PFFs group (Figure 32F). Analyzing one SN

section, no significant microglia differences were observed between the groups (Figure 33B).
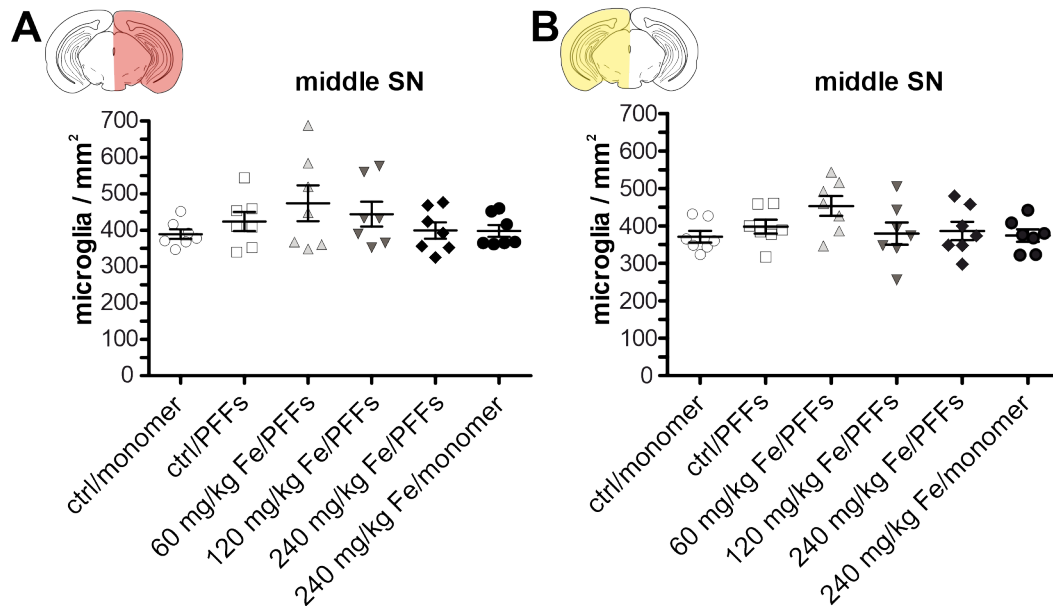
Figure 33. Analysis of CD11b+ cells in a nigral section of iron- and α-syn-treated mice. CD11b+ cells in one SN section were analyzed separately for the **(A)** ipsilateral and **(B)** contralateral hemisphere (n = 6-7). Data given as mean ± SEM. One-way ANOVA.

Since T cells also play an important role in the immune response infiltrating the brain (Brochard et al., 2009; González et al., 2013; Kurkowska-Jastrzebska et al., 1999), mouse brain sections were immunolabeled for the T cell marker CD3 (Figure 34A). As for the microglia analysis, CD3+ cells were quantified within three striatal sections (Figure 34B-D). Within the injected hemisphere of single sections, no significant differences in T cell amounts were found between the different treatment groups. Taking the average of the T cell counts per mouse over the three sections, no significant group differences were observed, neither at the injected hemisphere (E) nor at the contralateral hemisphere (F).
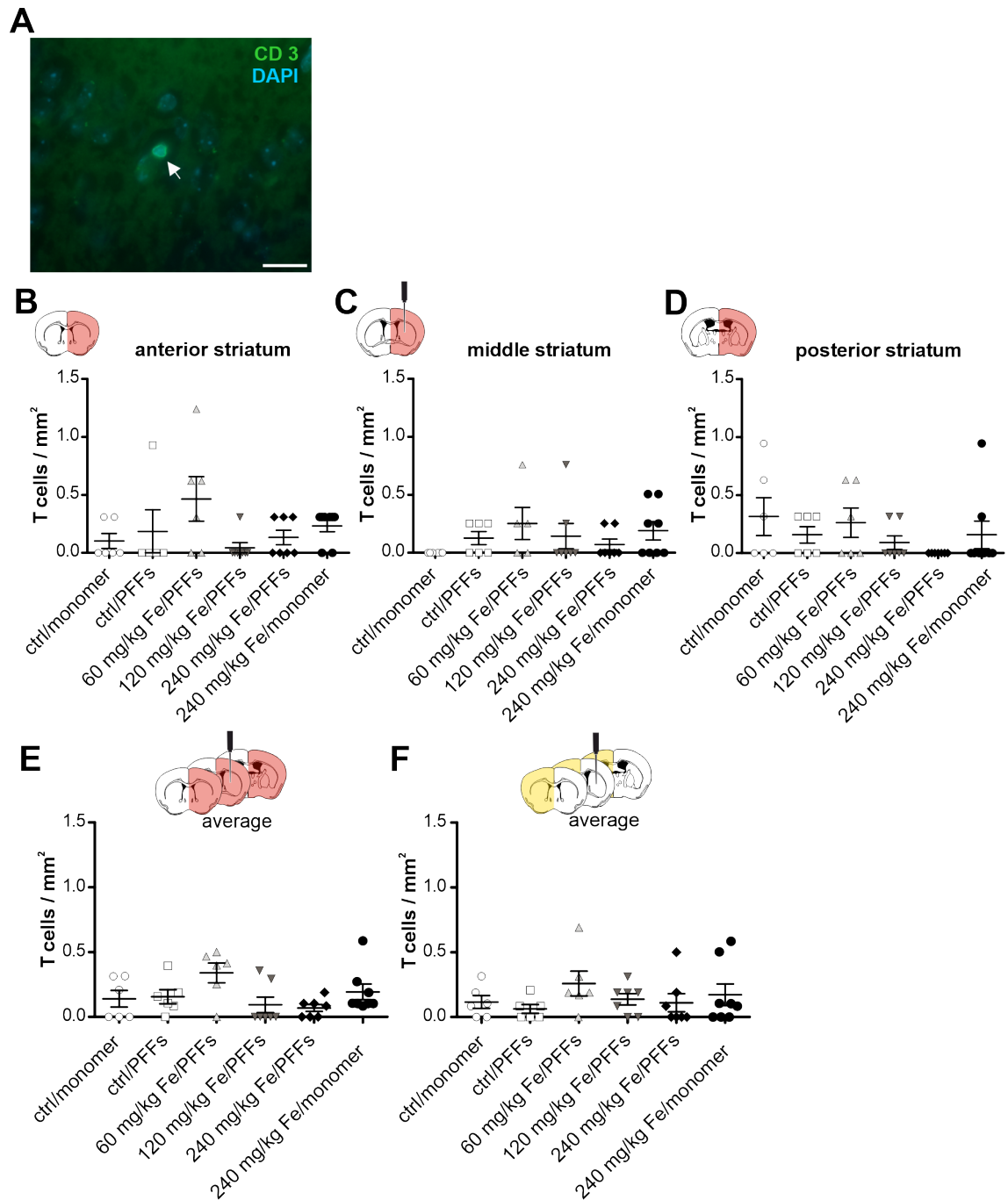
Figure 34. CD3+ T cell analysis in striatal sections of iron- and α-syn-treated mice. Brain sections were immunolabeled for CD3 and DAPI. Scale bar 20 µm. **(A)** Exemplary image of an immunostained CD3+ T cell indicated with an arrow. Scale bar 20 µm. At the ipsilateral hemisphere, T cell quantification is shown within the following striatal sections: **(B)** anterior, **(C)** middle and **(D)** posterior striatum. **(E,F)** Averaged T cell amounts within the striatum **(E)** at the injected hemisphere and **(F)** at the contralateral hemisphere. Data given as mean ± SEM; n = 5-8; Kruskal-Wallis test.

Only one sectional plane of the SN was analyzed regarding T cell numbers, but no significant iron- or PFFs-induced effect was found (Figure 35). For all mentioned T cell analyses Kruskal-Wallis test was used.
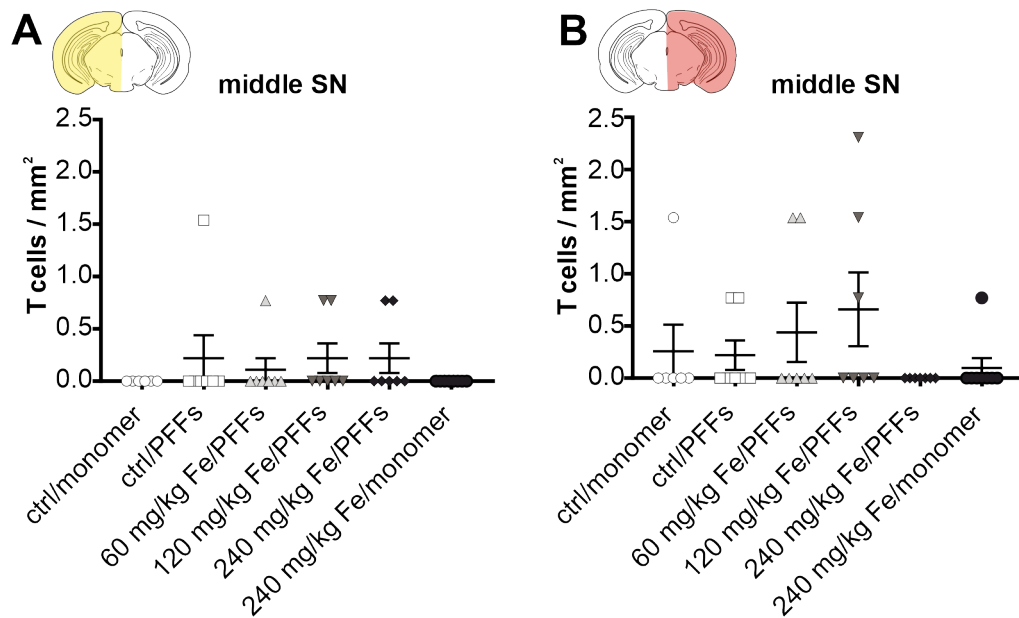
Figure 35. T cell analysis in a nigral section of iron- and α-syn-treated mice. T cell quantification in one SN section at the **(A)** contralateral and **(B)** ipsilateral hemisphere. n = 6-8. Data given as mean ± SEM; Kruskal-Wallis test.

3.3 The influence of iron on the α-syn pathology *in vitro*

After demonstrating the effect of iron on α-syn pathology in the brain of C57BL/6J mice, the present analysis aimed to elucidate if iron also influences α-syn transmission in cortex neurons obtained from E 18.5 wild-type mouse embryos. To establish the iron-treatment paradigm in cortex cultures, cells were treated with different concentrations of iron and afterwards stained for iron by means of a Prussian blue staining to assess the iron load in cultures. To exclude iron-induced toxicity, a ToxiLight assay was used. Iron-mediated alterations of α-syn spreading *in vitro* were analyzed in microfluidic chambers. To this, cells were treated with iron and α-syn PFFs or monomers.

3.3.1 Iron treatment of cortex neurons

To verify that iron treatment of cortex cultures indeed led to high amounts of iron in the culture, a Prussian blue staining combined with DAB staining was used to detect iron resulting in a brown color of the target. Microscopy images showed that the amount of iron is higher in cells treated with 100 µM iron compared to treatment with lower iron dosages (Figure 36A).

In another experiment, iron-induced toxicity in cortex neurons at specific time points after treatment was analyzed (Figure 36B). A ToxiLight bioassay kit was used measuring the release of adenylate kinase from damaged cells. Cells were treated with 10, 50, 100 or 200 µM iron. As a control, cells were treated with vehicle solution. To perform the assay, medium was collected directly before treatment (div2), at the end of the treatment (24 h post treatment start), at div7 and at div14. The statistical analysis revealed no significant cytotoxicity or dosage-dependent effects of iron at the different measurement timepoints (two-way ANOVA with repeated measures).

A

B
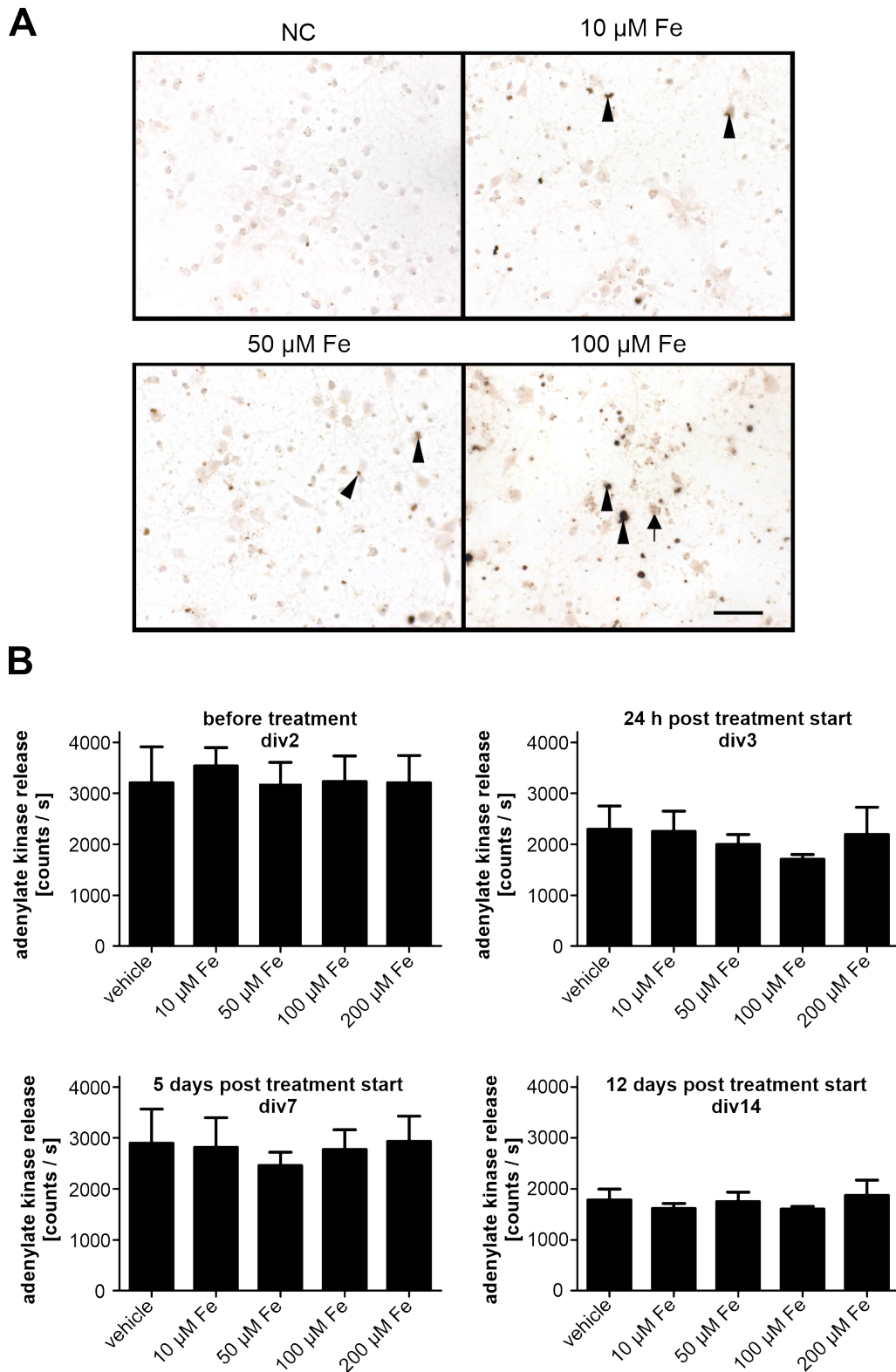
Figure 36. Cytotoxicity in cortex neuron cultures following iron treatment. (A) Exemplary micrographs of cells stained for iron using a modified Prussian blue staining protocol. Cells were treated with 10, 50, 100 or 200 µM Fe at div2 for 24h. The control cells were treated with vehicle. Arrowheads show large intracellular iron deposits; the arrow indicates smaller iron-positive puncta within a cell. NC: negative control. **(B)** ToxiLight analysis of cortex neurons treated with different iron concentrations at div2 for 24h. Cell medium was collected at div2, div3, div7 and div14 (n = 4 cultures). ANOVA for repeated measures.

3.3.2 Microfluidic chamber model – the influence of iron on α-syn spreading

To analyze if iron affects the α-syn spreading following PFFs treatment *in vitro*, the microfluidic chamber model was used. Cortex neurons were seeded in one compartment of the chamber and treated with iron and α-syn PFFs at 2 d and 3 d post preparation, respectively (Figure 37A). At div7, freshly prepared cortex neurons were seeded in the secondary cell compartment. At div14, cells were fixed and stained with an antibody recognizing pS129-α-syn.
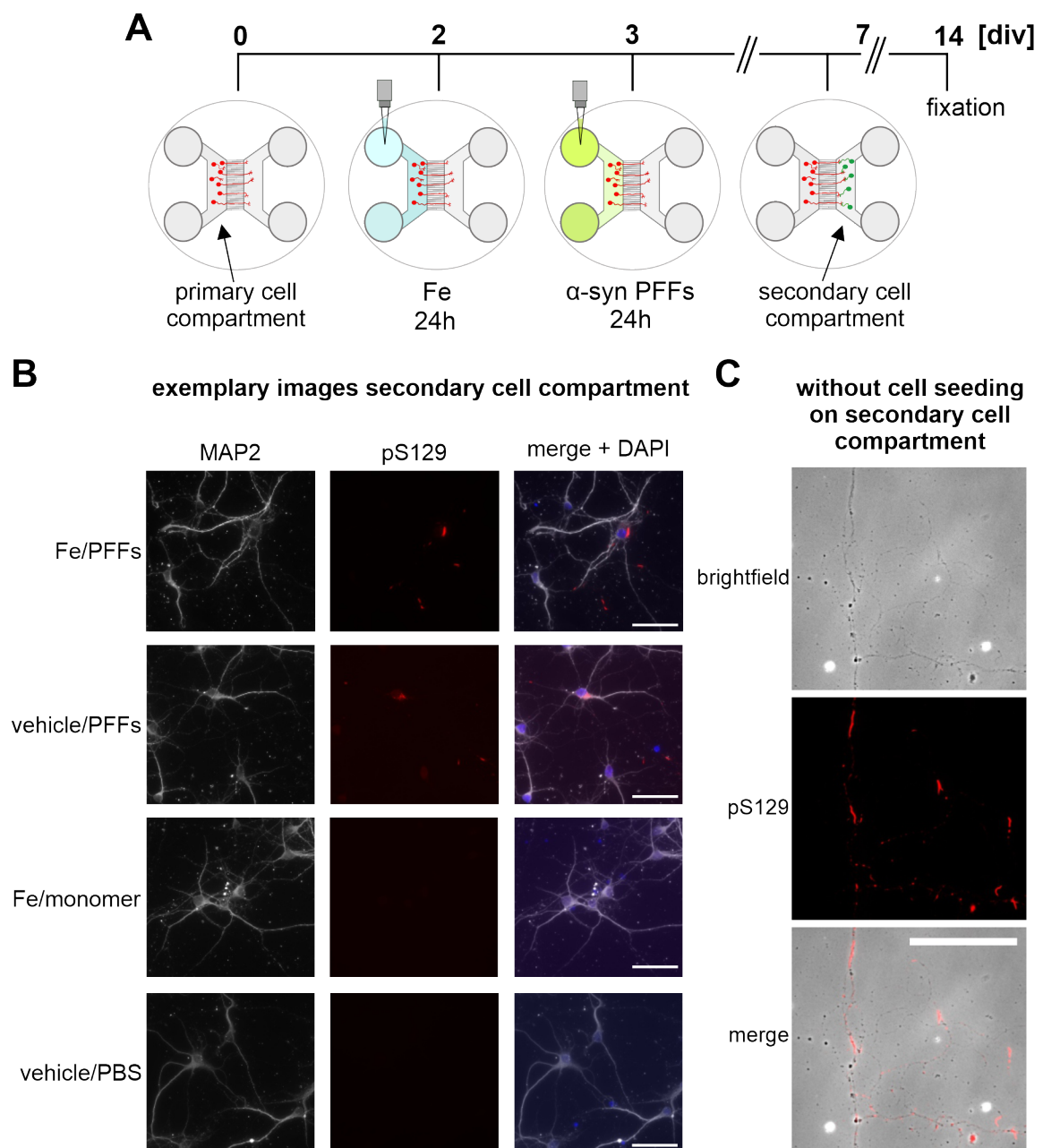
Figure 37. Experimental layout and exemplary micrographs of α-syn spreading signal in microfluidic chambers. (A) Experimental layout. Cells in microfluidic chambers were treated with iron and α-syn PFFs for 24 h each. **(B)** Exemplary micrographs of intracellular pS129-α-syn signal appearing in the secondary cell compartment. MAP2 was used as a neuronal marker. Scale bar 50 μm. **(C)** Exemplary micrograph of α-syn signal in axons at the secondary cell compartment. In this exemplary chamber no cells were seeded to the secondary cell compartment. The cells were treated with PFFs. Spread α-syn fibrils were only transferred via axons to the secondary cell compartment. Scale bar 100 μm.

Immunocytochemical staining revealed the presence of pS129-α-syn in cell bodies and axons at the secondary cell compartment in PFFs conditions. No signal was observed in monomer- or PBS-treated cells (Figure 37B). To more clearly visualize the distribution of pS129-α-syn, in some chambers cells were only seeded in the primary cell compartment and neurites thereof grew to the secondary cell compartment (Figure 37C). The micrograph shows that the pS129 signal was exclusively located in neurites within the secondary cell compartment. This suggests that PFFs, uptaken by cells in the primary cell compartment, spread from the perikarya to the neurites and no extracellular PFFs were observed travelling independently through the grooves to the secondary cell compartment.

The α-syn signal was quantified by a threshold-based method. Subtracting the signal results of the PBS-treated chambers, monomer-treated cells showed neglectable signal at the secondary cell compartment (Figure 38). A statistical analysis (Kruskal-Wallis test with 3 determined Dunn's post hoc comparisons: Fe/monomer vs. Fe/PFFs, vehicle/monomer vs. vehicle/PFFs, Fe/PFFs vs. vehicle/PFFs) revealed a significant difference of Fe/monomer-treated cells compared to Fe/PFFs-treated cells (*$p < 0.05$). With vehicle treatment, the PFFs condition also significantly differed from its monomer control group (*$p < 0.05$). Comparing α-syn PFFs conditions, no significant difference was found between iron-treated and vehicle-treated cortex neurons (Fe/PFFs 0.015 ± 0.0048 vs vehicle/PFFs 0.013 ± 0.0042). In summary, the α-syn spreading results indicate that iron treatment did not significantly influence the α-syn amounts spread to the secondary cell compartment in microfluidic chambers.
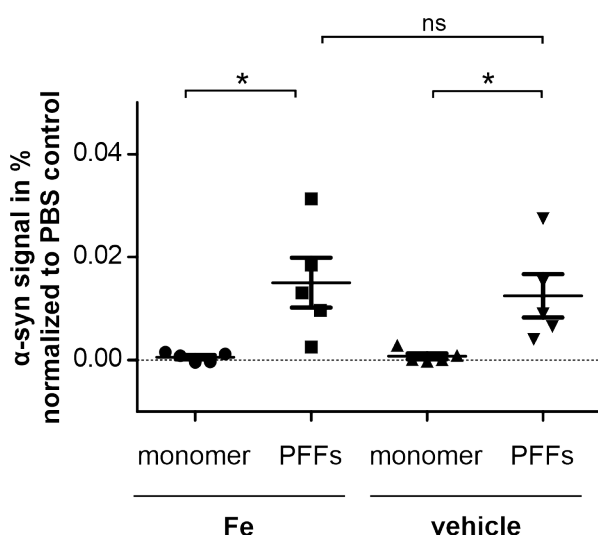
Figure 38. Quantification of pS129-α-syn signal in the secondary cell compartment of microfluidic chambers. Cells were immunolabeled for pS129-α-syn. The graph shows a quantification of α-syn signal within the secondary cell compartment of microfluidic chambers (average of 1-3 chambers per culture, n of cultures = 5, each data point within the scatter plot represents one culture). Signal of all conditions was normalized to the respective PBS control. Kruskal-Wallis test with three selected Dunn's post hoc comparisons; *p < 0.05.

3.4 Therapeutic approach: The influence of fasudil on the α-syn pathology

Finally, we aimed to elucidate if treatment with the ROCK inhibitor fasudil could affect α-syn spreading pathology in mice. Fasudil has previously been shown to reduce α-syn aggregation *in vitro* and also *in vivo* using the A53T mouse model (Tatenhorst et al., 2016). In the current study, mice were injected with α-syn PFFs or monomers. One PFFs-injected group was treated with 30 mg fasudil /kg bw which was supplied via the drinking water, according to the previously published protocol (Tatenhorst et al., 2016) (Figure 39A). Motor behavior from doi to sacrifice and neuron survival at 90 dpi were analyzed to assess the health status of PFFs-injected mice. Later, pS129-α-syn signal was quantified in multiple brain sections to assess if fasudil alters spreading pathology, described in chapter 3.4.3. Therefore, two different quantification methods were used.

3.4.1 Motor behavior analysis

To determine if PFFs treatment induced changes in motor behavior, mice performed the rotarod test weekly between doi and sacrifice (Figure 39A). The treatment (monomer/vehicle, PFFs/vehicle, PFFs/fasudil) of the mice and the interaction of 'treatment × time' did not significantly affect the performance on the rotating rod (Figure 39B; ANOVA with repeated measures). Only the variable 'time' (weeks before sacrifice)

showed a significant influence, meaning that the time on the rod for the average of all animals changed over time (****p < 0.0001).
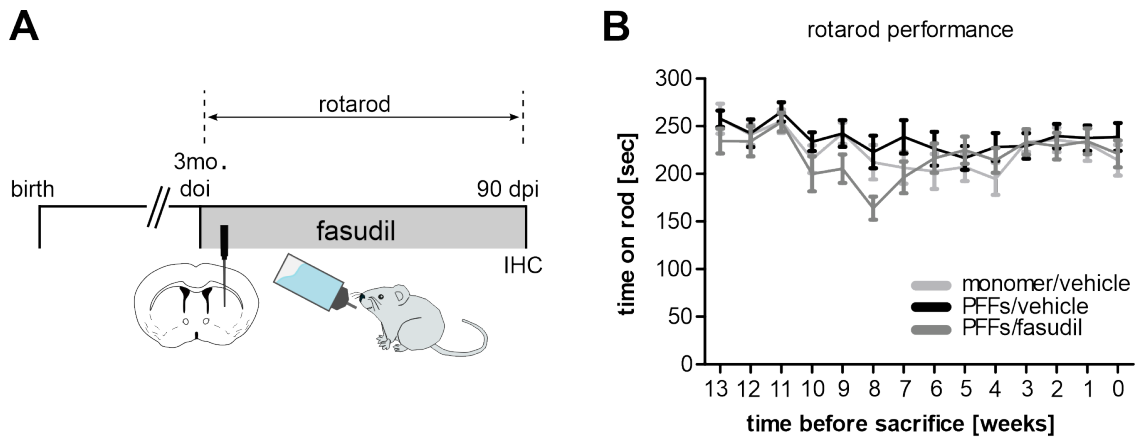
Figure 39. Experimental layout and evaluation of motor behavior of α-syn PFFs-injected mice treated with fasudil. **(A)** Experimental layout. C57BL/6J mice were injected with α-syn PFFs or monomers at 3 months (3mo.) of age and one group of the PFF-injected animals was treated with fasudil via drinking water between injection day (doi) and sacrifice at 90 dpi. Rotarod was performed weekly. **(B)** Results of the weekly performed rotarod test starting 13 weeks before sacrifice. The graph shows the averaged performance of mice per treatment group (monomer/vehicle n = 8, other groups n = 10) over time. Data given as mean ± SEM, one-way ANOVA with repeated measures.

3.4.2   Dopaminergic neuron survival

In order to investigate effects of α-syn PFFs on neuronal loss in mice, TH+ neurons as well as Nissl+ neurons were stereologically quantified in nigral brain sections at 90 dpi. Nissl staining was used to identify the total neuron count in SNpc. At the ipsilateral hemisphere, α-syn PFFs-injected mice showed lower counts for TH+ neurons compared to monomer-injected mice but these results did not differ significantly (Figure 40A; monomer/vehicle 11232 ± 862.5; PFFs/vehicle 10016 ± 432.0; PFFs/fasudil 8858 ± 774.4 cells). The same trend was observed in Nissl+ neurons in the injected hemisphere (Figure 40B;   monomer/vehicle   13282 ± 965.7;   PFFs/vehicle   12133 ± 457.5;   PFFs/fasudil 10629 ± 905.1 cells). At the contralateral SNpc also no significant group differences were found, neither in the quantification of TH+ neurons (Figure 40C; monomer/vehicle 11217 ± 852.7; PFFs/vehicle 11273 ± 592.6; PFFs/fasudil 10373 ± 558.3 cells) nor in Nissl+   neurons   (Figure   40D;   monomer/vehicle   13569 ± 959.2;   PFFs/vehicle 13492 ± 678.6; PFFs/fasudil 12432 ± 654.0 cells).
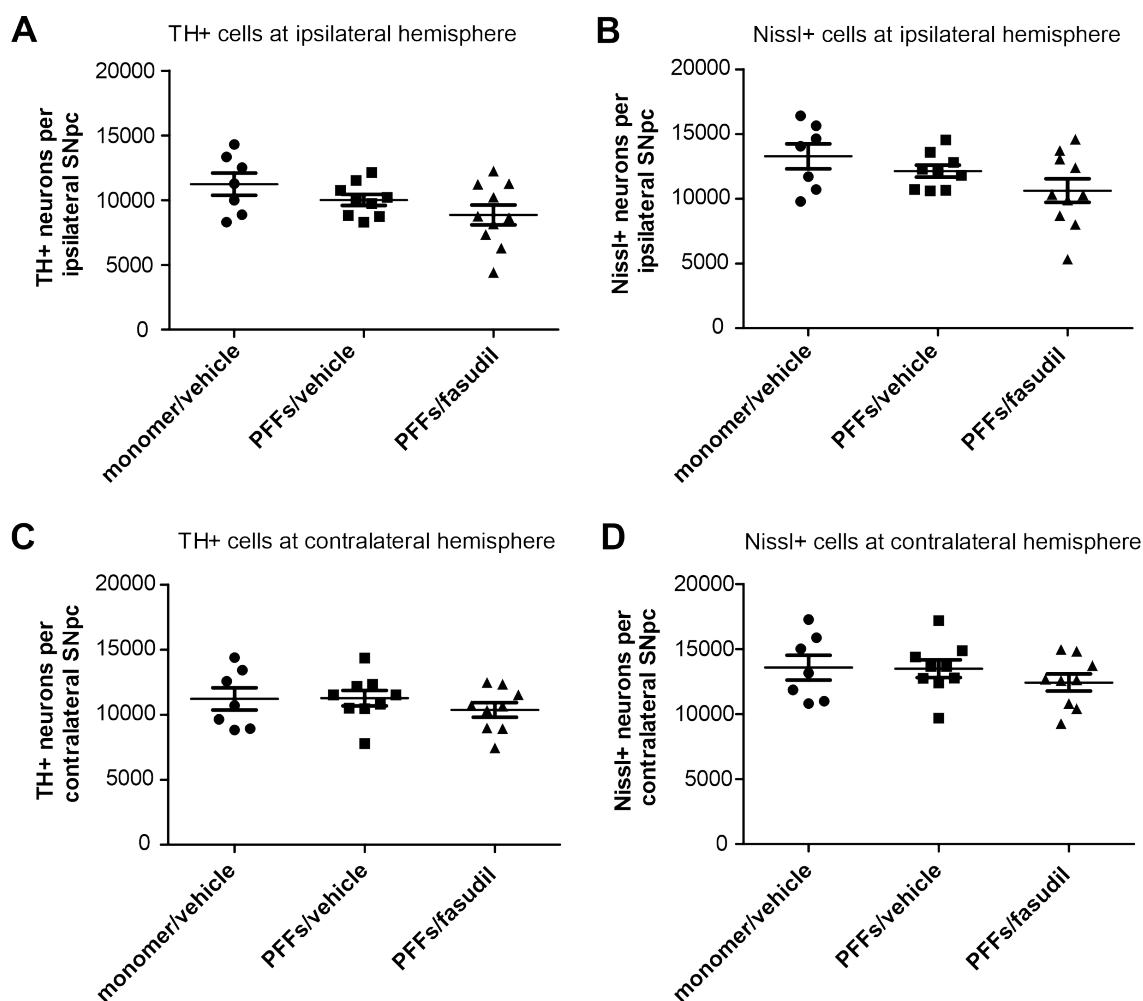
Figure 40. Quantification of nigral TH+ and Nissl+ neurons of mice injected with α-syn PFFs or monomers and treated with fasudil. TH+ and total (Nissl+) neuron count was analyzed at 90 dpi. **(A,B)** Stereological quantification of **(A)** TH+ and **(B)** Nissl+ neurons at the ipsilateral hemisphere. **(C,D)** Stereological quantification of **(C)** TH+ and **(D)** Nissl+ neurons at the contralateral hemisphere. Data shown as mean ± SEM; monomer/vehicle n = 7, PFFs/vehicle n = 9, PFFs/fasudil n = 9; one-way ANOVA.

3.4.3   The effect of fasudil treatment on α-syn spreading *in vivo*

A major aim of this study was to investigate if the ROCK inhibitor fasudil had a beneficial impact on α-syn spreading pathology. Therefore, six coronal brain sections were analyzed. Paxinos atlas coordinates (Paxinos and Franklin, 2003) are described in chapter 3.2.3.1. The sections were stained with an antibody recognizing α-syn fibrils (pS129). The pS129-α-syn amounts were quantitatively analyzed using two approaches – manual quantification and threshold-based quantification.

3.4.3.1 Manual quantification of α-syn

In a manual quantification approach, pS129-α-syn immunostained sections were covered with a grid (150 μm × 150 μm per grid box) and analyzed as described in the according method chapter 2.2.5.1.1. The signal was rated per grid box using a color code grading system corresponding to low, medium and high signal amounts, respectively: yellow = 1-5 α-syn structures, orange = 6-10 α-syn structures, red = > 10 α-syn structures per box.

In a first analysis, it was aimed to describe how much area of each brain section was generally affected (independent on the pS129 α-syn quantity evaluated in each counted box). Therefore, a sum of all rated boxes (boxes with low, medium, high signal amounts) in the contralateral or the injected hemisphere was calculated individually for each section and relativized to the total box number of the corresponding hemisphere to obtain a percentage (%). The monomer control group did not show pS129-α-syn signal in any of the analyzed sections, neither in the injected nor in the contralateral hemisphere (Figure 41A,B). In all sections, PFFs-injected mice and PFFs-injected mice with fasudil treatment showed no significant differences in the total area affected by α-syn analyzing both hemispheres separately. In a next step, the signal output of all six sections demonstrated in Figure 41A was averaged per group. These results of the injected hemisphere are shown in Figure 41 C,D. The size of the affected area averaged over all sections (injected hemisphere) did not differ between the groups (Figure 41D).

Comparing the averaged usage of the three different rating stages (low, medium and strong signal) between both PFFs-treatment groups, no significant difference was found. In an equal frequency in both groups, grid boxes were rated to contain low, medium or strong signal. The graph displays that low signal amounts were observed within largest parts of the α-syn-affected area (Figure 41C).

Since for monomer-injected animals with vehicle-treatment no pS129-α-syn signal was expected, both PFFs groups were always additionally analyzed with a Student's t-test showing no significant difference between the groups in all mentioned analyses.
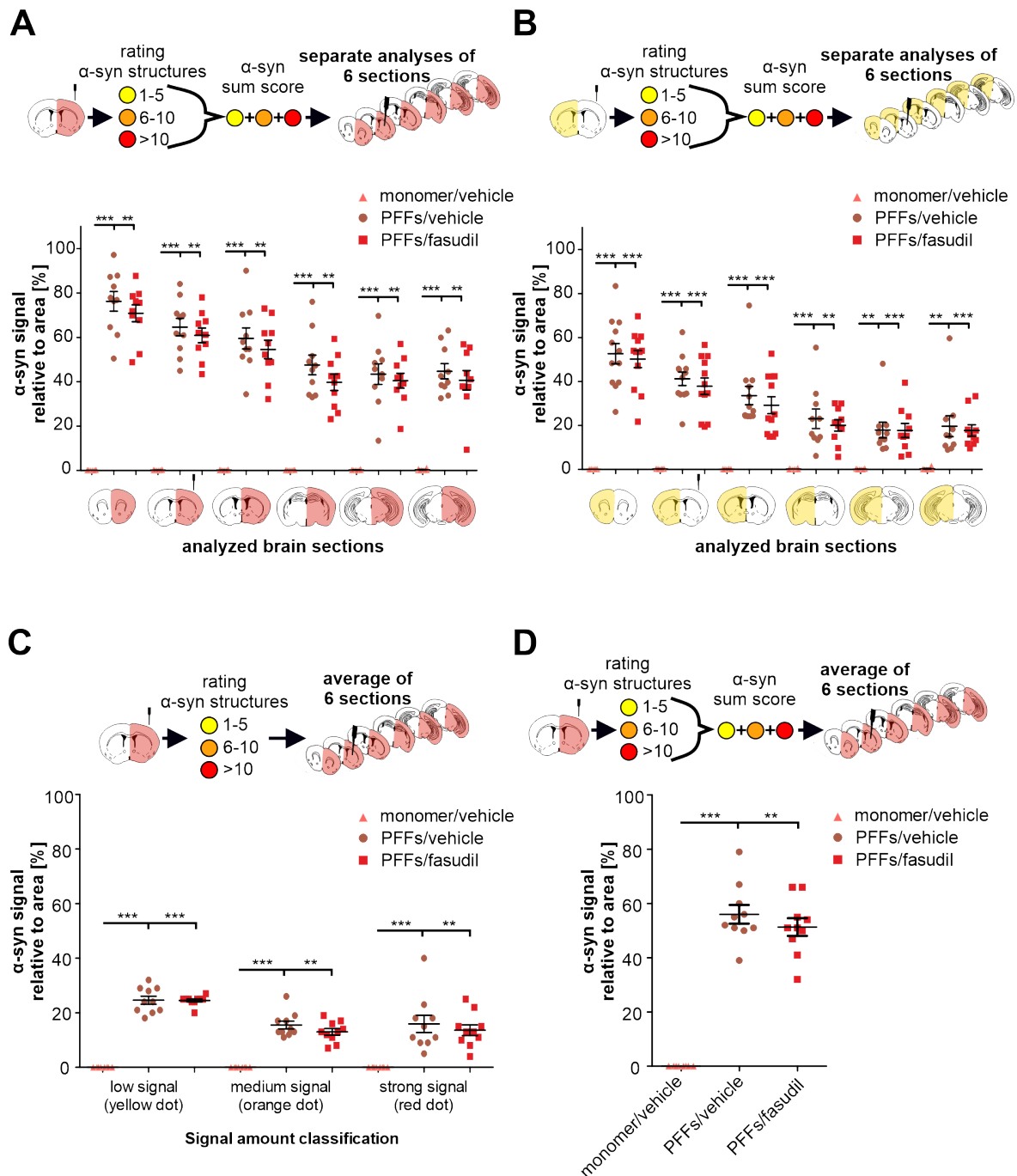
Figure 41. Manual quantification of α-syn spreading in brain sections of fasudil-treated mice. Six coronal brain sections were immunolabeled with an antibody recognizing pS129-α-syn. Signal was manually analyzed using a color code rating scale. For each brain section, a sum of α-syn-positive grid boxes was separately generated for either **(A)** the injected or **(B)** the contralateral hemisphere. The sum was normalized to the total area. **(C)** Group-specific usage of the three different rating stages (low, medium, strong signal) at the injected hemisphere averaged over all sections. **(D)** Average of all sum scores of the injected hemisphere in six brain sections, which were presented in **(A)**. Data are shown as mean ± SEM; n = 8-10; Kruskal-Wallis test with Dunn's post hoc test.

3.4.3.2 Threshold-based quantification of α-syn

In order to verify the results of the manual α-syn quantification approach shown in chapter 3.4.3.1, in a second analysis a threshold-based quantification in ImageJ was performed. The same six coronal brain sections were analyzed. At the injected hemisphere, monomer-injected animals showed no pS129-α-syn signal (Figure 42A).
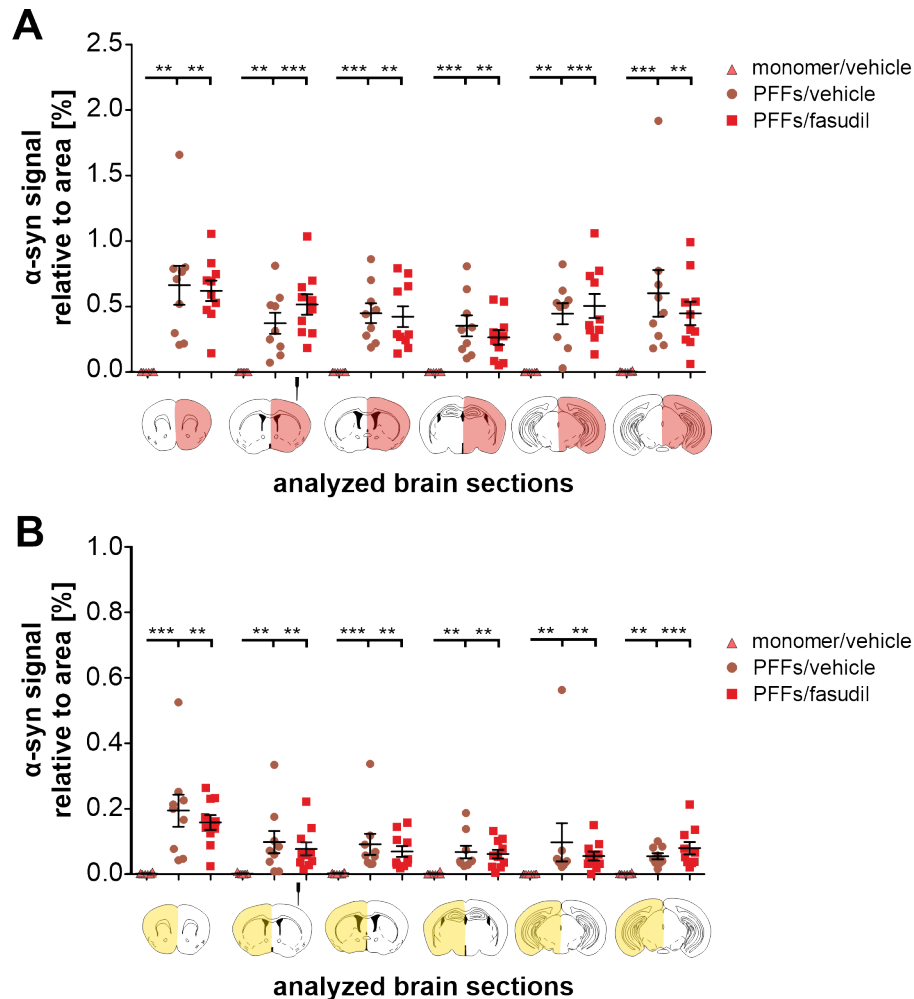
Figure 42. Threshold-based quantification of pS129-α-syn in brain sections of fasudil-treated mice. At 90 dpi, pS129-α-syn signal in brain sections of PFFs-injected and fasudil-treated mice was analyzed with the particle analysis tool of the software ImageJ. All six sections were selected based on the Paxinos mouse brain atlas (Paxinos and Franklin, 2003). Quantification of pS129-α-syn signal is shown in separate graphs representing either the **(A)** injected hemisphere or **(B)** the contralateral hemisphere. Scatter plots are used representing α-syn signal of each evaluated mouse per group (n = 8-10) separately for each analyzed brain section. No outliers were excluded from the analysis. It was defined that outliers were not removed, when the strong deviation only occurred in one hemisphere of the mouse brain section. Data are presented as mean ± SEM; Kruskal-Wallis test with Dunn's post hoc test.

In all sections, PFFs-injected animals (with and without fasudil) differed significantly from monomer-injected mice. Fasudil-treated mice did not significantly differ in their pS129-α-syn signal amount from mice without fasudil treatment (Kruskal-Wallis test with Dunn's post hoc test). Since for monomer-injected animals no pS129-α-syn-positive signal was expected, both PFFs groups were additionally analyzed with a Student's t-test showing no significant difference between the groups. Analyzing the contralateral hemisphere, also no significant differences between the PFFs groups were found (Figure 42B).

4   Discussion

Until today, the diagnosis of PD relies on the occurrence of specific motor symptoms that arise relatively late in the progression of the disease. Up to now, a prevention or cure of the disease is not possible. At the time of diagnosis, the pathomechanisms that mediate PD are quite progressed, including the degeneration of the majority of nigrostriatal projections and dopaminergic neurons within the SN. The current state of research is aware of many individual influencing factors such as LB formation and spreading or metal dyshomeostasis, even though the details of PD pathogenesis remain unclear. It is inconclusive if pathological alterations in the PD brain such as α-syn aggregation, metal dyshomeostasis, oxidative stress or mitochondrial dysfunction represent a cause or consequence of the disease.

One aim of the present work was to determine the distribution of iron and other elements in PD on a subcellular level. Therefore, in the first part of this doctoral thesis, elemental concentrations were analyzed in dopaminergic neurons of midbrain tissue from PD patients and controls using nanofocus XRF as a powerful technique to map and quantify trace elements simultaneously. The distribution of elements in two LBs was analyzed to reveal which elements were strongly correlated to α-syn pathology. Furthermore, the present work aimed to determine in more detail, if iron affects spreading of α-syn pathology in a mouse model of PD and secondly if the ROCK inhibitor fasudil has any therapeutic effects in the α-syn spreading paradigm. Iron is the most studied trace element in the context of PD and is already known to interact with α-syn, considered as one of the most relevant proteins for the pathogenesis of PD. Therefore, the second part of this doctoral thesis sheds light on the effect of iron on α-syn spreading pathology both *in vivo* and *in vitro*. Finally, in a therapeutic approach, the mouse model of α-syn PFFs injections was used to evaluate if α-syn spreading could be modified by ROCK inhibition by fasudil.

4.1   PD characteristics in postmortem midbrain tissue of patients

In previous studies, cerebrospinal fluid (CSF), serum or plasma samples of PD patients were used to analyze the quantities of iron and other trace elements in different biofluids demonstrating a dyshomeostasis of some elements in PD (Ahmed and Santosh, 2010; Gangania et al., 2017; Maass et al., 2018; Zhao et al., 2013). Differences in trace elemental content have been described even in hair samples of PD patients and controls

(Forte et al., 2005). Therefore, trace elements are considered as potential biomarkers for PD. In the present study, X-ray based techniques were used to gain further insight into the role of trace elements within the SN of PD patients (Joppe et al., 2020).

4.1.1 PD-related changes in trace element concentrations in neuromelanin-positive neurons

Since the main pathophysiological changes in PD take place within the SN, analyzing the dyshomeostasis of trace elements in neuromelanin-positive neurons within the SN is important.

Previous studies using X-ray-based techniques revealed significant differences in the accumulation of trace elements such as copper, iron or zinc in cell bodies within the SN from PD patients compared to controls (Carboni et al., 2017b; Davies et al., 2014; Szczerbowska-Boruchowska et al., 2012). In this work, we took advantage of the nanofocus beamline to measure more precisely absolute concentrations of trace elements within neuromelanin-positive neurons of SN tissue from PD patients and controls using XRF. Analyzing elemental concentrations on a single-cell level as a new approach, our analyses enabled to assess inter- and intraindividual differences (Joppe et al., 2020).

The current study was a follow-up study to a previously conducted measurement assessing elemental content in neuromelanin-positive neurons from one single PD and one CO patient (Carboni et al., 2017b). For a better reliability of the present study, the sample size and respective neuron count were increased and as mentioned above a higher magnification employing a nanofocus beamline was used to precisely determine element levels within cell bodies. A great advantage of using XRF as detection method is that tissue can be left in a native state for the analysis and it was able to detect in total 12 trace elements simultaneously: iron, manganese, copper, zinc, arsenic, selenium, bromine, calcium, potassium, chlorine, sulfur and phosphorus. Comparing the results of the present and the pilot study, the same PD-related trends were observed such as an increase of iron and zinc and a decrease of copper. However, even though the sample size was increased no significant differences were found in all measured trace elements. Only copper levels showed marginal significance, being lower in PD patients.

Copper is an important biometal in the brain. A corresponding dyshomeostasis of copper within the SN of PD patients has been already shown previously using inductively

coupled plasma spectroscopy (Dexter et al., 1991). More precisely, particle-induced X-ray emission (PIXE) and XRF analyses could verify the copper reduction in neuromelanin-positive neurons in the SN and showed same effects in the locus coeruleus of PD and incidental LB disease patients (Davies et al., 2014). The data of the present study demonstrated similar results for copper in nigral neurons. However, important variances of the data prevented the results to be significant on the 5 % level.

An essential conclusion from the XRF data presented here was that although we could reproduce known trends in bioelemental quantifications for iron, copper and other elements, the observed inter- and intraindividual differences were important. In contrast to bulk analyses performed previously, we can show that elemental dysregulation does not affect all neurons in the same extent. This is not only true on an individual patient level, but even neurons from one patient can show different bioelemental amounts.

Quantifying iron as the most described trace element in the context of PD, the present data could not verify the assumption of global iron enrichment in all nigral neurons of PD patients. This could also have implications for selective vulnerability of particular neuron groups. Analyzing the iron content in SN tissue with a microprobe mass analyzer, a study demonstrated a significant increase of the averaged iron signal in neuromelanin granules in PD patient tissue compared to tissue of controls (Good et al., 1992). Using X-ray based techniques, the aforementioned findings of an increased iron content in SN neurons could be verified (Davies et al., 2014). Both, measurements of single neuromelanin-positive neurons in SN using PIXE and XRF (Davies et al., 2014) as well as rapid-scanning XRF mapping of a whole section containing SN (Popescu et al., 2009), showed increased iron levels in PD samples. In the current study, we performed a local XRF analysis in neurons in the SN instead of averaging element concentrations over a wide part of the SN. This could be one reason for the high variance observed in our data. As a consequence of the high resolution, limiting the total imaging area, a further characterization of the scanned SN regions could not be conducted. It was not possible to determine if the measured cells were e.g. part of different nigrosomes.

Furthermore, the disease state seems to impact iron amounts. A study using quantitative susceptibility mapping (QSM) showed that in patients with advanced disease state significantly higher iron values in QSM were found compared to patient with mild progression or controls. These results presume that the further the disease progressed the

higher is the iron accumulation in the SN (An et al., 2018). Demonstrating higher iron levels in SNpc but lower iron serum levels in PD patients, a ratio of both iron levels in SNpc and in serum revealed a significant increase of iron in PD patients compared to controls (Costa-Mallen et al., 2017) . Thereby, the authors concluded that in PD patients nigral and blood iron levels go in dyshomeostasis assuming a causal relation of both findings (Costa-Mallen et al., 2017).

In addition to iron and copper as the most prominent PD-related trace elements, some studies already referred to dysregulated levels of selenium in PD patients. Accordingly, selenium was found to be significantly increased in blood plasma and CSF of patients (Maass et al., 2018; Zhao et al., 2013). Being an essential trace element in the brain, selenium is involved in neurogenesis modulation and the maintenance of redox balance or dynamics in mitochondria, but most interesting for PD is its antioxidant role (Cardoso et al., 2015). In the present study, selenium levels in neuromelanin-positive neurons of PD patients were tendentially reduced, however, the observed effect was influenced by strong interindividual differences. One study showed that a selenium-deficient diet could impact the vulnerability of dopaminergic neurons (Kim et al., 2000). This observation would fit the hypothesis of less selenium in dopaminergic neurons of PD patients. A recent epidemiological study analyzing soil compositions suggested a close relation of selenium to PD. They found that PD mortality significantly anticorrelated with selenium levels in geographical regions (Sun, 2018).

For arsenic, zinc and manganese, PD and CO samples in the present study showed relatively similar distributions. For zinc and manganese, this goes in line with the results of an ICP-MS analysis (Genoud et al., 2017). One study reported an opposing relationship of zinc and iron, meaning that in brain regions where increased iron levels are found zinc levels are often reduced. This effect is vice versa in other brain regions (Popescu et al., 2009). However, analyzing neuromelanin-positive neurons with PIXE, the zinc concentration did not significantly differ between the PD and control group (Davies et al., 2014). One study, conducted similarly to our experiment, detected significant concentration changes in nigral neurons of PD patients in sulfur, chlorine, iron, calcium and zinc. In the extracellular space they showed significant differences for phosphorus, sulfur, chlorine, rubidium, iron and zinc. However, the authors stated significance below the 10 % level ($p < 0.1$) (Szczerbowska-Boruchowska et al., 2012). Although significant differences were found in the aforementioned study, some trace element concentrations varied strongly

within the PD group (Szczerbowska-Boruchowska et al., 2012). These observations fit the intragroup variances demonstrated in the present study.

A suitable explanation for the detection of bromine showing high concentrations in single cells in the present analysis has not been found so far. Unlikely, the samples exhibited a contamination with bromine. The present results were in line with a published investigation showing also bromine in SN neurons with a high interindividual variance (Szczerbowska-Boruchowska et al., 2012). This high variance in bromine levels led to the speculation that some patients took occasionally medication that contained bromine. For example, the anti-anxiety agent bromazepam or the anti-Parkinsonian drug bromocriptine contain bromine. The latter one is an ergoline dopamine agonist widely used in the past to treat PD patients (Brooks, 2000; Guttman, 1997). However, the usage of these drugs has not been documented in the available medical records and thus cannot be proven neither excluded.

In a CSF-based study, samples of PD patients showed reduced values of lead, chromium, cobalt, iron, silicon and tin, whereat the strongest differences compared to CO patients were shown for lead and chromium (Alimonti et al., 2007). Analyzing brain tissue, in the present study these elements could not be detected with the exception of iron. The case that some studies detected different trace elements in their samples can partly be explained by the different detection methods used. Not all methods are equal in sensitivity and specificity. In one study, the elemental content was determined in SN tissue from healthy individuals without neuropathological findings using both PIXE and energy-dispersive X-ray spectroscopy (EDX). They detected iron, manganese, chromium and zinc with PIXE while EDX analyses could quantify iron, zinc, aluminum and silicon concentrations in tissue (Pánik et al., 2018). This indicates that in order to provide a complete elemental profile of PD it would be useful to combine different X-ray based methods in future studies.

Even though no significant differences in trace elements were found, the question arose if an unsupervised clustering approach could correctly identify samples of PD or CO patients based on the combination of trace elements. Merely, 65.5 % of the samples were classified correctly based on the concentrations from iron, zinc, copper, selenium, arsenic, manganese and bromine. In another study analyzing neurons in SN, concentrations of chlorine, iron, bromine, calcium and zinc were statistically significant to discriminate

samples from the two groups using a multiple discrimination analysis (Szczerbowska-Boruchowska et al., 2012). The latter study used a comparable sample size to the present study of four PD and four CO patients (4-10 cells each). In our case, the strong variance between the used samples prevented from replicating the previous literature.

One general issue of using tissue from patients of high age is that the medical histories of age-matched controls are quite heterogeneous, which could have significantly influenced the results. Three patients of the CO group were diagnosed with different kinds of cancer while one patient suffered from MS. It must be considered that MS is also a neurological disorder. In general, it is difficult to get brain samples from high age CO patients with a detailed medical record but without any clear pathology or at least without neurodegenerative pathology. The inclusion of different disease types in the CO group as well as the small sample size in the present study might explain the limited differences in trace element abundancies of PD and CO patients. In another study using a machine-learning algorithm for group discrimination, an elemental profile of selenium, iron, arsenic, nickel, magnesium and strontium was shown to discriminate CSF samples of the PD and CO group (Maass et al., 2018). Therefore, the elemental profile is possibly also dependent on the used biological source material (e.g. brain tissue, serum, plasma, CSF).

Taken together, our data resemble the results of previous studies analyzing elemental concentrations in neuromelanin-positive neurons, but our analyses did not reach statistical significance comparing PD and CO patients. One important reason is still the low sample size which is owed to a high time expenditure for XRF measurements with the used resolution and the restricted measurement time at the synchrotron. The novel single cell analysis in our study indicated that elemental concentrations are not necessarily similar between PD patients and could even strongly vary between neurons within the same patient. Nevertheless, these results are relevant indicating on the one hand that trace elemental changes could possibly be related to PD subtypes and on the other hand that particular neuron groups probably have a selective vulnerability for a dyshomeostasis of trace elements such as iron.

4.1.2   X-ray-based characterization of LBs and their elemental composition

LBs containing α-syn aggregates are one of the main hallmarks of PD. Here, LBs were identified in postmortem midbrain tissue sections from PD patients and analyzed with X-ray-based techniques in order to investigate these subcellular protein inclusions with a high

spatial resolution. XRD was used to noninvasively localize and characterize crystalline structures whereas XRF enabled an analysis of the elemental concentrations in LBs (Joppe et al., 2020).

First, the question if α-syn can be detected solely based on the XRD signal was investigated. In future experiments, this would enable an identification of α-syn-containing LB without any processing of the tissue. So far, α-syn-containing LBs always had to be visualized by immunohistochemical stainings (Spillantini et al., 1998), which possibly affects the elemental composition of the LBs due to the processing of the section like washing and staining. The XRD data did not conclusively show α-syn present in the LB, but as an indication it showed higher amounts of β-sheet proteins in the LB-defined ROI compared to β-sheet protein amounts in a neuron of a CO patient. Prospective XRD-based studies might shed light on the structural quality of LBs.

Further analyses aimed to determine the elemental content of LBs, since little is known about trace element abundancies and their distribution in LBs of PD patients, even if several studies suggest an interaction of α-syn with trace elements especially with iron. It has been shown that iron can bind to α-syn and that the binding affinity is even increased for phosphorylated α-syn (Binolfi et al., 2006; Lu et al., 2011; Peng et al., 2010b). Another study suggested that α-syn levels are regulated by iron due to its 5´-UTR, which shows a close homology to the IRE of the ferritin mRNA (Friedlich et al., 2007). Therefore, it is relevant to further investigate the interplay of iron and α-syn in the disease state. Due to the fact that iron, but also copper and manganese were found to foster α-syn aggregation as previously reviewed (Carboni and Lingor, 2015), accumulation of these elements in α-syn aggregate-containing LBs was conceivable. Using immunohistochemical stainings, it has been already shown that iron deposits overlap with LBs (Castellani et al., 2000). *In vitro* and *in vivo* it was demonstrated that arsenic fostered the accumulation of α-syn (Cholanians et al., 2016), thus it might also be overabundant in LBs. Regarding the possible role of selenium for LB pathology, previous studies indicated that selenoproteins as Selenoprotein P (Sepp1) or GPX4 were colocalized with LBs (Bellinger et al., 2011, 2012). This observation would argue for selenium enrichment in LBs.

To gain further insight into the elemental composition of LBs XRF analyses were conducted. In one LB, iron, zinc, manganese, selenium, arsenic and bromine were locally enriched, whereas copper was decreased in the middle of the LB. Since Naphthol As-BI

phosphate contains bromine and was added during the staining procedure of these sections, this could possibly explain strong bromine signal in the area of the LB. In a recent study, the elemental content was assessed in the olfactory bulb of patients with laser ablation-ICP-MS (LA-ICP-MS) and the colocalization of α-syn aggregates with trace elements was analyzed (Gardner et al., 2017). Thereto, LA-ICP-MS results had to be combined with immunohistochemically stained α-syn aggregates. The analyses showed decreased amounts of copper in α-syn aggregates confirming the results of the present study. Iron amounts were decreased in their analysis. An increase of zinc again was in line with the observation in the present study (Gardner et al., 2017).

The analysis of a second LB showed a different elemental composition. Only the absence of copper and the increase in bromine in the second LB were in accordance with the results of the first measured LB. Interestingly, the enrichment of iron could not be shown in the second LB.

Due to the above-mentioned studies showing a clustering of LBs and iron (Castellani et al., 2000) and a general affinity of iron to bind α-syn (Binolfi et al., 2006; Peng et al., 2010b) it was hypothesized that at least iron clustered in both measured LBs. However, *in vitro* experiments revealed that iron could also indirectly trigger the aggregation of α-syn (Levin et al., 2011; Li et al., 2011; Xiao et al., 2018) hypothesizing that both targets can impact each other not necessarily requiring cluster formation of iron and α-syn aggregates in LBs.

Taken together, the current data demonstrated for the first time trace element abundancies and their distribution in LBs using XRF with nanofocus resolution. The two measured LBs showed a heterogeneous elemental pattern. One possible explanation for this heterogeneity could be that two LBs of different developmental stages were measured. There is a possibility that both LBs are of different 'ages' and that accumulation of for example iron or selenium is dependent on the age of the LB. More analyses of individual LBs are needed to describe the variety of elemental profiles of LBs and to discuss the relevance of different trace elements for LB pathology. Regarding the XRD analysis, it was not possible to visualize explicitly crystalline structures of α-syn in the LB, but we were able to detect β-sheet protein amounts. It is assumed that α-syn does potentially not crystallize under the chosen conditions of the current experiment.

4.1.3   The role of cholesterol in midbrain tissue of PD patients

Using XRD, a previous study of our group revealed increased amounts of cholesterol crystals in one midbrain sample of a PD patient compared to one MS sample. Cholesterol was mainly located in the extracellular space and not within SN neurons (Carboni et al., 2017b). Since no statistical conclusion could be drawn from this analysis, we aimed to investigate cholesterol amounts in a bigger sample cohort, using lipid extraction and following GC-MS to quantify the cholesterol amounts in midbrain tissue.

In the present study, PD patients showed increased cholesterol levels in midbrain tissue reaching marginal statistical significance in comparison to CO samples. However, the interpretation of this data requires caution, as three samples of the CO group originated from cancer patients, whereas the majority of seven patients were diagnosed with MS. Therefore, it cannot be excluded that the observed cholesterol increase is biased by the overrepresentation of MS patients in the CO group. Little is known about cholesterol levels in the brain of MS patients so far, but other sample sources have been analyzed in some studies. In one study, plasma hydroxycholesterol levels increased in MS patients within five years of disease progression (Fellows Maxwell et al., 2019). Another study showed reduced levels of specific hydroxycholesterols in plasma for relapsing-remitting MS patients (Crick et al., 2017). In CSF, 25-hydroxycholesterol was increased for these patients whereas no difference was detected in cholesterol levels (Crick et al., 2017). In serum, total cholesterol and low density lipoprotein (LDL) cholesterol profiles were positively correlated with the disability status of MS patients (Ďurfinová et al., 2018). Even if no specific changes of cholesterol levels in the SN of MS patients are known so far, it must be kept in mind, that the heterogeneity in patients from the CO group (MS or cancer) could have influenced the output in the present study.

In contrast to our PD study, different studies investigated cholesterol levels in source material such as plasma or serum of PD patients. Studies investigating plasma levels of PD patients showed that higher levels of total or LDL cholesterol were possibly associated with a decreased risk to develop PD. Furthermore, higher plasma levels of LDL cholesterol led to a better motor function over time in PD patients (Huang et al., 2016; Sterling et al., 2016). High cholesterol levels in serum were also associated with a decreased risk for individuals to develop PD symptomatology and with a retardation of the clinical

progression of PD (Huang et al., 2011; De Lau et al., 2006; Rozani et al., 2018; Simon et al., 2007).

Inversely to blood and serum samples, in brain tissue of PD patients, increased cholesterol levels were found which confirms the data of the present study. One study investigated cholesterol content in the visual cortex as a region without LB pathology. Both, a lipidomics approach using liquid chromatography mass spectrometry as well as a validation with high performance liquid chromatography (HPLC), showed a significant increase of cholesterol in PD patients (Cheng et al., 2011). Oxysterols amounts were also increased. The authors therefore suggested an upregulation of the metabolism of cholesterol through oxysterols in the visual cortex and that this is probably related to selective expression changes in genes which play a role in lipid metabolism. Regions known to be affected by LB pathology in PD such as anterior cingulate cortex or amygdala did not show altered cholesterol amounts compared to controls (Cheng et al., 2011).

In contrast, another study showed that metabolites of oxidative cholesterol were increased in cortex tissue of DLB patients compared to controls (Bosco et al., 2006). The results of the present study of an increase in cholesterol amounts in brain regions of PD patients thereby go partially in line with the literature. Although an above-mentioned study could not relate cholesterol increase to α-syn pathology in tissue of PD patients, other investigations suggest a link of both targets. Based on the results of the present study, a relation of cholesterol and α-syn pathology was also conceivable, since the analyzed midbrain is commonly known to be affected by α-syn pathology as also mentioned in the previous chapter. In an *in vitro* model with SH-SY5Y cells overexpressing α-syn, cholesterol metabolites were also increased. The study further suggested that cholesterol accelerated the aggregation of α-syn (Bosco et al., 2006). In primary neurons, the linkage of cholesterol and α-syn aggregates was confirmed, showing that a cholesterol synthesis inhibitor reduced α-syn aggregation-induced damage of synapses (Bate and Williams, 2015). Furthermore, cholesterol was postulated to mediate the interaction of α-syn oligomers and charge-neutral membranes (van Maarschalkerweerd et al., 2015). In an MPTP model of PD, hypercholesterolemia fostered the degeneration of dopaminergic neurons in the midbrain of mice and led therefore to a worsening of PD pathology and symptomatology (Paul et al., 2017). A study in C. elegans reported that the neutral cholesterol ester hydrolase 1 (NCEH-1) attenuated the α-syn-dependent neurodegeneration (Zhang et al., 2017b). The results of most of the mentioned studies thereby lead to the

assumption that cholesterol interacts with α-syn, which fosters the aggregation of α-syn and supports α-syn-related neurodegeneration.

Taken together, our study reports a cholesterol increase in the SN of PD patients. It supports the literature on higher cholesterol levels in the brain of PD patients. Furthermore, not only trace elements, as described in the previous chapter, have been related to α-syn aggregation and pathology as a hallmark in PD, but also cholesterol has been shown to be linked with α-syn in previous literature. Due to the characteristic of α-syn being a common denominator for different possible targets in PD, the next chapters will exclusively address effects on α-syn pathology in mice *in vivo* and cortex neurons *in vitro*.

4.2 Iron-dependent modulation of α-syn spreading pathology *in vivo*

As mentioned in the previous chapter, a dyshomeostasis and relating thereto the enrichment of iron in PD has been reported in various studies using different biological sample sources from patients. Additionally, the positive effects of iron chelators on motor performance and iron levels in the SN, caudate nucleus and dentate nucleus of PD patients are evidence for a pertinent role of iron increase in the disease state of PD (Devos et al., 2014; Martin-Bastida et al., 2017). Using preclinical cell and animal models, various positive effects of iron chelators were verified. The treatment of rodents or primates with chelators as deferiprone (Carboni et al., 2017a), clioquinol (Billings et al., 2016; Finkelstein et al., 2016) or VK-28 (Mandel et al., 2004) or with the quinazolinone compound PBT434 (Finkelstein et al., 2017) prevented the accumulation of iron in SN, formation of nigral α-syn aggregates, loss of dopaminergic neurons in the SN and rescued motor as well as cognitive functions of the animals. Chelating iron in PD models therefore consistently improved the health status and demonstrated already that iron seems to affect the α-syn pathology in PD models. *In vitro* experiments verified that iron can bind to α-syn (Binolfi et al., 2006; Davies et al., 2011; Peng et al., 2010b) and facilitates its aggregation (Golts et al., 2002; Kostka et al., 2008; Levin et al., 2011; Uversky et al., 2001). Since these studies provide evidence for an interaction of iron and α-syn, the question arose if these interactions could also have an influence on the spreading of α-syn pathology in the brain.

In order to analyze the spreading pathology, the generation of α-syn PFFs and their injection into rodent brain regions such as striatum, SN or cortex are commonly used methods that are accurately described in literature provided protocols (Patterson et al.,

2019a; Polinski et al., 2018; Zhang et al., 2019a). To induce the iron brain load, mice were postnatally treated at p10 - p17 with different dosages of iron. The present iron intoxication model has also been used in several studies (Billings et al., 2016; Kaur et al., 2007; Peng et al., 2009, 2010a). In the present study, an intrastriatal injection of PFFs effected PFFs seeding which triggered α-syn propagation throughout the brain in the following weeks. Analyses demonstrated an iron-related reduction of pS129-α-syn amounts in the brain as well as a prevention of microglia accumulation in the injection site. Iron and α-syn treatment-related behavioral changes will be discussed first in the following chapter.

4.2.1 The influence of iron and α-syn on motor and cognitive behavior

In order to assess whether iron and α-syn PFFs treatment induced abnormalities in terms of cognitive or motor behavior of mice, the NOR and rotarod test were performed. The rotarod test is a commonly used behavioral test for PD animal models. Pure muscle strength, coordination skills and endurance belong to the abilities which are required to perform the rotarod test properly.

In the present study, iron and α-syn treatment did not influence the performance on the weekly implemented rotarod test over a time frame of 90 dpi. The results go in line with previous investigations showing no significant motor abnormalities for PFFs-injected animals at 90 dpi. Iron does not seem to accelerate an PFFs-induced motor dysfunction in mice. In a study using intrastriatal injections of 5 μg of the same protein as in the present study, also no effects of PFFs injections on the rotarod were observed at 90 dpi but on 180 dpi (Luk et al., 2012a). In another study, 10 μg PFFs were injected and led to a significant motor decline detected with the rotarod at three months post injection (Masuda-Suzukake et al., 2014). These data suggest a dose-dependent motor decline in regard to the amount of PFFs injected.

The mentioned studies used the wire hang test as an additional indicator for motor decline but showed inconsistent results. Whereas an intrastriatal injection of 5 μg PFFs showed significant differences in mice at 90 dpi (Luk et al., 2012a), a higher dosage (10 μg PFFs) did not lead to motor decline (Masuda-Suzukake et al., 2014). Furthermore, recent studies suggested that bilateral compared to unilateral injections of PFFs and the injection of shorter fibrils compared to long fibrils significantly influence the effect on motor behavior (Froula et al., 2019; Patterson et al., 2019b).

To conclude, in our selected setup, the result of an unchanged motor behavior for PFFs-injected mice at 90 dpi was as expected compared with a previous study. The literature suggests that longer time is needed for PFFs to impair motor behavior, which could be accelerated by the injection of higher PFFs dosages. Indeed, in this study the motor behavioral analysis was mainly performed to record concomitant effects of the treatment. The time frame of 90 dpi was selected, since at this time a well-advanced spreading of α-syn fibrils through the brain has been previously reported (Luk et al., 2012a), and the main focus of the present study was on influencing the α-syn spreading. For future investigations targeting the effect of PFFs on the motor function, bilateral injections and the control over the length of injected fibrils needs to be considered to seed PFFs more effectively in terms of their effect on motor decline.

Not much is known about direct effects of postnatal iron treatment on motor behavior. In one study, Sprague-Dawley rats were treated with 120 mg/kg bw iron between postnatal day 10 and 17. These rats did not show any abnormalities in motor behavior assessed by rotarod performance at 200 days of age (Chen et al., 2015). A53T mice treated with a low iron dosage (40 mg/kg bw) showed a reduced learning ability in the rotarod test but overall a stable motor performance (Carboni et al., 2017a). This effect on learning ability was not found in the present study using wild-type mice. Another study analyzing behavior of iron-treated NMRI mice (37 mg/kg body weight) showed alterations in spontaneous motor behavior (Fredriksson et al., 1999). The few found studies investigating motor behavior of iron-treated animals therefore deal with other mouse models or another species.

As a conclusion of the rotarod data, our results resemble the literature showing little evidence for motor abnormalities on the rotarod after neonatal iron treatment or α-syn PFF injections measured up to 90 dpi / 6 months of age. The accumulation of both treatments did also not result in a premature onset of motor decline compared to other studies. Thus, in the selected time frame, iron seems not to foster pathological effects of PFFs on brain regions important for the locomotor system such as the SN.

Regarding the effect of iron on cognitive performances, iron treatment has been shown to induce cognitive decline in terms of memory function in mice and rats (Fredriksson et al., 2000; de Lima et al., 2005b, 2005a, 2007; Schröder et al., 2001). Therefore, in the present study object recognition was analyzed in terms of STM and LTM using the NOR test. The NOR was performed twice – before α-syn PFFs injection and at

90 dpi. At three months of age (before α-syn injection), mice treated with the highest iron dosage showed an impaired LTM compared to the low iron dosage group. However, at six months of age (90 dpi), LTM impairment of iron-treated mice was absent. In turn, at 90 dpi, the PFFs injection significantly impaired LTM compared to the monomer injection of mice. The combination of iron and PFFs did not worsen the effect compared to PFFs-injected animals without iron treatment. At both measured time points, STM was not affected by the treatment conditions.

At three months of age, iron treatment of rats at postnatal days 12-14 showed similar effects of a cognitive impairment on LTM but absent consequences on STM (de Lima et al., 2007). Iron treatment of Wistar rats affected LTM independent on the postnatal period when iron was applied (postnatal days 5-7, 12-14, 19-21 or 30-32), however, measuring STM only rats treated with iron between p19-21 showed a significant decline in object recognition memory (de Lima et al., 2005b). These results indicate that the treatment time point significantly influences if iron affects STM. Accordingly, in the present study, STM of iron-treated mice was not affected because iron was applied too early (at p10-17). The reasons for iron-induced cognitive impairment are not fully resolved. It is assumed that oxidative stress in connection with iron overload could impair the cognitive function. Accordingly, lipid peroxidation and protein carbonylation were found within the hippocampus, cortex and SN post neonatal iron intoxication (Dal-Pizzol et al., 2001). The induction of oxidative stress and damage due to iron accumulation further supports cell death in neurodegenerative diseases (Zecca et al., 2004).

The present study showed for the first time cognitive decline due to intrastriatally seeded PFFs measured by the NOR at 90 dpi. A study using intracerebroventricular injections of α-syn showed that the injection of neither PFFs nor monomers but of oligomeric α-syn species induced a significant decline in LTM at 10-15 dpi (La Vitola et al., 2018). Concretely, small extracellular α-syn oligomers were found to disturb the synaptic plasticity, which could impair both the memory function and cognitive ability (Martin et al., 2012). Using the Y-maze test, intrastriatally PFFs-injected mice did not show any learning or memory decline at six months post injection (Luk et al., 2012a; Masuda-Suzukake et al., 2013). However, in a recent rat study combining viral vector mediated α-syn overexpression in prefrontal cortex with human α-syn PFFs inoculations into the striatum cognitive impairments were observed using the delayed matching to position (DMTP) test, the delayed nonmatching to position (DNMTP) test and the 5-choice serial

reaction time task (5-CSRTT) (Espa et al., 2019). Therefore, PFFs injections were shown to affect different cognitive functions measured by different tests. Whereas the present study plead for an LTM dysfunction in terms of object recognition, no deficits were found in working memory analyzing spontaneous alternation behavior in literature. Spatial and working memory were affected in models where α-syn injections were combined with α-syn overexpression.

Using the NOR test, the distance moved in the arena of iron- and α-syn-treated mice was also analyzed in the present study as a variable of general mobility. Before α-syn injection, in the LTM condition, mice with the highest iron dosage were running significantly less in the arena compared to mice from the other two iron conditions. It is assumed that this is rather a separate effect than a cause for less interest on the novel object of this mouse group. Since the duration at the novel object was recorded as main LTM variable, one would rather expect that mice which move less show LTM values distorted upwards in terms of the duration spent at the novel object.

Taken together, the present results showed that the highest iron dosage as well as α-syn PFFs seeding affected the LTM separately. Both targets together did not worsen the effect in the used model meaning that no interaction effect of both treatments was found. Comparing the present results with previous literature, the time point of the observation at 90 dpi could have been one major reason for the treatment-induced minor impairments observed in motor and cognitive behavior. Indeed, the behavioral analyses were mainly performed to record concomitant effects of the treatment. The focus was not necessarily on inducing motor or cognitive deficits. In general, available literature indicates that at the used measurement time points motor and cognitive decline seem to be test-specific, meaning that the test itself and its sensitivity also strongly influence the output. Possible reasons for the PFFs-induced cognitive decline are further discussed in chapter 4.2.3.

4.2.2 Quantification analyses of iron

Iron accumulation is an accompanying effect of aging which provides a possible explanation for an age-dependent susceptibility for neurodegenerative diseases (Ashraf et al., 2018). In PD, iron increase within the SN is widely reported. One explanation for iron accumulation in the SN is that neuromelanin which mainly occurs within the dopaminergic neurons in SN has a high affinity to bind iron. In PD samples, further iron deposits were found in brain regions as putamen and globus pallidus (Jellinger et al., 1990; Wang et al.,

2016; Ward et al., 2014). A recent MRI study with PD patients and controls analyzing the iron content in different brain regions showed an iron increase in the fascicula nigrale, globus pallidus, red nucleus, putamen, caudate nucleus and SN of PD patients (Chen et al., 2019).

To investigate the role of iron in neurodegeneration, models enriching brain iron in rodents were used to analyze iron effects in context of PD (Billings et al., 2016, 2019; Kaur et al., 2007) and other NDDs such as Huntington's disease (Agrawal et al., 2018; Berggren et al., 2015, 2016). The used protocol of treating mice postnatally over several days with carbonyl iron per gavage is a common model in PD research (Billings et al., 2016; Carboni et al., 2017a; Chen et al., 2015; Finkelstein et al., 2016, 2017; Kaur et al., 2007; Peng et al., 2009, 2010a; Schröder et al., 2001). The most commonly used treatment concentration of iron is our middle dosage of 120 mg/kg bw iron (Chen et al., 2015; Kaur et al., 2007; Peng et al., 2009, 2010a; Schröder et al., 2001). In the present study, dosages of 60 and 240 mg/kg iron were additionally tested to enrich iron content in the brain.

In order to proof that the used iron treatment method induced an enrichment within the mouse brain, the iron content in whole brains and nigral brain sections was analyzed.

First, the total iron content in whole mouse brains was measured by hyphenated ICP spectrometry. Since this analysis could not detect any differences in the iron amount, it was postulated that iron enrichment happened in small and specific brain regions. By that, an analysis including the whole brain mass and thereby the iron variance of many brain regions would average out the iron increase in a few specific iron enriched areas. This hypothesis corresponds perfectly to a recently published study quantifying iron content within the midbrain, caudate putamen, cerebellum and cortex of wild-type and A53T mice treated postnatally with iron. Only in the midbrain a significant difference between iron-treated and control mice were observed with ICP-MS. With LA-ICP-MS raster scanning of mouse brain sections they could further specify that the observed iron effect in the midbrain can be attributed to the strong iron increase within the SN (Billings et al., 2019).

Indeed, our XRF analysis of single sections of the SN showed higher amounts of nigral iron for iron-treated mice sacrificed at six months of age. Due to time restricted measurements at the synchrotron, only tissue from the 60 and 120 mg/kg iron groups could be measured and compared to control samples. Our observation goes in line with previous studies. An ICP-MS analysis performed at five months of age also demonstrated

significantly higher iron concentrations in SN tissue of iron-treated wild-type mice. Even higher iron concentrations were reached when A53T mice were neonatally treated with iron (Billings et al., 2016). Using the same iron treatment protocol as in the present study, at two months of age, iron-treated B6D2 mice showed a significant iron increase in SN tissue measured by ICP-MS and in sections measured with MRI (Kaur et al., 2007). In one study treating NMRI mice with an amount of iron which is even lower than the lowest dosage of the present study, they found an iron enrichment within the basal ganglia but not in the frontal cortex which was also analyzed at four months of age using AAS (Fredriksson et al., 1999).

Furthermore, studies used the model of iron enrichment to test iron chelator effects in the context of PD which showed predominantly positive effects on behavior, neuronal loss and nigral iron content of wild-type and A53T mice (Billings et al., 2016, 2019). One of these studies mentioned equal effects of clioquinol and L-DOPA treatment on nigral iron amounts, midbrain protein carbonyl levels and dopaminergic neuron counts in iron-treated wild-type mice (Billings et al., 2019).

Treatment with chelators showed also benefits in other PD models, in which mice were not treated with iron to induce an enrichment. In A53T mice, iron chelator (clioquinol) treatment without previous iron enrichment led to a reduced formation of α-syn aggregates, reduced cell loss as well as motor and cognitive decline, and prevented a reduction of dendritic spine density of spiny neurons in hippocampus and striatum (Finkelstein et al., 2016). Besides using the A53T mice to further link iron accumulation with PD pathology, MPTP toxicity models were used. Iron chelation was found to prevent MPTP-induced oxidative stress and neuronal cell loss (Kaur et al., 2003). In A53T mice, MPTP was shown to elevate the nigral iron levels. In the same study, the quinazolinone compound PBT434 reduced nigral iron levels and showed beneficial effects on nigral dopaminergic neuron loss, on nigral α-syn accumulation and on the motor decline after MPTP or 6-OHDA treatment (Finkelstein et al., 2017). These studies indicate that iron dyshomeostasis is related to other pathomechanisms in PD, highlighting its important role as a therapeutic target in PD.

Taken together, the mentioned studies as well as the results of the present analysis emphasize that iron intoxication models indeed elevate iron levels within the brain of rodents in specific brain regions. Combined approaches using iron chelators already

showed the efficacy in preventing effects of iron intoxication. Positive effects of iron chelators in A53T mice or in toxin-based PD models (e.g. MPTP treatment) further emphasized the link of iron with other PD pathomechanisms. The impact of iron on α-syn pathology in PD was previously investigated in terms of α-syn aggregation. The present study focusses on the effect of iron on α-syn spreading, which will be further discussed in the following chapters.

4.2.3   PFFs seeding in the brain and its effect on motor behavior and memory

Brain sections were analyzed at 90 dpi to assess quantitative and qualitative differences in the propagation behavior of α-syn fibrils. Previous rodent studies reported advanced PFFs-induced α-syn spreading at 90 dpi, however, the pathology extent depended on the concentration of PFFs-injected and on the genotype of the animals (Blumenstock et al., 2017; Kim et al., 2016; Luk et al., 2012b, 2012a; Shimozawa et al., 2017; Terada et al., 2018). The intrastriatal injection used in the present study is the most common method to seed α-syn PFFs in the brain but as recently reviewed there are also other models administering α-syn by gut injections, intraglossally, intramuscularly, intraperitoneally, through the sciatic nerve or as injections into the hippocampus, olfactory bulb or SN (Chung et al., 2019).

The first intent was to analyze if the PFFs-induced α-syn spreading pattern corresponds to the previous literature independent on the postnatal treatment (control or iron). The α-syn spreading pattern of the present study overlaps with affected brain regions in similar studies using intrastriatal PFFs injections of wild-type mice analyzed at 30 dpi, 60 dpi or 180 dpi. However, compared to studies with other injection sites, the affected brain regions differ (Chung et al., 2019). An experiment with similar settings as the present study detected same affected brain regions (Luk et al., 2012a). Both studies show a high involvement of cortical areas (cingulate, motor, insular, somatosensory, medial parietal association, temporal, visual, auditory ectorhinal, entorhinal and perirhinal cortex), amygdaloid nuclei (basal, lateral, central and intercalated amygdaloid nuclei) as well as a spreading to the SN and amygdalopiriform transition area (Luk et al., 2012a).

Even if other similar studies did not provide spreading maps, they confirmed that the ipsilateral striatum, SN, auditory cortex, amygdala and anterior cingulate cortex were affected by the PFFs-based propagation pathology (Kim et al., 2016; Terada et al., 2018) which resembles the data of the present study. A recent publication used intrastriatal PFFs

injections in mice to establish a network model. Therefore, the authors first quantitatively analyzed PFFs-induced spreading at 1, 3 and 6 months post injection (Henderson et al., 2019). The overall pattern of spreading at 3 months resemble the affected brain regions of the present data. The authors further paired the quantitative results with a network diffusion model integrating the anatomical connectivity and could show that PFFs spreading over time can be traced based on a synaptic connection network. Accordingly, this approach could demonstrate the vulnerability of regions to α-syn spreading. Henderson and colleagues identified the basolateral amygdala, rostral cortical regions and the piriform cortex as the most vulnerable regions in this model (Henderson et al., 2019), which were also affected in the present study.

In line with previous approaches, the current study could also show that the α-syn-affected regions are mostly anatomically interconnected. There is wide evidence that the striatum is innervated by the mainly affected brain regions such as the amygdala (Cho et al., 2013), motor cortex (McGeorge and Faull, 1989), the cingulate cortex (Kunishio and Haber, 1994), the somatosensory cortex (Wall et al., 2013), the insular cortex (Chikama et al., 1997), the ectorhinal cortex (Hunnicutt et al., 2016), the entorhinal cortex (Totterdell and Meredith, 1997), the perirhinal cortex (Hunnicutt et al., 2016), and the SN (Lynd-Balta and Haber, 1994). The spreading of α-syn to regions innervating the injection site are indicative for a retrograde transmission of α-syn fibrils as previously described (Paumier et al., 2015).

However, both anterograde and retrograde spreading of α-syn was documented in a model of intrastriatal injections of LB extracts in mice and monkeys (Recasens et al., 2014). Pathology of α-syn in regions innervated by the striatum (SNpr, entopeduncular nucleus or globus pallidus) would suggest an anterograde spreading. Interestingly, α-syn pathology was only found within the SNpr in our model but could not be verified in other mentioned brain regions of anterograde spreading. Indeed, this observation fits to the results of previous connectome analyses of α-syn spreading (Henderson et al., 2019; Mezias et al., 2020; Oliveira et al., 2019). All three studies reported a stronger propensity of α-syn to spread retrogradely. Mezias and colleagues observed that the spreading direction is shifting after time. They found that in the first months post injection retrograde spreading is predominant, but later than a post-injection period of nine months both propagation directions influenced the detected spreading pattern. It is supposed that the direction then further shifts to anterograde spreading. Since misfolded α-syn could have an influence on

the anterograde transport protein kinesin and on the retrograde transport protein dynein, the authors assume that this link could possibly be causative for the shift (Mezias et al., 2020). Henderson and colleagues investigated α-syn spreading at six months post injection as the longest time period and did not report such a shift (Henderson et al., 2019).

In order to get a more precise insight on α-syn spreading to regions anatomically connected to the injection site, a connectome-based analysis was performed using the Allen Brain Atlas connectivity platform (©2020 Allen Institute for Brain Science. Allen Mouse Brain Connectivity Atlas, available from: https://connectivity.brain-map.org/). The analysis highlighted that several anatomical connections were affected by α-syn spreading but it also revealed the vulnerability of many other brain regions. Connectome-specific and unspecific α-syn spreading differences between iron-treated and control animals are discussed in chapter 4.2.4. It is striking that not all anatomical connections were affected, and the affected ones showed unequal α-syn amounts. As an assumption, this could be related to the availability of different neuron types within different brain regions. The spreading pattern could be also dependent on transmitter-specific circuits. For example, according to the connectome the globus pallidus or thalamic nuclei as part of the GABAergic circuits of the basal ganglia should have been affected but they showed no α-syn pathology. Therefore, neurotransmitters could possibly be relevant for α-syn propagation pattern. One study suggested that the vulnerability of brain regions could be related to the count of neuronal projections between the areas and the projection length meaning that a higher count and shorter projections could increase the vulnerability. However, they also reported that some regions with a short length of projections were not affected by α-syn which again highlights that anatomical connectivity is important but not exclusively determining α-syn spreading pathology (Oliveira et al., 2019).

In the context of affected brain regions, the question arose, if the effect of PFFs on object recognition memory could be explained by the presence of α-syn aggregates within crucial brain regions. Indeed, the insular, perirhinal and prefrontal cortex were affected which can be associated to memory function. The insular cortex was found to play an important role for object recognition memory since its cholinergic activity contributes to the familiarization with a specific object (Bermudez-Rattoni et al., 2005). Another study mentioned both insular and perirhinal cortex as essential areas for the consolidation of familiar objects (Balderas et al., 2008). Furthermore, involvement of the ventromedial prefrontal cortex in consolidation and reconsolidation of object recognition memory was

shown in LTM (after 24 h) but not in STM (after 3 h) (Akirav and Maroun, 2006). In the rodent's brain, the different parts of the prefrontal cortex are not clearly defined. In the present study, pS129-α-syn signal was observed within the infralimbic, prelimbic and cingulate cortex. Whereas the cingulate cortex (area 1) is commonly known to be a part of the dorsomedial prefrontal cortex and the infralimbic cortex as part of the ventromedial cortex, the prelimbic cortex is inhomogeneously assigned to either the ventromedial or dorsomedial cortex (Laubach et al., 2018). Furthermore, it was shown that the LTM of object recognition is dependent on hippocampal integrity (Clarke et al., 2010). Interestingly, in our model, hippocampus was only rarely affected.

In STM, the entorhinal cortex was assigned to memory of object details and spatial locations (Suzuki et al., 1997). In the present study, no STM decline was found, although the entorhinal cortex was affected by α-syn pathology. However, motor deficits were also not observed even though strong α-syn pathology was present in the motor cortex and SN. One possible explanation for this observation is that at the timepoint of sacrifice the pyramidal tracts were not affected enough by α-syn aggregate pathology to induce motor deficits. Furthermore, a fundamental reason for motor deficits would be the degeneration of dopaminergic neurons inside the SN. However, PFFs-induced neurodegeneration in the SN was found to take place at later time points (Luk et al., 2012a; Paumier et al., 2015).

Figure 43 provides an overview on the above-mentioned brain regions which are associated with object recognition in LTM and STM conditions, and simultaneously recapitulates the α-syn pathology for each region of PFFs-injected mice either treated with iron or with vehicle. This depiction summarizes that the mentioned regions are affected by α-syn pathology, which could explain why PFFs-injected mice showed a cognitive decline in the NOR test at 90 dpi. In the NOR test, PFFs-injected mice did not perform different from each other when they were treated with either iron or vehicle. Nevertheless, pS129-α-syn pathology differences can be observed between both treatment groups. In several brain regions associated with object recognition, mice of the control group showed stronger pathology. These results suggest that the α-syn pathology in both groups exceeds a certain limit resulting in cognitive deficits, but pathology differences were not strong enough to observe different severity levels of cognitive decline.

Taken together, the current study demonstrated PFF-induced α-syn spreading to both, anatomically connected and other brain regions. Specific brain regions affected by α-syn pathology provide an explanation for PFFs-induced cognitive deficits.
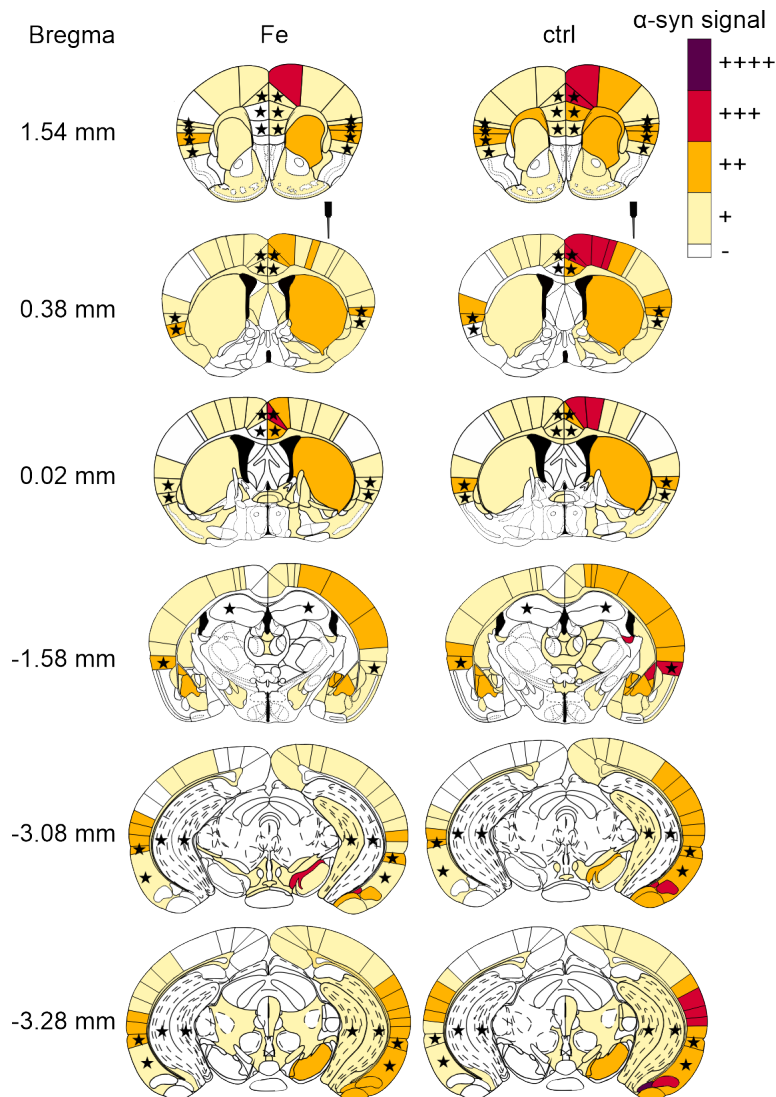
Figure 43. The detection of pS129-α-syn pathology in brain regions related to object recognition. This illustration represents the results shown in Figure 29 rating the pS129-α-syn signal amount per brain region by using a 5-stage-rating. Averaged results are shown for PFFs-injected mice treated with either iron or vehicle (ctrl). Black stars highlight brain areas which are associated with objection recognition as reported in previous literature (Akirav and Maroun, 2006; Balderas et al., 2008; Bermudez-Rattoni et al., 2005; Clarke et al., 2010; Laubach et al., 2018; Suzuki et al., 1997).

4.2.4 The influence of iron on α-syn spreading

Aiming to analyze if iron impacts the α-syn spreading pathology in the brain, postnatal iron treatment was combined with intrastriatal α-syn PFFs injections in mice. Due to the effects of iron on α-syn aggregation (Golts et al., 2002; Kostka et al., 2008; Uversky

et al., 2001), it was supposed that iron could lead to disease progression by enhancing PFFs-induced α-syn spreading.

Contrary to our expectations, the threshold-based pS129-α-syn quantification in whole brain sections revealed that higher iron amounts resulted in lower pS129-α-syn values. The PFFs group without iron treatment showed significantly more pS129-α-syn signal within the nigral brain section and within the averaged signal over all six sections compared to mice treated with the highest iron dosage.

These results raised the question how postnatal iron supplementation affects α-syn amounts in the brain. In PD patients, a colocalization of iron with LBs was shown (Castellani et al., 2000). Furthermore, it is known that iron can bind to α-syn (Binolfi et al., 2006; Peng et al., 2010b) and that this binding affinity was even increased when α-syn was phosphorylated at Y125 or S129 at the C-terminal region (Lu et al., 2011). One hypothesis explaining the present results could be that PFFs and iron clustered and spread differently than PFFs-induced spreading without iron treatment. In this context, it must be claimed that it is still not completely understood how α-syn strains spread from cell to cell, but there exist many suggestions.

The most prominent theory based on data from PFFs-injection studies is the axonal transport of α-syn fibrils. Spreading to anatomically connected regions assuming anterograde and retrograde transport as observed in the present study supports this hypothesis. *In vitro* studies also suggested the ability of PFFs to be intercellularly transmitted through a transsynaptic passage (Emmanouilidou and Vekrellis, 2016; Tran et al., 2014; Volpicelli-Daley et al., 2011). Another approach supports the hypothesis that pathological forms of α-syn are released from the cell through non-classical exocytosis (Jang et al., 2010; Lee et al., 2005). Furthermore, the results of other studies indicate an exosome-mediated transmission of a-syn from cell to cell (Alvarez-Erviti et al., 2011; Emmanouilidou et al., 2010; Xia et al., 2019) or an intercellular transfer through tunneling nanotubes (Abounit et al., 2016; Dieriks et al., 2017). However, it is also unknown if or how iron-α-syn-complexes could be transmitted from cell to cell or if iron impedes fibrils transmission such as the transsynaptic transport.

If iron would impede transsynaptic transport to neurons from interconnected brain regions, this would support the hypothesis that α-syn aggregates follow different spreading routes in iron-treatment conditions. In other words, iron could be involved in changing the

spreading pattern so that α-syn spreading followed other routes, passing regions not analyzed in our evaluation. The α-syn spreading maps should provide insight into what happened to the pS129-α-syn in iron conditions. Referring to the α-syn spreading maps, overall, the affected brain regions were similar between iron- and control-treated animals, varying in the amount of pS129-α-syn detected in the areas. Hypothesizing that iron probably changes spreading routes of α-syn, in some brain regions iron-treated animals showed more signal compared to the control group or showed small signal amounts in regions where control animals lacked any signal. The latter effect was predominantly seen at the contralateral hemisphere in regions such as cingulate cortex (area 2), piriform cortex, ventral pallidum, primary visual cortex, secondary visual cortex (lateral part) or retrosplenial granular cortex. Interestingly, the retrosplenial granular cortex serves as a hub for regions as e.g. cingulate cortex and visual cortex, which are therefore connected. All of these connected areas were found to be involved in processing of perceptions in terms of direction, location, landmarks and navigation of mammalian species (Mitchell et al., 2018). This spreading to different regions compared to the control condition indicates altered spreading routes in iron-treated animals.

On the one hand, the performed connectivity analysis of the present study further supports the idea of an iron-dependent pS129-α-syn redistribution pattern, since PFFs-injected mice treated with the highest iron dosage showed significantly less α-syn signal in regions anatomically connected to the injection site. In addition, in these mice a higher number of other, connectome-independent regions were α-syn-affected, however, this number was not significantly different from the number of regions affected in the control group. Iron-treated animals did also not show significantly more α-syn signal in other, connectome-independent brain regions. Therefore, on the other hand, these results support the idea that iron possibly contributes to a mechanism that degrades pS129-α-syn aggregates, as it will be further discussed in chapter 4.2.5. But as mentioned in the previous paragraph, it could also be that α-syn spreads to regions not analyzed in this study. Either way, the aforementioned results suggest that iron impacts the connectome-based α-syn spreading, even if the mechanism is not fully elucidated yet.

Iron-treated animals showed α-syn spreading differences in brain regions compared to control mice in all sectional planes so that an influence of iron on rather short or long axonal connections is unlikely from these results. A human study on adults reported that an intrastriatal enrichment of iron was associated with a decreased functional cross-talk of the

striatum to other resting-state networks including brain areas distant from striatum. Furthermore, a reduced intrinsic connectivity within the striatum was associated to a higher iron content and was particularly observed in the caudate network (Salami et al., 2018). A MRI-based study on PD patients and controls verified a possible negative correlation of nigral iron load and functional connectivity and suggested that a striatal interconnectivity dysfunction mediates this correlation (Guan et al., 2019). The results of both studies plead for a change in connectivity after iron intoxication in the present mouse model which could have affected α-syn propagation. Other hypotheses would be that iron accumulation could be possibly linked to demyelination which could influence the pathology, or that iron accumulation affects specific cell types such as glia cells important for the α-syn transport to specific brain regions.

An iron-dependent neuroinflammation which could influence pS129-α-syn spreading would be also conceivable. Microglia and T cell accumulation were analyzed to assess if iron influenced the migration or proliferation of both cell types. The results of an unexpected iron-induced prevention of microglia migration are further discussed in the next chapter.

4.2.5 The influence of iron on fibril-induced accumulation of immune cells

Neuroinflammation is a well-documented hallmark of different NDDs including PD. Neuroinflammatory mechanisms are known to be mediated by glia cells in terms of microgliosis and reactive astrogliosis or by the infiltration of peripheral immune cells such as T cells (Lee et al., 2010b; Wang et al., 2015a). As highlighted in the previous chapter, a prevention of α-syn spreading was observed in iron-treated animals. In order to investigate the hypothesis that iron affected α-syn spreading through an immune response, microglia accumulation and T cell infiltration into the injection site and SN were analyzed. These cell quantifications should enable to draw a conclusion on possible pathomechanisms.

First, striatal sections were immunolabeled with a CD11b marker. The CD11b marker recognizes microglia as the main phagocytic cells of the brain as well as peripheral macrophages. In the present model, the injection of α-syn PFFs induced a significant increase in CD11b+ cells within the striatum of PFFs-injected mice without iron treatment compared to monomer-treated animals. This accumulation of microglia could either be a result of microglia migration or proliferation. Interestingly, in iron-PFFs-treated animals this effect of increased microglia numbers was absent.

Previous studies showed that extracellularly available neuron-released α-syn species could activate microglial cells and mediate their migration (Kim et al., 2013; Lee et al., 2010a; Zhang et al., 2005). In the present study, we expected that extracellularly available PFFs after their injection would trigger microglia accumulation in the striatum. Another study investigated this process in more detail and showed that α-syn binds to the cell adhesion molecule Integrin α-M (CD11b) and induces microglia migration (Wang et al., 2015b). Accordingly, CD11b-binding of α-syn acting as a chemoattractant triggered the activation of NADPH oxidase 2 (Nox2) which induced H_2O_2 production. Afterwards, the Lyn kinase (SFK member) recognized H_2O_2-changes within the microglia and caused an actin filament rearrangement as well as directional microglia migration through phosphorylation of the F-actin–associated protein cortactin (Wang et al., 2015b). In other studies, it was in turn suggested that microglia migration triggered by α-syn was dependent on β1-integrin (Kim et al., 2014) and that a microglia-dependent increase in proliferation and cytokine production was impacted by an interaction of oligomeric α-syn and the Toll-like receptor 2 (Kim et al., 2013, 2014). Furthermore, a strong correlation of microglia density and α-syn density was shown. Accordingly, α-syn fibrils showed a higher density of α-syn than ribbons or oligomers so that fibrils increased the density of present microglia more than other α-syn species (Peelaerts et al., 2015). This result further explains why PFFs-injected animals in the present study showed significantly increased amounts of CD11b+ microglia in the injection site compared to monomer-injected mice.

In a study using intrastriatal PFFs injections similar to the present study, MHCII-positive microglia were quantified in brain regions of the injected rats. Within the striatum as injection site a microglia peak was reached at two months post injection. In the following two months the microglia amount decreased to normal levels. Interestingly, the observed microglia peak at two months almost resembled the peak of neuritic α-syn aggregates within the striatum, which however decreased in a slower rate (Duffy et al., 2018). Furthermore, in the α-syn-affected agranular insular cortex increased microglia amounts were found at two months post injection (Duffy et al., 2018). These results further plead for a α-syn-dependent microglia migration in the model used in our study. The mentioned study additionally showed that within the SN a significant increase of MHCII-positive microglia was found at 2, 4 and 5 months post injection but this effect was absent after 1, 3 and 6 months (Duffy et al., 2018). Confirming the mentioned study, in the present data no significant PFFs-related microglia difference was found within the SN at 90 dpi.

Even if the cited studies provide an explanation for the observed intrastriatal microglia increase in the PFFs group without iron treatment, the role of migrated or proliferated microglia within the injection site is not fully understood. Microglia were shown to be the major scavenger cells of α-syn aggregates. Hereby, the activation level of the present microglia is crucial to degrade α-syn and prevent its spreading (Lee et al., 2008). However, due to the conformational state of α-syn within the striatum in the present study, clearance mechanisms appear rather unlikely, as the phagocytic ability of the microglia is inhibited in the presence of higher aggregates (Choi et al., 2015; Park et al., 2008). Specifically, aggregated α-syn bound to FcγRIIB and induced an upregulated expression of FcγRIIB impeding microglia-mediated phagocytosis (Choi et al., 2015).

In the present study, PFFs-injected animals without iron treatment showed more PFFs-induced α-syn spreading and a significant increase of microglia in the injection site compared to iron-treated animals. These data rather support the hypothesis that migrating microglia in PFFs-injected mice without iron treatment facilitate α-syn spreading. This hypothesis is supported by a recent study showing that LPS-induced microglia activation in mice previously injected with a virus overexpressing α-syn enhanced α-syn spreading. After LPS-injection, stronger α-syn spreading to intrastriatally grafted dopaminergic neurons was shown. The authors further suggested that the activation state of microglia is highly influencing the α-syn spreading, since an IL-4 injection instead of LPS did not significantly increase α-syn transmission (George et al., 2019). In an MSA *in vitro* model, α-syn aggregates were also shown to be taken up by microglia-like cells. Starting from the uptake site, these cells carrying α-syn migrated to distal places and did not degrade α-syn. The authors therefore suggested that microglia could act as a transporter for α-syn (Valdinocci et al., 2018). This would further explain why α-syn spreading signal was not solely observed within brain regions anatomically associated to the connectome in the present study. Since microglia not necessarily travel along axons, it would be conceivable that microglia transport α-syn to brain regions which are not related to the connectome.

In a recent study, α-syn oligomers-containing-exosomes derived from PD patients were intrastriatally injected in mice, uptaken by microglial cells and triggered their activation. Same effects were shown *in vitro* using BV-2 cells. Since exosome-treated BV-2 cells exhibited increased amounts of accumulated α-syn, an augmented α-syn secretion into the extracellular space and a dysregulation of autophagy, the authors supposed that microglia are important for exosomal-related α-syn transmission (Xia et al., 2019). So far,

it is not clear by which underlying mechanism α-syn aggregates are uptaken in microglia. Of course, in the present study, injected fibrils in the extracellular space were not packed in exosomes so that the latter study deals with another uptake-mechanism. Nevertheless, fibrils could have been firstly taken up by neurons and could then have been released in exosomes as discussed in chapter 4.2.4. To conclude this part, it is assumed that the injected α-syn PFFs led to activation and migration of microglia which could be involved in the PFFs-induced α-syn spreading.

Iron-treated mice of the present study showed less microglia accumulation and less α-syn pathology. In the following I will discuss effects of iron on microglia and how this might be related to less α-syn spreading. In one study, effects of iron overload and its lysosomal iron transporter natural resistance-associated macrophage protein-1 (Nramp1) were investigated *in vivo* and *in vitro*. In conditions with functional Nramp1, iron-overload in mice and BV-2 cells facilitated microglia-mediated degradation of α-syn oligomers compared to the nonfunctional Nramp1 condition (Wu et al., 2017). This leads to the assumption, that iron pre-conditioning could be involved in α-syn degradation in the present study.

Another study showed that iron overload enhanced pro-inflammatory responses such as cytokine release of IL-1β and TNFα in microglia activated by LPS or MPP+ (Wang et al., 2013). This leads to the hypothesis that an induced inflammation fostered the degradation of α-syn aggregates in the present study. Accordingly, in one study, mice received an intraventricular injection of recombinant adeno-associated virus mediated expression of Interleukin (IL)-6 and additionally an intrahippocampal injection of α-syn fibrils. The results showed that inflammatory pre-conditioning of mouse brains reduced the α-syn pathology mediated by the injection of α-syn fibrils (Koller et al., 2017). Also in preclinical AD models, triggered inflammation was shown to attenuate the proteinopathy (Herber et al., 2007; Shaftel et al., 2007). Thus, it is conceivable that iron pre-conditioning could provoke similar effects on α-syn pathology. However, it is still unknown if iron overload itself provokes inflammation in the brain. Another study reported that classical activation of microglia impaired microglia migration (Lively and Schlichter, 2013). Therefore, it is supposed that iron overload led to an impairment of microglia and their migration and to an inflammatory pre-conditioning, causing less α-syn fibrils pathology and spreading. However, these hypotheses need to be confirmed in further studies.

In another experiment, the presence of T cells in the striatum and SN were analyzed. It is known from MPTP mouse models of PD that CD4+ and CD8+ T cells infiltrate the brain and especially the SN (Brochard et al., 2009; González et al., 2013; Kurkowska-Jastrzebska et al., 1999). Against the expectations, in the present study, no significant intergroup differences in T cell amounts within the striatum or the SN were observed. Based on the literature, an increase of T cells would be expected in PFFs-treated animals. In a study by Harms and colleagues short α-syn fibrils were not only able to activate and recruit microglia but also peripheral cells as monocytes, macrophages and lymphocytes (Harms et al., 2017). Specifically, 8 weeks post α-syn PFFs injection into the SN of rats a significant T cell infiltration as well as monocytes/macrophages infiltration was observed within the SN. However, microglia amounts did not increase within the injection site (Harms et al., 2017). In comparison to the present study, Harms and colleagues used a higher α-syn dosage (8 µg), a different injection site (SN), different animal species (rats) and an earlier time point of analysis (8 weeks post injection). Especially the latter mismatch could explain the different output in our study. Probably the acute immune response of T cells occurred earlier, and the analysis time point in our study was therefore too late to detect an infiltration. Another study made aware that the response of T cells could differ regarding different species of α-syn (monomer, nitrated, fibrillar). This means that changes in conformational stages of α-syn probably influence the type of T cell response during disease progression. An α-syn variant specificity of the response of CD4-positive T cells was recently shown, indicating the strongest CD4+ T cell infiltration into the brain after fibril treatment (Olesen et al., 2018). However, the authors injected α-syn (2×100 µg) subcutaneously in mice so that the method strongly differs from the method used in the present study which could also explain the different findings.

4.2.6 Limitations and outlook of the α-syn spreading model

In order to analyze the contribution of iron to PFFs-induced α-syn spreading, well-established and published methods were used as discussed in previous chapters. However, one general issue of PFFs injections into the brain is the possibility of PFFs reflux into the injection channel. Even if the needle was always left in place for another 4 min after the intrastriatal injection to avoid reflux, it must be considered that some PFFs were probably taken up by the motor cortex as part of the injection channel. Therefore, the interpretation of strong α-syn signal inside the motor cortex requires careful consideration of the

possibility that this is not necessarily a result of anterograde/retrograde spreading but might be caused by reflux during the injection.

The present study and its analysis methods provide a comprehensive insight into iron-dependent effects on α-syn spreading but spreading routes could not be holistically tracked. Thus, it is not clear if iron induced a degeneration or redistribution of α-syn aggregates. In order to complete our data in future studies, light sheet microscopy coupled with brain clearing methods (Becker et al., 2012; Costantini et al., 2015; Qi et al., 2019) will be the striking approach to-be for α-syn propagation experiments, answering the question of the iron's role in PFFs-induced α-syn spreading. However, so far, no studies are available using this technique to track α-syn spreading.

The comparison of α-syn spreading maps to the connectome already showed that iron reduced α-syn spreading to anatomically connected regions. Furthermore, several brain regions were affected in PFFs-injected mice treated with either iron or vehicle which did not resemble the connectome. Even if this could be a hint for different involved α-syn propagation mechanisms, another reason could be that the used connectome does not fully fit to the injection site in the present model. The connectome maps were generated based on two injection experiments of the Allen Mouse Brain Connectivity Atlas (©2020 Allen Institute for Brain Science. Allen Mouse Brain Connectivity Atlas) with injection sites fitting to the radius of our injection site. However, they injected much less volume and the injections were therefore much more specific. Even if the connectome maps of both experiments were combined, the injection site of the present study is not fully represented so that possibly more brain regions could belong to the connectome than described. Therefore, the connectome of the present injection site needs further investigation to fully define the effect of iron in the present model.

Moreover, in further studies iron accumulation in different brain sections should be mapped and overlaid with pS129-α-syn signal in the brain. This analysis would help to answer the question if iron and α-syn cluster together in the brain. Comparing the present α-syn spreading results with iron distribution maps shown in different publications (Billings et al., 2019; Morello et al., 2009; Zumbrennen-Bullough et al., 2014) can already provide insights on the effects of iron on α-syn spreading. Providing iron maps of coronal brain sections of untreated wild-type mice, studies reported predominant iron accumulation in the SN and basal ganglia especially in the globus pallidus as well as within the caudate-

putamen nucleus (Morello et al., 2009; Zumbrennen-Bullough et al., 2014). Indeed, in the SNpc the present α-syn analysis showed more α-syn signal in iron-treated mice compared to the control group. However, this pathology difference was only observed in one of the two measured nigral sections at the injected hemisphere and was not statistically significant. Regarding the iron availability in the globus pallidus and caudate-putamen nucleus, one sectional plane used in the present study resembled the sections used in above-mentioned studies (Bregma -1.58 mm). In these brain regions, the iron group did not differ in α-syn signal from the control group.

In a mouse study with a postnatal, oral iron treatment of mice between p10-17 which are comparable conditions to the present study, the distribution of iron deposits was illustrated in one nigral sectional plane for one vehicle- and one iron-treated mouse (Billings et al., 2019). Taking a closer look at these maps, the iron-intoxicated brain section showed in general more iron and a specific enrichment in parts such as the hippocampus and cortical regions. Most interestingly, there was a strong iron accumulation in the area where the entorhinal cortex, the amygdalopiriform transition area, the amygdalohippocampal area and the posteromedial cortical amygdaloid nucleus are located (Billings et al., 2019). In these regions, strong α-syn pathology could be observed in the present study, but the control group showed either more or equal α-syn amounts in these regions compared to the iron group. Thus, it is assumed that α-syn is rather not increased in regions with enriched iron accumulation. This could support the hypothesis that iron does not cluster with α-syn aggregates in this disease model but rather effects α-syn pathology indirectly for example by affecting the microglia accumulation as discussed in chapter 4.2.5.

4.3 The effect of iron on α-syn spreading in cortical neurons

After demonstrating the effect of iron on α-syn spreading in the brain of C57BL/6J mice, the present analysis aimed to elucidate if iron would influence spreading of seeded α-syn PFFs *in vitro* using cortical neurons. Therefore, cells in one compartment of a microfluidic chamber were treated with iron and α-syn PFFs. The transport of pS129-α-syn to the secondary cell compartment was analyzed. In cells treated with iron, no significant changes of the pS129-α-syn transmission to cells in the secondary cell compartment were observed compared to the transmission in vehicle-treated cells.

The usage of microfluidic chambers to track the intracellular propagation of α-syn fibrils from one compartment to the other is a common model. Both, anterograde and retrograde propagation has been confirmed seeding PFFs either to the soma or the neurites, respectively (Volpicelli-Daley et al., 2011). Transmission of α-syn fibrils to second order neurons has also been described in the same device (Freundt et al., 2012). In another study, intercellular propagation was further investigated with a microfluidic device existing of three successive cell-containing chambers. This model showed α-syn aggregate arrival in the third chamber at 14 days post PFFs seeding (Tran et al., 2014). The mentioned studies showed that the microfluidic chamber itself is a practicable device to analyze α-syn propagation. In general, the present data could also verify α-syn fibrils propagation to the secondary cell compartment. Iron likely affects transmission mechanisms of α-syn which cannot be reproduced to a full extent with this setup.

As already discussed in chapter 4.2.4, the literature mentions several mechanisms underlying α-syn transmission from cell to cell such as axonal transport and transsynaptic transmission, nonclassical exocytosis, exosome-mediated transmission or tunneling nanotubes. One microfluidic chamber experiment suggested that synapses were not required to transmit fibrils to second-order neurons, since α-syn was already transmitted to these neurons at a time point when synapses have not been formed (Freundt et al., 2012).

Discussing contributory factors and circumstances of α-syn uptake and transport, a study using primary neurons revealed that the internalization of misfolded α-syn was associated with lysosomal processing. A dysfunctional lysosomal integrity was suggested to accelerate the transmission of α-syn (Karpowicz et al., 2017). Another study showed that lymphocyte-activation gene 3 (LAG3) bound to pathologic α-syn and thereby initiated its transmission and toxicity. Specifically, LAG3 was involved in the endocytosis of exogeneous α-syn fibrils (Mao et al., 2016). Furthermore, the internalization, fibrillation and propagation of α-syn was suggested to be mediated by members of the syndecan (SDC) family, especially by SDC3 (Hudák et al., 2019). Even if the ability of iron to foster α-syn aggregation has been extensively studied as discussed in the previous chapters, little is known about its possible effects on the above-mentioned mechanisms of α-syn propagation.

In one study, oligomers were generated by applying iron and an organic solvent to α-syn. These oligomers were found to improve synaptic transmission mediated by the AMPA-receptor but they did not enhance the NMDA receptor-mediated transmission (Hüls

et al., 2011). Therefore, iron possibly impacts α-syn spreading indirectly by helping to generate specific α-syn conformations that were more prone to spread compared to the PFFs used in the present study. This could further explain why an iron-related effect on α-syn spreading was found in our *in vivo* model but not in the *in vitro* model. In the mouse brain, injected recombinant PFFs function as seeds and trigger aggregation and spreading of these aggregates throughout the brain. Iron could affect the α-syn aggregation and these aggregates are possibly prone to spread differently, which would support an iron-dependent redistribution of α-syn. Different spreading pattern cannot be investigated in the used microfluidic chamber model, but it can be assumed from the results that iron does not affect the uptake of the recombinant PFFs applied to the somata of neurons and their spreading.

Furthermore, a recent publication using SN4741 cells showed that iron promoted α-syn aggregation indirectly by decreasing the expression of TFEB. TFEB functions as transcriptional regulator of the autophagosome-lysosome pathway. Thereby, the TFEB-mediated autophagosome-lysosome fusion was inhibited resulting in enhanced α-syn aggregation. In addition, the authors showed that cell-to-cell transmission of α-syn was also enhanced by iron enrichment, whereas TFEB overexpression attenuated this effect (Xiao et al., 2018). They further speculated that iron could foster a lysosomal dysfunction by TFEB-mediation, leading to an increased α-syn release via exosomes. The effect of lysosomal dysfunction on α-syn exosomal release and transmission has already been shown (Alvarez-Erviti et al., 2011). One study is interesting in this context of α-syn pathology that investigated another trace element: Mn^{2+} has also been shown to trigger the secretion of misfolded α-syn in exosomal vesicles (Harischandra et al., 2019). Therefore, it is possible that iron only affects one particular mechanism of transmission depending on the applied α-syn conformation. The microfluidic chamber model in the present study rather investigates axonal transport and transmission so that this model is probably not sensitive enough to investigate iron-affected mechanisms of α-syn fibrils spreading. Further experiments should also test if alterations in parameters as time point and duration of iron treatment or its dosage would change the output of this experiment.

In regard to the *in vivo* study discussed in chapter 4.2 iron-related changes on α-syn spreading were supposed to be mediated through its effect on microglia. Accordingly, microglia could facilitate the spreading of α-syn. Since in the *in vitro* experiment only neurons were investigated, this could provide an explanation for absent iron-dependent changes in the spreading pathology. It could therefore be possible that iron rather impacts

α-syn uptake or transmission to other cell types such as microglia. In the context of exosomal release, one study suggested that microglia probably support α-syn transmission via exosomes. In their experiment, BV-2 cells were treated with exosomes containing oligomeric α-syn derived from PD patients. This treatment triggered an inhibition of autophagy, an intracellular accumulation of α-syn in the microglia as well as accelerated secretion of the protein suggesting a crucial role of microglia in the exosomal-mediated transmission (Xia et al., 2019).

Of course, *in vitro* experiments do not fully mimic the circumstances as present in brains, simply due to the complexity of the brain e.g. with its diversity of cell types and its connectivity. The possibility that iron affects rather α-syn spreading to other cell types or affects α-syn propagation indirectly through its effects on glia cells as discussed in chapter 4.2.5 provide explanations why no difference on α-syn spreading was found in iron-treated cortical neuron cultures. Therefore, further studies are needed, investigating the effect of iron on α-syn spreading in different cells types as microglia or mixed cultures to unravel which mechanism was responsible for the modulation of α-syn spreading in iron-treated mice.

4.4   Therapeutic approach: the influence of fasudil on α-syn spreading

Up till now, prevention or cure of PD is impossible so that therapeutic investigations are needed to reveal new target mechanisms and test the effectiveness of possible drugs. In NDDs, the signaling pathway of ROCK has been described as an interesting target. As recently reviewed, ROCK is involved in several cellular processes of NDDs such as autophagy, synaptic dysfunction or degeneration of axons (Koch et al., 2018). The ROCK inhibitor fasudil is a drug approved to treat sub-arachnoid hemorrhage-induced vasospasms in clinical use (Suzuki et al., 2007, 2008). In context of neurodegeneration, fasudil gained especially attention for its beneficial effects on animal- and cell-based ALS models (Günther et al., 2017; Tönges et al., 2014). Therefore, a multicenter clinical phase IIa trial is currently investigating disease-modifying effects of fasudil treatment in ALS patients (Lingor et al., 2019). Furthermore, the interest arose to analyze the effect of fasudil in PD due to the ability of fasudil to bind α-syn and its attenuating effects on e.g. α-syn aggregation or cell loss in toxin-based or α-syn mutation-based PD models (He et al., 2016; Li et al., 2017; Tatenhorst et al., 2016; Tönges et al., 2012; Zhang et al., 2019b; Zhao et al., 2015). Since the distribution of α-syn-containing LBs in the brain is the major characteristic

of PD pathology besides the degeneration of dopaminergic neuron in the SN, the current study aimed at preventing α-syn fibrils spreading through the brain of PFF-injected mice.

First, possible side effects of the α-syn PFFs injections were ruled out by investigating motor function of the mice and neuronal loss in the SN at 90 dpi. In the present study, mice injected with PFFs behaved similar to monomer-injected animals on the rotarod, irrespective of whether they were treated with fasudil or not. As extensively discussed in chapter 4.2.1, in the used conditions, an inconspicuous motor performance of PFFs-injected mice was expected based on the existing literature (Luk et al., 2012a). Previous studies did not report negative effects of fasudil treatment on motor behavior of mice (Tatenhorst et al., 2016; Tönges et al., 2014) so that unaltered motor behavior of these mice was expected.

Second, it was analyzed if PFFs injections induced neurotoxic effects at 90 dpi in form of neuronal loss within the SN as a brain region directly connected to the injection site. One study already showed that fasudil treatment in an MPTP mouse model of PD could rescue dopaminergic neurons in the SN from degeneration (Tönges et al., 2012). In a 6-OHDA model, fasudil treatment was not sufficient enough to prevent dopaminergic cell loss (Tatenhorst et al., 2014). In the present analysis, PFFs injections did not lead to a significant cell loss at 90 dpi compared to monomer-injected mice. Accordingly, PFFs-injected animals with additional fasudil treatment showed similar cell amounts as monomer-injected animals. This observation goes in line with the literature showing that neuronal loss in the SN of PFFs-treated rodents occurred at later time points, such as 180 dpi (Luk et al., 2012a; Paumier et al., 2015). Thereby, it has been ensured that α-syn spreading could not have been massively influenced by neurodegeneration mechanism at the timepoint of analysis.

With two quantification methods, it was shown that fasudil did not prevent PFFs-induced α-syn spreading through the brain. The pS129-α-syn pathology was similar in fasudil-treated PFFs-injected mice compared to PFFs-injected mice with vehicle-treatment. These results were against the expectations, since a previous study already showed a close link of fasudil to α-syn pathology. The authors observed that fasudil could bind to tyrosine residues Y133 and Y136 in the C-terminal region of α-syn and led to a reduction of α-syn aggregation *in vitro*. In A53T mice, fasudil treatment resulted in less motor and cognitive decline and in less α-syn aggregation in the midbrain of A53T animals (Tatenhorst et al.,

2016). Furthermore, using a model of tauopathy, fasudil treatment of Drosophila reduced tau pathology by an enhancement of autophagy (Gentry et al., 2016).

It may be that fasudil does not target the recombinant PFFs used in the present model. The aforementioned PD study reporting beneficial fasudil effects used a transgenic mouse model (Tatenhorst et al., 2016) so that the experimental conditions as well as the seeding mechanism could differ to the present study. Nigral injections of different α-syn strains in the rat brain showed differences in the efficiency of seeding and spreading of α-syn dependent on the used pathogenic α-syn strains such as fibrils, ribbons or oligomers (Peelaerts et al., 2015). It is possible that fasudil does not target the recombinant PFFs used in the present work but would have an influence on seeding or spreading of other α-syn strains. Furthermore, the fasudil dosage used in the present study was taken over from another experiment (Tatenhorst et al., 2016) but could be a too low-dosed treatment in this acute model of an immense PFFs seeding in the brain.

Assuming a main transsynaptic transmission of fibrils, we supposed that fasudil likely affects the spreading pathology via synapses. The role of ROCK activity in synaptic function has been described in different studies (Koch et al., 2018). Furthermore, the inhibition of ROCK is already known to enhance the size of the postsynaptic density, alter the morphology of dendritic spines, and trigger long-term potentiation (Nakayama et al., 2000; Swanger et al., 2015). The fact that no differences in spreading pathology were found could entail that α-syn fibrils are differently transmitted or fasudil is not able to stop α-syn transmission via synapses.

Bringing together the present result with the iron PFFs *in vivo* study discussed in chapter 4.2, another reason to assume spreading prevention by fasudil was its known attenuating effects on inflammatory responses (Scheiblich and Bicker, 2017). The possible contribution of microglia on α-syn propagation has been extensively discussed in chapter 4.2.5. In that chapter, it was also assumed that the beneficial influence of iron on spreading resulted from its attenuating effect on microglia accumulation in the injection site, which has to be further investigated. In the context of fasudil, an anti-inflammatory effect was assumed, which could prevent PFFs-induced microglia migration and the contribution of microglia in α-syn spreading. Accordingly, in several PD rodent studies, predominantly using the MPTP-intoxication model, fasudil or other ROCK inhibitors were shown to inhibit the inflammatory response, e.g. in terms of microglia accumulation or activation

(Barcia et al., 2012; He et al., 2016; Li et al., 2017; Zhao et al., 2015). These inhibitory effects of fasudil on inflammation have also been described in studies analyzing fasudil in context of MS (Guo et al., 2014, 2019; Wang et al., 2019). In an AD model, rats were intracerebroventricularly injected with $A\beta_{1-42}$. Treatment with fasudil reduced $A\beta$-induced neurodegeneration in the hippocampus. The prevention of the neurodegeneration was also linked to a fasudil-depending suppression of the inflammatory response, such as microglia activation and proliferation (Song et al., 2013). If microglia play a crucial role in the α-syn propagation, we would have expected a significantly reduced α-syn spreading after treatment with the ROCK-inhibitor fasudil. The application method could provide a possible reason why fasudil did not mitigate the severity of the α-syn pathology in the present study. The administered dosage in the literature (20-40 mg/kg bw) investigating inflammatory responses in PD models was always similar to the dosage applied in the current study (30 mg/kg bw). However, in the present study fasudil was applied via drinking water whereas the above-mentioned studies used a daily intraperitoneal injection of fasudil (He et al., 2016; Li et al., 2017; Zhao et al., 2015). These methodological differences might also explain the lack of an effect of fasudil treatment on α-syn spreading in our study.

Taken together, it was assumed that fasudil treatment affects α-syn spreading due to its inhibitory effects on the synapse-related ROCK and its attenuating effects on the inflammatory response. In contrast, fasudil supplementation via drinking water did not alter α-syn spreading in PFFs-injected mice in the present analysis. On the one hand, the applied dosage of α-syn PFFs was probably too high or the dosage of fasudil too low to affect the α-syn spreading appropriately. On the other hand, the effect of fasudil could be α-syn species dependent, which would include the hypothesis that fasudil did not target the applied PFFs in our model. Within the scope of the doctoral thesis, effects of fasudil on inflammation and transsynaptic α-syn transmission could not be proven and need further investigation.

5 Concluding remarks

The experiments conducted within the scope of this doctoral thesis highlight α-syn pathology in PD as the major interface for known pathomechanisms and possible triggers of PD. The propagation of α-syn is a major hallmark in PD. Thus, investigating the relation of α-syn spreading with targets known to affect α-syn aggregation is an auspicious way to explore underlying pathomechanisms of disease progression, contributing to the development of new therapeutic strategies for PD patients.

For the first time, a combination of X-ray techniques and an immunohistochemical staining allowed the visualization of trace elements as well as the detection of β-sheet rich structures in two nigral LBs of tissue from PD patients. Further experiments need to assess whether LBs present a sub-stratified elemental profile. Measurements of trace element concentrations in nigral neurons of PD-diagnosed end-stage patients revealed strong intra- and interindividual differences which argue for different subgroups of disease rather than a homogeneous pathology. Copper was identified as the most discriminating element comparing PD and control tissue. The present results highlight the strong variance of human samples which prevents to detect PD-relevant pathogenic trace element alterations in small sample sizes as feasible in synchrotron-based studies. In a side project using lipid extraction, a higher sample size was used to assess the role of cholesterol in PD, validating a cholesterol increase in PD samples.

Since iron is the main described trace element in context of PD and related to α-syn aggregation, we were interested in analyzing its influence on α-syn spreading. In an acute mouse model of postnatal iron intoxication and intrastriatal α-syn PFFs injections, high-dosed iron treatment modulated α-syn spreading and additionally suppressed the accumulation of microglia in the striatum. Our data indicate that microglia probably accumulate in the injection site to support α-syn spreading and that iron attenuates this microglia-mediated spreading. Our results lead to the hypothesis that iron either supports a redistribution of α-syn aggregate spreading in the brain or mediates indirectly α-syn aggregate degradation. Both, iron and PFFs treatment, affected LTM at different time points, underscoring its relevance for pathogenesis.

In vitro, microfluidic chambers were shown as a useful model to investigate α-syn PFFs spreading from cortical cells of one compartment to the other. However, this model

was not able to reproduce our *in vivo* data regarding an iron-dependent modulation of α-syn spreading. This suggests, that other cell types, e.g. microglia, are involved in iron-mediated effects, which were not studied in the present microfluidic chamber model.

Finally, we analyzed if ROCK inhibition through an oral fasudil administration attenuated α-syn spreading. No side effects of PFFs or fasudil treatment in form of cytotoxicity or motor decline were observed. Fasudil appeared ineffective concerning the prevention or attenuation of α-syn spreading in mice. On the one hand, the applied dosage of α-syn PFFs was probably too high so that fasudil in its applied dosage could not affect the α-syn spreading appropriately. On the other hand, the effect of fasudil is probably α-syn species dependent including the hypothesis that fasudil did not target the applied PFFs.

Taken together, the present study underlines the heterogeneity of the pathology in PD patients and argues for different subgroups of the disease rather than for one homogeneous pathology. Iron was shown to modulate α-syn spreading and to affect behavior, rendering it an auspicious therapeutic target. The results support the approach to test iron chelators as therapeutic strategies, which is currently realized by a clinical trial testing the effectiveness of deferiprone in PD patients (FAIRPARKII, NCT02655315). More experiments are needed to even better understand the role of iron and ROCK inhibition in α-syn spreading pathology, and the present results may help to develop new experimental designs based on arising questions and, in translational prospective, to search for promising treatment opportunities for PD.

6 Summary

Parkinson's disease (PD) is the second most prevalent neurodegenerative disease affecting approximately 1 % of the population above 60 years of age. It affects preferentially the extrapyramidal system, causing severe deficits in motor function. So far, the progression of the disease can neither be delayed nor cured. The dyshomeostasis of trace elements, especially of iron, and the presence of alpha-synuclein (α-syn) aggregate-containing Lewy bodies (LBs) in the brain are two main pathologic events playing a crucial role in PD. The underlying pathomechanisms for spreading of α-syn through the brain are still unknown, but PD-related targets such as trace elements or the rho-associated protein kinase (ROCK) were suggested to affect its aggregation pathology. Identifying triggers that affect α-syn propagation is of fundamental importance since they could be considered as auspicious targets for new therapeutic strategies.

In the present study, the elemental content of nigral neurons of PD patients and control patients without neurodegeneration was analyzed using X-ray fluorescence (XRF) and it was found that intracellular element concentrations differ substantially within and between patients. Copper was the most discriminating element between the groups. On a subcellular level, X-ray diffraction revealed the presence of β-sheet protein structures in a LB, whereas XRF measurements identified a varying distribution of trace elements such as iron, selenium or copper within two LBs. Furthermore, the relation of iron and α-syn was examined. With the objective to investigate the influence of iron on α-syn propagation through the brain, a murine α-syn fibrils injection model was combined with iron intoxication and revealed reducing and redistribution effects of iron on α-syn spreading and a reduced microglia accumulation. Both iron and α-syn fibrils treatment resulted in long-term memory dysfunction in the novel object recognition test. Moreover, the influence of iron on α-syn spreading was investigated in cortical neurons using microfluidic chambers. Spreading of α-syn seemed not to be affected by iron *in vitro*, arguing for a more systemic mode of action *in vivo*. Since the ROCK inhibitor fasudil showed multiple protective effects in PD mouse models previously, we analyzed its effects on α-syn spreading *in vivo*. Here, the application of fasudil did not alter α-syn propagation. Taken together, the present work investigates the influence of trace elements, particularly iron, and ROCK inhibition on α-syn spreading and thus contributes to a better understanding of PD pathophysiology and to the identification of auspicious targets for new therapeutic strategies.

7 Appendix

The following pages contain supplementary tables which are related to the results shown in chapter 3.2.3.2 and describe the α-syn pathology in brain regions of PFFs-injected mice treated with vehicle or iron. Each table is related to a specific coronal brain section which is named after its distance to the Bregma, as stated in the Paxinos atlas. The individual brain regions were also abbreviated according to the Paxinos atlas (Paxinos and Franklin, 2003). Empty spaces in the column "p" of each table imply "no significant difference" referring to the respective performed Mann-Whitney-U test.

Suppl. Table 1. Quantification of pS129-α-syn in individual brain regions in section 'Bregma 1.54 mm'. The averaged α-syn group signal is shown for affected brain regions in section 'Bregma 1.54 mm'. Abbreviations are used according to the Paxinos atlas (Paxinos and Franklin, 2003). Signal in each brain region was rated according to a 5-stage scale from 0 (no α-syn signal) to 4 (severe α-syn pathology) and the group means as well as SEM values are presented per hemisphere. The 'code' is a simplified representation of the pathology rating to which the group means were again classified to (−, +, ++, +++, ++++). The code thereby represents the assessment stages used in Figure 29 and differences regarding these 5 stages (−, +, ++, +++, ++++) between the two groups (240 mg/kg Fe/PFFs and control/PFFs) were marked in bold. For a statistical comparison, Mann-Whitney-U-test was performed for each brain region per hemisphere. Where applicable p-values are stated ($\#p < 0.1$; $*p < 0.05$; $**p < 0.01$).

Bregma 1.54 mm; interaural 5.34 mm — α-syn pathology

Brain regions	Abbreviation Paxinos	Injected hemisphere — control Mean	SEM	Code	240mg/kg Fe Mean	SEM	Code	p	Contralateral hemisphere — control Mean	SEM	Code	240mg/kg Fe Mean	SEM	Code	p
accumbens nucleus, core	acbC	**0.17**	**0.17**	**+**	**0.00**	**0.00**	**-**		0.00	0.00	-	0.00	0.00	-	
accumbens nucleus, shell	AcbSh	0.67	0.21	+	0.71	0.29	+		0.17	0.17	+	0.14	0.14	+	
agranular insular area	AID	1.83	0.60	++	1.29	0.42	++		1.83	0.60	++	1.14	0.46	++	
agranular insular area	AIV	0.33	0.33	+	0.29	0.18	+		0.50	0.22	+	0.29	0.18	+	
caudal interstitial nucleus of medial longitudinal fasciculus	CI	0.50	0.34	+	0.43	0.30	+		0.00	0.00	-	0.00	0.00	-	
cingulate cortex, area 1	Cg1	**2.17**	**0.48**	**+++**	**1.00**	**0.44**	**+**		0.50	0.22	+	0.43	0.30	+	
cingulum, anterior forceps of corpus callosum, external capsule	cg fmi ec	**1.83**	**0.40**	**++**	**0.86**	**0.40**	**+**		**1.33**	**0.42**	**++**	**1.00**	**0.31**	**+**	
dorsal endopiriform nucleus	DEn	0.33	0.21	+	0.14	0.14	+		0.00	0.00	-	0.00	0.00	-	
dysgranular insular cortex	DI	1.83	0.54	++	1.29	0.52	++		**1.33**	**0.49**	**++**	**0.71**	**0.36**	**+**	
granular insular cortex	GI	0.50	0.22	+	0.57	0.30	+		0.50	0.22	+	0.43	0.30	+	
infralimbic cortex	IL	0.33	0.21	+	0.14	0.14	+		**0.17**	**0.17**	**+**	**0.00**	**0.00**	**-**	
prelimbic cortex	PrL	**1.50**	**0.50**	**++**	**0.14**	**0.14**	**+**	*	**0.33**	**0.21**	**+**	**0.00**	**0.00**	**-**	
primary motor cortex	M1	**1.50**	**0.43**	**++**	**0.71**	**0.36**	**+**		0.67	0.21	+	0.14	0.14	+	
somatosensory 1, jaw region; primary somatosensory cortex	S1J S1	0.50	0.34	+	0.14	0.14	+		**0.17**	**0.17**	**+**	**0.00**	**0.00**	**-**	
striatum	Cpu	1.33	0.42	++	1.14	0.26	++		1.00	0.26	+	0.29	0.18	+	
supplementary motor cortex	M2	2.83	0.54	+++	2.29	0.47	+++		1.00	0.26	+	0.86	0.34	+	

Suppl. Table 2. Quantification of pS129-α-syn in individual brain regions in section 'Bregma 0.38 mm'. The averaged α-syn group signal is shown for affected brain regions in section 'Bregma 0.38 mm'. Abbreviations are used according to the Paxinos atlas (Paxinos and Franklin, 2003). Signal in each brain region was rated according to a 5-stage scale from 0 (no α-syn signal) to 4 (severe α-syn pathology) and the group means as well as SEM values are presented per hemisphere. The 'code' is a simplified representation of the pathology rating to which the group means were again classified to (−, +, ++, +++, ++++). The code thereby represents the assessment stages used in Figure 29 and differences regarding these 5 stages (−, +, ++, +++, ++++) between the two groups (240 mg/kg Fe/PFFs and control/PFFs) were marked in bold. For a statistical comparison, Mann-Whitney-U-test was performed for each brain region per hemisphere. Where applicable p-values are stated (#$p < 0.1$; *$p < 0.05$; **$p < 0.01$).

Bregma 0.38 mm; interaural 4.18 mm														
		Injected hemisphere						**Contralateral hemisphere**						
		Control			**240mg/kg Fe**				**Control**			**240mg/kg Fe**			
Brain regions	**Abbreviation Paxinos**	**Mean**	**SEM**	**Code**	**Mean**	**SEM**	**Code**	**p**	**Mean**	**SEM**	**Code**	**Mean**	**SEM**	**Code**	**p**
adrenergic group C1 OR claustrum	C1	0.33	0.21	+	0.43	0.20	+		0.50	0.34	+	0.57	0.43	+	
agranular insular area	AIP	0.67	0.21	+	0.57	0.30	+		**0.00**	**0.00**	**-**	**1.14**	**0.40**	**++**	*
cingulate cortex, area 1	Cg1	**2.17**	**0.60**	**+++**	**1.57**	**0.30**	**++**		0.67	0.33	+	0.29	0.18	+	
cingulate cortex, area 2	Cg2	**1.83**	**0.60**	**++**	**0.86**	**0.26**	**+**		**0.00**	**0.00**	**-**	**0.29**	**0.18**	**+**	
corpus callosum; external capsule	cc ec	0.67	0.33	+	0.57	0.30	+		**0.00**	**0.00**	**-**	**0.43**	**0.20**	**+**	
dorsal endopiriform nucleus	DEn	0.67	0.21	+	0.14	0.14	+		0.17	0.17	+	0.14	0.14	+	
granular insular cortex; dysgranular insular cortex	GI DI	2.00	0.45	++	1.14	0.34	++		**1.67**	**0.49**	**++**	**0.71**	**0.47**	**+**	
interstitial nucleus of posterior limb of anterior commissure	IPACL	0.17	0.17	+	0.14	0.14	+		**0.17**	**0.17**	**+**	**0.00**	**0.00**	**-**	
lateral preoptic nucleus	LPO	**0.17**	**0.17**	**+**	**0.00**	**0.00**	**-**		0.00	0.00	-	0.00	0.00	-	
lateral septal nucleus	LSV	**0.00**	**0.00**	**-**	**0.14**	**0.14**	**+**		**0.00**	**0.00**	**-**	**0.14**	**0.14**	**+**	
lateral septal nucleus LSI	LSI	**0.00**	**0.00**	**-**	**0.14**	**0.14**	**+**		**0.00**	**0.00**	**-**	**0.14**	**0.14**	**+**	
nuclei of stria terminalis	BSTLV	**0.17**	**0.17**	**+**	**0.00**	**0.00**	**-**		0.00	0.00	-	0.00	0.00	-	
nuclei of stria terminalis	BSTMV BSTMA	**0.17**	**0.17**	**+**	**0.00**	**0.00**	**-**		0.00	0.00	-	0.00	0.00	-	
nuclei of stria terminalis	BSTLD	0.17	0.17	+	0.29	0.29	+		0.00	0.00	-	0.00	0.00	-	
olfactory tubercle	Tu	**0.00**	**0.00**	**-**	**0.57**	**0.20**	**+**	*	0.00	0.00	-	0.00	0.00	-	
piriform cortex	Pir	0.33	0.33	+	0.43	0.30	+		**0.00**	**0.00**	**-**	**0.14**	**0.14**	**+**	
primary motor cortex	M1	**2.50**	**0.43**	**+++**	**1.00**	**0.22**	**+**	*	0.83	0.48	+	0.29	0.18	+	

Suppl. Table 2 continued.

Brain regions	Abbreviation Paxinos	Control Mean	SEM	Code	240mg/kg Fe Mean	SEM	Code	p	Control Mean	SEM	Code	240mg/kg Fe Mean	SEM	Code	p
Bregma 0.38 mm; interaural 4.18 mm									α-syn pathology						
		Injected hemisphere							**Contralateral hemisphere**						
second somatosensory cortex	S2	**1.50**	**0.50**	**++**	**0.29**	**0.18**	**+**	#	**1.83**	**0.54**	**++**	**0.29**	**0.18**	**+**	*
somatosensory 1, dysgranular zone	S1DZ	1.00	0.63	+	0.29	0.18	+		0.00	0.00	-	0.00	0.00	-	
somatosensory 1, forelimb region	S1FL	**1.67**	**0.61**	**++**	**0.86**	**0.26**	**+**		0.67	0.33	+	0.29	0.18	+	
somatosensory 1, hindlimb region	S1HL	**2.50**	**0.43**	**+++**	**1.14**	**0.34**	**++**	*	0.83	0.31	+	0.14	0.14	+	
somatosensory 1, barrel field	S1BF	0.50	0.34	+	0.29	0.18	+		0.00	0.00	-	0.00	0.00	-	
striatum	CPu	1.50	0.22	++	1.57	0.30	++		0.67	0.21	+	0.57	0.30	+	
supplementary motor cortex	M2	**2.67**	**0.42**	**+++**	**2.00**	**0.44**	**++**		1.00	0.45	+	0.57	0.20	+	
ventral pallidum	VP	0.17	0.17	+	0.57	0.20	+		0.00	0.00	-	0.00	0.00	-	

Suppl. Table 3. Quantification of pS129-α-syn in individual brain regions in section 'Bregma 0.02 mm'. The averaged α-syn group signal is shown for affected brain regions in section 'Bregma 0.02 mm'. Abbreviations are used according to the Paxinos atlas (Paxinos and Franklin, 2003). Signal in each brain region was rated according to a 5-stage scale from 0 (no α-syn signal) to 4 (severe α-syn pathology) and the group means as well as SEM values are presented per hemisphere. The 'code' is a simplified representation of the pathology rating to which the group means were again classified to (−, +, ++, +++, ++++). The code thereby represents the assessment stages used in Figure 29 and differences regarding these 5 stages (−, +, ++, +++, ++++) between the two groups (240 mg/kg Fe/PFFs and control/PFFs) were marked in bold. For a statistical comparison, Mann-Whitney-U-test was performed for each brain region per hemisphere. Where applicable p-values are stated ($\#p < 0.1$; $*p < 0.05$; $**p < 0.01$).

Bregma 0.02 mm; interaural 3.82 mm									α-syn pathology						
		Injected hemisphere							Contralateral hemisphere						
		Control			240mg/kg Fe				Control			240mg/kg Fe			
Brain regions	Abbreviation Paxinos	Mean	SEM	Code	Mean	SEM	Code	p	Mean	SEM	Code	Mean	SEM	Code	p
agranular insular area	AIP	0.50	0.22	+	0.25	0.16	+		0.67	0.21	+	0.38	0.26	+	
anterior part of anterior commissure	aca	**0.00**	**0.00**	**-**	**0.13**	**0.13**	**+**		0.17	0.17	+	0.13	0.13	+	
caudal interstitial nucleus of medial longitudinal fasciculus	CI	0.33	0.21	+	0.38	0.18	+		0.33	0.21	+	0.13	0.13	+	
cingulate cortex, area 1	Cg1	**1.50**	**0.22**	**++**	**2.13**	**0.40**	**+++**		0.17	0.17	+	0.38	0.18	+	
cingulate cortex, area 2	Cg2	**1.00**	**0.26**	**+**	**1.25**	**0.16**	**++**		**0.17**	**0.17**	**+**	**0.00**	**0.00**	**-**	
corpus callosum	cc	0.17	0.17	+	0.13	0.13	+		**0.17**	**0.17**	**+**	**0.00**	**0.00**	**-**	
dorsal endopiriform nucleus	DEn	0.17	0.17	+	0.13	0.13	+		**0.17**	**0.17**	**+**	**0.00**	**0.00**	**-**	
granular insular cortex; dysgranular insular cortex	GI DI	**1.50**	**0.56**	**++**	**1.00**	**0.27**	**+**		**1.17**	**0.48**	**++**	**0.63**	**0.18**	**+**	
Internal capsule	ic	**0.00**	**0.00**	**-**	**0.13**	**0.13**	**+**		0.00	0.00	-	0.00	0.00	-	
interstitial nucleus of posterior limb of anterior commissure	IPACL	**0.00**	**0.00**	**-**	**0.13**	**0.13**	**+**		0.00	0.00	-	0.00	0.00	-	
lateral preoptic nucleus	LPO	0.33	0.21	+	0.13	0.13	+		0.00	0.00	-	0.00	0.00	-	
lateral globus pallidus	LGP	**0.00**	**0.00**	**-**	**0.13**	**0.13**	**+**		0.00	0.00	-	0.00	0.00	-	
lateral septal nucleus	LSD	0.00	0.00	-	0.00	0.00	-		0.00	0.00	-	0.00	0.00	-	
lateral septal nucleus	LSV	0.00	0.00	-	0.00	0.00	-		0.00	0.00	-	0.00	0.00	-	
nuclei of stria terminalis	BSTMA	**0.00**	**0.00**	**-**	**0.25**	**0.16**	**+**		0.00	0.00	-	0.00	0.00	-	
nuclei of stria terminalis	BSTLD	**0.67**	**0.67**	**+**	**0.00**	**0.00**	**-**		0.00	0.00	-	0.00	0.00	-	
nuclei of stria terminalis	BSTLV	**0.00**	**0.00**	**-**	**0.13**	**0.13**	**+**		0.00	0.00	-	0.00	0.00	-	

Suppl. Table 3 continued.

Brain regions	Abbreviation Paxinos	α-syn pathology													
		Injected hemisphere							Contralateral hemisphere						
		Control			240mg/kg Fe			p	Control			240mg/kg Fe			p
		Mean	SEM	Code	Mean	SEM	Code		Mean	SEM	Code	Mean	SEM	Code	
nuclei of stria terminalis	BSTMV	**0.00**	**0.00**	**-**	**0.13**	**0.13**	**+**		0.00	0.00	-	0.00	0.00	-	
nuclei of stria terminalis	BSTLI	**0.00**	**0.00**	**-**	**0.38**	**0.38**	**+**		**0.00**	**0.00**	**-**	**0.13**	**0.13**	**+**	
piriform cortex	Pir	0.33	0.21	+	0.25	0.16	+		**0.00**	**0.00**	**-**	**0.13**	**0.13**	**+**	
posterior part of anterior commissure	acp	**0.00**	**0.00**	**-**	**0.13**	**0.13**	**+**		0.17	0.17	+	0.13	0.13	+	
posterior part of anterior commissure	acp (below IPACL)	**0.00**	**0.00**	**-**	**0.13**	**0.13**	**+**		**0.00**	**0.00**	**-**	**0.38**	**0.18**	**+**	
primary motor cortex	M1	**2.33**	**0.49**	**+++**	**1.00**	**0.38**	**+**	#	0.50	0.22	+	0.25	0.16	+	
second somatosensory cortex	S2	0.50	0.34	+	0.13	0.13	+		0.33	0.21	+	0.25	0.16	+	
septofimbrial nucleus	SFI	0.00	0.00	-	0.00	0.00	-		0.00	0.00	-	0.00	0.00	-	
somatosensory 1, dysgranular zone	S1DZ	**0.00**	**0.00**	**-**	**0.13**	**0.13**	**+**		0.00	0.00	-	0.00	0.00	-	
somatosensory 1, forelimb region	S1FL	0.33	0.33	+	0.25	0.16	+		0.17	0.17	+	0.25	0.16	+	
somatosensory 1, hindlimb region	S1HL	0.83	0.40	+	0.63	0.32	+		0.33	0.21	+	0.25	0.16	+	
somatosensory 1, barrel field	S1BF	0.00	0.00	-	0.00	0.00	-		0.00	0.00	-	0.00	0.00	-	
striatum	CPu	1.50	0.22	++	1.25	0.25	++		0.33	0.21	+	0.25	0.16	+	
supplementary motor cortex	M2	**2.50**	**0.22**	**+++**	**1.75**	**0.31**	**++**		0.67	0.21	+	0.38	0.18	+	
ventral endopiriform nucleus	VEn	**0.17**	**0.17**	**+**	**0.00**	**0.00**	**-**		0.00	0.00	-	0.00	0.00	-	

Bregma 0.02 mm; interaural 3.82 mm

Suppl. Table 4. Quantification of pS129-α-syn in individual brain regions in section 'Bregma -1.58 mm'. The averaged α-syn group signal is shown for affected brain regions in section 'Bregma -1.58 mm'. Abbreviations are used according to the Paxinos atlas (Paxinos and Franklin, 2003). Signal in each brain region was rated according to a 5-stage scale from 0 (no α-syn signal) to 4 (severe α-syn pathology) and the group means as well as SEM values are presented per hemisphere. The 'code' is a simplified representation of the pathology rating to which the group means were again classified to (−, +, ++, +++, ++++). The code thereby represents the assessment stages used in Figure 29 and differences regarding these 5 stages (−, +, ++, +++, ++++) between the two groups (240 mg/kg Fe/PFFs and control/PFFs) were marked in bold. For a statistical comparison, Mann-Whitney-U-test was performed for each brain region per hemisphere. Where applicable p-values are stated (#$p < 0.1$; *$p < 0.05$; **$p < 0.01$).

Bregma -1.58 mm; interaural 2.22 mm								α-syn pathology							
		Injected hemisphere							Contralateral hemisphere						
		Control			240mg/kg Fe				Control			240mg/kg Fe			
Brain regions	Abbreviation Paxinos	Mean	SEM	Code	Mean	SEM	Code	p	Mean	SEM	Code	Mean	SEM	Code	p
accessory basal amygdaloid nucleus; accessory basal amygdaloid nucleus; ventromedial hypothalamic nucleus (central part)	BMA VMHC BMP	0.83	0.48	+	1.00	0.33	+		**0.00**	**0.00**	**-**	**0.38**	**0.18**	**+**	
amygdalostriatal transition area; striatum	AStr CPu	**1.00**	**0.26**	**+**	**0.00**	**0.00**	**-**	**	0.17	0.17	+	0.25	0.16	+	
anterior cortical nucleus of amygdala	ACo	0.00	0.00	-	0.00	0.00	-		0.00	0.00	-	0.00	0.00	-	
Basal amygdaloid nucleus	BLV	0.17	0.17	+	0.38	0.18	+		**0.17**	**0.17**	**+**	**0.00**	**0.00**	**-**	
basal amygdaloid nucleus	BLA	2.00	0.52	++	1.75	0.53	++		1.67	0.67	++	1.50	0.33	++	
central amygdaloid nucleus	CeMPV	1.67	0.49	++	1.63	0.56	++		0.50	0.22	+	0.13	0.13	+	
central amygdaloid nucleus	CeC	**0.83**	**0.40**	**+**	**1.38**	**0.53**	**++**		0.50	0.22	+	0.25	0.16	+	
central amygdaloid nucleus	CeL	1.17	0.48	++	1.88	0.67	++		**0.17**	**0.17**	**+**	**0.00**	**0.00**	**-**	
central medial nucleus	CM	**0.17**	**0.17**	**+**	**0.00**	**0.00**	**-**		**0.17**	**0.17**	**+**	**0.00**	**0.00**	**-**	
corpus callosum	cc	**0.33**	**0.21**	**+**	**0.00**	**0.00**	**-**		**0.17**	**0.17**	**+**	**0.00**	**0.00**	**-**	
dorsal endopiriform nucleus	DEn	0.17	0.17	+	0.50	0.27	+		**0.00**	**0.00**	**-**	**0.88**	**0.35**	**+**	#
ectorhinal cortex	Ect	**1.83**	**0.54**	**++**	**0.88**	**0.30**	**+**		**1.17**	**0.48**	**++**	**0.25**	**0.16**	**+**	#
intercalated amygdaloid nuclei	I	**1.17**	**0.48**	**++**	**1.00**	**0.42**	**+**		**0.83**	**0.54**	**+**	**0.00**	**0.00**	**-**	
intermediodorsal thalamic nucleus	IMD	0.17	0.17	+	0.38	0.18	+		0.17	0.17	+	0.38	0.18	+	
medial amygdaloid nucleus (posterodorsal subdivision)	MePD	0.33	0.21	+	0.13	0.13	+		0.00	0.00	-	0.00	0.00	-	
medial amygdaloid nucleus (posteroventral subdivision)	MePV	**0.17**	**0.17**	**+**	**0.00**	**0.00**	**-**		0.00	0.00	-	0.00	0.00	-	

Suppl. Table 4 continued.

Bregma -1.58 mm; interaural 2.22 mm

| Brain regions | Abbreviation Paxinos | Injected hemisphere | | | | | | | Contralateral hemisphere | | | | | | |
| | | Control | | | 240mg/kg Fe | | | | Control | | | 240mg/kg Fe | | | |
		Mean	SEM	Code	Mean	SEM	Code	p	Mean	SEM	Code	Mean	SEM	Code	p
lateral amygdaloid nucleus	LaVL	**1.67**	**0.61**	**++**	**0.50**	**0.38**	**+**		**1.50**	**0.67**	**++**	**0.88**	**0.35**	**+**	
lateral amygdaloid nucleus	LaDL	**2.17**	**0.54**	**+++**	**0.88**	**0.48**	**+**		1.67	0.49	++	1.13	0.40	++	
lateral hypothalamic area	LH	**0.17**	**0.17**	**+**	**0.00**	**0.00**	**-**		0.00	0.00	-	0.00	0.00	-	
lateral parietal association cortex	LPtA	**1.33**	**0.33**	**++**	**0.88**	**0.23**	**+**		0.17	0.17	+	0.13	0.13	+	
lateral posterior nucleus	LPMR	**0.17**	**0.17**	**+**	**0.00**	**0.00**	**-**		0.00	0.00	-	0.00	0.00	-	
medial forebrain bundle	mfb	0.50	0.22	+	0.25	0.16	+		**0.00**	**0.00**	**-**	**0.13**	**0.13**	**+**	
medial parietal association cortex	MPtA	**1.17**	**0.31**	**++**	**0.75**	**0.25**	**+**		0.17	0.17	+	0.25	0.16	+	
mediodorsal thalamic nucleus, medial part	MDM	**0.17**	**0.17**	**+**	**0.00**	**0.00**	**-**		0.00	0.00	-	0.00	0.00	-	
nigrostriatal fibers	ns	**0.00**	**0.00**	**-**	**0.13**	**0.13**	**+**		**0.00**	**0.00**	**-**	**0.13**	**0.13**	**+**	
nucleus of stria terminalis	BSTIA	1.33	0.42	++	1.00	0.50	+		**1.00**	**0.63**	**+**	**0.00**	**0.00**	**-**	*
paraventricular thalamic nucleus	PV	0.50	0.34	+	0.63	0.18	+		0.50	0.34	+	0.63	0.18	+	
perirhinal cortex	PRh	**2.17**	**0.40**	**+++**	**1.00**	**0.27**	**+**	*	1.33	0.61	++	1.13	0.52	++	
periventricular hypothalamic nucleus	Pe	0.00	0.00	-	0.00	0.00	-		**0.17**	**0.17**	**+**	**0.00**	**0.00**	**-**	
piriform cortex	pir	0.67	0.49	+	0.38	0.18	+		0.00	0.00	-	0.00	0.00	-	
posterolateral cortical amygdaloid nucleus	PLCo	0.00	0.00	-	0.00	0.00	-		0.00	0.00	-	0.00	0.00	-	
posterior thalamic nuclear group	Po	**0.17**	**0.17**	**+**	**0.00**	**0.00**	**-**		0.00	0.00	-	0.00	0.00	-	
retrosplenial granular cortex	RSG	0.17	0.17	+	0.13	0.13	+		0.00	0.00	-	0.00	0.00	-	
retrosplenial agranular cortex	RSA	0.67	0.33	+	0.63	0.26	+		0.00	0.00	-	0.00	0.00	-	
rhomboid thalamic nucleus	Rh	**0.33**	**0.21**	**+**	**0.00**	**0.00**	**-**		**0.33**	**0.21**	**+**	**0.00**	**0.00**	**-**	
second somatosensory cortex	S2	2.00	0.45	++	1.25	0.49	++		0.50	0.22	+	0.13	0.13	+	
somatosensory 1, barrel field	S1BF	1.17	0.31	++	1.25	0.37	++		0.50	0.22	+	0.25	0.16	+	
somatosensory 1, trunk region	S1Tr	1.50	0.34	++	1.25	0.31	++		0.67	0.21	+	0.25	0.16	+	
stria terminalis	st	**2.83**	**0.65**	**+++**	**0.63**	**0.50**	**+**		**0.17**	**0.17**	**+**	**0.00**	**0.00**	**-**	
ventral endopiriform nucleus	VEn	**0.00**	**0.00**	**-**	**0.13**	**0.13**	**+**		0.00	0.00	-	0.00	0.00	-	
ventrolateral thalamic nucleus	VL	**0.17**	**0.17**	**+**	**0.00**	**0.00**	**-**		0.00	0.00	-	0.00	0.00	-	
ventromedial thalamic nucleus	VM	**0.50**	**0.34**	**+**	**0.00**	**0.00**	**-**		0.00	0.00	-	0.00	0.00	-	

α-syn pathology

Suppl. Table 5. Quantification of pS129-α-syn in individual brain regions in section 'Bregma -3.08 mm'. The averaged α-syn group signal is shown for affected brain regions in section 'Bregma -3.08 mm'. Abbreviations are used according to the Paxinos atlas (Paxinos and Franklin, 2003). Signal in each brain region was rated according to a 5-stage scale from 0 (no α-syn signal) to 4 (severe α-syn pathology) and the group means as well as SEM values are presented per hemisphere. The 'code' is a simplified representation of the pathology rating to which the group means were again classified to (−, +, ++, +++, ++++). The code thereby represents the assessment stages used in Figure 29 and differences regarding these 5 stages (−, +, ++, +++, ++++) between the two groups (240 mg/kg Fe/PFFs and control/PFFs) were marked in bold. For a statistical comparison, Mann-Whitney-U-test was performed for each brain region per hemisphere. Where applicable p-values are stated (#$p < 0.1$; *$p < 0.05$; **$p < 0.01$).

Bregma -3.08 mm; interaural 0.72 mm | α-syn pathology

Brain regions	Abbreviation Paxinos	Injected hemisphere Control Mean	SEM	Code	240mg/kg Fe Mean	SEM	Code	p	Contralateral hemisphere Control Mean	SEM	Code	240mg/kg Fe Mean	SEM	Code	p
amygdalohippocampal area	AHiPM	1.67	0.76	++	1.50	0.50	++		0.00	0.00	-	0.00	0.00	-	
amygdalopiriform transition area	APIR	**2.33**	**0.67**	**+++**	**1.33**	**0.61**	**++**		0.00	0.00	-	0.00	0.00	-	
basal amygdaloid nucleus	BLP	2.83	0.75	+++	2.33	0.80	+++		0.00	0.00	-	0.00	0.00	-	
cingulum	cg	**0.33**	**0.21**	**+**	**0.00**	**0.00**	**-**		0.33	0.21	+	0.17	0.17	+	
ectorhinal cortex	Ect	**2.00**	**0.52**	**++**	**0.83**	**0.54**	**+**		1.33	0.49	++	1.33	0.42	++	
entorhinal cortex, lateral part	LEnt	**1.83**	**0.48**	**++**	**0.67**	**0.33**	**+**	#	0.67	0.21	+	0.83	0.31	+	
habenulointerpeduncular tract	fr	**0.33**	**0.33**	**+**	**0.00**	**0.00**	**-**		**0.17**	**0.17**	**+**	**0.00**	**0.00**	**-**	
hippocampus (dentate gyrus, stratum lucidem, stratum radiatum, pyramidal cell layer, CA3 field)	DG Mol GrDG PoDG SLu Rad Or Py CA3	0.17	0.17	+	0.50	0.34	+		0.00	0.00	-	0.00	0.00	-	
interpeduncular fossa	IPF	0.17	0.17	+	0.17	0.17	+		0.17	0.17	+	0.17	0.17	+	
mammillary peduncle	mp	**0.00**	**0.00**	**-**	**0.17**	**0.17**	**+**		**0.00**	**0.00**	**-**	**0.33**	**0.21**	**+**	
medial lemniscus	ml	**0.00**	**0.00**	**-**	**0.33**	**0.21**	**+**		0.00	0.00	-	0.00	0.00	-	
medial terminal nucleus of accessory optic tract	MT	**0.00**	**0.00**	**-**	**0.50**	**0.50**	**+**		0.00	0.00	-	0.00	0.00	-	
peripenduncular nucleus	PP	**0.17**	**0.17**	**+**	**0.00**	**0.00**	**-**		0.00	0.00	-	0.00	0.00	-	
perirhinal cortex	PRh	1.83	0.48	++	1.33	0.42	++		1.17	0.40	++	1.33	0.42	++	
posterior forceps of corpus callosum; commissure of fornix	fmj dhc	**0.17**	**0.17**	**+**	**0.00**	**0.00**	**-**		0.00	0.00	-	0.00	0.00	-	
posteromedial cortical amygdaloid nucleus	PMCo	**1.33**	**0.49**	**++**	**0.33**	**0.21**	**+**		0.00	0.00	-	0.00	0.00	-	

Suppl. Table 5 continued.

Brain regions	Abbreviation Paxinos	Injected hemisphere							Contralateral hemisphere						
		Control			240mg/kg Fe				Control			240mg/kg Fe			
		Mean	SEM	Code	Mean	SEM	Code	p	Mean	SEM	Code	Mean	SEM	Code	p
primary auditory area	Au1	**1.17**	**0.48**	**++**	**0.83**	**0.31**	**+**		0.00	0.00	-	0.00	0.00	-	
primary visual cortex	V1	1.00	0.26	+	0.67	0.33	+		**0.00**	**0.00**	**-**	**0.17**	**0.17**	**+**	
retrosplenial granular cortex	RSG	0.17	0.17	+	0.17	0.17	+		0.00	0.00	-	0.00	0.00	-	
retrosplenial agranular cortex	RSA	0.33	0.21	+	0.33	0.21	+		0.00	0.00	-	0.00	0.00	-	
secondary auditory cortex, dorsal area	AuD	**1.50**	**0.43**	**++**	**0.83**	**0.31**	**+**		0.00	0.00	-	0.00	0.00	-	
secondary auditory cortex, ventral area	AuV	**1.50**	**0.50**	**++**	**1.00**	**0.52**	**+**		**0.33**	**0.21**	**+**	**1.33**	**0.61**	**++**	
secondary visual cortex, lateral part	V2L	**1.50**	**0.34**	**++**	**1.00**	**0.37**	**+**		**0.00**	**0.00**	**-**	**0.17**	**0.17**	**+**	
substantia nigra, lateral part	SNL	0.00	0.00	-	0.00	0.00	-		0.00	0.00	-	0.00	0.00	-	
substantia nigra, pars compacta (compact part)	SNC	**2.00**	**0.26**	**++**	**2.17**	**0.54**	**+++**		0.00	0.00	-	0.00	0.00	-	
substantia nigra, pars reticularis (reticular part)	SNR	0.50	0.22	+	0.50	0.34	+		0.00	0.00	-	0.00	0.00	-	
supramammillary nucleus	SuM	0.00	0.00	-	0.00	0.00	-		**0.00**	**0.00**	**-**	**0.17**	**0.17**	**+**	
temporal cortex, association area	TeA	1.50	0.56	++	1.17	0.48	++		**0.67**	**0.33**	**+**	**1.67**	**0.67**	**++**	
ventral tegmental area	VTA	0.50	0.22	+	0.67	0.21	+		**0.00**	**0.00**	**-**	**0.17**	**0.17**	**+**	
visual cortex 2, mediolateral part	V2ML	0.33	0.21	+	0.67	0.33	+		0.00	0.00	-	0.00	0.00	-	
visual cortex 2, mediomedial part	V2MM	0.50	0.22	+	0.33	0.21	+		0.00	0.00	-	0.00	0.00	-	
zona incerta	ZI	0.00	0.00	-	0.00	0.00	-		**0.00**	**0.00**	**-**	**0.17**	**0.17**	**+**	

Bregma -3.08 mm; interaural 0.72 mm — α-syn pathology

Suppl. Table 6. Quantification of pS129-α-syn in individual brain regions in section 'Bregma -3.28 mm'. The averaged α-syn group signal is shown for affected brain regions in section 'Bregma -3.28 mm'. Abbreviations are used according to the Paxinos atlas (Paxinos and Franklin, 2003). Signal in each brain region was rated according to a 5-stage scale from 0 (no α-syn signal) to 4 (severe α-syn pathology) and the group means as well as SEM values are presented per hemisphere. The 'code' is a simplified representation of the pathology rating to which the group means were again classified to (−, +, ++, +++, ++++). The code thereby represents the assessment stages used in Figure 29 and differences regarding these 5 stages (−, +, ++, +++, ++++) between the two groups (240 mg/kg Fe/PFFs and control/PFFs) were marked in bold. For a statistical comparison, Mann-Whitney-U-test was performed for each brain region per hemisphere. Where applicable p-values are stated (#$p < 0.1$; *$p < 0.05$; **$p < 0.01$).

Bregma -3.28 mm; interaural 0.52 mm																
		Injected hemisphere							**Contralateral hemisphere**							
		Control			**240mg/kg Fe**				**Control**			**240mg/kg Fe**			
Brain regions	**Abbreviation Paxinos**	**Mean**	**SEM**	**Code**	**Mean**	**SEM**	**Code**	**p**	**Mean**	**SEM**	**Code**	**Mean**	**SEM**	**Code**	**p**
amygdalohippocampal area	AHiPM	**3.20**	**0.80**	**++++**	**1.13**	**0.55**	**++**	#	0.00	0.00	-	0.00	0.00	-	
amygdalopiriform transition area	APir	**3.00**	**0.77**	**+++**	**2.00**	**0.63**	**++**		0.00	0.00	-	0.00	0.00	-	
cingulum	cg	0.20	0.20	+	0.50	0.19	+		0.20	0.20	+	0.25	0.16	+	
commissure of fornix	dhc	0.00	0.00	-	0.00	0.00	-		0.00	0.00	-	0.00	0.00	-	
dorsal nucleus of medial geniculate body	MGD	**0.20**	**0.20**	**+**	**0.00**	**0.00**	**-**		0.00	0.00	-	0.00	0.00	-	
ectorhinal cortex	Ect	2.00	0.00	++	1.75	0.49	++		**1.00**	**0.32**	**+**	**1.38**	**0.42**	**++**	
entorhinal cortex, lateral part	LEnt	1.80	0.49	++	1.75	0.45	++		0.80	0.20	+	0.75	0.16	+	
hippocampus, inner part (dentate gyrus, stratum lucidem, stratum radiatum, oriens layer, pyramidal cell layer, CA3 field)	DG Mol GrDG PoDG SLu Rad Or Py CA3	0.20	0.20	+	0.50	0.19	+		0.00	0.00	-	0.00	0.00	-	
hippocampus, outer part (CA1 field, oriens layer, pyramidal cell layer, stratum radiatum, Stratum lacunosummoleculare)	CA1 Or Py Rad LMol	0.80	0.37	+	0.38	0.26	+		0.00	0.00	-	0.00	0.00	-	
interfascicular nucleus	IF	**0.00**	**0.00**	**-**	**0.13**	**0.13**	**+**		**0.00**	**0.00**	**-**	**0.13**	**0.13**	**+**	
magnocellular nucleus of medial geniculate body	MGM	**0.20**	**0.20**	**+**	**0.00**	**0.00**	**-**		0.00	0.00	-	0.00	0.00	-	
medial lemniscus	ml	0.80	0.20	+	0.75	0.49	+		0.00	0.00	-	0.00	0.00	-	
medial terminal nucleus of accessory optic tract	MT	0.60	0.24	+	0.38	0.18	+		0.00	0.00	-	0.00	0.00	-	
medial geniculate body	MGV	0.00	0.00	-	0.00	0.00	-		0.00	0.00	-	0.00	0.00	-	

Suppl. Table 6 continued.

Brain regions	Abbreviation Paxinos	Mean	SEM	Code	Mean	SEM	Code	p	Mean	SEM	Code	Mean	SEM	Code	p
Bregma -3.28 mm; interaural 0.52 mm							**α-syn pathology**								
		Injected hemisphere							**Contralateral hemisphere**						
		Control			**240mg/kg Fe**				**Control**			**240mg/kg Fe**			
parabigeminal nucleus	PAG	0.20	0.20	+	0.13	0.13	+		0.00	0.00	-	0.00	0.00	-	
parabrachial pigmented nucleus	PBP	0.60	0.24	+	0.25	0.16	+		0.00	0.00	-	0.00	0.00	-	
peripenduncular nucleus	PP	1.00	0.32	+	0.50	0.27	+		0.00	0.00	-	0.00	0.00	-	
perirhinal cortex	PRh	2.00	0.32	++	1.88	0.35	++		**1.00**	**0.32**	**+**	**1.13**	**0.40**	**++**	
posterior intralaminar thalamic nucleus	PIL	0.00	0.00	-	0.00	0.00	-		0.00	0.00	-	0.00	0.00	-	
posteromedial cortical amygdaloid nucleus	PMCo	1.40	0.60	++	1.13	0.55	++		0.00	0.00	-	0.00	0.00	-	
postthalamic nuclear group (triangular part); deep mesencephalic nucleus	PoT DpMe	0.20	0.20	+	0.25	0.16	+		**0.00**	**0.00**	**-**	**0.13**	**0.13**	**+**	
primary auditory area	Au1	**2.20**	**0.37**	**+++**	**1.13**	**0.44**	**++**		**1.60**	**0.24**	**++**	**0.25**	**0.16**	**+**	**
primary visual cortex	V1	0.40	0.24	+	0.38	0.18	+		0.00	0.00	-	0.00	0.00	-	
retrosplenial granular cortex	RSG	**0.00**	**0.00**	**-**	**0.25**	**0.16**	**+**		0.00	0.00	-	0.00	0.00	-	
retrosplenial agranular cortex	RSA	0.40	0.40	+	0.50	0.19	+		0.00	0.00	-	0.00	0.00	-	
secondary auditory cortex, dorsal area	AuD	1.40	0.40	++	1.25	0.41	++		0.60	0.40	+	0.25	0.16	+	
secondary auditory cortex, ventral area	AuV	**2.20**	**0.37**	**+++**	**1.13**	**0.44**	**++**		**1.60**	**0.24**	**++**	**0.88**	**0.30**	**+**	
secondary visual cortex, lateral part	V2L	1.00	0.32	+	1.00	0.42	+		**0.00**	**0.00**	**-**	**0.25**	**0.16**	**+**	
subiculum	S	1.00	0.45	+	0.88	0.40	+		0.20	0.20	+	0.13	0.13	+	
substantia nigra, lateral part	SNL	0.00	0.00	-	0.00	0.00	-		0.00	0.00	-	0.00	0.00	-	
substantia nigra, pars compacta (compact part)	SNC	1.40	0.51	++	1.13	0.35	++		0.00	0.00	-	0.00	0.00	-	
substantia nigra, pars compacta (compact part);next to PBP	SNC	0.80	0.37	+	0.75	0.41	+		0.00	0.00	-	0.00	0.00	-	
substantia nigra, pars reticularis (reticular part)	SNR	1.40	0.51	++	1.13	0.23	++		0.00	0.00	-	0.00	0.00	-	
suprageniculate thalamic nucleus	SG	**0.20**	**0.20**	**+**	**0.00**	**0.00**	**-**		0.00	0.00	-	0.00	0.00	-	
temporal cortex, association area	TeA	**2.20**	**0.37**	**+++**	**1.75**	**0.41**	**++**		1.20	0.58	++	1.50	0.42	++	
ventral tegmental area	VTA	0.60	0.24	+	0.38	0.18	+		0.40	0.24	+	0.13	0.13	+	
visual cortex 2, mediolateral part	V2ML	0.40	0.24	+	0.63	0.26	+		0.00	0.00	-	0.00	0.00	-	
visual cortex 2, mediomedial part	V2MM	0.20	0.20	+	0.50	0.19	+		0.00	0.00	-	0.00	0.00	-	

8 References

Abbas, M.M., Xu, Z., and Tan, L.C.S. (2018). Epidemiology of Parkinson's Disease—East Versus West. Mov. Disord. Clin. Pract. *5*, 14–28.

Abeyawardhane, D.L., Fernández, R.D., Murgas, C.J., Heitger, D.R., Forney, A.K., Crozier, M.K., and Lucas, H.R. (2018). Iron redox chemistry promotes antiparallel oligomerization of α-synuclein. J. Am. Chem. Soc. *140*, 5028–5032.

Abounit, S., Bousset, L., Loria, F., Zhu, S., Chaumont, F., Pieri, L., Olivo-Marin, J., Melki, R., and Zurzolo, C. (2016). Tunneling nanotubes spread fibrillar α-synuclein by intercellular trafficking of lysosomes. EMBO J. *35*, 2120–2138.

Agrawal, S., Berggren, K.L., Marks, E., and Fox, J.H. (2018). Impact of high iron intake on cognition and neurodegeneration in humans and in animal models: a systematic review. Nutr. Rev. *75*, 456–470.

Ahmed, S.S.S.J., and Santosh, W. (2010). Metallomic profiling and linkage map analysis of early parkinson's disease: A new insight to aluminum marker for the possible diagnosis. PLoS One *5*, e11252.

Akirav, I., and Maroun, M. (2006). Ventromedial prefrontal cortex is obligatory for consolidation and reconsolidation of object recognition memory. Cereb. Cortex *16*, 1759–1765.

Alimonti, A., Bocca, B., Pino, A., Ruggieri, F., Forte, G., and Sancesario, G. (2007). Elemental profile of cerebrospinal fluid in patients with Parkinson's disease. J. Trace Elem. Med. Biol. *21*, 234–241.

Alvarez-Erviti, L., Seow, Y., Schapira, A.H., Gardiner, C., Sargent, I.L., Wood, M.J.A., and Cooper, J.M. (2011). Lysosomal dysfunction increases exosome-mediated alpha-synuclein release and transmission. Neurobiol. Dis. *42*, 360–367.

Alves, G., Forsaa, E.B., Pedersen, K.F., Dreetz Gjerstad, M., and Larsen, J.P. (2008). Epidemiology of Parkinson's disease. J. Neurol. *255*, 18–32.

An, H., Zeng, X., Niu, T., Li, G., Yang, J., Zheng, L., Zhou, W., Liu, H., Zhang, M., Huang, D., et al. (2018). Quantifying iron deposition within the substantia nigra of Parkinson's disease by quantitative susceptibility mapping. J. Neurol. Sci. *386*, 46–52.

Angelova, D.M., and Brown, D.R. (2018). Model senescent microglia induce disease related changes in α-synuclein expression and activity. Biomolecules *8*, 67.

Appel-Cresswell, S., Vilarino-Guell, C., Encarnacion, M., Sherman, H., Yu, I., Shah, B., Weir, D., Thompson, C., Szu-Tu, C., Trinh, J., et al. (2013). Alpha-synuclein p.H50Q, a novel pathogenic mutation for Parkinson's disease. Mov. Disord. *28*, 811–813.

Arai, Y., Yamazaki, M., Mori, O., Muramatsu, H., Asano, G., and Katayama, Y. (2001). α-Synuclein-positive structures in cases with sporadic Alzheimer's disease: Morphology and its relationship to tau aggregation. Brain Res. *888*, 287–296.

Ashiotis, G., Deschildre, A., Nawaz, Z., Wright, J.P., Karkoulis, D., Picca, F.E., and Kieffer, J. (2015). The fast azimuthal integration Python library: pyFAI. J. Appl. Crystallogr. *48*, 510–519.

Ashraf, A., Clark, M., and So, P.-W. (2018). The Aging of Iron Man. Front. Aging Neurosci. *10*.

Baba, M., Nakajo, S., Tu, P.H., Tomita, T., Nakaya, K., Lee, V.M., Trojanowski, J.Q., and Iwatsubo, T. (1998). Aggregation of alpha-synuclein in Lewy bodies of sporadic Parkinson's disease and dementia with Lewy bodies. Am. J. Pathol. *152*, 879–884.

Badiola, N., de Oliveira, R.M., Herrera, F., Guardia-Laguarta, C., Gonçalves, S.A., Pera, M., Suárez-Calvet, M., Clarimon, J., Outeiro, T.F., and Lleó, A. (2011). Tau enhances α-synuclein aggregation and toxicity in cellular models of synucleinopathy. PLoS One *6*, 1–9.

Balderas, I., Rodriguez-Ortiz, C.J., Salgado-Tonda, P., Chavez-Hurtado, J., McGaugh, J.L., and Bermudez-Rattoni, F. (2008). The consolidation of object and context recognition memory involve different regions of the temporal lobe. Cold Spring Harb. Lab. Press *15*, 618–624.

Balestrino, R., and Schapira, A.H. V (2019). Parkinson disease. Eur. J. Neurol. *27*, 27–42.

Barcia, C., Ros, C.M., Annese, V., Sauvage, M.A.C. De, Ros-Bernal, F., Gómez, A., Yuste, J.E., Campuzano, C.M., De Pablos, V., Fernandez-Villalba, E., et al. (2012). ROCK/Cdc42-mediated microglial motility and gliapse formation lead to phagocytosis of degenerating dopaminergic neurons in vivo. Sci. Rep. *2*, 1–13.

Bate, C., and Williams, A. (2015). α-synuclein-induced synapse damage in cultured neurons is mediated by cholesterol-sensitive activation of cytoplasmic phospholipase A2. Biomolecules *5*, 178–193.

Becker, K., Jährling, N., Saghafi, S., Weiler, R., and Dodt, H.U. (2012). Chemical clearing and dehydration of GFP expressing mouse brains. PLoS One *7*, 1–6.

Bellinger, F.P., Bellinger, M.T., Seale, L.A., Takemoto, A.S., Raman, A. V., Miki, T., Manning-Boğ, A.B., Berry, M.J., White, L.R., and Ross, G.W. (2011). Glutathione peroxidase 4 is associated with neuromelanin in substantia nigra and dystrophic axons in putamen of Parkinson's brain. Mol. Neurodegener. *6*, 8.

Bellinger, F.P., Raman, A. V., Rueli, R.H., Bellinger, M.T., Dewing, A.S., Seale, L.A., Andres, M.A., Uyehara-Lock, J.H., White, L.R., Ross, G.W., et al. (2012). Changes in selenoprotein P in substantia nigra and putamen in Parkinson's disease. J. Parkinsons. Dis. *2*, 115–126.

Bendor, J.T., Logan, T.P., and Edwards, R.H. (2013). The function of α-synuclein. Neuron *79*, 1044–1066.

Bennett, R.E., DeVos, S.L., Dujardin, S., Corjuc, B., Gor, R., Gonzalez, J., Roe, A.D., Frosch, M.P., Pitstick, R., Carlson, G.A., et al. (2017). Enhanced Tau Aggregation in the Presence of Amyloid β. Am. J. Pathol. *187*, 1601–1612.

Berg, D., Marek, K., Ross, G.W., and Poewe, W. (2012). Defining at-risk populations for Parkinson's disease: Lessons from ongoing studies. Mov. Disord. *27*, 656–665.

Berggren, K.L., Chen, J., Fox, J., Miller, J., Dodds, L., Dugas, B., Vargas, L., Lothian, A., McAllum, E., Volitakis, I., et al. (2015). Neonatal iron supplementation potentiates oxidative stress, energetic dysfunction and neurodegeneration in the R6/2 mouse model of Huntington's disease. Redox Biol. *4*, 363–374.

Berggren, K.L., Lu, Z., Fox, J.A., Dudenhoeffer, M., Agrawal, S., and Fox, J.H. (2016). Neonatal Iron Supplementation Induces Striatal Atrophy in Female YAC128 Huntington's Disease Mice. J. Huntingtons. Dis. *5*, 53–63.

Bermudez-Rattoni, F., Okuda, S., Roozendaal, B., and McGaugh, J.L. (2005). Insular cortex is involved in consolidation of object recognition memory. Learn. Mem. *12*, 447–449.

Bevins, R.A., and Besheer, J. (2006). Object recognition in rats and mice: a one-trial non-matching-to-sample learning task to study "recognition memory." Nat. Protoc. *1*, 1306.

Biesemeier, A., Eibl, O., Eswara, S., Audinot, J.N., Wirtz, T., Pezzoli, G., Zucca, F.A., Zecca, L., and Schraermeyer, U. (2016). Elemental mapping of Neuromelanin organelles of human Substantia Nigra: correlative ultrastructural and chemical analysis by analytical transmission electron microscopy and nano-secondary ion mass spectrometry. J. Neurochem. *138*, 339–353.

Billings, J.L., Hare, D.J., Nurjono, M., Volitakis, I., Cherny, R. a., Bush, A.I., Adlard, P. a., and Finkelstein, D.I. (2016). Effects of Neonatal Iron Feeding and Chronic Clioquinol Administration on the Parkinsonian Human A53T Transgenic Mouse. ACS Chem. Neurosci. *7*, 360–366.

Billings, J.L., Gordon, S.L., Rawling, T., Doble, P.A., Bush, A.I., Adlard, P.A., Finkelstein, D.I., and Hare, D.J. (2019). l-3,4-dihydroxyphenylalanine (l-DOPA) modulates brain iron, dopaminergic neurodegeneration and motor dysfunction in iron overload and mutant alpha-synuclein mouse models of Parkinson's disease. J. Neurochem. *150*, 88–106.

Billingsley, K.J., Bandres-Ciga, S., Saez-Atienzar, S., and Singleton, A.B. (2018). Genetic risk factors in Parkinson's disease. Cell Tissue Res. *373*, 9–20.

Binolfi, A., Rasia, R.M., Bertoncini, C.W., Ceolin, M., Zweckstetter, M., Griesinger, C., Jovin, T.M., and Fernández, C.O. (2006). Interaction of α-synuclein with divalent metal ions reveals key differences: A link between structure, binding specificity and fibrillation enhancement. J. Am. Chem. Soc. *128*, 9893–9901.

Blumenstock, S., Rodrigues, E.F., Peters, F., Blazquez-Llorca, L., Schmidt, F., Giese, A., and Herms, J. (2017). Seeding and transgenic overexpression of alpha-synuclein triggers dendritic spine pathology in the neocortex. EMBO Mol. Med. *9*, 716–731.

Boddaert, N., Sang, K.H.L.Q., Rötig, A., Leroy-Willig, A., Gallet, S., Brunelle, F., Sidi, D., Thalabard, J.C., Munnich, A., and Cabantchik, Z.I. (2007). Selective iron chelation in Friedreich ataxia: Biologic and clinical implications. Blood *110*, 401–408.

Bosco, D.A., Fowler, D.M., Zhang, Q., Nieva, J., Powers, E.T., Wentworth, P., Lerner, R.A., and Kelly, J.W. (2006). Elevated levels of oxidized cholesterol metabolites in Lewy body disease brains accelerate α-synuclein fibrilization. Nat. Chem. Biol. *2*, 249–253.

Bourassa, M.W., and Miller, L.M. (2012). Metal imaging in neurodegenerative diseases. Metallomics *4*, 721–738.

Braak, H., Del Tredici, K., Rüb, U., de Vos, R.A.I., Jansen Steur, E.N.H., and Braak, E. (2003). Staging of brain pathology related to sporadic Parkinson's disease. Neurobiol. Aging *24*, 197–211.

Braak, H., Ghebremedhin, E., Rüb, U., Bratzke, H., and Del Tredici, K. (2004). Stages in

the development of Parkinson's disease-related pathology. Cell Tissue Res. *318*, 121–134.

Breydo, L., Wu, J.W., and Uversky, V.N. (2012). α-Synuclein misfolding and Parkinson's disease. Biochim Biophys Acta *1822*, 261–285.

Brochard, V., Combadière, B., Prigent, A., Laouar, Y., Perrin, A., Beray-Berthat, V., Bonduelle, O., Alvarez-Fischer, D., Callebert, J., Launay, J.M., et al. (2009). Infiltration of CD4+ lymphocytes into the brain contributes to neurodegeneration in a mouse model of Parkinson disease. J. Clin. Invest. *119*, 182–192.

Brooks, D.J. (2000). Dopamine agonists: Their role in the treatment of Parkinson's disease. J. Neurol. Neurosurg. Psychiatry *68*, 685–689.

Bunaciu, A.A., Udriştioiu, E. gabriela, and Aboul-Enein, H.Y. (2015). X-Ray Diffraction: Instrumentation and Applications. Crit. Rev. Anal. Chem. *45*, 289–299.

Carboni, E., and Lingor, P. (2015). Insights on the interaction of alpha-synuclein and metals in the pathophysiology of Parkinson ' s disease. Metallomics *7*, 395–404.

Carboni, E., Tatenhorst, L., Tönges, L., Barski, E., Dambeck, V., Bähr, M., and Lingor, P. (2017a). Deferiprone Rescues Behavioral Deficits Induced by Mild Iron Exposure in a Mouse Model of Alpha-Synuclein Aggregation. NeuroMolecular Med. *19*, 309–321.

Carboni, E., Nicolas, J.-D., Töpperwien, M., Stadelmann-Nessler, C., Lingor, P., and Salditt, T. (2017b). Imaging of neuronal tissues by x-ray diffraction and x-ray fluorescence microscopy: evaluation of contrast and biomarkers for neurodegenerative diseases. Biomed. Opt. Express *8*, 4331–4347.

Cardoso, R., Roberts, B.R., Bush, A.I., and Hare, D.J. (2015). Selenium, selenoproteins and neurodegenerative diseases. Metallomics *7*, 1213–1228.

Castellani, R.J., Siedlak, S.L., Perry, G., and Smith, M.A. (2000). Sequestration of iron by Lewy bodies in Parkinson's disease. Acta Neuropathol. *100*, 111–114.

Chen, H., Wang, X., Wang, M., Yang, L., Yan, Z., Zhang, Y., and Liu, Z. (2015). Behavioral and neurochemical deficits in aging rats with increased neonatal iron intake: Silibinin's neuroprotection by maintaining redox balance. Front. Aging Neurosci. *7*, 206.

Chen, Q., Chen, Y., Zhang, Y., Wang, F., Yu, H., Zhang, C., Jiang, Z., and Luo, W. (2019). Iron deposition in Parkinson's disease by quantitative susceptibility mapping. BMC Neurosci. *20*, 1–8.

Cheng, D., Jenner, A.M., Shui, G., Cheong, W.F., Mitchell, T.W., Nealon, J.R., Kim, W.S., McCann, H., Wenk, M.R., Halliday, G.M., et al. (2011). Lipid Pathway Alterations in Parkinson's Disease Primary Visual Cortex. PLoS One *6*, e17299.

Cheng, H.-C., Ulane, C.M., and Burke, R.E. (2010). Clinical Progression in Parkinson's Disease and the Neurobiology of Axons. Ann Neurol. *67*, 715–725.

Chikama, M., McFarland, N.R., Amaral, D.G., and Haber, S.N. (1997). Insular cortical projections to functional regions of the striatum correlate with cortical cytoarchitectonic organization in the primate. J. Neurosci. *17*, 9686–9705.

Cho, Y.T., Ernst, M., and Fudge, J.L. (2013). Cortico-amygdala-striatal circuits are organized as hierarchical subsystems through the primate amygdala. J. Neurosci. *33*,

14017–14030.

Choi, Y.R., Kang, S.J., Kim, J.M., Lee, S.J., Jou, I., Joe, E.H., and Park, S.M. (2015). FcγRIIB mediates the inhibitory effect of aggregated α-synuclein on microglial phagocytosis. Neurobiol. Dis. *83*, 90–99.

Cholanians, A.B., Phan, A. V., Ditzel, E.J., Camenisch, T.D., Lau, S.S., and Monks, T.J. (2016). Arsenic induces accumulation of α-synuclein: Implications for synucleinopathies and neurodegeneration. Toxicol. Sci. *153*, 271–281.

Chung, H.K., Ho, H.-A., Pérez-Acuña, D., and Lee, S.-J. (2019). Modeling α-Synuclein Propagation with Preformed Fibril Injections. J. Mov. Disord. *12*, 139–151.

Clarke, J.R., Cammarota, M., Gruart, A., Izquierdo, I., and Delgado-García, J.M. (2010). Plastic modifications induced by object recognition memory processing. Proc. Natl. Acad. Sci. U. S. A. *107*, 2652–2657.

Connolly, B.S., and Lang, A.E. (2014). Pharmacological Treatment of Parkinson Disease. Jama *311*, 1670–1683.

Costa-Mallen, P., Gatenby, C., Friend, S., Maravilla, K.R., Hu, C., Cain, K.C., Agarwal, P., and Anzai, Y. (2017). Brain Iron Concentrations in Regions of Interest and Relation with Serum Iron Levels in Parkinson Disease. J Neurol Sci. *378*, 38–44.

Costantini, I., Ghobril, J.P., Di Giovanna, A.P., Allegra Mascaro, A.L., Silvestri, L., Müllenbroich, M.C., Onofri, L., Conti, V., Vanzi, F., Sacconi, L., et al. (2015). A versatile clearing agent for multi-modal brain imaging. Sci. Rep. *5*, 1–9.

Crick, P.J., Griffiths, W.J., Zhang, J., Beibel, M., Abdel-Khalik, J., Kuhle, J., Sailer, A.W., and Wang, Y. (2017). Reduced Plasma Levels of 25-Hydroxycholesterol and Increased Cerebrospinal Fluid Levels of Bile Acid Precursors in Multiple Sclerosis Patients. Mol. Neurobiol. *54*, 8009–8020.

Dal-Pizzol, F., Klamt, F., Frota, M.L.C., Andrades, M.E., Caregnato, F.F., Vianna, M.M.R., Schröder, N., Quevedo, J., Izquierdo, I., Archer, T., et al. (2001). Neonatal iron exposure induces oxidative stress in adult Wistar rat. Dev. Brain Res. *130*, 109–114.

Davies, K.M., Bohic, S., Carmona, A., Ortega, R., Cottam, V., Hare, D.J., Finberg, J.P.M., Reyes, S., Halliday, G.M., Mercer, J.F.B., et al. (2014). Copper pathology in vulnerable brain regions in Parkinson's disease. Neurobiol. Aging *35*, 858–866.

Davies, P., Moualla, D., and Brown, D.R. (2011). Alpha-synuclein is a cellular ferrireductase. PLoS One *6*, e15814.

Deas, E., Cremades, N., Angelova, P.R., Ludtmann, M.H.R., Yao, Z., Chen, S., Horrocks, M.H., Banushi, B., Little, D., Devine, M.J., et al. (2016). Alpha-Synuclein Oligomers Interact with Metal Ions to Induce Oxidative Stress and Neuronal Death in Parkinson's Disease. Antioxid. Redox Signal. *24*, 376–391.

DeLong, M.R., and Wichmann, T. (2007). Circuits and circuit disorders of the basal ganglia. Arch. Neurol. *64*, 20–24.

Devos, D., Moreau, C., Devedjian, J.C., Kluza, J., Petrault, M., Laloux, C., Jonneaux, A., Ryckewaert, G., Garçon, G., Rouaix, N., et al. (2014). Targeting Chelatable Iron as a Therapeutic Modality in Parkinson's Disease. Antioxid. Redox Signal. *21*, 195–210.

REFERENCES

Dexter, D.T., Carayon, A., Javoy-Agid, F., Agid, Y., Wells, F.R., Daniel, S.E., Lees, A.J., Jenner, P., and Marsden, C.D. (1991). Alterations in the Levels of Iron, Ferritin and Other Trace Metals in Parkinson's Disease and Other Neurodegenerative Diseases Affecting the Basal Ganglia. Brain *114*, 1953–1975.

Dexter, D.T., Statton, S.A., Whitmore, C., Freinbichler, W., Weinberger, P., Tipton, K.F., Della Corte, L., Ward, R.J., and Crichton, R.R. (2011). Clinically available iron chelators induce neuroprotection in the 6-OHDA model of Parkinson's disease after peripheral administration. J. Neural Transm. *118*, 223–231.

Dieriks, B.V., Park, T.I.H., Fourie, C., Faull, R.L.M., Dragunow, M., and Curtis, M.A. (2017). α-synuclein transfer through tunneling nanotubes occurs in SH-SY5Y cells and primary brain pericytes from Parkinson's disease patients. Sci. Rep. *7*, 1–11.

Dodani, S.C., Domaille, D.W., Nam, C.I., Miller, E.W., Finney, L.A., Vogt, S., and Chang, C.J. (2011). Calcium-dependent copper redistributions in neuronal cells revealed by a fluorescent copper sensor and X-ray fluorescence microscopy. Proc. Natl. Acad. Sci. *108*, 5980–5985.

Dorsey, E.R., and Bloem, B.R. (2018). The Parkinson pandemic - A call to action. JAMA Neurol. *75*, 9–10.

Dorsey, E.R., Elbaz, A., Nichols, E., Abd-Allah, F., Abdelalim, A., Adsuar, J.C., Ansha, M.G., Brayne, C., Choi, J.Y.J., Collado-Mateo, D., et al. (2018). Global, regional, and national burden of Parkinson's disease, 1990–2016: a systematic analysis for the Global Burden of Disease Study 2016. Lancet Neurol. *17*, 939–953.

Dowding, I., and Haufe, S. (2018). Powerful Statistical Inference for Nested Data Using Sufficient Summary Statistics. Front. Hum. Neurosci. *12*, 103.

Duffy, M.F., Collier, T.J., Patterson, J.R., Kemp, C.J., Luk, K.C., Tansey, M.G., Paumier, K.L., Kanaan, N.M., Fischer, D.L., Polinski, N.K., et al. (2018). Lewy body-like alpha-synuclein inclusions trigger reactive microgliosis prior to nigral degeneration. J. Neuroinflammation *15*, 1–18.

Ďurfinová, M., Procházková, Petrleničová, D., Bystrická, Z., Orešanská, K., Kuračka, and Líška, B. (2018). Cholesterol level correlate with disability score in patients with relapsing-remitting form of multiple sclerosis. Neurosci. Lett. *687*, 304–307.

Ebrahimi-Fakhari, D., Cantuti-Castelvetri, I., Fan, Z., Rockenstein, E., Masliah, E., Hyman, B.T., McLean, P.J., and Unni, V.K. (2011). Distinct roles in vivo for the Ubiquitin-Proteasome system and the Autophagy-Lysosomal Pathway in the Degradation of α-Synuclein. J. Neurosci. *31*, 14508–14520.

Emmanouilidou, E., and Vekrellis, K. (2016). Exocytosis and Spreading of Normal and Aberrant a-Synuclein. Brain Pathol. *26*, 398–403.

Emmanouilidou, E., Melachroinou, K., Roumeliotis, T., Garbis, S.D., Ntzouni, M., Margaritis, L.H., Stefanis, L., and Vekrellis, K. (2010). Cell-Produced α-Synuclein Is Secreted in a Calcium-Dependent Manner byExosomes and Impacts Neuronal Survival. J. Neurosci. *30*, 6838–6851.

Espa, E., Clemensson, E.K.H., Luk, K.C., Heuer, A., Björklund, T., and Cenci, M.A. (2019). Seeding of protein aggregation causes cognitive impairment in rat model of cortical synucleinopathy. Mov. Disord. 1–12.

Fahrni, C.J. (2007). Biological applications of X-ray fluorescence microscopy: exploring the subcellular topography and speciation of transition metals. Curr. Opin. Chem. Biol. *11*, 121–127.

Febbraro, F., Giorgi, M., Caldarola, S., Loreni, F., and Romero-ramos, M. (2012). α-Synuclein expression is modulated at the translational level by iron. Neuroreport *23*, 576–580.

Fellows Maxwell, K., Bhattacharya, S., Bodziak, M. Lou, Jakimovski, D., Hagemeier, J., Browne, R.W., Weinstock-Guttman, B., Zivadinov 4, R., and Ramanathan, M. (2019). Oxysterols and Apolipoproteins in Multiple Sclerosis: A 5-year Follow-up Study. J. Lipid Res. *60*, 1190–1198.

Fernández, B., Ferrer, I., Gil, F., and Hilfiker, S. (2017). Biomonitorization of iron accumulation in the substantia nigra from Lewy body disease patients. Toxicol. Reports *4*, 188–193.

Fernsebner, K., Zorn, J., Kanawati, B., Walker, A., and Michalke, B. (2014). Manganese leads to an increase in markers of oxidative stress as well as to a shift in the ratio of Fe(II)/(III) in rat brain tissue. Metallomics *6*, 921–931.

Finkelstein, D.I., Hare, D.J., Billings, J.L., Sedjahtera, A., Nurjono, M., Arthofer, E., George, S., Culvenor, J.G., Bush, A.I., and Adlard, P.A. (2016). Clioquinol Improves Cognitive, Motor Function, and Microanatomy of the Alpha-Synuclein hA53T Transgenic Mice. ACS Chem. Neurosci. *7*, 119–129.

Finkelstein, D.I., Billings, J.L., Adlard, P.A., Ayton, S., Sedjahtera, A., Masters, C.L., Wilkins, S., Shackleford, D.M., Charman, S.A., Bal, W., et al. (2017). The novel compound PBT434 prevents iron mediated neurodegeneration and alpha-synuclein toxicity in multiple models of Parkinson's disease. Acta Neuropathol. Commun. *5*, 53.

Fonseca, T.L. da, Villar-Piqué, A., and Outeiro, T.F. (2015). The Interplay between Alpha-Synuclein Clearance and Spreading. Biomolecules *5*, 435–471.

Fornai, F., Schlüter, O.M., Lenzi, P., Gesi, M., Ruffoli, R., Ferrucci, M., Lazzeri, G., Busceti, C.L., Pontarelli, F., Battaglia, G., et al. (2005). Parkinson-like syndrome induced by continuous MPTP infusion: Convergent roles of the ubiquitin-proteasome system and α-synuclein. Proc. Natl. Acad. Sci. U. S. A. *102*, 3413–3418.

Forte, G., Alimonti, A., Violante, N., Di Gregorio, M., Senofonte, O., Petrucci, F., Sancesario, G., and Bocca, B. (2005). Calcium, copper, iron, magnesium, silicon and zinc content of hair in Parkinson's disease. J. Trace Elem. Med. Biol. *19*, 195–201.

Fredriksson, A., Schröder, N., Eriksson, P., Izquierdo, I., and Archer, T. (1999). Neonatal iron exposure induces neurobehavioural dysfunctions in adult mice. Toxicol. Appl. Pharmacol. *159*, 25–30.

Fredriksson, A., Schröder, N., Eriksson, P., Izquierdo, I., and Archer, T. (2000). Maze learning and motor activity deficits in adult mice induced by iron exposure during a critical postnatal period. Dev. Brain Res. *119*, 65–74.

Freundt, E.C., Maynard, N., Clancy, E.K., Roy, S., Bousset, L., Sourigues, Y., Covert, M., Melki, R., Kirkegaard, K., and Brahic, M. (2012). Neuron-to-neuron transmission of α-synuclein fibrils through axonal transport. Ann. Neurol. *72*, 517–524.

Friedlich, A.L., Tanzi, R.E., and Rogers, J.T. (2007). The 5′-untranslated region of

Parkinson's disease α-synuclein messengerRNA contains a predicted iron responsive element. Mol. Psychiatry *12*, 222–223.

Froula, J.M., Castellana-Cruz, M., Anabtawi, N.M., Camino, J.D., Chen, S.W., Thrasher, D.R., Freire, J., Yazdi, A.A., Fleming, S., Dobson, C.M., et al. (2019). Defining α-synuclein species responsible for Parkinson's disease phenotypes in mice. J. Biol. Chem. *294*, 10392–10406.

Fu, H., Hardy, J., and Duff, K.E. (2018). Selective vulnerability in neurodegenerative diseases. Nat. Neurosci. *21*, 1350–1358.

Gan, L., Cookson, M.R., Petrucelli, L., and La Spada, A.R. (2018). Converging pathways in neurodegeneration, from genetics to mechanisms. Nat. Neurosci. *21*, 1300–1309.

Gangania, M.K., Batra, J., Kushwaha, S., and Agarwal, R. (2017). Role of Iron and Copper in the Pathogenesis of Parkinson's Disease. Indian J. Clin. Biochem. *32*, 353–356.

Gao, H.M., Zhang, F., Zhou, H., Kam, W., Wilson, B., and Hong, J.S. (2011). Neuroinflammation and α-synuclein dysfunction potentiate each other, driving chronic progression of neurodegeneration in a mouse model of Parkinson's disease. Environ. Health Perspect. *119*, 807–814.

Gardner, B., Dieriks, B. V., Cameron, S., Mendis, L.H.S., Turner, C., Faull, R.L.M., and Curtis, M.A. (2017). Metal concentrations and distributions in the human olfactory bulb in Parkinson's disease. Sci. Rep. *7*, 1–14.

Genoud, S., Roberts, B.R., Gunn, A.P., Halliday, G.M., Lewis, S.J.G.G., Ball, H.J., Hare, D.J., and Double, K.L. (2017). Subcellular compartmentalisation of copper, iron, manganese, and zinc in the Parkinson's disease brain. Metallomics *9*, 1447–1455.

Gentry, E.G., Henderson, B.W., Arrant, A.E., Gearing, M., Feng, Y., Riddle, N.C., and Herskowitz, J.H. (2016). Rho kinase inhibition as a therapeutic for progressive supranuclear palsy and corticobasal degeneration. J. Neurosci. *36*, 1316–1323.

George, J.M. (2002). The synucleins. Genome Biol. *3*.

George, S., Rey, N.L., Tyson, T., Esquibel, C., Meyerdirk, L., Schulz, E., Pierce, S., Burmeister, A.R., Madaj, Z., Steiner, J.A., et al. (2019). Microglia affect α-synuclein cell-to-cell transfer in a mouse model of Parkinson's disease. Mol. Neurodegener. *14*, 1–22.

Giasson, B.I., Duda, J.E., Quinn, S.M., Zhang, B., Trojanowski, J.Q., and Lee, V.M.-Y. (2002). Neuronal alpha-synucleinopathy with severe movement disorder in mice expressing A53T human alpha-synuclein. Neuron *34*, 521–533.

Goedert, M., Clavaguera, F., and Tolnay, M. (2010). The propagation of prion-like protein inclusions in neurodegenerative diseases. Trends Neurosci. *33*, 317–325.

Golts, N., Snyder, H., Frasier, M., Theisler, C., Choi, P., and Wolozin, B. (2002). Magnesium inhibits spontaneous and iron-induced aggregation of α-synuclein. J. Biol. Chem. *277*, 16116–16123.

González, H., Contreras, F., Prado, C., Elgueta, D., Franz, D., Bernales, S., and Pacheco, R. (2013). Dopamine Receptor D3 Expressed on CD4 + T Cells Favors Neurodegeneration of Dopaminergic Neurons during Parkinson's Disease. J. Immunol. *190*, 5048–5056.

Good, P.F., Olanow, C.W., and Perl, D.P. (1992). Neuromelanin-containing neurons of the substantia nigra accumulate iron and aluminum in Parkinson's disease: a LAMMA study. Brain Res. *593*, 343–346.

Grochowski, C., Blicharska, E., Krukow, P., Jonak, K., Maciejewski, M., Szczepanek, D., Jonak, K., Flieger, J., and Maciejewski, R. (2019). Analysis of Trace Elements in Human Brain: Its Aim, Methods, and Concentration Levels. Front. Chem. *7*, 115.

Guan, X., Zhang, Y., Wei, H., Guo, T., Zeng, Q., Zhou, C., Wang, J., Gao, T., Xuan, M., Gu, Q., et al. (2019). Iron-related nigral degeneration influences functional topology mediated by striatal dysfunction in Parkinson's disease. Neurobiol. Aging *75*, 83–97.

Günther, R., Balck, A., Koch, J.C., Nientiedt, T., Sereda, M., Bähr, M., Lingor, P., and Tönges, L. (2017). Rho kinase inhibition with fasudil in the SOD1G93A mouse model of amyotrophic lateral sclerosis-symptomatic treatment potential after disease onset. Front. Pharmacol. *8*, 17.

Guo, M.F., Meng, J., Li, Y.H., Yu, J.Z., Liu, C.Y., Feng, L., Yang, W.F., Li, J.L., Feng, Q.J., Xiao, B.G., et al. (2014). The inhibition of Rho kinase blocks cell migration and accumulation possibly by challenging inflammatory cytokines and chemokines on astrocytes. J. Neurol. Sci. *343*, 69–75.

Guo, S. De, Liu, C.Y., Yu, J.W., Chai, Z., Wang, Q., Mi, X.T., Song, G. Bin, Li, Y.H., Yang, P.W., Feng, L., et al. (2019). Nasal delivery of Fasudil-modified immune cells exhibits therapeutic potential in experimental autoimmune encephalomyelitis. CNS Neurosci. Ther. *25*, 783–795.

Guttman, M. (1997). Double-blind comparison of pramipexole and bromocriptine treatment with placebo in advanced Parkinson's disease. Neurology *49*, 1060–1065.

Harischandra, D.S., Rokad, D., Neal, M.L., Ghaisas, S., Manne, S., Sarkar, S., Panicker, N., Zenitsky, G., Jin, H., Lewis, M., et al. (2019). Manganese promotes the aggregation and prion-like cell-to-cell exosomal transmission of α-synuclein. Sci. Signal. *12*, eaau4543.

Harms, A.S., Delic, V., Thome, A.D., Bryant, N., Liu, Z., Chandra, S., Jurkuvenaite, A., and West, A.B. (2017). α-Synuclein fibrils recruit peripheral immune cells in the rat brain prior to neurodegeneration. Acta Neuropathol. Commun. *5*, 85.

Hayes, M.W., Fung, V.S.C., Kimber, T.E., and O'Sullivan, J.D. (2019). Updates and advances in the treatment of Parkinson disease. Med. J. Aust. *211*, 277–283.

He, Q., Li, Y. hua, Guo, S., Wang, Y., Lin, W., Zhang, Q., Wang, J., Ma, C., and Xiao, B.-G. (2016). Inhibition of Rho-kinase by Fasudil protects dopamine neurons and attenuates inflammatory response in an intranasal lipopolysaccharide-mediated Parkinson's model. Eur. J. Neurosci. *43*, 41–52.

He, Z., Guo, J.L., McBride, J.D., Narasimhan, S., Kim, H., Changolkar, L., Zhang, B., Gathagan, R.J., Yue, C., Dengler, C., et al. (2017). Amyloid-β plaques enhance Alzheimer's brain tau-seeded pathologies by facilitating neuritic plaque tau aggregation. Nat. Med. *24*, 29–38.

Helferich, A.M., Ruf, W.P., Grozdanov, V., Freischmidt, A., Feiler, M.S., Zondler, L., Ludolph, A.C., McLean, P.J., Weishaupt, J.H., and Danzer, K.M. (2015). α-Synuclein interacts with SOD1 and promotes its oligomerization. Mol. Neurodegener. *10*, 1–16.

Henderson, M.X., Cornblath, E.J., Darwich, A., Zhang, B., Brown, H., Gathagan, R.J., Sandler, R.M., Bassett, D.S., Trojanowski, J.Q., and Lee, V.M.Y. (2019). Spread of α-synuclein pathology through the brain connectome is modulated by selective vulnerability and predicted by network analysis. Nat. Neurosci. *22*, 1248–1257.

Herber, D.L., Mercer, M., Roth, L.M., Symmonds, K., Maloney, J., Wilson, N., Freeman, M.J., Morgan, D., and Gordon, M.N. (2007). Microglial activation is required for Aβ clearance after intracranial injection of lipopolysaccharide in APP transgenic mice. J. Neuroimmune Pharmacol. *2*, 222–231.

Höpken, H.-H. (2005). Untersuchungen zum Eisenstoffwechsel neuraler Zellen. Eberhard-Karls-University Tübingen.

Hornykiewicz, O. (1998). Biochemical aspects of Parkinson's disease. Neurology *51*, S2-9.

Hoyer, W., Antony, T., Cherny, D., Heim, G., Jovin, T.M., and Subramaniam, V. (2002). Dependence of α-Synuclein Aggregate Morphology on Solution Conditions. J. Mol. Biol. *322*, 383–393.

Hoyer, W., Cherny, D., Subramaniam, V., and Jovin, T.M. (2004). Impact of the Acidic C-Terminal Region Comprising Amino Acids 109−140 on α-Synuclein Aggregation in Vitro. Biochemistry *43*, 16233–16242.

Hsu, L.J., Sagara, Y., Arroyo, A., Rockenstein, E., Sisk, A., Mallory, M., Wong, J., Takenouchi, T., Hashimoto, M., and Masliah, E. (2000). A-Synuclein Promotes Mitochondrial Deficit and Oxidative Stress. Am. J. Pathol. *157*, 401–410.

Huang, X., Auinger, P., Eberly, S., Oakes, D., Schwarzschild, M., Ascherio, A., Mailman, R., and Chen, H. (2011). Serum cholesterol and the progression of parkinson's disease: Results from DATATOP. PLoS One *6*, e22854.

Huang, X., Alonso, A., Guo, X., David, M., Lichtenstein, M.L., Ballantyne, C.M., Mosley, T.H., Chen, H., State, P., and Hershey, M.S. (2016). Statins, plasma cholesterol and risk of Parkinson's disease: a prospective study. Mov Disord. *30*, 552–559.

Huang, X., Ng, S.Y.E., Chia, N.S.Y., Setiawan, F., Tay, K.Y., Au, W.L., Tan, E.K., and Tan, L.C.S. (2019). Non-motor symptoms in early Parkinson's disease with different motor subtypes and their associations with quality of life. Eur. J. Neurol. *26*, 400–406.

Hudák, A., Kusz, E., Domonkos, I., Jósvay, K., Kodamullil, A.T., Szilák, L., Hofmann-Apitius, M., and Letoha, T. (2019). Contribution of syndecans to cellular uptake and fibrillation of α-synuclein and tau. Sci. Rep. *9*, 16543.

Hüls, S., Högen, T., Vassallo, N., Danzer, K.M., Hengerer, B., Giese, A., and Herms, J. (2011). AMPA-receptor-mediated excitatory synaptic transmission is enhanced by iron-induced α-synuclein oligomers. J. Neurochem. *117*, 868–878.

Hunnicutt, B.J., Jongbloets, B.C., Birdsong, W.T., Gertz, K.J., Zhong, H., and Mao, T. (2016). A comprehensive excitatory input map of the striatum reveals novel functional organization. Elife *5*, 1–32.

Ishizawa, T., Mattila, P., Davies, P., Wang, D., and Dickson, D.W. (2003). Colocalization of tau and alpha-synuclein epitopes in Lewy bodies. J. Neuropathol. Exp. Neurol. *62*, 389–397.

Jackson-Lewis, V., and Przedborski, S. (2007). Protocol for the MPTP mouse model of Parkinson's disease. Nat. Protoc. *2*, 141–151.

James, S.A., Myers, D.E., de Jonge, M.D., Vogt, S., Ryan, C.G., Sexton, B.A., Hoobin, P., Paterson, D., Howard, D.L., Mayo, S.C., et al. (2011). Quantitative comparison of preparation methodologies for x-ray fluorescence microscopy of brain tissue. Anal. Bioanal. Chem. *401*, 853–864.

Jang, A., Lee, H., Suk, J., Jung, J., Kim, K., and Lee, S. (2010). Non-classical exocytosis of alpha-synuclein is sensitive to folding states and promoted under stress conditions. J. Neurochem. *113*, 1263–1274.

Jellinger, K., Paulus, W., Grundke-Iqbal, I., Riederer, P., and Youdim, M.B.H. (1990). Brain iron and ferritin in Parkinson's and Alzheimer's diseases. J. Neural Transm. - Park. Dis. Dement. Sect. *2*, 327–340.

Jeon, G.S., Shim, Y.M., Lee, D.Y., Kim, J.S., Kang, M.J., Ahn, S.H., Shin, J.Y., Geum, D., Hong, Y.H., and Sung, J.J. (2019). Pathological Modification of TDP-43 in Amyotrophic Lateral Sclerosis with SOD1 Mutations. Mol. Neurobiol. *56*, 2007–2021.

Johnson, M.E., Stecher, B., Labrie, V., Brundin, L., and Brundin, P. (2019). Triggers, Facilitators, and Aggravators: Redefining Parkinson's Disease Pathogenesis. Trends Neurosci. *42*, 4–13.

Joppe, K., Roser, A.-E., Maass, F., and Lingor, P. (2019). The Contribution of Iron to Protein Aggregation Disorders in the Central Nervous System. Front. Neurosci. *13*, 15.

Joppe, K., Nicolas, J.-D., Grünewald, T.A., Eckermann, M., Salditt, T., and Lingor, P. (2020). Elemental quantification and analysis of structural abnormalities in neurons from Parkinson's-diseased brains by X-ray fluorescence microscopy and diffraction. Biomed. Opt. Express *11*, 3423–3443.

Karpowicz, R.J., Haney, C.M., Mihaila, T.S., Sandler, R.M., Petersson, E.J., and Lee, V.M.Y. (2017). Selective imaging of internalized proteopathic -synuclein seeds in primary neurons reveals mechanistic insight into transmission of synucleinopathies. J. Biol. Chem. *292*, 13482–13497.

Karydas, A.G., Czyzycki, M., Leani, J.J., Migliori, A., Osan, J., Bogovac, M., Wrobel, P., Vakula, N., Padilla-Alvarez, R., Menk, R.H., et al. (2018). An IAEA multi-technique X-ray spectrometry endstation at Elettra Sincrotrone Trieste: Benchmarking results and interdisciplinary applications. J. Synchrotron Radiat. *25*, 189–203.

Kaur, D., Yantiri, F., Rajagopalan, S., Kumar, J., Mo, J.Q., Boonplueang, R., Viswanath, V., Jacobs, R., Yang, L., Beal, M.F., et al. (2003). Genetic or Pharmacological Iron Chelation Prevents MPTP-Induced Neurotoxicity In Vivo. Neuron *37*, 899–909.

Kaur, D., Peng, J., Chinta, S.J., Rajagopalan, S., Di Monte, D. a., Cherny, R. a., and Andersen, J.K. (2007). Increased murine neonatal iron intake results in Parkinson-like neurodegeneration with age. Neurobiol. Aging *28*, 907–913.

Ki, C.S., Stavrou, E.F., Davanos, N., Lee, W.Y., Chung, E.J., Kim, J.Y., and Athanassiadou, A. (2007). The Ala53Thr mutation in the a-synuclein gene in a Korean family with Parkinson disease. Clin. Genet. *71*, 471–473.

Kim, C., Ho, D.H., Suk, J.E., You, S., Michael, S., Kang, J., Lee, S.J., Masliah, E., Hwang, D., Lee, H.J., et al. (2013). Neuron-released oligomeric α-synuclein is an

endogenous agonist of TLR2 for paracrine activation of microglia. Nat. Commun. *4*, 1562.

Kim, C., Cho, E.D., Kim, H.K., You, S., Lee, H.J., Hwang, D., and Lee, S.J. (2014). B1-Integrin-Dependent Migration of Microglia in Response To Neuron-Released A-Synuclein. Exp. Mol. Med. *46*, 1–10.

Kim, C., Lv, G., Lee, J.S., Jung, B.C., Masuda-Suzukake, M., Hong, C.S., Valera, E., Lee, H.J., Paik, S.R., Hasegawa, M., et al. (2016). Exposure to bacterial endotoxin generates a distinct strain of α-synuclein fibril. Sci. Rep. *6*, 1–12.

Kim, H.-C., Jhoo, W.-K., Shin, E.-J., and Bing, G. (2000). Selenium deficiency potentiates methamphetamine-induced nigral neuronal loss; comparison with MPTP model. Brain Res. *862*, 247–252.

Koch, J.C., Tatenhorst, L., Roser, A.E., Saal, K.A., Tönges, L., and Lingor, P. (2018). ROCK inhibition in models of neurodegeneration and its potential for clinical translation. Pharmacol. Ther. *189*, 1–21.

Koch, Y., Helferich, A.M., Steinacker, P., Oeckl, P., Walther, P., Weishaupt, J.H., Danzer, K.M., and Otto, M. (2016). Aggregated α-Synuclein Increases SOD1 Oligomerization in a Mouse Model of Amyotrophic Lateral Sclerosis. Am. J. Pathol. *186*, 2152–2161.

Koller, E.J., Brooks, M.M.T., Golde, T.E., Giasson, B.I., and Chakrabarty, P. (2017). Inflammatory pre-conditioning restricts the seeded induction of α-synuclein pathology in wild type mice. Mol. Neurodegener. *12*, 1–13.

Konnova, E.A., and Swanberg, M. (2018). Animal models of Parkinson ' s disease. In Parkinson's Disease: Pathogenesis and Clinical Aspects, T. Stoker, and J. Greenland, eds. (Brisbane (AU): Codon Publications), pp. 83–106.

Kordower, J.H., Chu, Y., Hauser, R. a, Freeman, T.B., and Olanow, C.W. (2008a). Lewy body-like pathology in long-term embryonic nigral transplants in Parkinson's disease. Nat. Med. *14*, 504–506.

Kordower, J.H., Chu, Y., Hauser, R.A., Olanow, C.W., and Freeman, T.B. (2008b). Transplanted dopaminergic neurons develop PD pathologic changes: A second case report. Mov. Disord. *23*, 2303–2306.

Kostka, M., Högen, T., Danzer, K.M., Levin, J., Habeck, M., Wirth, A., Wagner, R., Glabe, C.G., Finger, S., Heinzelmann, U., et al. (2008). Single particle characterization of iron-induced pore-forming α-synuclein oligomers. J. Biol. Chem. *283*, 10992–11003.

Kramer, M.L., and Schulz-Schaeffer, W.J. (2007). Presynaptic α-synuclein aggregates, not Lewy bodies, cause neurodegeneration in dementia with lewy bodies. J. Neurosci. *27*, 1405–1410.

Krüger, R., Kuhn, W., Müller, T., Woitalla, D., Graeber, M., Kösel, S., Przuntek, H., Epplen, J.T., Schöls, L., and Riess, O. (1998). Ala30Pro mutation in the gene encoding alpha-synuclein in Parkinson's disease. Nat. Genet. *18*, 106–108.

Kump, P., and Vogel-Mikuš, K. (2018). Quantification of 2D elemental distribution maps of intermediate-thick biological sections by low energy synchrotron µ-X-ray fluorescence spectrometry. J. Instrum. *13*, C05014.

Kunishio, K., and Haber, S.N. (1994). Primate cingulostriatal projection: Limbic striatal versus sensorimotor striatal input. J. Comp. Neurol. *350*, 337–356.

Kurkowska-Jastrzebska, I., Wrońska, A., Kohutnicka, M., Członkowski, A., and Członkowska, A. (1999). MHC class II positive microglia and lymphocytic infiltration are present in the substantia nigra and striatum in mouse model of Parkinson's disease. Acta Neurobiol. Exp. (Wars). *59*, 1–8.

De Lau, L.M.L., and Breteler, M.M.B. (2006). Epidemiology of Parkinson's disease. Lancet Neurol *5*, 525–535.

De Lau, L.M.L., Koudstaal, P.J., Hofman, A., and Breteler, M.M.B. (2006). Serum cholesterol levels and the risk of Parkinson's disease. Am. J. Epidemiol. *164*, 998–1002.

Laubach, M., Amarante, L.M., Swanson, K., and White, S.R. (2018). What, if anything, is rodent prefrontal cortex? ENeuro *5*, e0315-18.2018.

Lázaro, D.F., Rodrigues, E.F., Langohr, R., Shahpasandzadeh, H., Ribeiro, T., Guerreiro, P., Gerhardt, E., Kröhnert, K., Klucken, J., Pereira, M.D., et al. (2014). Systematic Comparison of the Effects of Alpha-synuclein Mutations on Its Oligomerization and Aggregation. PLoS Genet. *10*.

Lee, E.-J., Woo, M.-S., Moon, P.-G., Baek, M.-C., Choi, I.-Y., Kim, W.-K., Junn, E., and Kim, H.-S. (2010a). α-Synuclein Activates Microglia by Inducing the Expressions of Matrix Metalloproteinases and the Subsequent Activation of Protease-Activated Receptor-1. J. Immunol. *185*, 615–623.

Lee, H.-J., Kim, C., and Lee, S.-J. (2010b). Alpha-Synuclein Stimulation of Astrocytes: Potential Role for Neuroinflammation and Neuroprotection. Oxid. Med. Cell. Longev. *3*, 283–287.

Lee, H.J., Patel, S., and Lee, S.J. (2005). Intravesicular localization and exocytosis of α-synuclein and its aggregates. J. Neurosci. *25*, 6016–6024.

Lee, H.J., Suk, J.E., Bae, E.J., and Lee, S.J. (2008). Clearance and deposition of extracellular α-synuclein aggregates in microglia. Biochem. Biophys. Res. Commun. *372*, 423–428.

Lees, A.J., Selikhova, M., Andrade, L.A., and Duyckaerts, C. (2008). The black stuff and Konstantin Nikolaevich Tretiakoff. Mov. Disord. *23*, 777–783.

Lesage, S., Anheim, M., Letournel, F., Bousset, L., Honoré, A., Rozas, N., Pieri, L., Madiona, K., Dürr, A., Melki, R., et al. (2013). G51D a-synuclein mutation causes a novel Parkinsonian-pyramidal syndrome. Ann. Neurol. *73*, 459–471.

Levin, J., Högen, T., Hillmer, A.S., Bader, B., Schmidt, F., Kamp, F., Kretzschmar, H.A., Bötzel, K., and Giese, A. (2011). Generation of ferric iron links oxidative stress to α-synuclein oligomer formation. J. Parkinsons. Dis. *1*, 205–216.

Li, H.T., Du, H.N., Tang, L., Hu, J., and Hu, H.Y. (2002). Structural transformation and aggregation of human α-synuclein in trifluoroethanol: Non-amyloid component sequence is essential and β-sheet formation is prerequisite to aggregation. Biopolymers *64*, 221–226.

Li, J.Y., Englund, E., Holton, J.L., Soulet, D., Hagell, P., Lees, A.J., Lashley, T., Quinn, N.P., Rehncrona, S., Björklund, A., et al. (2008). Lewy bodies in grafted neurons in

subjects with Parkinson's disease suggest host-to-graft disease propagation. Nat. Med. *14*, 501–503.

Li, W., Jiang, H., Song, N., and Xie, J. (2011). Oxidative stress partially contributes to iron-induced alpha-synuclein aggregation in SK-N-SH cells. Neurotox. Res. *19*, 435–442.

Li, Y.H., Yu, J.W., Xi, J.Y., Yu, W.B., Liu, J.C., Wang, Q., Song, L.J., Feng, L., Yan, Y.P., Zhang, G.X., et al. (2017). Fasudil Enhances Therapeutic Efficacy of Neural Stem Cells in the Mouse Model of MPTP-Induced Parkinson's Disease. Mol. Neurobiol. *54*, 5400–5413.

de Lima, M.N.M., Laranja, D.C., Caldana, F., Grazziotin, M.M., Garcia, V.A., Dal-Pizzol, F., Bromberg, E., and Schröder, N. (2005a). Selegiline protects against recognition memory impairment induced by neonatal iron treatment. Exp. Neurol. *196*, 177–183.

de Lima, M.N.M., Polydoro, M., Laranja, D.C., Bonatto, F., Bromberg, E., Moreira, J.C.F., Dal-Pizzol, F., and Schröder, N. (2005b). Recognition memory impairment and brain oxidative stress induced by postnatal iron administration. Eur. J. Neurosci. *21*, 2521–2528.

de Lima, M.N.M., Presti-Torres, J., Caldana, F., Grazziotin, M.M., Scalco, F.S., Guimarães, M.R., Bromberg, E., Franke, S.I.R., Henriques, J.A.P., and Schröder, N. (2007). Desferoxamine reverses neonatal iron-induced recognition memory impairment in rats. Eur. J. Pharmacol. *570*, 111–114.

Lingor, P., Teusch, N., Schwarz, K., Mueller, R., Mack, H., Bähr, M., and Mueller, B.K. (2007). Inhibition of Rho kinase (ROCK) increases neurite outgrowth on chondroitin sulphate proteoglycan in vitro and axonal regeneration in the adult optic nerve in vivo. J. Neurochem. *103*, 181–189.

Lingor, P., Tönges, L., Pieper, N., Bermel, C., Barski, E., Planchamp, V., and Bähr, M. (2008). ROCK inhibition and CNTF interact on intrinsic signalling pathways and differentially regulate survival and regeneration in retinal ganglion cells. Brain *131*, 250–263.

Lingor, P., Weber, M., Camu, W., Friede, T., Hilgers, R., Leha, A., Neuwirth, C., Günther, R., Benatar, M., Kuzma-Kozakiewicz, M., et al. (2019). ROCK-ALS: Protocol for a Randomized, Placebo-Controlled, Double-Blind Phase IIa Trial of Safety, Tolerability and Efficacy of the Rho Kinase (ROCK) Inhibitor Fasudil in Amyotrophic Lateral Sclerosis. Front. Neurol. *10*, 1–11.

Lively, S., and Schlichter, L.C. (2013). The microglial activation state regulates migration and roles of matrix-dissolving enzymes for invasion. J. Neuroinflammation *10*, 75.

Lohmann, S., Bernis, M.E., Tachu, B.J., Ziemski, A., Grigoletto, J., and Tamgüney, G. (2019). Oral and intravenous transmission of α-synuclein fibrils to mice. Acta Neuropathol. *138*, 515–533.

Longhena, F., Faustini, G., Spillantini, M.G., and Bellucci, A. (2019). Living in promiscuity: The multiple partners of alpha-synuclein at the synapse in physiology and pathology. Int. J. Mol. Sci. *20*, 1–24.

Loria, F., Vargas, J.Y., Bousset, L., Syan, S., Salles, A., Melki, R., and Zurzolo, C. (2017). α-Synuclein transfer between neurons and astrocytes indicates that astrocytes play

a role in degradation rather than in spreading. Acta Neuropathol. *134*, 789–808.

Lu, L., Neff, F., Alvarez-Fischer, D., Henze, C., Xie, Y., Oertel, W.H., Schlegel, J., and Hartmann, A. (2005). Gene expression profiling of Lewy body-bearing neurons in Parkinson's disease. Exp. Neurol. *195*, 27–39.

Lu, Y., Prudent, M., Fauvet, B., Lashuel, H. a, and Girault, H.H. (2011). Phosphorylation of alpha-Synuclein at Y125 and S129 alters its metal binding properties: implications for understanding the role of alpha-Synuclein in the pathogenesis of Parkinson's Disease and related disorders. ACS Chem Neurosci *2*, 667–675.

Luk, K.C., Kehm, V., Carroll, J., Zhang, B., Brien, P.O., Trojanowski, J.Q., and Lee, V.M.-Y. (2012a). Pathological α-Synuclein Transmission Initiates Parkinson-like Neurodegeneration in Nontransgenic Mice. Science (80-.). *338*, 949–953.

Luk, K.C., Kehm, V.M., Zhang, B., O'Brien, P., Trojanowski, J.Q., and Lee, V.M.Y. (2012b). Intracerebral inoculation of pathological α-synuclein initiates a rapidly progressive neurodegenerative α-synucleinopathy in mice. J. Exp. Med. *209*, 975–986.

Lynd-Balta, E., and Haber, S.N. (1994). The organization of midbrain projections to the striatum in the primate: Sensorimotor-related striatum versus ventral striatum. Neuroscience *59*, 625–640.

van Maarschalkerweerd, A., Vetri, V., and Vestergaard, B. (2015). Cholesterol facilitates interactions between α-synuclein oligomers and charge-neutral membranes. FEBS Lett. *589*, 2661–2667.

Maass, F., Michalke, B., Leha, A., Boerger, M., Zerr, I., Koch, J.-C., Tönges, L., Bähr, M., and Lingor, P. (2018). Elemental fingerprint as a cerebrospinal fluid biomarker for the diagnosis of Parkinson's disease. J. Neurochem. *145*, 342–351.

Mandel, S., Maor, G., and Youdim, M.B.H. (2004). Iron and α-synuclein in the substantia nigra of MPTP-treated mice. J. Mol. Neurosci. *24*, 401–416.

Mao, X., Ou, M.T., Karuppagounder, S.S., Kam, T.I., Yin, X., Xiong, Y., Ge, P., Umanah, G.E., Brahmachari, S., Shin, J.H., et al. (2016). Pathological α-synuclein transmission initiated by binding lymphocyte-activation gene 3. Science (80-.). *353*.

Marras, C., Beck, J.C., Bower, J.H., Roberts, E., Ritz, B., Ross, G.W., Abbott, R.D., Savica, R., Van Den Eeden, S.K., Willis, A.W., et al. (2018). Prevalence of Parkinson's disease across North America. Npj Park. Dis. *4*, 21.

Martin-Bastida, A., Ward, R.J., Newbould, R., Piccini, P., Sharp, D., Kabba, C., Patel, M.C., Spino, M., Connelly, J., Tricta, F., et al. (2017). Brain iron chelation by deferiprone in a phase 2 randomised double-blinded placebo controlled clinical trial in Parkinson's disease. Sci. Rep. *7*, 1–9.

Martin, Z.S., Neugebauer, V., Dineley, K.T., Kayed, R., Zhang, W., Reese, L.C., and Taglialatela, G. (2012). α-Synuclein oligomers oppose long-term potentiation and impair memory through a calcineurin-dependent mechanism: Relevance to human synucleopathic diseases. J. Neurochem. *120*, 440–452.

Masuda-Suzukake, M., Nonaka, T., Hosokawa, M., Oikawa, T., Arai, T., Akiyama, H., Mann, D.M.A., and Hasegawa, M. (2013). Prion-like spreading of pathological α-synuclein in brain. Brain *136*, 1128–1138.

Masuda-Suzukake, M., Nonaka, T., Hosokawa, M., Kubo, M., Shimozawa, A., Akiyama, H., and Hasegawa, M. (2014). Pathological alpha-synuclein propagates through neural networks. Acta Neuropathol. Commun. *2*, 88.

Matyash, V., Liebisch, G., Kurzchalia, T. V., Shevchenko, A., and Schwudke, D. (2008). Lipid extraction by methyl- *tert* -butyl ether for high-throughput lipidomics. J. Lipid Res. *49*, 1137–1146.

McDowall, J.S., Ntai, I., Hake, J., Whitley, P.R., Mason, J.M., Pudney, C.R., and Brown, D.R. (2017). Steady-State Kinetics of α-Synuclein Ferrireductase Activity Identifies the Catalytically Competent Species. Biochemistry *56*, 2497–2505.

McGeorge, A.J., and Faull, R.L.M. (1989). The organization of the projection from the cerebral cortex to the striatum in the rat. Neuroscience *29*, 503–537.

McLeary, F., Rcom-H'cheo-Gauthier, A., Goulding, M., Radford, R., Okita, Y., Faller, P., Chung, R., and Pountney, D. (2019). Switching on Endogenous Metal Binding Proteins in Parkinson's Disease. Cells *8*, 179.

Meredith, G.., Totterdell, S., Petroske, E., Santa Cruz, K., Callison, R.., and Lau, Y.-S. (2002). Lysosomal malfunction accompanies alpha-synuclein aggregation in a progressive mouse model of Parkinson's disease. Brain Res. *956*, 156–165.

Mezias, C., Rey, N., Brundin, P., and Raj, A. (2020). Neural connectivity predicts spreading of alpha-synuclein pathology in fibril-injected mouse models: Involvement of retrograde and anterograde axonal propagation. Neurobiol. Dis. *134*, 104623.

Mitchell, A.S., Czajkowski, R., Zhang, N., Jeffery, K., and Nelson, A.J.D. (2018). Retrosplenial cortex and its role in spatial cognition. Brain Neurosci. Adv. *2*, 239821281875709.

Mobarra, N., Shanaki, M., Ehteram, H., Nasiri, H., Sahmani, M., Saeidi, M., Goudarzi, M., Pourkarim, H., and Azad, M. (2016). A review on iron chelators in treatment of iron overload syndromes. Int. J. Hematol. Stem Cell Res. *10*, 239–247.

Moreau, C., Danel, V., Devedjian, J.C., Grolez, G., Timmerman, K., Laloux, C., Petrault, M., Gouel, F., Jonneaux, A., Dutheil, M., et al. (2018). Could conservative iron chelation lead to neuroprotection in amyotrophic lateral sclerosis? Antioxid. Redox Signal. *29*, 742–748.

Morello, N., Tonoli, E., Logrand, F., Fiorito, V., Fagoonee, S., Turco, E., Silengo, L., Vercelli, A., Altruda, F., and Tolosano, E. (2009). Haemopexin affects iron distribution and ferritin expression in mouse brain. J. Cell. Mol. Med. *13*, 4192–4204.

Nakayama, A.Y., Harms, M.B., and Luo, L. (2000). Small GTPases Rac and Rho in the maintenance of dendritic spines and branches in hippocampal pyramidal neurons. J. Neurosci. *20*, 5329–5338.

Nguyen-Legros, J., Bizot, J., Bolesse, M., and Pulicani, J.P. (1980). "Diaminobenzidine black" as a new histochemical demonstration of exogenous iron. Histochemistry *66*, 239–244.

Obeso, J.A., Rodriguez-Oroz, M.C., Rodriguez, M., Lanciego, J.L., Artieda, J., Gonzalo, N., and Olanow, C.W. (2000). Pathophysiology of the basal ganglia in Parkinson's disease. Trends Neurosci. *23*, S8–S19.

Oh, S.W., Harris, J.A., Ng, L., Winslow, B., Cain, N., Mihalas, S., Wang, Q., Lau, C., Kuan, L., Henry, A.M., et al. (2014). A mesoscale connectome of the mouse brain. Nature *508*, 207–214.

Oikawa, T., Nonaka, T., Terada, M., Tamaoka, A., Hisanaga, S.I., and Hasegawa, M. (2016). α-Synuclein fibrils exhibit gain of toxic function, promoting tau aggregation and inhibiting microtubule assembly. J. Biol. Chem. *291*, 15046–15056.

Okuzumi, A., Kurosawa, M., Hatano, T., Takanashi, M., Nojiri, S., Fukuhara, T., Yamanaka, T., Miyazaki, H., Yoshinaga, S., Furukawa, Y., et al. (2018). Rapid dissemination of alpha-synuclein seeds through neural circuits in an in-vivo prion-like seeding experiment. Acta Neuropathol. Commun. *6*, 96.

Olesen, M.N., Christiansen, J.R., Petersen, S.V., Jensen, P.H., Paslawski, W., Romero-Ramos, M., and Sanchez-Guajardo, V. (2018). CD4 T cells react to local increase of α-synuclein in a pathology-associated variant-dependent manner and modify brain microglia in absence of brain pathology. Heliyon *4*, E00513.

Oliveira, M.A.P., Arreckx, S., Monte, D. Di, Preciat, G.A., Ulusoy, A., and Fleming, R.M.T. (2019). The connectome is necessary but not sufficient for the spread of alpha - synuclein pathology in rats. BioRxiv.

Ortega, R., Carmona, A., Roudeau, S., Perrin, L., Dučić, T., Carboni, E., Bohic, S., Cloetens, P., and Lingor, P. (2016). α-Synuclein Over-Expression Induces Increased Iron Accumulation and Redistribution in Iron-Exposed Neurons. Mol. Neurobiol. *53*, 1925–1934.

De Pablo-Fernández, E., Lees, A.J., Holton, J.L., and Warner, T.T. (2019). Prognosis and Neuropathologic Correlation of Clinical Subtypes of Parkinson Disease. JAMA Neurol. *76*, 470–479.

Pace, M.C., Xu, G., Fromholt, S., Howard, J., Giasson, B.I., Lewis, J., and Borchelt, D.R. (2018). Differential induction of mutant SOD1 misfolding and aggregation by tau and α-synuclein pathology. Mol. Neurodegener. *13*, 1–15.

Pandolfo, M., Arpa, J., Delatycki, M.B., Le Quan Sang, K.H., Mariotti, C., Munnich, A., Sanz-Gallego, I., Tai, G., Tarnopolsky, M.A., Taroni, F., et al. (2014). Deferiprone in Friedreich ataxia: A 6-month randomized controlled trial. Ann. Neurol. *76*, 509–521.

Pánik, J., Kopáni, M., Zeman, J., Ješkovský, M., Kaizer, J., and Povinec, P.P. (2018). Determination of metal elements concentrations in human brain tissues using PIXE and EDX methods. J. Radioanal. Nucl. Chem. *3*, 2313–2319.

Park, J.Y., Paik, S.R., Jou, I., and Park, S.M. (2008). Microglial phagocytosis is enhanced by monomeric α-synuclein, not aggregated α-synuclein: Implications for Parkinson's disease. Glia *56*, 1215–1223.

Parkinson, J. (1817). An Essay on the Shaking Palsy (London).

Pasanen, P., Myllykangas, L., Siitonen, M., Raunio, A., Kaakkola, S., Lyytinen, J., Tienari, P.J., Pöyhönen, M., and Paetau, A. (2014). A novel α-synuclein mutation A53E associated with atypical multiple system atrophy and Parkinson's disease-type pathology. Neurobiol. Aging *35*, 2180.e1-5.

Patterson, J.R., Polinski, N.K., Duffy, M.F., Kemp, C.J., Luk, K.C., Volpicelli-Daley, L.A., Kanaan, N.M., and Sortwell, C.E. (2019a). Generation of Alpha-Synuclein

REFERENCES

Preformed Fibrils from Monomers and Use In Vivo. J. Vis. Exp. *2*.

Patterson, J.R., Duffy, M.F., Kemp, C.J., Howe, J.W., Collier, T.J., Stoll, A.C., Miller, K.M., Patel, P., Levine, N., Moore, D.J., et al. (2019b). Time course and magnitude of alpha-synuclein inclusion formation and nigrostriatal degeneration in the rat model of synucleinopathy triggered by intrastriatal α-synuclein preformed fibrils. Neurobiol. Dis. *130*, 104525.

Paul, R., Choudhury, A., Kumar, S., Giri, A., Sandhir, R., and Borah, A. (2017). Cholesterol contributes to dopamineneuronal loss in MPTP mouse model of Parkinson's disease: Involvement of mitochondrial dysfunctions and oxidative stress. PLoS One *12*, 1–22.

Paumier, K.L., Luk, K.C., Manfredsson, F.P., Kanaan, N.M., Lipton, J.W., Collier, T.J., Steece-Collier, K., Kemp, C.J., Celano, S., Schulz, E., et al. (2015). Intrastriatal injection of pre-formed mouse α-synuclein fibrils into rats triggers α-synuclein pathology and bilateral nigrostriatal degeneration. Neurobiol. Dis. *82*, 185–199.

Paxinos, G., and Franklin, K.B.J. (2003). The Mouse Brain in Stereotaxic Coordinates (London: Elsevier Academic Press).

Peelaerts, W., and Baekelandt, V. (2016). α-Synuclein strains and the variable pathologies of synucleinopathies. J. Neurochem. *139*, 256–274.

Peelaerts, W., Bousset, L., Van der Perren, A., Moskalyuk, A., Pulizzi, R., Giugliano, M., Van den Haute, C., Melki, R., and Baekelandt, V. (2015). α-Synuclein strains cause distinct synucleinopathies after local and systemic administration. Nature *522*, 340–344.

Peng, J., Stevenson, F.F., Oo, M.L., and Andersen, J.K. (2009). Iron-enhanced paraquat-mediated dopaminergic cell death due to increased oxidative stress as a consequence of microglial activation. Free Radic. Biol. Med. *46*, 312–320.

Peng, J., Oo, M.L., and Andersen, J.K. (2010a). Synergistic effects of environmental risk factors and gene mutations in Parkinson's disease accelerate age-related neurodegeneration. J Neurochem. *115*, 1363–1373.

Peng, Y., Wang, C., Xu, H., Liu, Y.-N., and Zhou, F. (2010b). Binding of α-Synuclein with Fe(III) and with Fe(II) and Biological Implications of the Resultant Complexes. J Inorg Biochem. *104*, 365–370.

Perls, M. (1867). Nachweis von Eisenoxyd in gewissen Pigmenten. Virchows Arch. Pathol. Anat. Physiol. Klin. Med. *39*, 42–48.

Pinotsi, D., Michel, C.H., Buell, A.K., Laine, R.F., Mahou, P., Dobson, C.M., Kaminski, C.F., and Kaminski Schierle, G.S. (2016). Nanoscopic insights into seeding mechanisms and toxicity of α-synuclein species in neurons. Proc. Natl. Acad. Sci. U. S. A. *113*, 3815–3819.

Planchamp, V., Bermel, C., Tönges, L., Ostendorf, T., Kügler, S., Reed, J.C., Kermer, P., Bähr, M., and Lingor, P. (2008). BAG1 promotes axonal outgrowth and regeneration in vivo via Raf-1 and reduction of ROCK activity. Brain *131*, 2606–2619.

Polinski, N.K., Volpicelli-Daley, L.A., Sortwell, C.E., Luk, K.C., Cremades, N., Gottler, L.M., Froula, J., Duffy, M.F., Lee, V.M.Y., Martinez, T.N., et al. (2018). Best practices for generating and using alpha-synuclein pre-formed fibrils to model Parkinson's disease in rodents. J. Parkinsons. Dis. *8*, 303–322.

182

Popescu, B.F.G., George, M.J., Bergmann, U., Garachtchenko, A. V., Kelly, M.E., McCrea, R.P.E., Lüning, K., Devon, R.M., George, G.N., Hanson, A.D., et al. (2009). Mapping metals in Parkinson's and normal brain using rapid-scanning x-ray fluorescence. Phys. Med. Biol. *54*, 651–663.

Qi, Y., Yu, T., Xu, J., Wan, P., Ma, Y., Zhu, J., Li, Y., Gong, H., Luo, Q., and Zhu, D. (2019). FDISCO: Advanced solvent-based clearing method for imaging whole organs. Sci Adv. *5*, eaau8355.

Recasens, A., and Dehay, B. (2014). Alpha-synuclein spreading in Parkinson's disease. Front. Neuroanat. *8*, 159.

Recasens, A., Dehay, B., Bové, J., Carballo-Carbajal, I., Dovero, S., Pérez-Villalba, A., Fernagut, P.O., Blesa, J., Parent, A., Perier, C., et al. (2014). Lewy body extracts from Parkinson disease brains trigger α-synuclein pathology and neurodegeneration in mice and monkeys. Ann. Neurol. *75*, 351–362.

Rocha, E.M., De Miranda, B., and Sanders, L.H. (2018). Alpha-synuclein: Pathology, mitochondrial dysfunction and neuroinflammation in Parkinson's disease. Neurobiol. Dis. *109*, 249–257.

Rozani, V., Gurevich, T., Giladi, N., El-Ad, B., Tsamir, J., Hemo, B., and Peretz, C. (2018). Higher serum cholesterol and decreased Parkinson's disease risk: A statin-free cohort study. Mov. Disord. *33*, 1298–1305.

Salami, A., Avelar-Pereira, B., Garzón, B., Sitnikov, R., and Kalpouzos, G. (2018). Functional coherence of striatal resting-state networks is modulated by striatal iron content. Neuroimage *183*, 495–503.

Salditt, T., and Dučić, T. (2014). X-Ray Microscopy for Neuroscience: Novel Opportunities by Coherent Optics. In Super-Resolution Microscopy Techniques in the Neurosciences, E.F. Fornasiero, and S.O. Rizzoli, eds. (Totowa, NJ: Humana Press), pp. 257–290.

Schapira, A.H.V., Chaudhuri, K.R., and Jenner, P. (2017). Non-motor features of Parkinson disease. Nat. Rev. Neurosci. *18*, 435–450.

Scheiblich, H., and Bicker, G. (2017). Regulation of Microglial Phagocytosis by RhoA/ROCK-Inhibiting Drugs. Cell. Mol. Neurobiol. *37*, 461–473.

Schober, A. (2004). Classic toxin-induced animal models of Parkinson's disease: 6-OHDA and MPTP. Cell Tissue Res. *318*, 215–224.

Schrag, A., Horsfall, L., Walters, K., Noyce, A., and Petersen, I. (2015). Prediagnostic presentations of Parkinson's disease in primary care: A case-control study. Lancet Neurol. *14*, 57–64.

Schröder, N., Fredriksson, A., Vianna, M.R.M., Roesler, R., Izquierdo, I., and Archer, T. (2001). Memory deficits in adult rats following postnatal iron administration. Behav. Brain Res. *124*, 77–85.

Scudamore, O., and Ciossek, T. (2018). Increased oxidative stress exacerbates α-synuclein aggregation in vivo. J. Neuropathol. Exp. Neurol. *77*, 443–453.

Seibert, J.A., and Boone, J.M. (2005). X-ray imaging physics for nuclear medicine technologists. Part 2: X-ray interactions and image formation. J. Nucl. Med. Technol. *33*,

3–18.

Shaftel, S.S., Johnson, R.E., Kerry, M., Banion, O., Shaftel, S.S., Kyrkanides, S., Olschowka, J.A., Miller, J.H., Johnson, R.E., and Banion, M.K.O. (2007). Sustained hippocampal IL-1 b overexpression mediates chronic neuroinflammation and ameliorates Alzheimer plaque pathology. J. Clin. Invest. *117*, 1594–1604.

Shimozawa, A., Ono, M., Takahara, D., Tarutani, A., Imura, S., Masuda-Suzukake, M., Higuchi, M., Yanai, K., Hisanaga, S.I., and Hasegawa, M. (2017). Propagation of pathological α-synuclein in marmoset brain. Acta Neuropathol. Commun. *5*, 12.

Simon, K.C., Chen, H., Schwarzschild, M., and Ascherio, A. (2007). Hypertension, hypercholesterolemia, diabetes, and risk of Parkinson disease. Neurology *69*, 1688–1695.

Singh, N., Tripathi, A., Wong, J., and Beserra, A. (2014). Brain Iron Homeostasis : From Molecular Mechanisms To Clinical Significance and Therapeutic Opportunities. Antioxid Redox Signal *20*, 1324–1363.

Solé, V.A.A., Papillon, E., Cotte, M., Walter, P., and Susini, J. (2007). A multiplatform code for the analysis of energy-dispersive X-ray fluorescence spectra. Spectrochim. Acta - Part B At. Spectrosc. *62*, 63–68.

Song, Y., Chen, X., Wang, L.Y., Gao, W., and Zhu, M.J. (2013). Rho kinase inhibitor fasudil protects against β-amyloid-induced hippocampal neurodegeneration in rats. CNS Neurosci. Ther. *19*, 603–610.

Spillantini, M.G., Schmidt, M.L., Lee, V.M., Trojanowski, J.Q., Jakes, R., and Goedert, M. (1997). Alpha-synuclein in Lewy bodies. Nature *388*, 839–840.

Spillantini, M.G., Crowther, R.A., Jakes, R., Hasegawa, M., and Goedert, M. (1998). alpha-Synuclein in filamentous inclusions of Lewy bodies from Parkinson' s disease and dementia with Lewy bodies. Proc. Natl. Acad. Sci. *95*, 6469–6473.

Stefanis, L., Emmanouilidou, E., Pantazopoulou, M., Kirik, D., Vekrellis, K., and Tofaris, G.K. (2019). How is alpha-synuclein cleared from the cell? J. Neurochem. *150*, 577–590.

Sterling, N.W., Lichtenstein, M., Lee, E.Y., Lewis, M.M., Evans, A., Eslinger, P.J., Du, G., Gao, X., Chen, H., Kong, L., et al. (2016). Higher plasma LDL-cholesterol is associated with preserved executive and fine motor functions in Parkinson's disease. Aging Dis. *7*, 237–245.

Strohäker, T., Jung, B.C., Liou, S., Fernandez, C.O., Riedel, D., Becker, S., Halliday, G.M., Bennati, M., Kim, W.S., Lee, S., et al. (2019). Structural heterogeneity of α - synuclein fibrils amplified from patient brain extracts. Nat Commun *10*, 5535.

Stroo, E., Koopman, M., Nollen, E.A.A., and Mata-Cabana, A. (2017). Cellular regulation of amyloid formation in aging and disease. Front. Neurosci. *11*, 1–17.

Sun, H. (2018). Association of soil selenium, strontium, and magnesium concentrations with Parkinson's disease mortality rates in the USA. Environ. Geochem. Health *40*, 349–357.

Surowka, A.D., Wrobel, P., Adamek, D., Radwanska, E., and Szczerbowska-Boruchowska, M. (2015). Synchrotron radiation based X-ray fluorescence shows changes in the elemental composition of the human substantia nigra in aged brains. Metallomics *7*, 1522–1531.

Suzuki, W.A., Miller, E.K., and Desimone, R. (1997). Object and place memory in the macaque entorhinal cortex. J. Neurophysiol. *78*, 1062–1081.

Suzuki, Y., Shibuya, M., Satoh, S.-I., Sugimoto, Y., and Takakura, K. (2007). A postmarketing surveillance study of fasudil treatment after aneurysmal subarachnoid hemorrhage. Surg. Neurol. *68*, 126–132.

Suzuki, Y., Shibuya, M., Satoh, S., Sugiyama, H., Seto, M., and Takakura, K. (2008). Safety and efficacy of fasudil monotherapy and fasudil-ozagrel combination therapy in patients with subarachnoid hemorrhage: sub-analysis of the post-marketing surveillance study. Neurol. Med. Chir. (Tokyo). *48*, 241–247; discussion 247-248.

Sveinbjornsdottir, S. (2016). The clinical symptoms of Parkinson's disease. J. Neurochem. *139*, 318–324.

Swanger, S.A., Mattheyses, A.L., Gentry, E.G., and Herskowitz, J.H. (2015). ROCK1 and ROCK2 inhibition alters dendritic spine morphology in hippocampal neurons. Cell. Logist. *5*, e1133266.

Szczerbowska-Boruchowska, M., Lankosz, M., Ostachowicz, J., Adamek, D., Krygowska-Wajs, A., Tomik, B., Szczudlik, A., Simionovici, A., and Bohic, S. (2004). Topographic and quantitative microanalysis of human central nervous system tissue using synchrotron radiation. X-Ray Spectrom. *33*, 3–11.

Szczerbowska-Boruchowska, M., Krygowska-Wajs, A., and Adamek, D. (2012). Elemental micro-imaging and quantification of human substantia nigra using synchrotron radiation based x-ray fluorescence -in relation to Parkinson's disease. J. Phys. Condens. Matter *24*, 244104.

Tanik, S.A., Schultheiss, C.E., Volpicelli-Daley, L.A., Brunden, K.R., and Lee, V.M.Y. (2013). Lewy body-like α-synuclein aggregates resist degradation and impair macroautophagy. J. Biol. Chem. *288*, 15194–15210.

Tatenhorst, L., Tönges, L., Saal, K.-A., Koch, J.C., Szegő, E.M., Bähr, M., and Lingor, P. (2014). Rho Kinase Inhibition by Fasudil in the Striatal 6-Hydroxydopamine Lesion Mouse Model of Parkinson Disease. J. Neuropathol. Exp. Neurol. *73*, 770–779.

Tatenhorst, L., Eckermann, K., Dambeck, V., Fonseca-Ornelas, L., Walle, H., Lopes da Fonseca, T., Koch, J.C., Becker, S., Tönges, L., Bähr, M., et al. (2016). Fasudil attenuates aggregation of α-synuclein in models of Parkinson's disease. Acta Neuropathol Commun *4*, 39.

Terada, M., Suzuki, G., Nonaka, T., Kametani, F., Tamaoka, A., and Hasegawa, M. (2018). The effect of truncation on prion-like properties of -synuclein. J. Biol. Chem. *293*, 13910–13920.

Thompson, A.C., Kirz, J., Attwood, D.T., Gullikson, E.M., Howells, M.R., Kortright, J.B., Liu, Y., Robinson, A.L., Underwood, J., Kim, K.-J., et al. (2009). X-Ray Data Booklet.

Tian, T., Zhang, J.C., Lei, H.Z., Zhu, Y., Shi, J.Y., Hu, J., Huang, Q., Fan, C.H., and Sun, Y.H. (2015). Synchrotron radiation X-ray fluorescence analysis of Fe, Zn and Cu in mice brain associated with Parkinson's disease. Nucl. Sci. Tech. *26*, 030506.

Tönges, L., Frank, T., Tatenhorst, L., Saal, K. a., Koch, J.C., Szego, É.M., Bähr, M., Weishaupt, J.H., and Lingor, P. (2012). Inhibition of rho kinase enhances survival of

dopaminergic neurons and attenuates axonal loss in a mouse model of Parkinson's disease. Brain *135*, 3355–3370.

Tönges, L., Günther, R., Suhr, M., Jansen, J., Balck, A., Saal, K.A., Barski, E., Nientied, T., Götz, A.A., Koch, J.C., et al. (2014). Rho kinase inhibition modulates microglia activation and improves survival in a model of amyotrophic lateral sclerosis. Glia *62*, 217–232.

Totterdell, S., and Meredith, G.E. (1997). Topographical organization of projections from the entorhinal cortex to the striatum of the rat. Neuroscience *78*, 715–729.

Tran, H.T., Chung, C.H.-Y., Iba, M., Zhang, B., Trojanowski, J.Q., Luk, K.C., and Lee, V.M.Y. (2014). α-Synuclein Immunotherapy Blocks Uptake and Templated Propagation of Misfolded α-Synuclein and Neurodegeneration. Cell Rep. *7*, 2054–2065.

Uversky, V.N. (2003). A protein-chameleon: conformational plasticity of alpha-synuclein, a disordered protein involved in neurodegenerative disorders. J. Biomol. Struct. Dyn. *21*, 211–234.

Uversky, V.N., Li, J., and Fink, A.L. (2001). Metal-triggered structural transformations, aggregation, and fibrillation of human α-synuclein: A possible molecular link between parkinson's disease and heavy metal exposure. J. Biol. Chem. *276*, 44284–44296.

Valdinocci, D., Grant, G.D., Dickson, T.C., and Pountney, D.L. (2018). Epothilone D inhibits microglia-mediated spread of alpha-synuclein aggregates. Mol. Cell. Neurosci. *89*, 80–94.

Vasconcellos, L.R.C., Dutra, F.F., Siqueira, M.S., Paula-neto, H.A., Dahan, J., and Kiarely, E. (2016). Protein aggregation as a cellular response to oxidative stress induced by heme and iron.

Velasco-Sánchez, D., Aracil, A., Montero, R., Mas, A., Jiménez, L., O'Callaghan, M., Tondo, M., Capdevila, A., Blanch, J., Artuch, R., et al. (2011). Combined therapy with idebenone and deferiprone in patients with Friedreich's ataxia. Cerebellum *10*, 1–8.

Virmani, T., Moskowitz, C.B., Vonsattel, J., and Fahn, S. (2015). Clinicopathological Characteristics of Freezing of Gait in Autopsy-Confirmed Parkinson 's Disease. Mov. Disord. *30*, 1874–1884.

La Vitola, P., Balducci, C., Cerovic, M., Santamaria, G., Brandi, E., Grandi, F., Caldinelli, L., Colombo, L., Morgese, M.G., Trabace, L., et al. (2018). Alpha-synuclein oligomers impair memory through glial cell activation and via Toll-like receptor 2. Brain. Behav. Immun. *69*, 591–602.

Vogel-Mikuš, K., Pongrac, P., and Pelicon, P. (2014). Micro-PIXE elemental mapping for ionome studies of crop plants. Int. J. PIXE *24*, 217–233.

Vogt, S., Maser, J., and Jacobsen, C. (2003). Data analysis for X-ray fluorescence imaging. J. Phys. IV *104*, 617–622.

Volpicelli-Daley, L.A., Luk, K.C., Patel, T.P., Tanik, S.A., Riddle, D.M., Stieber, A., Meaney, D.F., Trojanowski, J.Q., and Lee, V.M.-Y. (2011). Exogenous α-Synuclein Fibrils Induce Lewy Body Pathology Leading to Synaptic Dysfunction and Neuron Death. Neuron *72*, 57–71.

Volpicelli-Daley, L.A., Luk, K.C., and Lee, V.M.-Y. (2014). Addition of exogenous α-

synuclein preformed fibrils to primary neuronal cultures to seed recruitment of endogenous α-synuclein to Lewy body and Lewy neurite–like aggregates. Nat. Protoc. *9*, 2135–2146.

Wall, N.R., De La Parra, M., Callaway, E.M., and Kreitzer, A.C. (2013). Differential innervation of direct- and indirect-pathway striatal projection neurons. Neuron *79*, 347–360.

Wang, J., Song, N., Jiang, H., Wang, J., and Xie, J. (2013). Pro-inflammatory cytokines modulate iron regulatory protein 1 expression and iron transportation through reactive oxygen/nitrogen species production in ventral mesencephalic neurons. Biochim. Biophys. Acta - Mol. Basis Dis. *1832*, 618–625.

Wang, J., Sui, R., Miao, Q., Wang, Q., Song, L., Yu, J., Li, Y., Xiao, B., and Ma, C. (2019). Effect of Fasudil on remyelination following cuprizone-induced demyelination. CNS Neurosci. Ther. *26*, 1–14.

Wang, J.Y., Zhuang, Q.Q., Zhu, L.B., Zhu, H., Li, T., Li, R., Chen, S.F., Huang, C.P., Zhang, X., and Zhu, J.H. (2016). Meta-analysis of brain iron levels of Parkinson's disease patients determined by postmortem and MRI measurements. Sci. Rep. *6*, 1–13.

Wang, N., Jin, X., Guo, D., Tong, G., and Zhu, X. (2017). Iron Chelation Nanoparticles with Delayed Saturation as an Effective Therapy for Parkinson Disease. Biomacromolecules *18*, 461–474.

Wang, Q., Liu, Y., and Zhou, J. (2015a). Neuroinflammation in Parkinson's disease and its potential as therapeutic target. Transl. Neurodegener. *4*, 1–9.

Wang, S., Chu, C.-H., Stewart, T., Ginghina, C., Wang, Y., Nie, H., Guo, M., Wilson, B., Hong, J.-S., and Zhang, J. (2015b). α-Synuclein, a chemoattractant, directs microglial migration via H2O2-dependent Lyn phosphorylation. Proc. Natl. Acad. Sci. U. S. A. *112*, E1926–E1935.

Ward, R.J., Zucca, F.A., Duyn, J.H., Crichton, R.R., and Zecca, L. (2014). The role of iron in brain ageing and neurodegenerative disorders. Lancet Neurol. *13*, 1045–1060.

Wu, K.C., Liou, H.H., Kao, Y.H., Lee, C.Y., and Lin, C.J. (2017). The critical role of Nramp1 in degrading α-synuclein oligomers in microglia under iron overload condition. Neurobiol. Dis. *104*, 61–72.

Xia, Y., Zhang, G., Han, C., Ma, K., Guo, X., Wan, F., Kou, L., Yin, S., Liu, L., Huang, J., et al. (2019). Microglia as modulators of exosomal alpha-synuclein transmission. Cell Death Dis. *10*, 174.

Xiao, Y., Chen, X., Huang, S., Li, G., Mo, M., Zhang, L., Chen, C., Guo, W., Zhou, M., Wu, Z., et al. (2018). Iron promotes α-synuclein aggregation and transmission by inhibiting TFEB-mediated autophagosome-lysosome fusion. J. Neurochem. *145*, 34–50.

Xilouri, M., Brekk, O.R., and Stefanis, L. (2013). α-Synuclein and protein degradation systems: a reciprocal relationship. Mol. Neurobiol. *47*, 537–551.

Xu, Q., Langley, M., Kanthasamy, A.G., and Reddy, M.B. (2017). Epigallocatechin Gallate Has a Neurorescue Effect in a Mouse Model of Parkinson Disease. J. Nutr. *147*, 1926–1931.

Yang, F., Yang, Y., Mao, C., Liu, L., Zheng, H., Hu, L., and Liu, C. (2013). Crosstalk

between the proteasome system and autophagy in the clearance of α-synuclein. Acta Pharmacol. Sin. *34*, 674–680.

Zarranz, J.J., Alegre, J., Gómez-Esteban, J.C., Lezcano, E., Ros, R., Ampuero, I., Vidal, L., Hoenicka, J., Rodriguez, O., Atarés, B., et al. (2004). The New Mutation, E46K, of a-Synuclein Causes Parkinson and Lewy Body Dementia. Ann. Neurol. *55*, 164–173.

Zecca, L., Gallorini, M., Schünemann, V., Trautwein, A.X., Gerlach, M., Riederer, P., Vezzoni, P., and Tampellini, D. (2001). Iron, neuromelanin and ferritin content in the substantia nigra of normal subjects at different ages: Consequences for iron storage and neurodegenerative processes. J. Neurochem. *76*, 1766–1773.

Zecca, L., Youdim, M.B.H., Riederer, P., Connor, J.R., and Crichton, R.R. (2004). Iron, brain ageing and neurodegenerative disorders. Nat. Rev. Neurosci. *5*, 863–873.

Zeineddine, R., Farrawell, N.E., Lambert-Smith, I.A., and Yerbury, J.J. (2017). Addition of exogenous SOD1 aggregates causes TDP-43 mislocalisation and aggregation. Cell Stress Chaperones *22*, 893–902.

Zhang, B., Kehm, V., Gathagan, R., Leight, S.N., Trojanowski, J.Q., Lee, V.M.-Y., and Luk, K.C. (2019a). Stereotaxic Targeting of Alpha-Synuclein Pathology in Mouse Brain Using Preformed Fibrils. Methods Mol Biol. *1948*, 45–57.

Zhang, P.L., Chen, Y., Zhang, C.H., Wang, Y.X., and Fernandez-Funez, P. (2018). Genetics of Parkinson's disease and related disorders. J. Med. Genet. *55*, 73–80.

Zhang, Q., Hu, C., Huang, J., Liu, W., Lai, W., Leng, F., Tang, Q., Liu, Y., Wang, Q., Zhou, M., et al. (2019b). ROCK1 induces dopaminergic nerve cell apoptosis via the activation of Drp1-mediated aberrant mitochondrial fission in Parkinson's disease. Exp. Mol. Med. *51*.

Zhang, Q.S., Heng, Y., Mou, Z., Huang, J.Y., Yuan, Y.H., and Chen, N.H. (2017a). Reassessment of subacute MPTP-treated mice as animal model of Parkinson's disease. Acta Pharmacol. Sin. *38*, 1317–1328.

Zhang, S., Glukhova, S.A., Caldwell, K.A., and Caldwell, G.A. (2017b). NCEH-1 modulates cholesterol metabolism and protects against α-synuclein toxicity in a C. elegans model of Parkinson's disease. Hum. Mol. Genet. *26*, 3823–3836.

Zhang, W.W., Wang, T., Pei, Z., Miller, D.S., Wu, X., Block, M.L., Wilson, B., Zhang, W.W., Zhou, Y., Hong, J.-S., et al. (2005). Aggregated alpha-synuclein activates microglia: a process leading to disease progression in Parkinson's disease. FASEB J. *19*, 533–542.

Zhao, H.-W.W., Lin, J., Wang, X.-B.B., Cheng, X., Wang, J.-Y.Y., Hu, B.-L.L., Zhang, Y., Zhang, X., and Zhu, J.-H.H. (2013). Assessing Plasma Levels of Selenium, Copper, Iron and Zinc in Patients of Parkinson's Disease. PLoS One *8*, e83060.

Zhao, Y.F., Zhang, Q., Xi, J.Y., Li, Y.H., Ma, C.G., and Xiao, B.G. (2015). Multitarget intervention of Fasudil in the neuroprotection of dopaminergic neurons in MPTP-mouse model of Parkinson's disease. J. Neurol. Sci. *353*, 28–37.

Zumbrennen-Bullough, K.B., Becker, L., Garrett, L., Hölter, S.M., Calzada-Wack, J., Mossbrugger, I., Quintanilla-Fend, L., Racz, I., Rathkolb, B., Klopstock, T., et al. (2014). Abnormal brain iron metabolism in Irp2 deficient mice is associated with mild neurological and behavioral impairments. PLoS One *9*.

9 Acknowledgements

I would like to express special thanks to Prof. Dr. Paul Lingor for giving me the opportunity to work on such an interesting field of study during my PhD and to be part of his group. I am thankful for his support and guidance. I also like to thank Prof. Dr. Mathias Bähr for having me in his department. Furthermore, I am grateful for the support, advice and inspiring discussions with my thesis advisory committee members Prof. Dr. Paul Lingor, Prof. Dr. Markus Zweckstetter and Prof. Dr. Tiago F. Outeiro.

I also like to thank the members of my extended examination board Prof. Dr. Tim Salditt, Prof. Dr. Christine Stadelmann-Nessler und Prof. Dr. Thomas Dresbach for agreeing to attend my PhD defense and assess my work.

Furthermore, I like to state my honest gratitude to the GGNB and Neuroscience office for the support in organizational issues during the last years and for making this doctoral thesis possible.

Many thanks go to my collaboration partners Prof. Dr. Bernhard Michalke, Prof. Dr. Katarina Vogel-Mikuš, Dr. Stefan Becker, Dr. Chi Wang Ip and Dr. Cornelia Herrfurth. Additionally, I am really grateful for the measurement time at the ESRF and I like to thank Prof. Dr. Tim Salditt and Dr. Jan-David Nicolas for their assistance at the beamline, guidance, helpful discussions and the support for the analyses of our collaboration project. It was a pleasure and a great experience to spend so many hours together with Jan-David Nicolas, Marina Eckermann and Kilian Frank in an amusing atmosphere at the beamline.

But work would not be that pleasant without nice colleagues I was spending time together every day, the great atmosphere in our lab and mutual help within the lab. My sincerely gratitude I would like to express to the former postdocs of our lab: Dr. Anna-Elisa Roser, Dr. Lars Tatenhorst and Dr. Eleonora Carboni. I am thankful for your supervision, guidance and for all the questions you answered and problems you solved with me. Anna, it was a pleasure to share the office with you. I am thankful for all your help, everything you have taught me, that you supported me so much and for the friendship we have. For technical support and advice, I want to thank especially Sabine Ceramella, Vivian Dambeck and Elisabeth Barski. Vivian, I am so thankful that I could ask you every stupid question, that you helped me so much and taught me so many things in the lab especially with cell culture. I am also grateful that I had Carmina Warth and Lucas Caldi Gomes as fellow

sufferer by my side, and I am thankful for your help in many stressful times. Lucas, with you I shared and went through so many happy, exciting, stressed but also frustrating moments during the PhD and I am so thankful that I found such a good friend in you and for all the deep talks we had. I am also happy for the few music gigs we had, which reminded me that I need a better work life balance.

I would like to express special thanks to my fiancé David for your support that you caught me up when I was stressed and for all the encouragement. Besides exciting moments there were also many frustrating and depressing situations where I was more than happy to have you by my side, bringing me back to reality. Thank you for believing in me.

Zuallerletzt möchte ich meiner Familie danken. Ich bin dankbar, dass meine Eltern, meine Geschwister und meine Omas immer hinter mir standen und mich unterstützt haben. Familiärer Zusammenhalt, gegenseitige Unterstützung und Gesundheit ist alles, was zählt. Ich möchte noch einmal meinen Eltern, meinen Geschwistern Tobias und Sina und meinem Verlobten David von Herzen danken, dass Ihr immer an mich geglaubt habt und mich in vielen anstrengenden Zeiten immer wieder aufgebaut habt.

10 Curriculum Vitae

Personal details

Name	Karina Joppe
Date and place of birth	13th of May 1993 in Einbeck, Germany
Nationality	German

Education

10/2016 – 03/2020 **PhD Thesis, Georg-August-University Göttingen**
GGNB Program "Cellular and Molecular Physiology of the Brain"
Doctoral Thesis "Alpha-synuclein spreading pathology in Parkinson's disease: the influence of iron and the Rho-kinase inhibitor fasudil"
Supervisor: Prof. Dr. Paul Lingor
University Medicine, Department of Neurology, Göttingen

10/2014 – 09/2016 **Master of Science, Philipps-University Marburg**
M.Sc. Program "Cognitive and Integrative Systems Neurosciences"
Master Thesis "The Analysis of α-Synuclein Spreading in the Brain in Mouse Models of Parkinson's Disease"
External supervisor in Göttingen: Prof. Dr. Paul Lingor
University Medicine, Department of Neurology, Göttingen

10/2011 – 09/2014 **Bachelor of Science, University of Trier**
B.Sc. Program "Psychology"
Bachelor Thesis "Der Einfluss von Intention und Ausgang auf die Beurteilung moralischer und konventioneller Normen bei Vorschulkindern"
External supervisor in Göttingen: Prof. Dr. Hannes Rakoczy
Georg-Elias-Müller-Institute, Department of Developmental Psychology, Göttingen

09/2003 – 06/2011 **Abitur, Gymnasium Paul-Gerhardt-Schule Dassel**